ABSTRACT

The thesis covers a range of topics relevant to the current and future gravitational-wave facilities. After the last science observing run, O3, that ended in March 2020, the aLIGO and VIRGO gravitational-wave detectors are undergoing upgrades to improve their sensitivity. My thesis focuses on the work done at the LIGO Hanford Observatory to facilitate these upgrade activities. I worked to develop two novel technologies with applications to gravitational-wave detectors. First, I developed a high-bandwidth, low-noise, flexure-based piezo-deformable mirror for active mode-matching. Mode-matching losses limit improvements from squeezing as they distort the ground state of the squeezed beam. For broadband sensitivity improvements from frequency-dependent squeezing, it is critical to ensure low mode-mismatch losses. These piezo-deformable mirrors are being installed at the aLIGO facilities. Second, I worked to develop and test a high-resolution wavefront sensor that employs a time-of-flight sensor. By achieving phase-locking between the demodulation signal for the time-of-flight sensor and the incident modulated laser beam, this camera is capable of sensing higher-order mode distortions of the incident beam.

Cosmic Explorer is a proposed next-generation gravitational-wave observatory in the United States that is planned to be operational by the mid-2030s. Cosmic Explorer along with Einstein Telescope will form a network of next-generation gravitational-wave detectors. I propose the science-goal-focused tunable design of the Cosmic Explorer detectors that allows for the possibility to tune with sensitivity at low, mid, and high frequencies. These tuning options give Cosmic Explorer the flexibility to target a diverse set of science goals with the same detector infrastructure. The technological challenges to achieve these tunable configurations is presented. I find that a 40 km Cosmic Explorer detector outperforms a 20 km in all key science goals other than access to post-merger physics. This suggests that Cosmic Explorer should include at least one 40 km facility. I also explore the detection prospects of core-collapse supernovae with the third-generation facilities – Cosmic Explorer and Einstein Telescope. I find that the weak gravitational-wave signature from core-collapse supernovae limits the likely sources to within our galaxy. This corresponds to a low event rate of two per century.

DETECTOR IMPROVEMENTS AND OPTIMIZATION TO ADVANCE GRAVITATIONAL-WAVE ASTRONOMY

By

Varun Srivastava

B.S. Indian Institute of Science Education and Technology
M.S. Indian Institute of Science Education and Technology, Pune

Dissertation
Submitted in Partial Fulfillment of the Requirements
for the degree of
Doctor of Philosophy in Physics

Syracuse University
February 2022

ACKNOWLEDGEMENTS

I would first like to thank my advisor Stefan Ballmer. I am very thankful for your support and guidance all through these years. I greatly admire your scientific temperament and aptitude, and this is what I strive to achieve. I could not have had a better graduate school experience than working in your research group in the Syracuse optics lab and the LIGO Hanford lab.

I can not think of anyone better than Jenne Driggers, Sheila Dwyer, and Jeff Kissel in explaining the intricacies of the LIGO detectors to graduate students like me. Thank you so much for your patience while teaching me different aspects of commissioning, and for finding the time to discuss and answer my doubts. I would like to thank Daniel Sigg for providing the answers commissioning puzzles, the amazing Thursday dinners and the best wines. Thank you Georgia and Craig for all the guidance with commissioning while working at Hanford. Special thanks to Georgia for the valuable feedback on the thesis. Thank you, Rick, Mike, and Felicia for helping me set up in Richland during the difficult Covid times. It has been a great pleasure working at the site because of all of you.

I would like to thank Fabrice Matichard and Peter Fritschel for their guidance during the development and testing of the SAMS PZT actuators. Thank you Gari-Lynn Billingskey, Camille Makarem, Rich Abbott, and Georgia Mansell for all the help with testing the prototype with the Zygo interferometer.

I have enjoyed working on the design and optimization work for Cosmic Explorer. It was great to be a part of the Cosmic Explorer Horizon Study team. Thank you, Evan Hall and Kevin Kuns for all the help, support and guidance with the work on the Horizon Study. I am extremely thankful to Joshua Smith, Matt Evans, and Chris Wipf for the guidance and support for different problems I faced. I would like to thank Philippe Landry, Jocelyn Read, Derek Davis, and Sathyaprakash for their immense support in the work on binary neutron-star post-merger and tidal optimizations. I would like to thank Duncan Brown and Adam Burrows for their guidance in the work on supernovae optimized gravitational-wave detectors. It has been a great learning experience being a part of this team.

I would like to thank Peter Saulson for the amazing course on gravitational-wave detectors. I greatly admire your teaching style in ensuring that each student understands physics at the fundamental limit without any jargon. Thank you for your guidance. Thank you, Fabian, Danny, and TVo for all the help and guidance in getting me acquainted with the lab work at Syracuse.

I would not have dared to transition from gravitational-wave data analysis to instrumentation if it was not for the wonderful learning experience at the 10 m prototype at AEI Hanover. I am thankful to Harald Leuck, David Wu, Vaishali Adya, and other members of the 10 m prototype lab for the amazing first experience while working on gravitational-wave instrumentation.

Special thanks to my mentor Sukanta Bose for your continued mentorship over the years. I am thankful for the opportunity to work at the IUCAA gravitational wave physics group. I thank Varun Bhalerao, Rajesh Nayak, Bhooshan Gadre, and other colleagues at IUCAA for providing a diverse outlook to the field of gravitational-wave astronomy. Thank you, Sourabh Dube, Seema Sharma, and Surjeet Singh, for your support, mentorship, and encouragement towards research.

I am thankful for the support of the physics department. Thank you, Phil, Charlie, and David at the machine shop for machining the SAMS project design changes in record time, which facilitated testing of the design. For the amazing friends and classmates - Chaitanya, Joe, Liz, Manu, Maxx, Nick, Ohana, Sarthak, and many more for all the fun at Syracuse. Special thanks to my school friends Archi, Shivam, Swapnil, and Vedant for their support over the years.

Erik, it was a pleasure working with you on developing the phase camera. Thank you, Ari, Danny, Derek, Erik, Nick, Steven, Elenna and Subham for making the work in the Syracuse gravitational-wave group fun. You are the people who made working here special and I miss all of you. I hope we continue having our ‘group meetings’ every week.

Thank you, Abhijit, Abhishek, and Vished for being there whenever I was at my lowest.

I would like to thank the Dawson family and the Peacock family for their support and love. To my love, Ellie, thank you for your love, support, and wonderful company. Thank you for proof reading all my papers. You made living through this pandemic so easy.

Lastly, I am very glad to have the love and support of all my family members. Thank you for your continued support and affirmation. Love you Mom, Dad, and Vini!

Contents

List of Tables

List of Figures

Dedicated to my Grandparents,
Surendra Tauji, and Shashi Taiji.

Preface

The work presented in this thesis stems from my participation in the LIGO Scientific Collaboration (LSC). This work does not reflect the scientific opinion of the LSC and it was not reviewed by the collaboration.

Chapter 1

Gravitational-Wave Detectors: Practical Limitation of the Current Facilities and the Promise of the Future!

This chapter outlines some of the aspects of Einstein's theory of General Relativity, which to date is the simplest and most complete theory of gravity. Next, I will briefly describe gravitational waves and ground-based detectors like aLIGO, VIRGO, which use laser interferometers to detect gravitational waves. Lastly, this chapter will discuss the fundamental and technical limitations of the current ground-based detectors and the proposed next-generation detectors, which will revolutionize our understanding of physics, astrophysics, and cosmology.

1.1 General Theory of Relativity

At the time of the formulation of the general theory of relativity, the observed precession of Mercury around the sun was unexplained. Newton's theory of gravity does not allow the possibility of precessing orbits. Moreover, the special theory of relativity postulates that no physical information can travel faster than the speed of light. This is a fundamental flaw in Newton's theory of gravity, which allows gravity to propagate at an infinite speed. In other words, Newton's theory of gravity lays out the gravitational field between two objects by the virtue of their mass, this field could propagate any distance without any time delay. This nature of fields that are allowed by Newton's theory of gravity is in flux with the postulates of the special theory of relativity.

Einstein's special relativity is based on two postulates. First, the laws of physics are the same everywhere (in all reference frames). Second, the speed of light in a vacuum is the same for any observer and is independent of the frame of reference. General relativity is an extension to the weak equivalence principle[1] with the first postulate of special relativity. General relativity conceptualizes that there is no difference between a object's motion (as in special relativity) when subjected to a gravitational field (g) and a freely falling inertial frame accelerating with g.

Using Einstein's equivalence principle and the conservation of the energy-momentum, one can derive the Einstein's equations for General Relativity

$$G_{\mu\nu} = \frac{8\pi G}{c^4} T_{\mu\nu} \tag{1.1}$$

where $G_{\mu\nu}$ is the curvature of space-time, $T_{\mu\nu}$ is the energy-momentum tensor. Wheeler described Einstein's field equation as 'Space-time tells matter how to move; matter tells space-time how to curve'. The coupled differential equations can be solved analytically or numerically with different approximations. General relativity explained the orbital precession of Mercury[2], and offered a large set of predictions that could be experimentally tested. Over hundreds years of tests to the general theory of relativity, no experimental deviations from theoretical predictions have been found.

The summary of key predictions of General Relativity and their first experimental verification is given below:

1. *Gravitational field bends the trajectory of light.* First experimental evidence of the bending of light by Eddington, 1919.

   The deviation in the observed location of the bright group of stars *Hyades* between the night and during the total solar eclipse of the sun in 1919 showed

---

[1] The weak equivalence principle (or the universality of free fall) states that the motion of any freely falling object in a gravitational field is independent of its composition.

[2] At the time of the formulation of General Relativity, the observation of precession in the orbit of Mercury was an unexplained phenomenon. Newton's theory of gravity does not allow for the precession of planetary orbits.

that light does bend in the gravitational field. Moreover, the observed angular deviation agreed with Einstein's prediction. This was the first experimental verification of one of the predictions of General Relativity.

2. *Gravitational Redshift.* The light source sent towards a gravitational well is blueshifted, whereas the one away from it is redshifted[3]. The first uncontested evidence of gravitational redshift was provided by Popper, 1954 [7].

   Popper estimated the redshift in the hydrogen line spectrum of white dwarf 40 Eridani B. The observed gravitational redshift was consistent with predictions from General Relativity.

3. *Gravitational waves.* In 1916, Einstein predicted gravitational waves from the field equations, described later in this chapter. Drawing parallels between electromagnetism, Einstein showed that in free space gravitational waves travel at the speed of light, and they have two polarizations. The LIGO detectors observed the first gravitational waves in 2015 [8].

   The gravitational waves from the merger of two black holes were observed using two ground-based laser interferometer LIGO detectors, discussed in §1.3. This gravitational-wave signal and the observed polarization were consistent with the predictions of General Relativity.

4. *Black Holes.* In 1915, Schwarzschild was the first to offer the first exact solution to the Einstein field equation (This was before Einstein solved it for gravitational waves). Schwarzschild coined the solutions as black holes but thought the solutions were physically meaningless.

   The first observation evidence on the existence of black holes came to light through X-ray observation of Cygnus X-1. The radial velocity profile suggested a compact binary star system of $3M_\odot$ and $12M_\odot$ objects [9, 10].

The incompleteness in the theory of General Relativity is the classical treatment of gravitational fields. In particular, General Relativity is not quantized and does not answer fundamental questions like particles responsible for mediating gravitational

---

[3] Blueshift implies that the observed frequency of a source is higher while redshift implies the observed frequency is lower.

interactions. That is, it does not predict a candidate particle that acts as a mediator of gravity. We will discuss gravitational waves in section §1.2. The LIGO detectors are discussed in the next section §1.3. Improved sensitivity of the gravitational-wave detectors will provide better tests of General Relativity, discussed in chapter 7. The current limitations to their sensitivity and the areas of active research to facilitate the science with the next-generation detectors is discussed in section §1.4.

1.2 Gravitational Waves

The thesis is focused on the upgrades and construction of instruments to observe gravitational-waves, along with the astrophysics, cosmology, fundamental physics that is offered by gravitational wave astronomy. Therefore, we will give a little deeper into the understanding of the origin of gravitational waves, and the required sensitivity to observe gravitational waves from astrophysical sources.

Consider small perturbations $h_{\alpha\beta}$ of the spacetime metric from the flat spacetime metric defined by the Minkowski metric $\eta_{\alpha\beta}$ with signature [-1, 1, 1, 1]. The spacetime metric $g_{\alpha\beta}$ can then be defined as

$$g_{\alpha\beta} = \eta_{\alpha\beta} + h_{\alpha\beta} \tag{1.2}$$

Under the weak field assumption, one can define raising and lowering operations on $h_{\alpha\beta}$ using the Minkowski metric according to

$$h^{\gamma}{}_{\beta} = \eta^{\gamma\alpha} h_{\alpha\beta} \quad \text{and} \quad h^{\gamma\delta} = \eta^{\delta\beta} h^{\gamma}{}_{\beta} \tag{1.3}$$

The trace h is then given by

$$h = h^{\alpha}{}_{\alpha} = \eta^{\alpha\gamma} h_{\gamma\alpha} \tag{1.4}$$

A trace reverse tensor of $h_{\alpha\beta}$ is defined as

$$\bar{h}^{\alpha\beta} = h^{\alpha\beta} - \frac{1}{2}\eta^{\alpha\beta} h \tag{1.5}$$

Using the Minkowski tensor, it can be shown the trace of $\bar{h}^{\alpha\beta}$ is equal to $-h$. Using these relationships that arise under the weak field approximation, the Einstein Eq. 1.1 simplifies to

$$G^{\alpha\beta} = -\frac{1}{2}\Big(\nabla^2 - \frac{1}{c^2}\frac{\partial^2}{\partial t^2}\Big)\bar{h}^{\alpha\beta} = \frac{8\pi G}{c^4} T^{\alpha\beta} \tag{1.6}$$

where $\bar{h}^{\alpha\beta}$ is the trace reverse tensor.

We find in the vacuum state ($T^{\alpha\beta}$=0), the Eq. 1.6 simplifies to a plane wave equation

$$\left(\nabla^2 - \frac{1}{c^2}\frac{\partial^2}{\partial t^2}\right)\bar{h}^{\alpha\beta} = 0 \tag{1.7}$$

with wave solutions given by

$$\bar{h}^{\alpha\beta} = A^{\alpha\beta} \cdot exp(i \cdot k_\mu x^\mu) \tag{1.8}$$

Next, using the Lorentz gauge condition on the wave solution in Eq. 1.8 yields

$$A^{\alpha\beta} k_\beta = 0 \tag{1.9}$$

which is identical to the electromagnetic wave equation — the amplitude of the wave $A^{\alpha\beta}$ is orthogonal to the direction of wave propagation k_β.

Further, the field must be gauge invariant which constrains the $A^{\alpha\beta}$ in two ways. First,

$$A^{\alpha}{}_{\alpha} = 0 \tag{1.10}$$

This condition yields that $A^{\alpha\beta}$ must be traceless. From Eq. 1.5, this implies that $\bar{h}^{\alpha\beta}$=$h^{\alpha\beta}$. Second,

$$A_{\alpha\beta} U^\beta = 0 \tag{1.11}$$

where U^β is a velocity four vector.

For a wave propagating in the z-direction, the requirements of Lorentz gauge and gauge invariance (using Eq. 1.9, 1.10 and 1.11) define the transverse-traceless gauge, that yields two independent elements in the the amplitude $A_{\alpha\beta}$. These two independent elements are the two polarizations of the gravitational waves predicted in General Relativity, represented by h_+ and $h_\times$.

$$A_{\alpha\beta} = \begin{bmatrix} 0 & 0 & 0 & 0 \\ 0 & h_{xx} = h_+ & h_{xy} = h_\times & 0 \\ 0 & h_{yx} = h_\times & h_{yy} = -h_+ & 0 \\ 0 & 0 & 0 & 0 \end{bmatrix} \tag{1.12}$$

In summary, we showed that the gravitational radiations in traveling in vacuum have two polarizations. Considering two points in space separated by a distance L. The distorted distance between them as the gravitational-wave passes through is given by

$$L' = \int_{x=0}^{x=L} |g_{\alpha\beta} dx^\alpha dx^\beta|^{1/2} \approx (1 + \frac{h_{xx}}{2})L \tag{1.13}$$

Thus, the propagation of gravitational-wave causes changes in the relative distance between points in space ($h \approx \Delta L/L$). However, we did not talk about the origin of gravitational or their physical amplitude from astrophysical sources.

Quadrupole Approximation

To understand the origin of gravitational waves, we will consider a source under periodic motion with frequency Ω. Thus, the source term in Eq. 1.6 can be approximated as

$$T^{\alpha\beta} = S^{\alpha\beta} exp(-i\Omega t) \tag{1.14}$$

Also assuming the scale of motion with the source is much lower than the wavelength of the gravitational wave Ω, which allows us to use the guess the gravitational wave solution as

$$\bar{h}^{\alpha\beta} = B^{\alpha\beta} exp(-i\Omega t) \tag{1.15}$$

Plugging Eq. 1.14 and 1.15 in Eq. 1.6 yields

$$(\nabla^2 + \Omega^2) B^{\alpha\beta} = \frac{16\pi G}{c^4} S^{\alpha\beta} \tag{1.16}$$

The above equation can be solved outside the source i.e. $S^{\alpha\beta}$. We define the inertia tensor given by

$$I_{jk} = \int T^{00} x_j x_k d^3x \tag{1.17}$$

Then the gravitational-wave amplitude in quadrupole approximation is given by

$$h_{jk} = \frac{2}{r} \frac{d^2 I_{jk}}{dt^2} \tag{1.18}$$

I will skip straight to the solution in transverse-traceless gauge for a wave propagating along the z-direction at a distance r from the source below

$$h_{xx} = -h_{yy} = -\Omega^2 (\bar{I}_{xx} - \bar{I}_{yy}) \frac{e^{i\Omega r}}{r} \tag{1.19}$$

$$h_{xy} = -2\Omega^2 \bar{I}_{xy} \frac{e^{i\Omega r}}{r} \tag{1.20}$$

where $\bar{I}_{jk}$ is the transverse-traceless quadrupole moment tensor.

$$\bar{I}_{jk} = I_{jk} - \frac{1}{3} \delta_{jk} I^l_l \tag{1.21}$$

The key implication that arises from quadrupole approximation is that gravitational waves are produced by time-varying quadrupole moment. Therefore, any spherically symmetric motion or cylindrically symmetric motion can not produce gravitational waves. To detect gravitational waves from binaries of black holes or neutron star requires a strain sensitivity ($\Delta L/L$) better than 10^{-23} Hz$^{-1/2}$ in broadband of frequencies from 10 to 2000 Hz.

1.3 Advanced LIGO Detectors

The advanced LIGO detectors are 4 km long dual-recycled Fabry-Perot interferometers to achieve this sensitivity. Fig. 1 shows the top-level design of the aLIGO detectors.

Achieving a strain sensitivity of 10^{-23} Hz$^{-1/2}$ below a kHz is incredibly challenging. The fundamental sources of noises that limit the aLIGO design sensitivity are discussed below. Additionally, to achieve this sensitivity over a sustained period of time one needs to achieve stable operation by effective control loops and keeping the overall 'technical' noises lower than the fundamental noises[4]. We discuss these noise sources in detail in section §1.4. The noise budget of the aLIGO detectors at design sensitivity is shown in figure 2.

- *Quantum Noise*: The quantum noise in the gravitational wave detectors manifests itself in two ways — photon shot noise and radiation pressure noise. The gravitational wave signal is measured by the differential motion of the two Fabry-Perot arms of the interferometer using the beam that leaks through the anti-symmetric port of the Michelson. The quantum nature of photons defines the fundamental uncertainty in the ability to count the number of photons at the photodetectors. The photon shot noise in the low frequency limit can be expressed as [11]

  $$h_{shot} = \frac{1}{nL}\sqrt{\frac{\hbar c\lambda}{2\pi P_{in}}} \tag{1.22}$$

  where n is the number of round trips, L is the length of the arms, P_{in} is the input power. The radiation pressure noise arises from the displacement of the test masses due to the momentum imparted by the flux of photons resonant in

---

[4] Technical embodies a wide set of noise sources — actuator noise, control loops, optical noises from mode-mismatch, scattering, etc. [1].

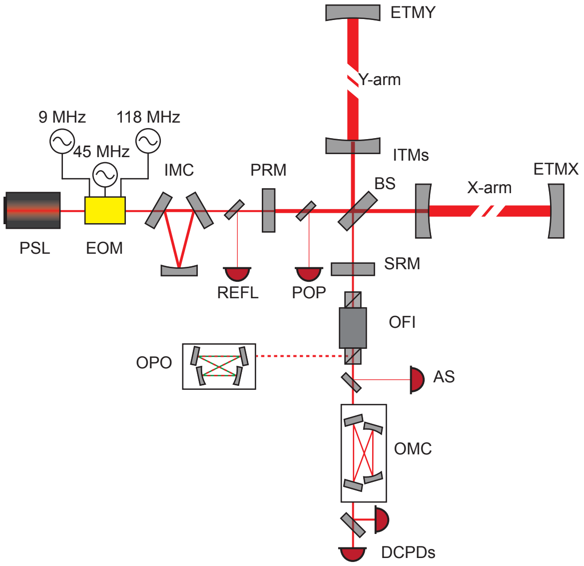

Figure 1: Simplified layout of the aLIGO detectors. The 2 W NPRO laser is amplified and stabilized in intensity using a reference cavity. Next the frequency of the amplified laser is stabilized using a premode cleaner. This infrastructure to stabilize the laser in frequency and intensity is referred as pre-stabilized laser (PSL). Next, the phase sidebands are introduced for length and angular control using an electro-optic modulator (EOM). The frequency of the laser then is further stabilized with an input-mode cleaner (IMC). The beam in transmission of the IMC enters the dual-recycled Fabry-Perot interferometer. The two Fabry-Perot cavities (X-arm and Y-arm) are formed with the input test mass (ITM) and the end test mass (ETM) separated by 4 km. The beamsplitter (BS) and the ITMs form the Michelson interferometer. In the symmetric port of the Michelson the power-recycling mirror (PRM) is a coupled cavity to reduce the reflected power which otherwise would leak when the anti-symmetric port is on a dark fringe. Lastly, at the anti-symmetric port of the Michelson the signal-recycling mirror (SRM) forms a coupled cavity with the ITMs which increases the effective input transmittance of the test masses, thus ‘recycling’ the anti-symmetric signal. Here signal recycling is a misnomer, signal extraction used in a more apt as the SRM changes the effective signal bandwidth. The anti-symmetric port of the Michelson is a DC readout on photodiodes (DCPDs) of the gravitational wave signal, which is first cleaned with the output-mode cleaner (OMC). The REFL, POP and AS are photodiodes ports that provide error signals for length and angular control.

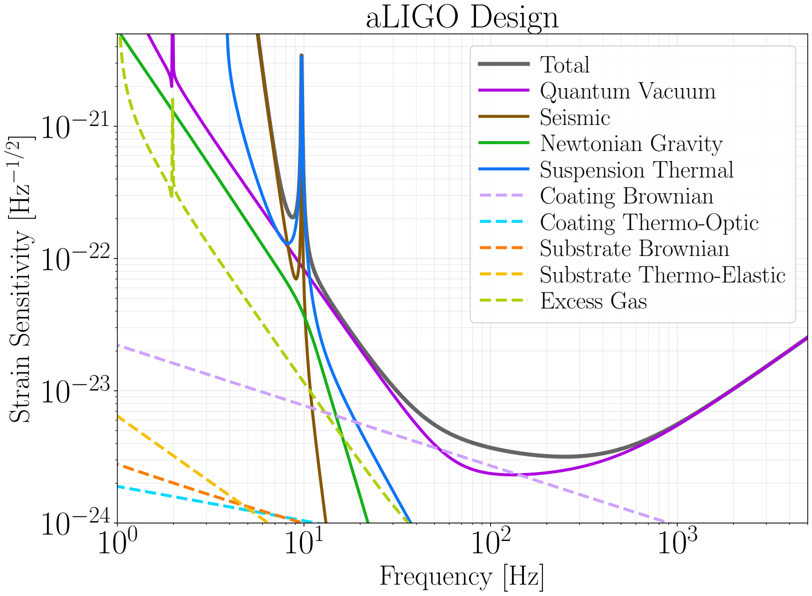

Figure 2: The noise budget of advanced LIGO detectors at design sensitivity.

the cavity. This can be expressed as [11]

$$h_{rp}(f) = \frac{n}{Lmf^2}\sqrt{\frac{2\hbar P_{in}}{\pi^3 c\lambda}} \tag{1.23}$$

where m is the mass of the test masses. The total quantum noise is the quadrature sum of the shot noise and the radiation pressure noise. Notice that from the equations above, the shot noise reduces with the number of round trips and the incident power whereas the radiation pressure noise worsens. Also, increasing the length of the arms scales both noises down, which is one big driver for bigger gravitational wave detectors. Lastly, the radiation pressure noise reduces with heavier test masses. However, there are practical limitations to the manufacture of bigger and heavier test masses with the required high optical quality.

- *Seismic*: The ambient ground motion from the seismic activity is several orders of magnitudes higher than what is required for the test masses in gravitational wave detectors. Typically the seismic activity at 100 Hz is of the order of 10^{-11} m/$\sqrt{\text{Hz}}$, which is substantially higher than 10^{-20} m/$\sqrt{\text{Hz}}$, which is the required to build the detectors sensitive enough to detect gravitational waves. To damp down this seismic motion aLIGO uses a quadruple suspension that acts as a low pass filter below the resonance frequencies, providing vibrational isolation to the test masses [12, 13]. In addition to the passive damping of the test masses from the suspensions, active damping is also required for actuation in the design of active feedback control loops. Therefore, test masses and other auxiliary optics in aLIGO detectors are both actively and passively damped. The low-frequency sensitivity of aLIGO design is limited by the residual seismic motion from the suspensions, which cannot provide effective damping at lower frequencies.

- *Newtonian Gravity*: The motion-induced on the test masses from the ambient seismic motion in the environmental surroundings. This noise also is most significant at frequencies below 10 Hz. With improved seismometers and environmental sensors, it is possible to subtract this noise [14, 15].

- *Thermal Noise*: The thermal noise arises due to the displacement noise of the test masses due to the Brownian motion of the atoms and molecules in suspensions, substrate, and coating of the test masses. The fluctuation-dissipation theorem states that for a linear system in thermodynamic equilibrium, the thermal fluctuations lead to dissipated power in the system and vice-versa. The thermal noise, therefore, increases with increased mechanical loss, and loss angle. Kindly refer to reference [16] for a detailed description. In figure 2, the suspension thermal, coating Brownian, coating thermo-optic, substrate Brownian, and substrate thermo-elastic contribute to the noise in aLIGO due to the coupling described above.

- *Excess Gas*: Any excess gas molecules in the chamber cause scattering of the main beam causes phase noise. Additionally, they also cause ambient motion of the test masses due to the force imparted on them. The aLIGO detectors are under ultra-high vacuum.

1.4 Technical Noises in Advanced LIGO Detectors

The previous section described the analytical estimate of the noise sources to advanced LIGO sensitivity. What is not captured in the earlier discussion is the challenge in the complex control schemes for operating the detector with all the coupled cavities, shown in figure 1, locked to the laser. To achieve this stable lock requires all degrees of freedoms to be suppressed. There are five degree of freedom in the length of different cavities

1. Michelson (MICH): The length of the Michelson from the beam splitter to the x (and y) test masses be l_x (and l_y). Then the Michelson length degree of freedom is $l_{MICH} = l_x - l_y$.

2. Power-recycling cavity (PRC): The length of the power recycling cavity ($l_{PRCL} = l_p + (l_x + l_y)/2$), where l_p is the length of from the beamsplitter to the power-recycling mirror.

3. Signal-recycling cavity (SRC): The length of the signal recycling cavity ($l_{SRCL} = l_s + (l_x + l_y)/2$), where l_s is the length of from the beamsplitter to the signal-recycling mirror.

4. Common arm (CARM): The common arm length of the two 4 km long Fabry-Perot arms L_x and L_y is $L_{CARM} = (L_x + L_y)/2$.

5. Differential arm (DARM): The differential arm length of the two 4 km long Fabry-Perot arms L_x and L_y is $L_{DARM} = L_x - L_y$.

Using the 9 MHz and the 45 MHz sidebands for Pound-Drever-Hall locking each of these degrees of freedom are actively controlled. The length of the input-mode cleaner and the output-mode cleaner are two additional length degrees of freedom that are actively controlled. Besides the need to actuate in length, angular degrees of freedom is of great relevance. Each pointing degree of freedom needs to be controlled in pitch and yaw. These can be broadly divided into two categories — arm and corner. The corner angular degree of freedom comprises input alignment, power recycling cavity, Michelson, and the signal recycling cavity. The arm angular degree of freedoms consists of the common and differential basis 'soft' and 'hard' modes [17, 18]. The complexity of the angular controls requires 16 degrees of freedom to be actively sensed and controlled for stable operation of the gravitational-wave detectors when the arm-cavities are on resonance.

To understand the performance of the gravitational wave detectors, we need to measure the contribution of each of the noise sources that were analytically estimated in the previous section. This allows to scope out coupling which can be minimized or improvements can be targeted to mitigate excess noise to improve the overall sensitivity of the detector. Fig. 3 shows the noise budget of the Hanford detector during the third observing run — O3. As is evident from the figure, the actual noise budget of the detector is a lot more complicated. Each of the noise sources in the figure is either calculated using optical models or material properties of the interferometer or projected by estimating the couplings from the auxiliary channels [1]. The noise sources shown in figure 3 are described below, refer to [1, 19] for details about this noise budget.

- *Auxiliary length control*: The noise coupling the the DARM readout arising from coupling from the various length degrees of freedom.
- *Alignment control*: The noise coupling the the DARM readout arising from angular sensing and control.
- *Beam jitter, Laser intensity, and Laser frequency*: The noise in laser intensity and frequency stabilization loops, and from the mode-mismatch causing beam jitter of the fundamental laser mode.
- *Scattered light*: The phase noise injected in DARM due to the scattering of the laser beam.
- *OMC length*: The noise coupling to DARM due to the length noise in the OMC.
- *Photodetector dark noise*: The electronic noise in the photodetector when there is no light incident on it is called dark noise.
- *PUM DAC noise*: The DARM control loop is controlled in advanced LIGO by driving the electrostatic drivers on the penultimate mass (PUM) of the suspension. The noise from digital-to-analog (DAC) of the control signal is referred to as PUM DAC noise.

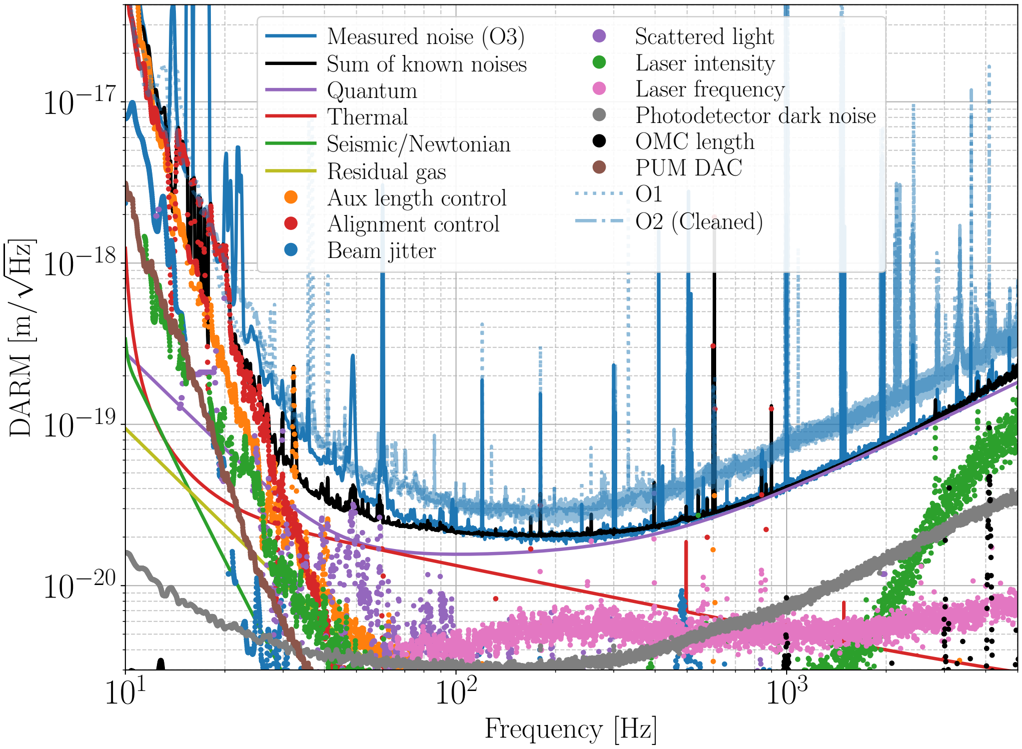

Figure 3: The noise budget of the LIGO Hanford detector during the O3 [1]. Note that the measured noise during O3 (blue) and sum of the noise sources (black) agrees well at frequencies above a 100 Hz. However, there is lack of understanding of the noise limiting us in the frequency band from 20-100 Hz. This unknown noise is referred to as 'Mystery noise'. Image source: O3 commissioning paper [1].

Chapter 2

Commissioning the aLIGO Hanford detector for O4 Science Run

This chapter presents the work on the ongoing projects at the LIGO Hanford Observatory. ‘Commissioning’ is a loose term that refers to a range of activities at each observatory. These activities range from upgrades to the various sub-systems within LIGO (laser, suspensions, squeezer, etc.), installation of new technologies to improve the sensitivity, hunting for noise couplings and their mitigation, and so on.

My key work during early O4 commissioning is the measurement of the noise coupling from the misalignment into the output-mode cleaner (OMC). This exercise was done as a part of noise budgeting discussed in the previous chapter. The goal was to investigate the noise coupling of the alignment sensing and control loop of the OMC. The recommended approach to measure this noise coupling is described in section §2.2.1. I budgeted the motion of the output relay optic (OM1, OM2, and OM3 mirrors) and found that at frequencies below 100 Hz, this control loop is limited by the local damping on the suspensions in all degrees of freedom. The OMC suspension is limited by local damping in length. At frequencies above 100 Hz, we find that the relay optic suspension drive outputs were limited by the noise from the 16-bit digital to analog conversion noise. The noise budget of each mirror and the corresponding solution to the technical limitations discussed above are discussed in section §2.2.2.

2.1 Misalignment and the Origin of Beam Jitter

To understand the origin of beam-jitter the Gaussian beam propagation is expressed in terms higher-order modes in the Hermite-Gauss basis. Assuming a one-dimensional spatial profile, the laser beam propagating in the positive z direction can be expressed as a superposition of the Hermite-Gaussian modes U_n as [20]

$$\begin{aligned} U_n(x,z) = \frac{\Gamma(\frac{n}{2}+1)}{\Gamma(n+1)} \cdot \frac{w_0}{w(z)} \cdot \mathcal{H}_n\left(\frac{\sqrt{2}x}{w(z)}\right)^{1/2} \cdot \exp\Big(i(n+1)\eta(z)\Big) \\ \exp\bigg(-x^2\Big(\frac{1}{w(z)^2}+\frac{ik}{2R(z)}\Big)\bigg)\exp(-ikz) \end{aligned} \tag{2.24}$$

where $k = 2\pi/\lambda$ and λ is the wavelength of the laser, $\Gamma(n)$ represents the Gamma function and $\mathcal{H}_n$ represents the n-th order of Hermite polynomial. At z=0, the beam waist radius is w_0, as the beam propagates the the beam waist radius is given by $w(z)$.

$$w_z = w_0\sqrt{1+\left(\frac{\lambda z}{\pi w_0^2}\right)} \tag{2.25}$$

The beam radius of curvature or the radius of the phase front as the beam propagates is given by $R(z)$.

$$R(z) = z\left(1+\left(\frac{\pi w_0^2}{\lambda z}\right)^2\right) \tag{2.26}$$

The quantity $\eta(z)$ represents the Guoy phase of the laser beam, which is the additional phase accumulated by the laser beam as it propagates relative to a plane-wave.

$$\eta(z) = tan^{-1}\left(\frac{\lambda z}{\pi w_0^2}\right) \tag{2.27}$$

There are four fundamental misalignments that arise in one-dimensional treatment of a two beam interferometer like the Fabry-Perot. Each misalignment excites the higher-order modes of the cavity, which is summarized below [21, 22]. For simplicity we will consider only the spatial features of Eq. 2.24. Now consider two beams in fundamental mode and their axis co-aligned with the z-axis; $E_1 = A_1U_0$ and $E_2 = A_2U_0$.

1. *Beam Tilts*: If the optical axis is tilted by a small angle α with respect to the reference beam. To, first-order in misalignment angle α the second beam can

be approximated as

$$\begin{aligned} E_2 &= A_2 \mathrm{exp}\left(-\frac{x^2}{w_0^2}\right)\mathrm{exp}(ik\alpha x) \\ &\approx A_2\left(U_0 + i\frac{kw_0}{\sqrt{2\pi}}\alpha U_1\right) \end{aligned} \tag{2.28}$$

The tilt misalignment causes a coupling to the first-order mode in the phase quadrature.

2. *Lateral Beam Displacement*: If the optical axis is laterally displaced by a_0 with respect to the beam axis.

$$\begin{aligned} E_2 &= A_2 \exp\left(-\frac{(x-a_0)^2}{w_0^2}\right) \\ &\approx A_2\left(U_0 + \frac{\sqrt{2}a_0}{\pi w_0}U_1\right) \end{aligned} \tag{2.29}$$

   The lateral beam of the optical axis causes an in-phase coupling to the first-order mode.

3. *Waist-Location Mismatch*: We assume that the waist size is w_0 but is displaced by b_0, then using Eq. 2.26 we get

$$R_2 = b_0\left(1 + \left(\frac{\pi w_0^2}{\lambda b_0}\right)^2\right) \tag{2.30}$$

   Now at z=0, assuming $b_0 << \pi w_0^2/\lambda$ we can estimate E_2 to first-order as

$$\begin{aligned} E_2 &= A_2 \exp\left(-\frac{x^2}{w_0^2} - \frac{kx^2}{2R_2}\right) \\ &\approx A_2\left(U_0 - i\frac{b_0}{2kw_0^2}(U_0 + U_2)\right) \end{aligned} \tag{2.31}$$

   The waist-location mismatch causes a coupling to the second-order mode, which is in the phase quadrature.

4. *Waist-Size Mismatch*: Considering the beam-size is mismatched by small amount Δw. Then the second beam to first-order in Δw is given by

$$\begin{aligned} E_2 &= A_2 \exp\left(-\frac{x^2}{(w_0+\Delta w)^2}\right) \\ &\approx A_2\left(U_0 + \frac{\Delta w}{2w_0}(U_0+U_2)\right) \approx A_2\left(U_0 + \frac{\Delta w}{2w_0}U_2\right) \end{aligned} \tag{2.32}$$

   The waist-size mismatch causes an coupling to the second-order mode.

Using these fundamental expressions, the error signals for actively mitigating these misalignments in a Fabry-Perot cavity can be derived and experimentally demonstrated to control each of these degrees of freedom [23, 24, 20]. Our focus is on the origin of the beam jitter due to higher-order modes that are induced by the misalignments in gravitational-wave detectors.

In summary, the above discussion shows that misalignments lead to a mismatched Gaussian beam, which can be expressed in the terms of the perfectly matched (unperturbed) basis. For a generic Hermite-Gaussian beam (HG^q), the mode-mismatch losses can then be defined as

$$\text{Power Overlap} = |\langle \mathrm{HG}^q | \mathrm{HG}^{q'} \rangle|^2 \tag{2.33}$$

where q are the complex beam parameters of the unperturbed system and q' are the parameters of the mismatched system.

$$q = z + i\frac{\pi w_0^2}{\lambda} = z + iz_R \tag{2.34}$$

where z is the distance from the waist and $z_R = \pi w_0^2/\lambda$ is the Rayleigh range. The phase front curvature R and waist size are then defined by

$$\frac{1}{q} = \frac{1}{R} - i\frac{\lambda}{\pi w^2} \tag{2.35}$$

Then using Eq. 2.34 and Eq. 2.24, the fundamental mode can then be expressed as

$$U_0(x) = \frac{A_1}{\sqrt{q}} \exp\left(-i\frac{kx}{2q} \right) \tag{2.36}$$

The power overlap can then be expressed as

$$\begin{aligned} |\langle \mathrm{HG}^q | \mathrm{HG}^{q'} \rangle|^2 &= \left| \frac{2i \cdot \sqrt{\mathcal{I}(q')\mathcal{I}(q)}}{q' - q^*} \right|^2 \\ &\approx 1 - |\epsilon|^2 + \mathcal{O}(\epsilon^3) \end{aligned} \tag{2.37}$$

where ϵ represents the loss in the power from the fundamental mode caused due to scatter into the higher-order modes [25].

The misalignment in tilt or beam position mismatch couple to the fluctuations of the input beam in the presence of static offsets [24]. The beam jitter is expressed as the derivative of the power-coupling expressed in Eq. 2.37, and therefore, is linear with the losses from mode-mismatch. This implies that the coupling goes to zero when the cavities are perfectly mode-matched. However, that is never truly possible as there is always a root mean square (RMS) motion of the suspended mirror. Therefore, close to the perfectly aligned state, there is a residual mean coupling due to the RMS motion of the mirrors. In a misaligned state, the coupling goes as a quadratic function as evident from the power overlap integral. In the next section, I describe the noise budgeting method for estimating the contribution of the output beam jitter coupling to the sensitivity of LIGO detectors.

2.2 Investigating Output Beam Jitter Noise Coupling

Fig. 1 shows the simplified beam path of the LIGO detectors. The actual beam path and sensor layout are a lot more complicated than shown in Fig. 4. The 55 m long signal-recycling cavity is folded with two steering mirrors SR2 and SR3. These mirrors are used for alignment and mode-matching the beam from the interferometer to the signal-recycling cavity.

The gravitational-wave signal is measured using the DC readout scheme which relies on the gravitational-wave signal beating against the fundamental mode of the carrier laser beam that leaks through the anti-symmetric port due to the differential-arm (DARM) offset [26]. This measurement can be polluted by the amplitude-modulated radio-frequency sidebands, the scattered (stray) carrier laser beam, and its higher-order modes. To suppress the noise from the former beams on the DC photodiodes, the aLIGO detectors use a bow-tie cavity as an output-mode cleaner (OMC), which is critically coupled to preferentially allow only the fundamental-mode of the carrier to pass through, thereby suppressing intensity and phase noise[1] [27].

Fig. 4 shows the three mirrors OM1, OM2, and OM3, in the path between the signal-recycling mirror and the OMC. Each of these mirrors is suspended with a single-stage tip-tilt suspension [28, 29]. The OMC is suspended with a two-stage suspension [30]. The mirrors OM1, OM2, OM3, and the OMC suspension can be used for the alignment of the carrier laser beam into the OMC.

---

[1] This is an ideal design statement. The design of the control loop, and the frequencies higher-order modes, may allow some modes to leak in the transmission of the OMC [3].

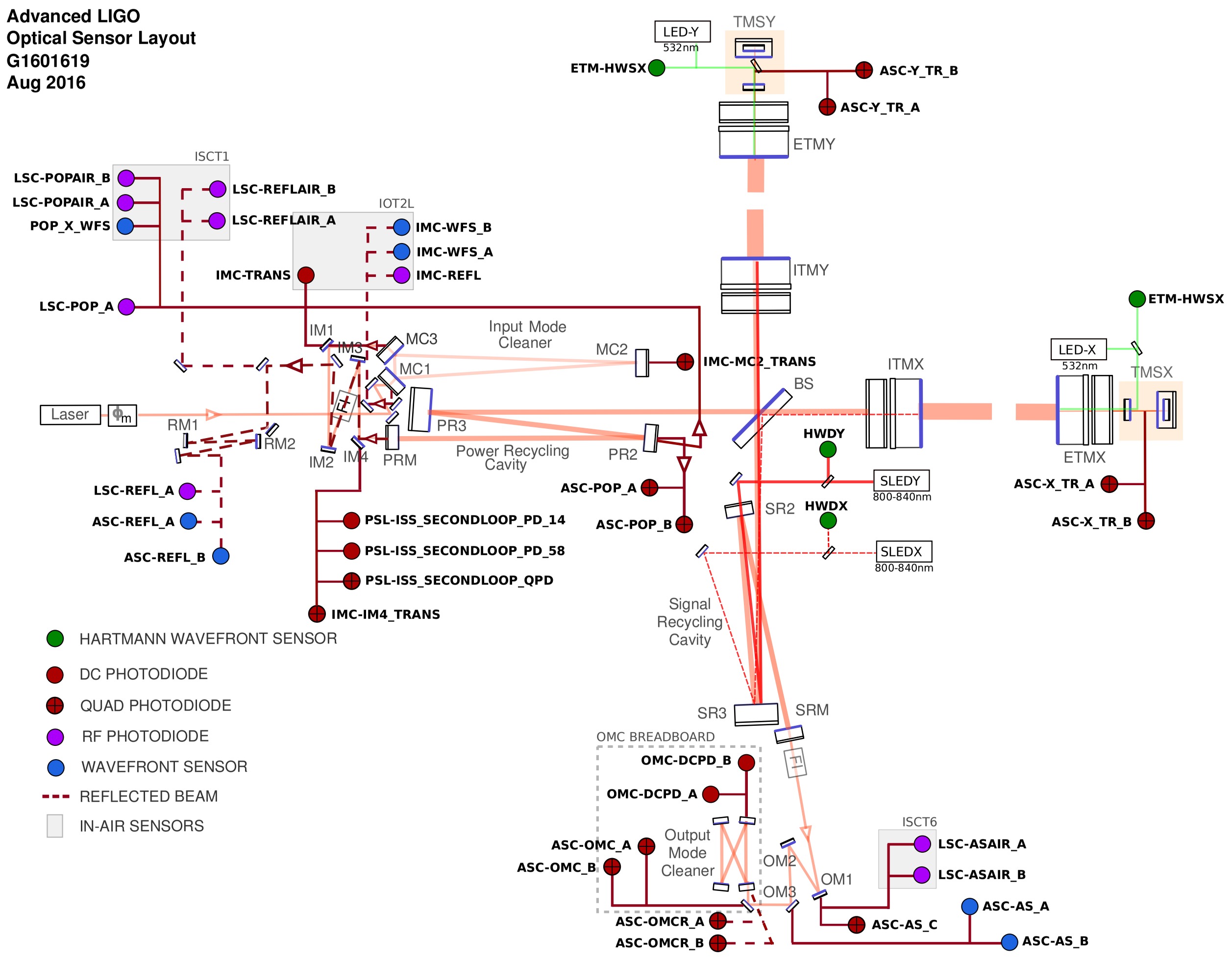

Figure 4: Detailed layout of the LIGO detectors, and sensor ports for active control and sensing [2].

The optimal alignment scheme (beacon) for the alignment into the OMC is presented in Smith et al. [31]. Additionally, there are two other approaches for alignment into the OMC at the LIGO detectors. For completeness, each of these is summarized below. Details of the alignment scheme can be found in Smith et al. [31].

1. *Standard dithering scheme*: In the standard dither scheme, the mirrors are mechanically excited at a given frequency (f_d) for a given degree of freedom (for example pitch). This causes an optical modulation of the beam pointing into the cavity. As an example, in the standard dither scheme at the LIGO Hanford Observatory, the OM1 and OM3 mirrors are dithered in pitch and yaw, at different frequencies. The error signal in a given degree of freedom is produced by demodulating the transmitted power at the corresponding dither frequency. The alignment error signal is servoed to maximize the power in the transmission of the OMC using the signal on the DCPDs at the dither frequencies f_d, see Fig. 4. However, due to the excess stray light due to the point absorbers during the third-observing run [3], the standard dither scheme worsened the broadband sensitivity of the Hanford facility by allowing the scattered light to leak through the OMC to maximize the transmitted power[2]. Instead, the quadrant photodiode (QPD) scheme discussed later was implemented during O3 observing run at the LIGO Hanford Observatory.

2. *Beacon*: This method was developed and employed during enhanced LIGO [31]. In addition to the standard dither excitation, the length of the DARM cavity can be modulated at a frequency f_b to produce a large modulation signal (i.e. beacon) on the DCPDs. The beacon loop servos to zero by maximizing the SNR. This method is currently not used at the LIGO facilities.

3. *QPD scheme*: There are two quadrant-photodiodes (QPDs) ASC-OMC_A and ASC-OMC_B in the transmission of the input steering mirror on the OMC suspension stage, see Fig. 4. The beam position on the two QPDs can be used to infer the alignment into the OMC. Inversely, once a 'good' alignment to the OMC is known, the suspensions are servoed to maintain that particular alignment state using the error signals derived from the corresponding beam positions on the QPDs.

---

[2] LHO alog:48454

The alignment of the beam into the OMC is relevant for two reasons, each of which can limit the sensitivity of the aLIGO detectors. First, the squeezing improvements will be limited if there is junk light that leaks through the OMC. This is possible as the alignment control loops are designed to maximize the power in transmission. Haocun Yu demonstrated improvements in the levels of squeezing by tweaking the alignment into the OMC at the LIGO Livingston detector [32]. This minimized the junk light, which otherwise limited improvements from squeezing. Second, the misalignment into the OMC causes power fluctuations (jitter) in the transmission that is a potential noise source. We will focus on the latter, in particular, on the measurement of the noise attributed to the OMC alignment control loop, and budget its noise contribution to the overall noise budget of the Hanford detector during the first pre-O4 commissioning phase in section §2.2.1. These measurements led to an investigation into the noise budgeting of the motion of the OM1, OM2, OM3, and OMC that is discussed in section §2.2.2.

2.2.1 Measurement and Projection of Alignment Control Noise of Output-Mode Cleaner

Due to the excess junk light due to the point absorber, the LIGO Hanford used the QPD scheme during the third observing run O3. This defective input test mass with the point absorber was replaced prior to the first O4 commissioning phase. No thermal-induced point defects were observed when the circulating power in the interferometer was increased to 260 kW as compared to the trends from O3[3]. Thus, before the measurement of the noise contribution due to the OMC alignment and sensing loop, we compared the noise due to the control signal in the standard dither scheme and the QPD scheme. It was found that both the dither and the QPD scheme have similar controls noise but the DARM optical gain was better for the QPD alignment sensing scheme[4]. The misalignment into the OMC causes output beam jitter in transmission, as discussed in section §2.1. For a two-dimensional beam, there are four alignment degrees of freedom into the OMC — beam position and angle

---

[3] LHO alog:58365

[4] LHO alog:58960

for each dimension[5]. In the nominally aligned state the coupling to beam jitter on DARM is small (attributed to the RMS motion of the mirrors), ideally zero.

To estimate the linear coupling of each OMC alignment loop to LIGO DARM sensitivity, we purposefully misalign the input to the cavity in the corresponding degree of freedom. The former coupling becomes quadratic in the misaligned state, as expressed in Eq. 2.37. The induced intensity noise on the DCPDs (see Fig. 4) appears as an excess broadband noise in DARM when the input is misaligned[6]. The misaligned degree of freedom is then excited with a broadband excitation to estimate the coupling coefficient in the nominally aligned state required to project the noise contribution from the given loop to DARM. The total noise from the OMC alignment sensing and control loop is the quadrature sum of the noise contribution from each degree of freedom.

Procedure to estimate OMC alignment and sensing noise to DARM

For each degree of freedom of the OMC alignment and sensing loop:

1. The OMC is misaligned by increasing the alignment offsets that changes the zero point of the loop. Naively, the OMC is misaligned by increasing the alignment offsets till there is observed 'excess' noise in DARM (channel: H1:CAL-CFTD_DELTAL_EXTERNAL_DQ).

2. As the OMC is misaligned, the optical response of the DARM changes. The 'excess' noise in DARM can therefore be misleading. It is important to apply closed-loop correction to the observed DARM noise spectrum. We use the optical gain readback (channel H1:CAL-CS_TDEP_KAPPA_C_OUTPUT) and apply closed loop corrections using the measured DARM optical gain and the measured open loop gain in the aligned state. The DARM open-loop gain was not measured in the misaligned state in May 2021. Therefore, the measured response in the aligned state is used, which is assumed to be unchanged. However, this is an approximation that asserts the unity-gain frequency (UGF) does

---

[5] X or Y, assuming Z is the direction of beam propagation. For consistency with the LIGO nomenclature of these degrees of freedom, I will refer to them as POS_X, POS_Y, ANG_X, and ANG_Y.

[6] It is very critical that all measured spectrum of DARM in the misaligned state are appropriately closed-loop corrected.

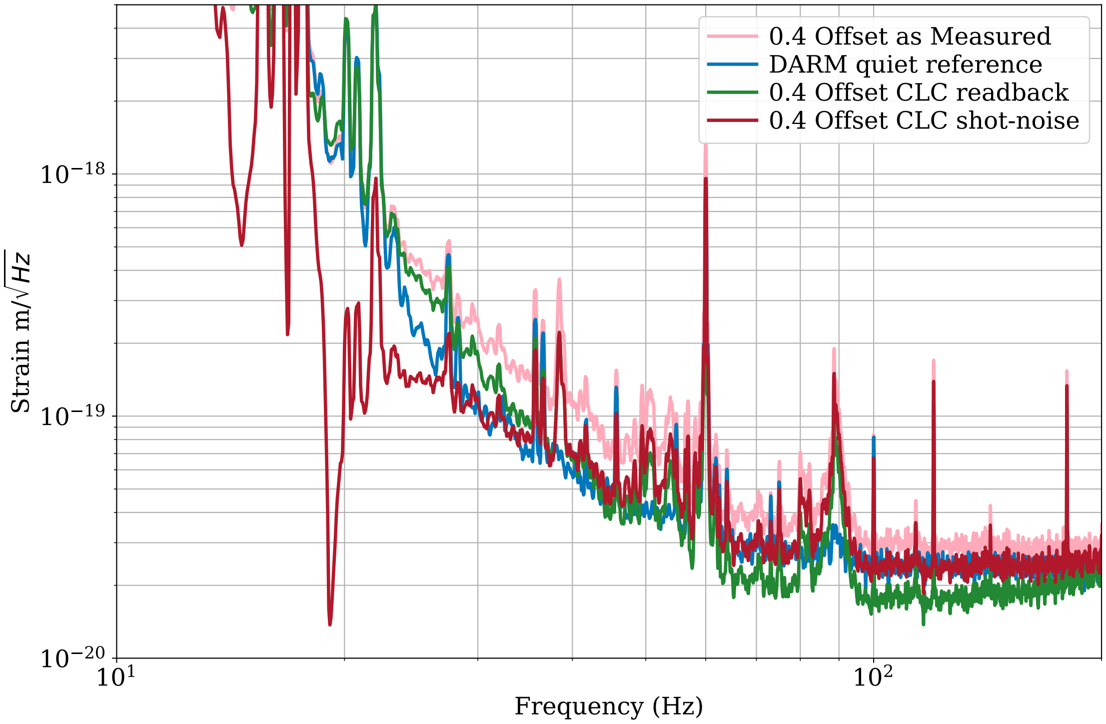

Figure 5: The blue trace is the quiet DARM noise spectrum in the nominally aligned state of the OMC. Increasing the offset in the POSX loop to 0.4 Cts, the 'apparent excess' noise observed in the DARM spectrum is shown in the pink trace. The DARM noise spectrum after applying closed-loop corrections using the measured optical gain (κ_c) and measured DARM response in the aligned state is shown in green. Note that this estimate of DARM noise is unphysical as the applied closed loop correction estimates a lower noise floor above 60 Hz as compared to the nominally 'quiet' DARM. We tweak κ_c by hand to ensure the closed-loop corrected DARM noise is consistent with the shot noise floor of nominally 'quiet' DARM shown in the dark red trace.

not change. Therefore, *it is recommended to measure the calibration function in the misaligned state and apply the closed-loop corrections to the observed noise spectrum, see Fig. 5.*

3. Next, the loop is then excited in a frequency band of 30-38 Hz, at different values of offset from zero to the highest value in the previous step, see Fig. 6. The loop is excited with at least four different values of offset to estimate the coupling coefficient of the loop. As before, the observed spectrum needs to be closed-loop corrected for a meaningful estimate of the observed noise. The RMS area in the excitation band provides the estimate of the noise at each value of offset, which is expected to be quadratic given by:

$$a^2 + b^2 \cdot \mathrm{Offset}^2$$

   where a model the residual motion of the mirror and b represents the quadratic coupling coefficient in the misaligned state on the OMC with offsets in the loop. Fitting the former quadratic to the measured excess noise in the excitation band provides the coupling coefficient (η_c) given by a/b.

4. The noise projection to DARM from this degree of freedom is given by $\eta_c \times \tilde{S}(f)$, where $\tilde{S}(f)$ is the closed-loop corrected spectrum with an offset in the loop (no broadband excitations).

Upper bound noise projection from output beam jitter

At the time of this measurement in May 2021, the open loop response of the DARM plant was not measured in the misaligned state. We use the closed-loop correction using the estimated value of κ_c and the open loop DARM response in the aligned state. *No excess noise was observed in DARM after applying the closed-loop corrections*[7]. If the observed noise is DARM is less than a factor of two from the quiet DARM reference, one cannot estimate the noise coupling to DARM. Therefore, these measurements cannot be used to estimate the noise contribution of the OMC alignment and sensing loop to DARM as estimates of η_c are meaningless. Instead, the upper

---

[7] alog:60278

bound noise contribution is estimated from these measurements. Thus, the measurement for any given OMC alignment sensing and control loop for a given degree of freedom (eg. POSX) can be summarized as follows[8]:

1. The nominal 'quiet' reference of DARM noise is measured.
2. The alignment into the OMC is misaligned by slowly increasing the offsets of the control loop. To ensure the loop has converged the value of κ_c and the drives to suspensions is monitored. The offset is increased till there is observed excess noise in the DARM spectra. For the POSX loop, the offset was increased from zero to 0.4.
3. Next, the alignment loop is excited in a frequency band at different values of offsets in the loop. The POSX loop was excited at an offset of 0.3, 0.2, 0.1 and no offset with the same broadband excitation in frequency band from 30 to 38 Hz. The spectra at each offset value with and without excitation is recorded.
4. The noise projection is then performed offline.
    - The recorded DARM spectra ($S'(f)$) are closed loop corrected using the κ_c according to the offset in the loop and the measured open loop response of DARM in the aligned state to get the closed loop corrected DARM ($S(f)$) according to

    $$S(f) = \frac{1}{1 - \kappa_c \mathrm{G}(f)} S'(f) \tag{2.38}$$

    where $\mathrm{G}(f)$ is the open loop response of DARM.
    - The upper bound of the coupling of a given degree of freedom to DARM ($\mathcal{U}_{dof}(f)$) can then be estimated by

    $$\mathcal{U}_{dof}(f) = \frac{S_{\text{Offset}}(f) - S_{\text{quiet}}(f)}{S^{\delta\text{E}}_{\text{Offset}}(f) - S^{\delta\text{E}=0}_{\text{Offset}}(f)} \tag{2.39}$$

    where S_{Offset} is the closed loop corrected noise in DARM for the corresponding offset, δE denotes the spectra with excitation. Thus, $S^{\delta\text{E}}_{\text{Offset}}$ denotes the closed loop corrected noise in DARM with a given offset while the loop was excited.

---

[8] alog:58970

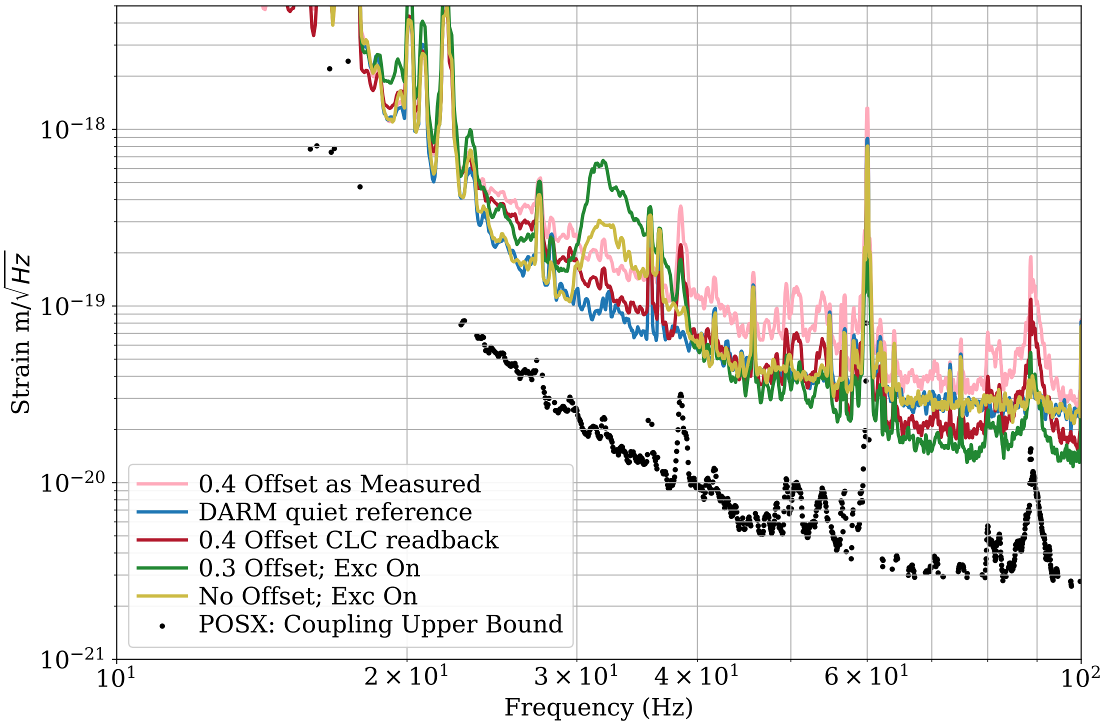

Figure 6: The pink trace shows the observed DARM noise spectrum when the POS-X loop is offset by 0.4. The red trace shows the measured DARM spectrum after the closed-loop corrections are applied to the measured spectrum with 0.4 Cts offset. The green(mustard) traces show the DARM spectrum when the POS-X loop is excited in the frequency range from 30-38 Hz with an offset of 0.3 (zero). The estimated upper bound of the noise from the POS-X loop is shown in black.

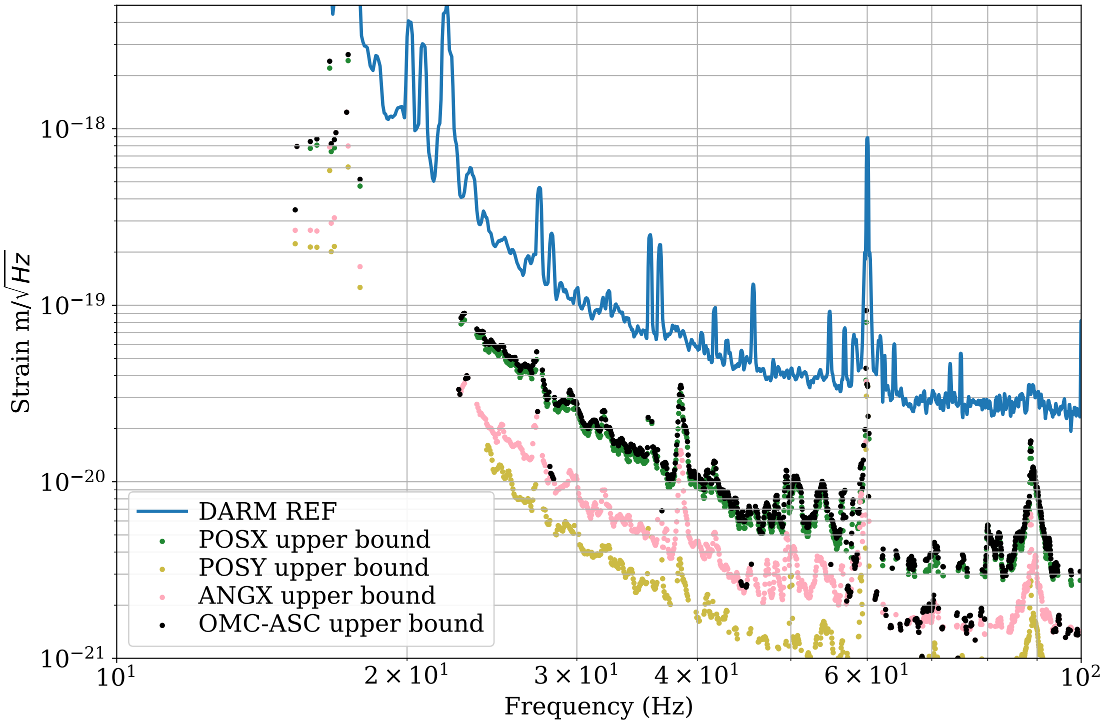

Figure 7: Estimating the upper bound on noise contribution from the OMC alignment and sensing loop. The noise is at least a factor of four below DARM in the broad range of frequency below 100 Hz.

The estimate the upper bound of the noise contribution to DARM from the POSX control loop, which is shown in Fig. 6. The upper bound of the noise contribution to DARM from other degrees of freedom is also estimated using the same approach. The total noise upper bound of the OMC alignment and sensing control loop is estimated as a quadrature sum and is shown in Fig. 7. The noise from the OMC alignment and sensing loop is at least a factor four below the DARM noise floor.

2.2.2 Noise Budget of the Output Mirror Suspensions

The detailed layout of the OMC alignment sensing and control loop is shown for the QPD scheme[9] in Fig. 8. The misalignment error signals are sensed using two QPDs (OMC:QPD A and B) on the OMC breadboard in reflection of the OMC, see Fig. 4. The pitch and yaw readouts of each QPD are used to estimate the beam position and angle into the OMC. This signal is filtered to suppress the 60 Hz peaks, calibration dither lines, and high-frequency signals to derive a meaningful alignment error signal for each degree of freedom of alignment into the OMC. Each of the alignment error signals is zeroed by actuating on the OM3 mirror suspension and the OMC suspensions in length, pitch and yaw. This signal is represented as the OM3 or OMC control signal in Fig. 8, which shows the top level scheme of the OMC alignment sensing and control loop.

Each suspended optic at the LIGO facilities is damped locally. This damping loop is independent of the interferometric error signals, therefore it is referred to as local. Fig. 8 shows these local damping loops for the OMC and the OM3 suspensions in shaded blue boxes. The OM mirrors are suspended using a single-stage suspension [28, 29]. They provide an additional $1/f^2$ isolation above the suspension resonance frequency. The OMC suspension is a double stage suspension, thus, it offers a $1/f^4$ isolation above the suspension resonance frequency [30]. The second stage of this suspension provides passive damping while the first stage of the OMC is actively damped. The AOSEM sensors are used to sense the mirror motion in the local damping loops (corresponding to the degree of freedom of the suspensions − pitch, yaw, longitudinal, etc). However, their sensitivity is limited to $\mathcal{O}$(nrad). The coil drivers actuators are used to damp the suspension motion both from the local damping loop and the interferometric OMC alignment sensing and control loop as shown in Fig. 8.

The total external motion of the OM3 and OMC from the filtered suspension response can then be estimated as the sum of the motion from local damping loops, the OMC alignment sensing and control loop, the electronic noise from the coil driver circuit, and the digitization noise from the digital to analog converters (DAC)[10]. We ignore the closed-loop corrections as we are interested in the frequencies much higher

---

[9] The control loop architecture is similar for the standard dither scheme.

[10] The units of Cts represents the drive in the digital counts from the LIGO digital system.

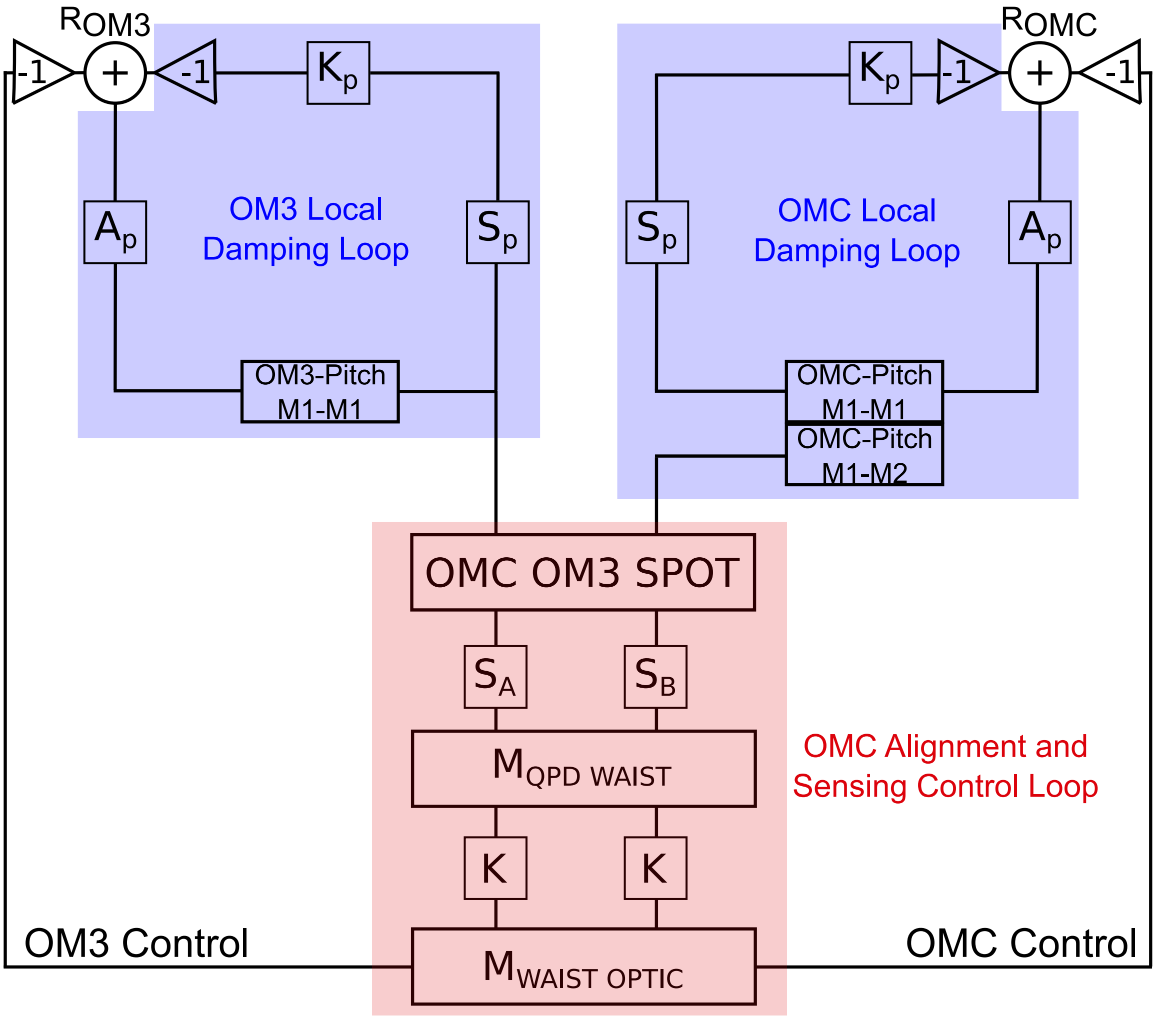

Figure 8: For pitch motion, the figure summarizes the design of the OMC alignment sensing and control loop is shown in the red block. The two quadrant photodiodes A and B provide the error signal for OM3 and OMC control by translating the inferred spot position ($\mathrm{M}_{\mathrm{QPD\ Waist}}$) on the photo-detectors to alignment state of the OMC and OM3 suspension. The blue blocks represent the local damping loop on the OM3 and the OMC suspensions. Together, they summarize all the drives to the OM3 mirror suspension and the OMC suspension, which governs the input beam pointing to the OMC. We use the reference points R_{OM3} and R_{OMC} to trace back all signals required to budget the motion of these suspensions.

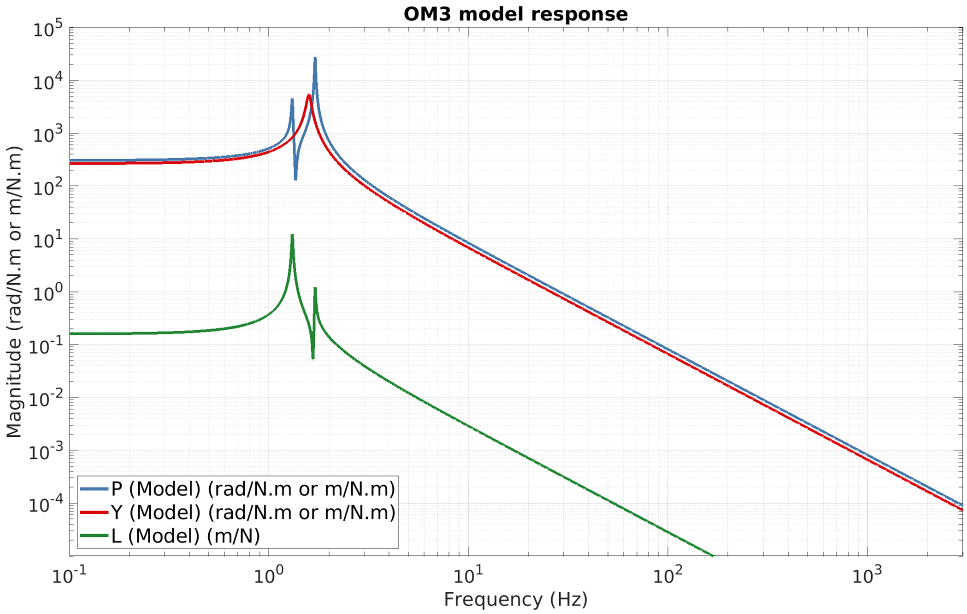

Figure 9: The modeled response of the single stage HTTS suspension used to for the output relay optics – OM1, OM2 and OM3.

than the UGF ($\mathcal{O}$(10 mHz)) of the damping and the OMC-ASC loops. With this assumption, each of these contributions is budgeted as follows:

1. *Local Damping*: The mirror motion from the local damping loop for a particular degree of freedom (dof) is given by

$$\begin{aligned}\delta\theta^{dof}_{damping}\left[\frac{\mu rad}{\mathrm{Hz}^{1/2}}\right] =&\delta\theta^{dof}(\text{single coil})\left[\frac{\mu rad}{Cts}\right]\\ &\times\mathcal{K}^{dof}_{damping}\times\mathcal{P}^{dof}_{\text{DAMP\_INPUT}}\left[\frac{Cts}{\mathrm{Hz}^{1/2}}\right]\end{aligned} \tag{2.40}$$

where $\mathcal{K}_{damping}$ are the local damping filters and $\mathcal{P}_{\text{DAMP\_INPUT}}$ is the power spectrum of the input damp signal that is generated by the AOSEMs. The quantity $\delta\theta$(single coil) is the motion of a single coil driver that is given by

$$\delta\theta^{dof}(\text{single coil})\left[\frac{\mu rad}{Cts}\right] = 4\times L^{dof}_{osem\ lever}[m]\times\mathcal{C}\left[\frac{\mu N}{Cts}\right]\times\mathcal{R}^{dof}\left[\frac{rad}{N.m}\right] \tag{2.41}$$

where $L_{osem\ lever}$ is the length of the lever arm of the AOSEM sensors for the pitch and yaw degrees of freedom and $\mathcal{R}$ is the model of the response of the suspension, as shown in Fig. 9. The quantity $\mathcal{C}$ is the suspension design dependent calibration factor expressed as

$$\mathcal{C}\left[\frac{\mu N}{Cts}\right] = 10^6\left[\frac{\mu m}{m}\right] \times DAC\left[\frac{V_{\text{differential}}}{Cts}\right] \times S\left[\frac{A}{V}\right] \times \nu\left[\frac{N}{A}\right] \tag{2.42}$$

where S is the coil driver transconductance and ν is the force coefficient of the coil driver. The estimated OM3 yaw motion from local damping is shown in blue trace in Fig. 12.

2. *OMC Alignment Sensing and Control Signal*: The motion attributed to the control signal from the OMC alignment loop can be estimated as

$$\delta\theta^{dof}_{control}\left[\frac{\mu rad}{\mathrm{Hz}^{1/2}}\right] = \alpha \times \delta\theta^{dof}(\text{single coil})\left[\frac{\mu rad}{Cts}\right] \times \mathcal{P}^{dof}_{\textsc{Control\_Out}}\left[\frac{Cts}{\mathrm{Hz}^{1/2}}\right] \tag{2.43}$$

where α is the input matrix element and $\mathcal{P}_{\textsc{Control\_Out}}$ is the power spectral density of the control signal. The green trace in Fig. 12 shows the OM3 yaw mirror motion due to the corresponding control signal input.

3. *Coil Driver Noise*: An electronic model was set up to estimate the noise in the HAM-A coil driver circuit used for the OM suspensions [33, 34]. Similarly, a separate model was set up to estimate the noise in the OMC coil driver circuit. The noise of an OP27 op-amp was used to model the noise of all op-amps in these circuits. Using the electronic model the total current noise of the HAM-A coil driver is estimated, see Fig. 10. The electronic noise in each coil driver can be projected to motion in the corresponding degree of freedom as

$$\begin{aligned}\delta\theta^{dof}_{coil\ driver}\left[\frac{\mu rad}{\mathrm{Hz}^{1/2}}\right] &= 2\times 10^6\left[\frac{\mu m}{m}\right] \times L^{dof}_{osem\ lever}[m] \\ &\times \mathcal{R}^{dof}\left[\frac{rad}{N.m}\right] \times \nu\left[\frac{N}{A}\right] \times \delta i\left[\frac{A}{\mathrm{Hz}^{1/2}}\right]\end{aligned} \tag{2.44}$$

The four coil drives are incoherent which is accounted by the factor of 2 upfront. The purple trace in Fig. 12 shows the motion in OM3 yaw due to the current HAM-A coil driver board.

4. *DAC Noise*: The OM suspensions are driven with a 16-bit DAC while the OMC suspension is driven with an 18-bit DAC. The DAC noise model by Jeff Kissel is used to estimate the DAC noise δD [35].

$$\delta\theta^{dof}_{\mathrm{DAC}}\left[\frac{\mu rad}{\mathrm{Hz}^{1/2}}\right] = \frac{1}{2}\times\delta\theta^{dof}(\text{single coil})\left[\frac{\mu rad}{Cts}\right] \times \mathrm{G}\cdot\delta D\left[\frac{Cts}{\mathrm{Hz}^{1/2}}\right] \tag{2.45}$$

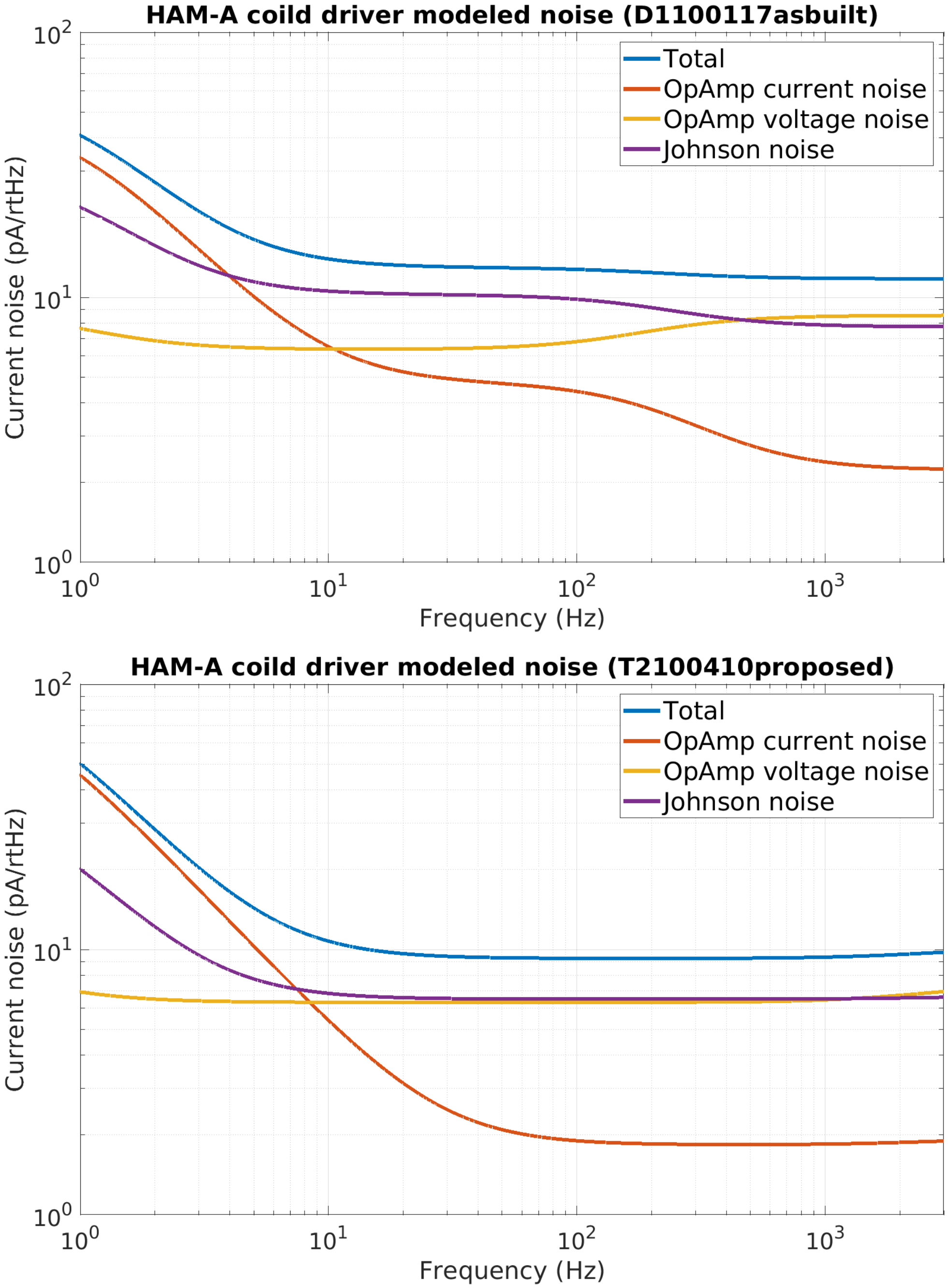

Figure 10: The total current noise of the HAM-A coil driver in the current configuration (top) and the total noise from the proposed HAM-A coil driver (below) with two zeros at 70 Hz and two poles at 1 Hz and 3 kHz.

where G is the gain of the coil driver circuit, which is derived from the model discussed previously. The red trace in Fig. 12 shows the current DAC noise that limits the OM3 mirror motion above 80 Hz.

A similar approach is applied to budget the motion of OM3 in other degrees of freedom, and OM1, OM2, OMC suspensions.

Estimating the coupling from the dither line in DARM

In this section, unlike the measurement of the projection of the noise from the OMC alignment sensing and control loop discussed in the previous section, a method to estimate the coupling of the motion of the output relay suspensions to DARM is presented. The calibrated dither amplitudes of the OM1 and OM3 suspensions can estimate the coupling of their motion on the DC photodiodes using the approach below[11].

1. The OM3 suspension is dithered in yaw at 2200.1 Hz with an amplitude of 130 Cts at the oscillator. Using Eq. 2.41 we can estimate the motion of OM3 in yaw according to

$$\delta\theta^{\mathrm{OM3}}_{yaw}\left[\frac{\mu rad}{\mathrm{Hz}^{1/2}}\right] = \delta\theta^{yaw}(\text{single coil})\left[\frac{\mu rad}{Cts}\right] \times \Delta^{\mathrm{OM3}}_{yaw}\left[\frac{Cts}{\mathrm{Hz}^{1/2}}\right] \tag{2.46}$$

   where $\Delta^{\mathrm{OM3}}_{yaw}$ is the root-mean square drive of a single coil of the OM3. The same approach can be employed to estimate the motion when the OMC alignment sensing and control loop was excited with a broadband frequency injection from 31 to 38 Hz in the aligned state (without any offset in the loop).

2. The corresponding relative intensity noise (RIN) on the DCPDs (see Fig. 4) is estimated as $P(f)/\langle P\rangle$, where P is the power on the DCPDs. The mean photocurrent on the DCPDs ($\bar{i}_{DC}$) was measured to be 20 mA. The corresponding coupling η from the DCPDs to the OM3 motion can then be estimated as

$$\eta\left[\frac{mA}{\mu rad}\right] = \bar{i}_{DC}\left[mA\right] \times RIN\left[\frac{1}{\mathrm{Hz}^{1/2}}\right] \times \frac{1}{\delta\theta^{\mathrm{OM3}}_{yaw}\left[\frac{\mu rad}{\mathrm{Hz}^{1/2}}\right]} \tag{2.47}$$

---

[11] For simplicity we will discuss the approach to estimate the OM3 yaw to the DCPDs. Note that one can estimate the coupling using this approach in the aligned and the misaligned state using the calibrated drive amplitudes and the measured RIN on the DCPD at the corresponding frequency.

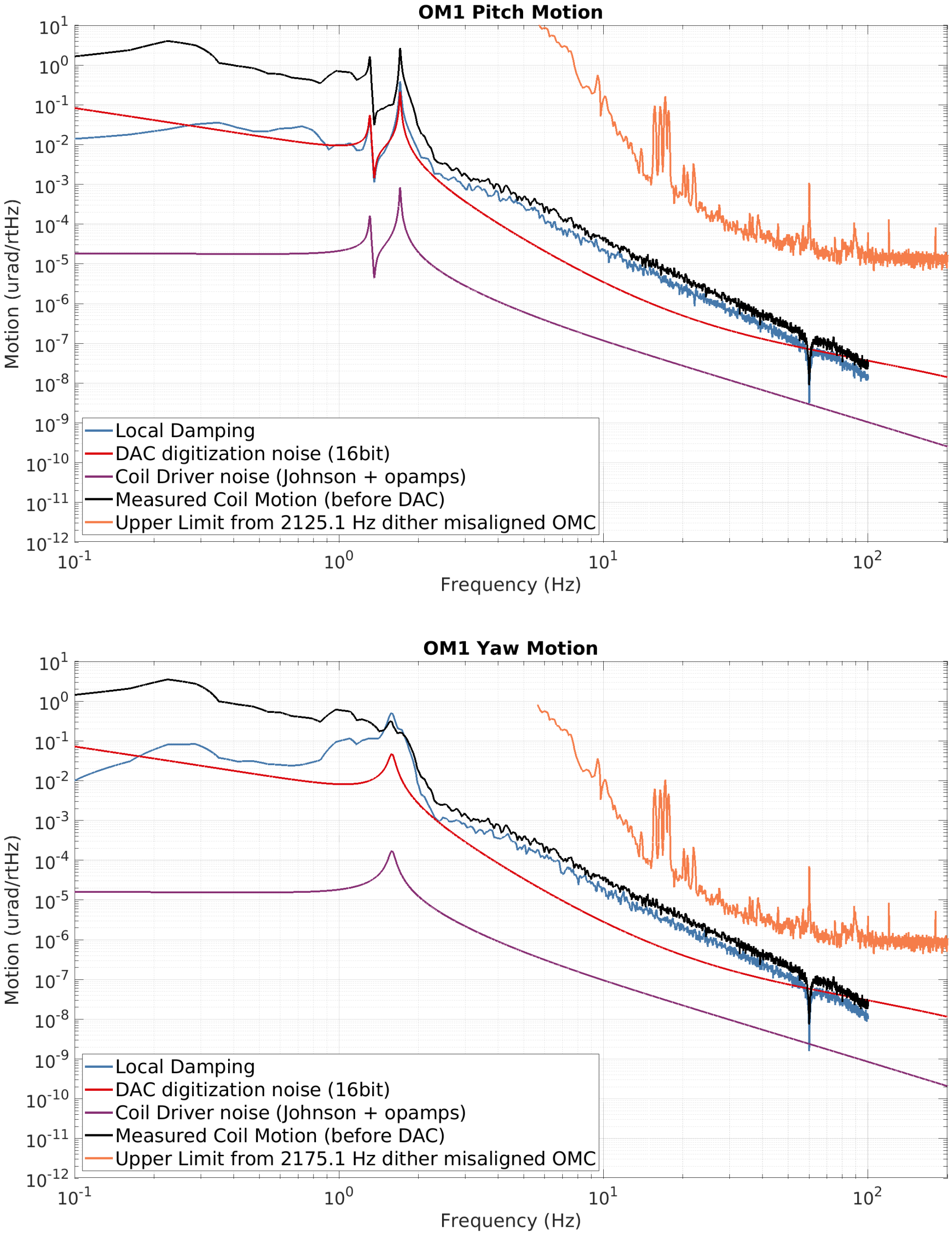

Figure 11: Noise budget of the current OM1 pitch (top) and yaw (bottom) motion. The estimated coupling to DARM suggest that the OM1 pitch motion is more than a factor of 10 lower to limit the sensitivity of the detector but the OM1 yaw motion is only a factor of 3 below DARM. Note that the coil motion total does not have the DAC noise contribution as the signal is picked off at the input to the coil-driver boards.

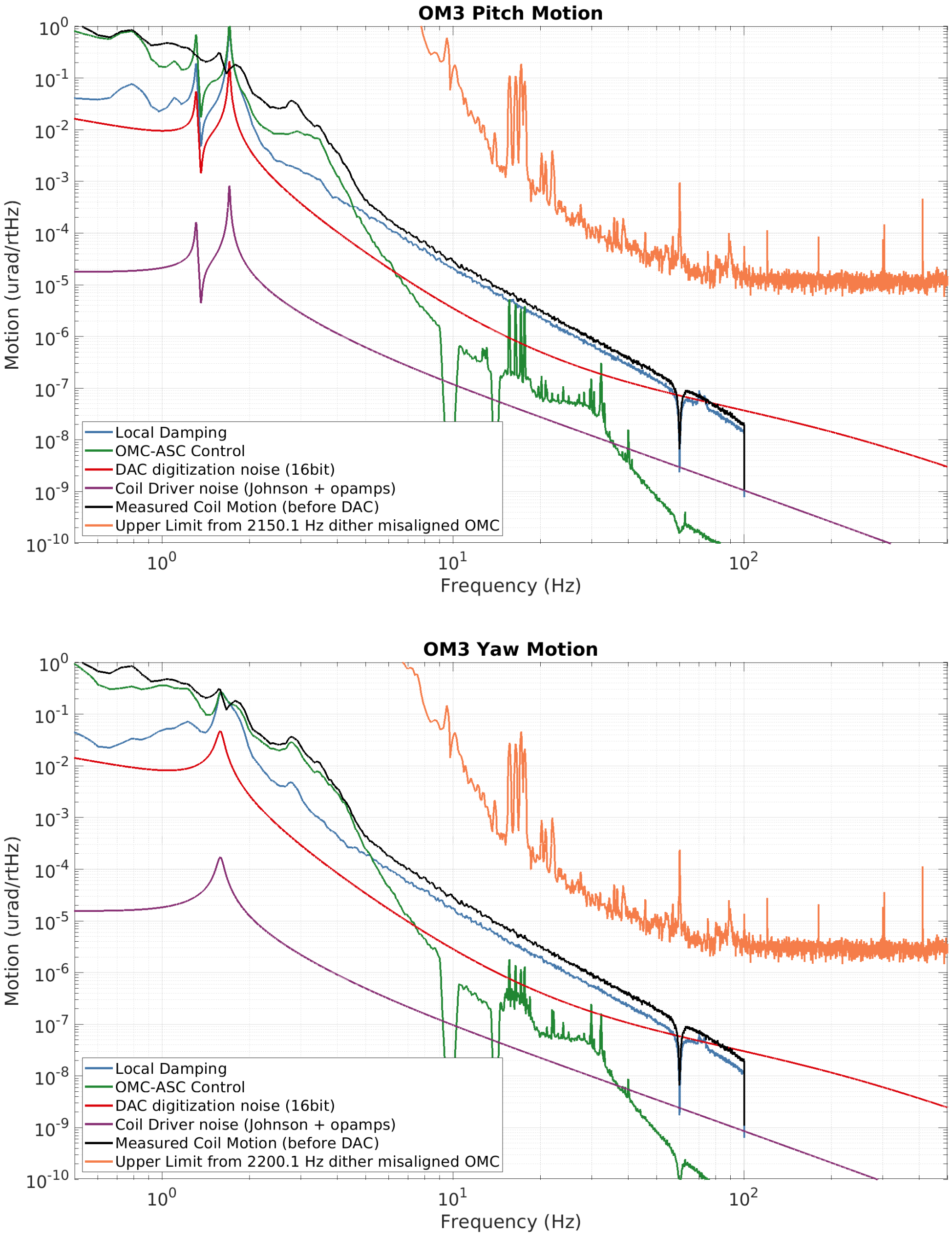

Figure 12: Noise budget of the current OM3 pitch (top) and yaw (bottom) motion. The estimated coupling to DARM suggest that the OM3 motion is more than a factor of 10 lower to limit the sensitivity of the detector. Note that the coil motion total does not have the DAC noise contribution as the signal is picked off at the input to the coil-driver boards.

At 2200.1 Hz, the estimated root-mean square RIN is $2.32 \cdot 10^{-7}$ $\text{Hz}^{-1/2}$. For the broadband excitation, the closed-loop corrected root-mean square RIN is $7.22 \cdot 10^{-8}$ $\text{Hz}^{-1/2}$.

3. The upper limit of the coupling to DARM (χ) can now be estimated using the corresponding value of η, and the closed-loop corrected readout of the DCPDs according to

$$\chi\left[\frac{\mu rad}{\text{Hz}^{1/2}}\right] = \frac{1}{\eta\left[\frac{mA}{\mu rad}\right]} \times \frac{P_{DCPD}}{1-\kappa_c G}\left[\frac{mA}{\text{Hz}^{1/2}}\right] \tag{2.48}$$

where κ_c is the optical gain and G is the open-loop gain of the DARM sensing loop.

The estimated coupling of OM1 and OM3 suspensions motion to DARM is shown in orange trace in Fig. 11 and Fig. 12. The estimated motion of the OM1 in pitch, and the OM3 in pitch and yaw is not limiting to the DARM sensitivity at the LIGO Hanford Observatory. However, *this estimate suggests that the OM1 yaw motion is less than a factor of 10 lower in the frequency band from 20 Hz to 80 Hz and may be limiting the DARM sensitivity in the low noise state of the interferometer.* Moreover, the OM1 yaw motion in the above frequency band is limited due to the local damping loops. These damping loops have now been improved to suppress excess motion above 10 Hz and is discussed in the next section.

Implications for the OM1, OM2, OM3 and OMC Suspensions

For the OM1, OM2, and OM3 mirror suspensions, for all degrees of freedom, it was found that local damping was limiting the suspension motion from 10 Hz to 80 Hz, above 80 Hz the limitation was due to the DAC digitization noise. For these suspensions, the damping loops are now improved for O4 and will provide almost a factor of ten improvement above 10 Hz compared to the previous local damping filters. It was found that the DAC digitization noise can be reduced at the expense of a more limited actuation range of the coil drivers. For the standard dither alignment scheme, a significant drive is required at 2 kHz from the coil drivers. Combining the range requirements from the required actuation range (using O3 coil driver output trend) and the drive requirement at 2 kHz for the dither alignment scheme, the DAC filters have now been improved. A factor of ten improvement above 80 Hz is estimated using the updated HAM-A coil driver circuit. With these two changes, we expect an overall factor of ten suppression above 10 Hz for the OM1, OM2, and OM3 mirror suspensions. The noise budget of the OM1 suspension with new proposed changes for each degree of freedom is shown in Fig. 13.

The longitudinal and pitch degrees of freedom of the OMC suspension was also found to be limited by local damping noise below 50 Hz. The local damping filters were updated to provide almost a factor of 20 improvement above 10 Hz for all degrees of freedom of the suspension motion. With the improved damping filters, the motion of the OMC suspension would be limited by the sensing noise of the OMC alignment loop in length, pitch, and yaw degrees of freedom. The improvements to the DARM sensitivity of LIGO Hanford Observatory will be characterized when the detector achieves low noise sensitivity during the ongoing commissioning phase by May or June 2022.

Future work

It is important to note that the measurement and estimation of the OMC alignment and sensing control loop presented here and the corresponding improvements in local damping mitigate the current noise levels due to beam misalignment but not beam quality of the input beam at the OMC. If a careful measurement presented earlier suggests that there is some coupling from OMC to DARM it is crucial to investigate the beam quality. The high-resolution wavefront sensor presented in chapter 4 can be installed in the transmission of OM1, which can provide a measure of both the beam quality and an estimate of the frequency-dependent loss from mode-mismatch. Mode-matching actuators presented in chapter 3 provide a viable option for active wavefront control to correct for these higher-order mode distortions.

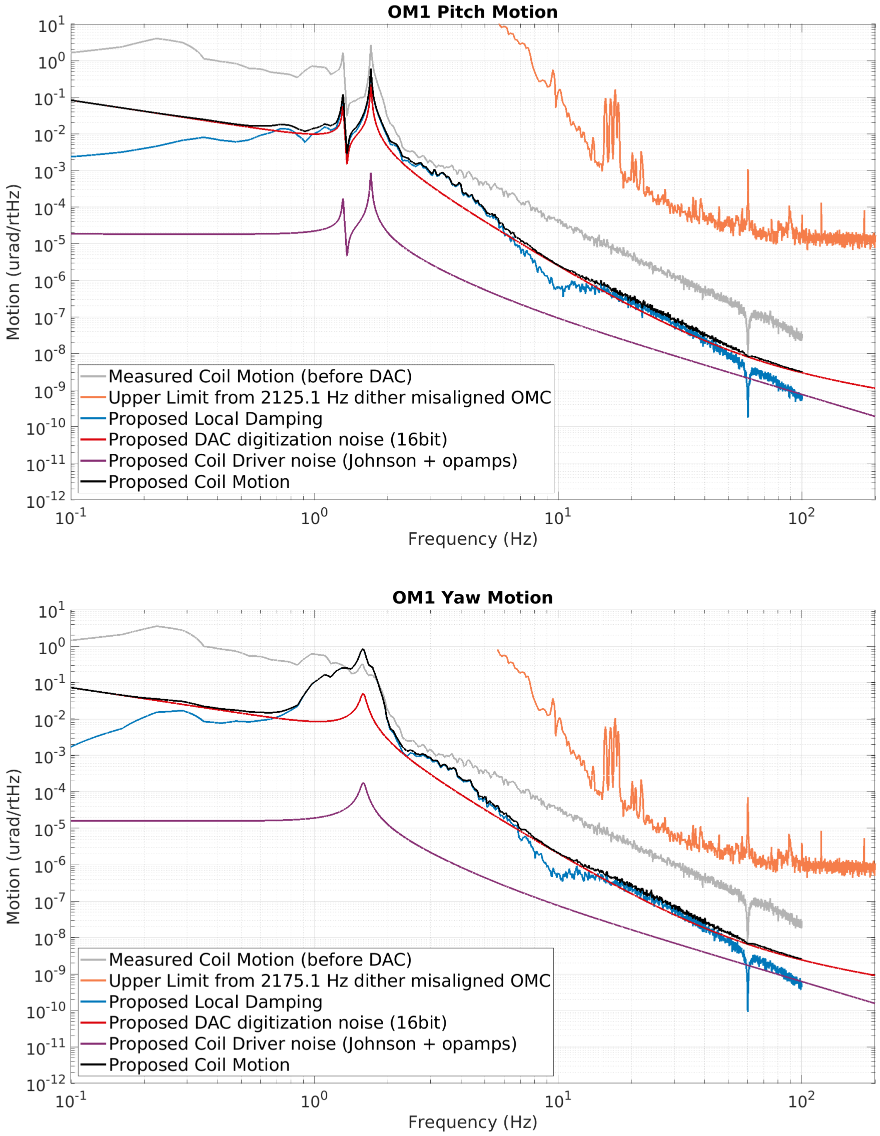

Figure 13: Noise budget of the OM1 suspension motion in pitch (top) and yaw (botton) after the proposed changes in local damping and the HAM-A coil drivers. We find these changes will be sufficient to suppress noise more than a factor of 10 below DARM in all degrees of freedom.

Chapter 3

Piezo-deformable Mirrors for Active Mode Matching in Advanced LIGO

The detectors of the laser interferometer gravitational-wave observatory (LIGO) are broadly limited by the quantum noise and rely on the injection of squeezed states of light to achieve their full sensitivity. Squeezing improvement is limited by mode mismatch between the elements of the squeezer and the interferometer. In the current LIGO detectors, there is no way to actively mitigate this mode mismatch. This paper presents a new deformable mirror for wavefront control that meets the active mode matching requirements of advanced LIGO. The active element is a piezo-electric transducer, which actuates on the radius of curvature of a 5 mm thick mirror via an axisymmetric flexure. The operating range of the deformable mirror is 120±8 mD in vacuum and an additional 200 mD adjustment range accessible out of vacuum. The scattering into higher-order modes is measured to be $<0.2\%$ over the nominal beam radius. These piezo-deformable mirrors meet the stringent noise and vacuum requirements of advanced LIGO and will be used for the next observing run (O4) to control the mode-matching between the squeezer and the interferometer[1].

---

[1] Varun Srivastava, Georgia Mansell, Camille Makarem, Minkyun Noh, Richard Abbott, Stefan Ballmer, GariLynn Billingsley, Aidan Brooks, Huy Tuong Cao, Peter Fritschel, Don Griffith, Wenxuan Jia, Marie Kasprzack, Myron MacInnis, Sebastian Ng, Luis Sanchez, Calum Torrie, Peter Veitch, and Fabrice Matichard. Opt. Express 30, 10491-10501 (2022).

3.1 Introduction

In September 2015 the Advanced LIGO (aLIGO) detectors [26] made the first direct observation of gravitational waves from a binary black hole merger [8]. This first detection kicked off the exciting new field of gravitational-wave astronomy. Since the first detection, aLIGO, together with the Advanced Virgo observatory [36], has undergone incremental upgrades to improve the sensitivity to gravitational waves, and subsequently observed 90 gravitational-wave events [37, 38, 39] from binary black holes [8], binary neutron stars [40, 41], and neutron-star black-hole binaries [42].

The aLIGO detectors are two dual-recycled Fabry-Pérot Michelson interferometers located in Hanford, Washington and Livingston, Louisiana. Incoming gravitational waves cause a minuscule displacement of the test masses - 40 kg mirrors which make up the 4km long arms of the Michelson interferometer. The gravitational-wave readout is a measure of the differential arm length of the interferometer. The sensitivity of the current gravitational-wave detectors is broadly limited by quantum noise [1]. Below 50 Hz, the quantum noise manifests itself as radiation pressure noise, as photons circulating in the arm Fabry-Pérot cavities impart momentum to the test masses. Above 100 Hz, the sensitivity of the detector is limited by quantum shot noise. The sensitivity of the aLIGO detectors is improved by the injection of squeezed states of light. In the most recent observing run (O3) frequency-independent squeezing was injected into the aLIGO detectors, reducing quantum shot noise by roughly 3 dB compared to when no squeezed light is injected [43].

The aLIGO detectors are currently being upgraded. One of the major upgrades for the next observing run (O4) is the implementation frequency-dependent squeezing. Frequency-dependent squeezing is achieved by reflecting squeezed light off a long-baseline filter cavity, with the filter cavity pole at the desired rotation frequency. For O4, a 297 m filter cavity will be installed at each of the LIGO sites. To maximize the squeezing improvement to detector sensitivity, the mode-matching losses between the various optical cavities need to be minimized. The negative effect of mode mismatch on squeezed photons is twofold: mode mismatch causes optical loss and adds phase noise to the squeezed beam [44]. For the next phase of LIGO upgrades after O4 (‘A+’), the goal is to achieve 6 dB of frequency-dependent squeezing improvement to the detector sensitivity [45, 46, 44]. The piezo-deformable mirrors developed here have critical applications in active wavefront control for future gravitational-wave detectors, like Cosmic Explorer [47], as frequency-dependent squeezing is integral in achieving their design sensitivity.

A common architecture of piezo-deformable mirrors utilizes a thin mirror bonded with a piezoelectric substrate, referred to as the unimorph [48, 49, 50]. The range of deformation is inversely proportional to the flexure rigidity, hence thinner unimorph mirrors yield a larger range of deformation. Current unimorph technology does not simultaneously meet the reflectivity, surface quality, actuation range, and low defocus noise requirements for mode-matching optics for aLIGO, discussed in section 3.2.

Presented here is the design and implementation of a new deformable mirror for active mode matching in aLIGO. The design uses a piezoelectric transducer (PZT) to apply a distributed bending moment on the mirror barrel via an axisymmetric flexure, thereby controlling the mirror radius of curvature. The flexure-based piezo-deformable mirrors presented here has a large operating range, a high bandwidth, and is compatible with ultra-high vacuum operation. Designed for two-inch diameter optics with 5 mm thickness, the scattering to higher-order modes is below 0.2% for beam radius less than 2 mm. An alternative thermally actuated design is being implemented in aLIGO concurrently with the piezo-deformable mirrors [51]. The thermal design has an increased operating range in vacuum compared to the piezo-deformable mirrors but offer a much lower bandwidth of $\mathcal{O}(1\ \mathrm{mHz})$ compared $\mathcal{O}(1\ \mathrm{Hz})$ that is achievable with the piezo-deformable mirrors.

The motivation and design requirements of the piezo-deformable mirrors for application in aLIGO and future upgrades are discussed in section 3.2. In section 3.3 the design of the flexure-based piezo-deformable mirror is presented. The performance results of the piezo-deformable mirror are summarized in section 3.4.

3.2 Requirements for aLIGO

The piezo-deformable mirrors will be used for mode-matching at two locations in the aLIGO beam path, shown in Fig. 14. First, between the squeezed light source and the filter cavity. Second, between the output of the filter cavity and the main interferometer. The required operating range of the piezo-deformable mirror is greater on

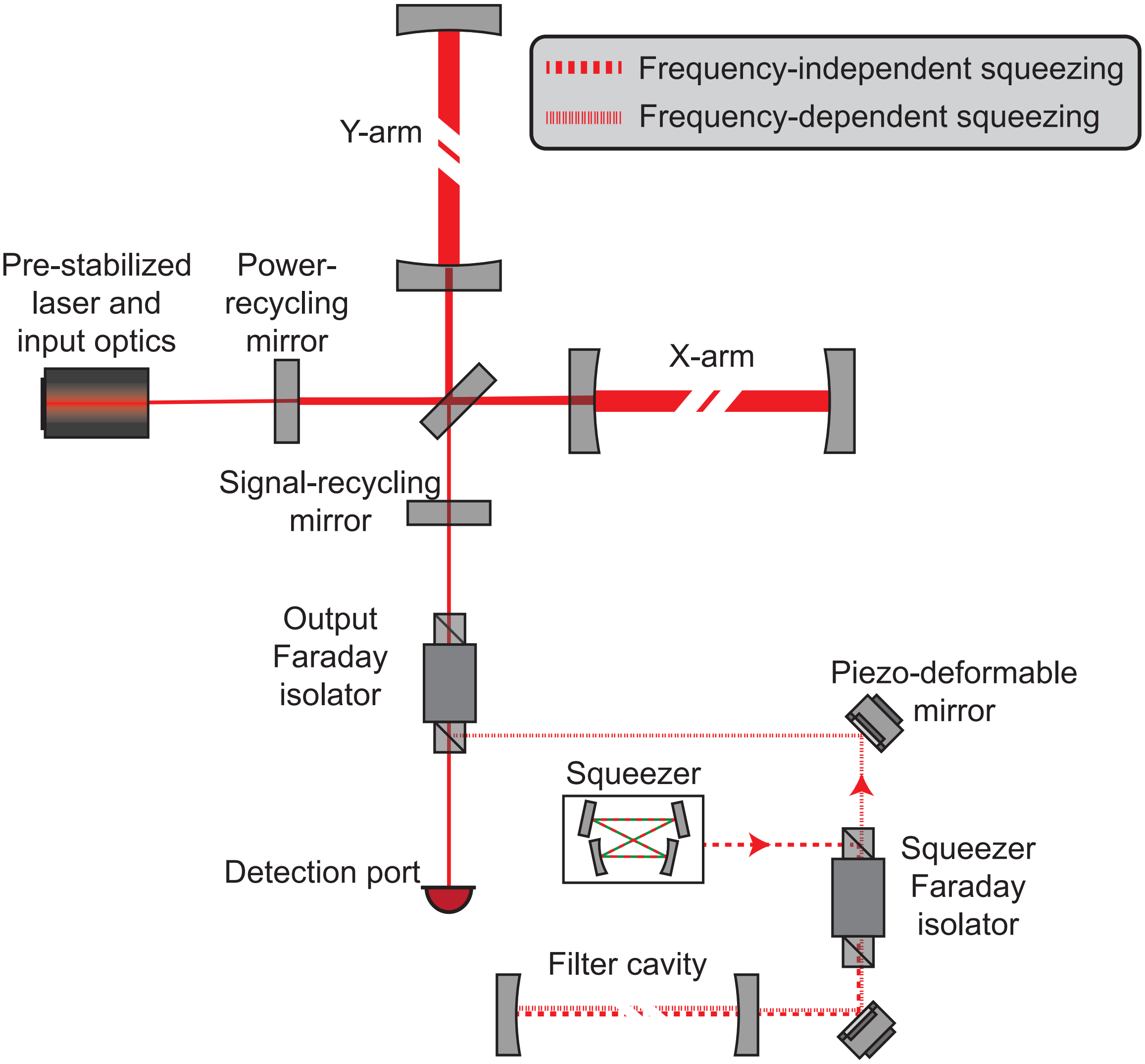

Figure 14: Simplified layout of the aLIGO detector with piezo-deformable mirrors in the squeezer path. In the aLIGO layout for O4, there is one piezo-deformable mirror between the squeezer and the filter cavity, and two piezo-deformable mirrors between the squeezer and output Faraday isolator. Only one is shown above for simplicity.

the filter cavity to interferometer path, as the mode shape of the beam from the interferometer is not as well known. However, for both of these ports, the mode-matching needs to be better than 96% to achieve the broadband improvements in sensitivity from 6 dB of frequency-dependent squeezing. Based on our simulations of the current and expected mode mismatch, a range of ±160 mD will be sufficient to correct for mode mismatch between the filter cavity and interferometer, and ±30 mD is required on the path between the squeezer and the filter cavity. During future upgrades, to assist in characterizing the mode mismatch between the cavities in the aLIGO detector, the radius of curvature of the piezo-deformable mirrors can be dithered at a frequency in the aLIGO detection band [1]. To achieve this, a high bandwidth $\mathcal{O}$(1-10 Hz) is needed on the piezo-deformable mirror actuators.

The aLIGO detectors have stringent requirements for any new optics added to the system. Any technical noise added to the gravitational-wave readout must be at least a factor of 10 below the design sensitivity. The piezo-deformable mirrors could inject technical noise through spurious changes in the defocus of the beam, higher-order mode content generated by the mirror surface, or displacement of the mirror surface. Any modes other than the fundamental Gaussian mode are considered to be higher-order modes. We require the higher-order modes induced by the piezo-deformable mirrors to be a factor of 10 below the mode-mismatch (L_{o}) requirement of 4%. This demands that the higher-order mode content (or scattering) from the piezo-deformable mirrors be less than 0.4%.

The defocus noise $S(f)$ arises from the fluctuations in the radius of curvature of the piezo-deformable mirrors. This induces a fluctuation in the mode-matching losses, which produces a proportional change in relative intensity noise transmitted to the detection port, resulting in an apparent displacement noise ($z(f)$). This apparent displacement noise for a given optic should be at least 10 times less than the displacement noise requirement in the aLIGO detectors so that it is not limiting the gravitational-wave detector sensitivity. The defocus noise is dependent on the beam size (w) at the piezo-deformable mirror, and is coupled to the displacement noise by

$$\frac{z(f)}{\mathcal{C}_{\mathrm{tf}}} \approx \frac{\pi w^2}{\lambda} \sqrt{L_{\mathrm{o}}} S(f), \tag{3.49}$$

where $\mathcal{C}_{\mathrm{tf}}$ is the transfer function from relative intensity noise to interferometer displacement noise, λ is the wavelength of the laser, and L_{o} is the dc mode matching requirement described above. An analogous coupling due to the relative intensity noise requirement of the coherent locking field to the detection port sets the on the defocus noise requirement in the filter cavity path [52], shown in Fig 14. Using this estimate $S(f)$ must be below 10^{-5} D/$\sqrt{\text{Hz}}$ above 100 Hz to meet the displacement noise requirement of the squeezer path. This is a conservative estimate because at the optimally tuned setting of the piezo deformable mirror the linear coupling from defocus noise to displacement noise goes to zero. Lastly, to damp displacement noise, and to soften the scattered light requirements, the piezo-deformable mirrors will be hung from double pendular suspensions, in a similar configuration to other aLIGO auxiliary optics [53].

3.3 Design

The piezo-deformable mirror is designed to meet the noise requirements described in section 3.2, while maintaining a fast response time for convenient commissioning. Fig. 15 shows the schematic of the piezo-deformable mirror. The key component is an inverted hat-shape axisymmetric flexure that converts a pushing force from the PZT into a distributed bending moment around the mirror circumference, thereby deforming the mirror for a radius of curvature. When a voltage is applied to the PZT, it elongates along the axial direction. The force associated with this elongation is distributed on the back of the flexure via the top aligner. The flexure is bolted to the body to constrain any motion along the circumference, and the axial force applied to the flexure produces a moment that causes spherical deformation on the mirror. Thus, by driving a voltage to the PZT one can actively change the radius of curvature of the mirror for mode-matching applications in aLIGO. The different components of the piezo-deformable mirror, see Fig. 15, along with their functions are described below.

- The *flexure* converts the axial force applied on the back to spherical deformation of the mirror surface. The mirror is held in the flexure due to the compression bias introduced after compression fitting.
- The radius of curvature of a 5 mm thick highly-reflective mirror is deformed

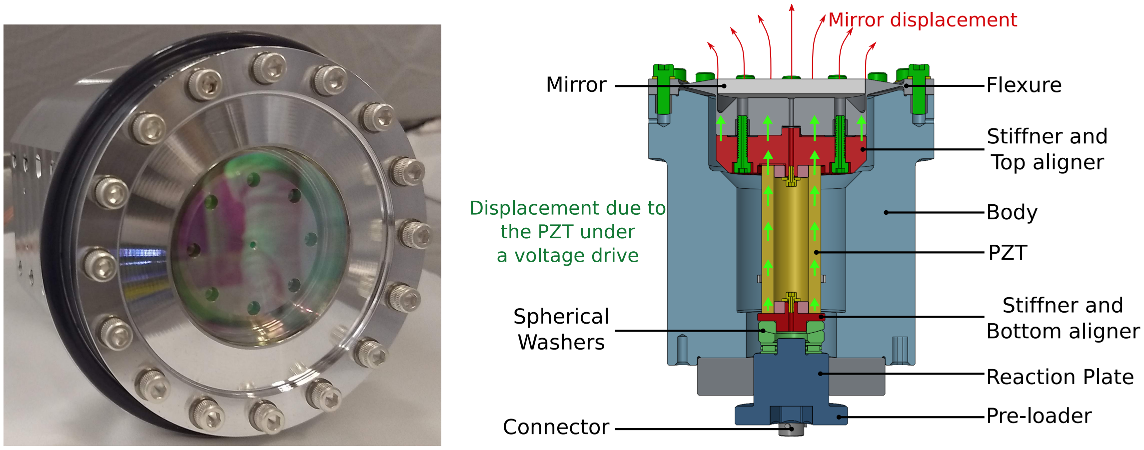

Figure 15: *Left:* An assembled flexure-based piezo-deformable mirror actuator for active mode matching in aLIGO. *Right:* The main components of an assembled piezo-deformable mirror. The mirror is compression fitted inside the flexure §3.7.1 and attached to the top aligner. This assembly is then attached to the body using 16 screws each torqued to 30 in-lbs. The piezoelectric transducer (PZT) stack, and the bottom aligner are inserted from the back, followed with the attachment of the reaction plate. The spherical washers and the thrust bearing are gently placed on the bottom aligner, and the pre-loader is torqued to at least 25 in-lbs to secure the assembly. The displacement of the PZT under a voltage bias is shown with green arrows. The flexure deforms the mirror radius of curvature due to the corresponding axial force generated by the PZT thrust. The mirror displacement is represented by red arrows.

for active wavefront control. These mirrors require a good barrel finish to minimize astigmatism, spherical aberrations, and coma which may arise from poor compression fitting. The process for compression fitting the mirror inside the flexure is discussed in section 3.7.1.

- The flexure with the compression fitted mirror is attached to the *body* with screws. To ensure radial symmetry each screw is torqued to 30 in-lbs.
- The PZT (Noliac NAC2125-H50-A02) is held inside the *body* with *top and bottom aligners*. These aligners ensure that the piezo is flush against the back surface of the flexure. It is important to ensure that there is no angular misalignment of the PZT upon assembly. The PZT has a half-bridge strain gauge bonded to it, which allows the read out of the strain on the piezo, discussed in section 3.7.2.
- The *reaction plate* serves the role of a hard boundary wall. The applied force at the back of the flexure depends linearly on the longitudinal displacement. The reaction plate ensures that the stroke from the PZT preferentially displaces the back surface of the flexure.
- The *pre-loader* is a fine threaded screw that goes through the reaction plate. The pre-loader ensures that the piezo is secured stiffly inside the body. We recommend that the pre-loader is torqued to at least 25 in-lbs to ensure the PZT stack is well constrained before the application of any voltage drive. The torque applied to the pre-loader provides static deformation to the radius of curvature of the mirror without any voltage drive to the PZT. The operating point or the optimal radius of curvature can be changed by further torquing the pre-loader. One can torque the pre-loader up to 100 in-lbs without any damage to the piezo or the mirror. In this design, the pre-loader torque cannot be adjusted under vacuum.

The piezo-deformable mirror offers two design variations for the assembly of the mirror and the flexure. First, a stainless steel (440C) flexure with an intermediate aluminum ring (6061) between the flexure and the mirror. The design concept is presented in [54]. This allows greater flexibility in design because the level of mirror compression fit can be adjusted by compensating accordingly the intermediate ring.

However, the Young's modulus of stainless steel is higher, which limits the actuation range of the piezo-deformable mirror. Also, the two-stage compression fitting — flexure and ring, followed by mirror in the flexure — makes compression fitting more challenging. The second variation of the design uses an aluminum (7075) flexure which is custom made for each mirror. This design, although tuned for each flexure-mirror pair, is easier to assemble. Moreover, the lower Young's modulus of aluminum provides a greater actuation range as it is easier to deform the flexure. We will reserve all discussions to the aluminum flexure-based piezo-deformable mirror in this paper.

Compression fitting the mirror into the flexure and installing the flexure assembly on the body induce minimal change to the defocus of the mirror. The defocus is defined as the inverse of the focal length. The net defocus of the piezo-deformable mirror (D_{PDM}) is given by

$$D_{\text{PDM}} \approx D_{\text{mirror}} + D_{\text{preload}} + D_{\text{actuation}} \tag{3.50}$$

where D_{mirror} is the defocus of the mirror, D_{preload} is the defocus due to the preload, and $D_{\text{actuation}}$ is the defocus due to the PZT actuation. The operating defocus D_{op} is set such that D_{mirror} and D_{preload} cancel out at half the maximum actuation voltage.

$$D_{\text{op}} = D_{\text{mirror}} + D_{\text{preload}} + D_{\text{actuation}}(V_{\text{max}}/2) \tag{3.51}$$

The operating defocus for production units to be installed in aLIGO varies depending on the optic placement along the beam.

3.4 Results

Multiple assemblies of the piezo-deformable mirrors were tested using the Zygo interferometer, which is used to characterize the aLIGO core optics [55]. The Zygo interferometer is a Fizeau topology, which uses a reference optic to measure the surface profile of a mirror under test. We use the Zygo interferometer to measure the deformed mirror surface of the piezo-deformable mirror with varying amounts of torque applied to the pre-loader, and when the piezo is driven with an external voltage. The measured deformation of the mirror was used to estimate the range of defocus and the higher-order mode content, which is discussed in sections §3.4.1

and §3.4.2. The defocus noise of the piezo-deformable mirror has also been measured in a separate Michelson interferometer and the preliminary results suggest that aLIGO requirements along the squeezer path are met by almost four orders of magnitude [56]. As part of the Michelson interferometer testing, the resonances of the piezo-deformable mirror assembly have been measured, with the lowest resonance at 386 Hz. With a 100 V bias on the PZT, we measure a bandwidth of 6.8 Hz for the piezo-deformable mirror. This bandwidth is limited by the driver electronics. During O4, the piezo-deformable mirror will be tuned occasionally to reduce mode-matching losses. In future upgrades, the fast response of the piezo-deformable mirrors allows the possibility to design feedback control loops to reduce mode-mismatch losses.

3.4.1 Defocus range of the piezo-deformable mirror

The piezo-deformable mirror actively changes the radius of curvature of the mirror when an external voltage is applied. We use the Zygo interferometer to measure the surface profile of the mirror in the assembled piezo-deformable mirror [55]. At different values of the piezo drive (from 0 V to 200 V), we measure the surface profile with a pixel resolution of 192 μm and with 100 averages. The surface profile was fit to linear and quadratic order over a circular region with a diameter of 25 mm. The quadratic term measures the defocus and the linear term measures the tilt of the mirror surface. Averaging the measured operating range from three different piezo-deformable mirror assemblies, each tested at different values of pre-loader torques, the piezo-deformable mirror offer an active operating range of 90±6 mD over 150 V of an external voltage. The PZT in the design can be driven up to 200 V offering an operating range of 120±8 mD. The pre-loader was torqued to different values to change the static defocus of the mirror. We find the change in preload from the minimum of 25 in-lbs to a maximum of 100 in-lbs offers approximately 200 mD of static adjustment range, see Fig. 16.

3.4.2 Higher-order mode scattering

The design specification requires the piezo-deformable mirror must induce less than 0.4% of higher-order mode power for Gaussian beams with a beam radius of less than 2 mm, see section 3.2. To estimate the higher-order mode content we define a nominal

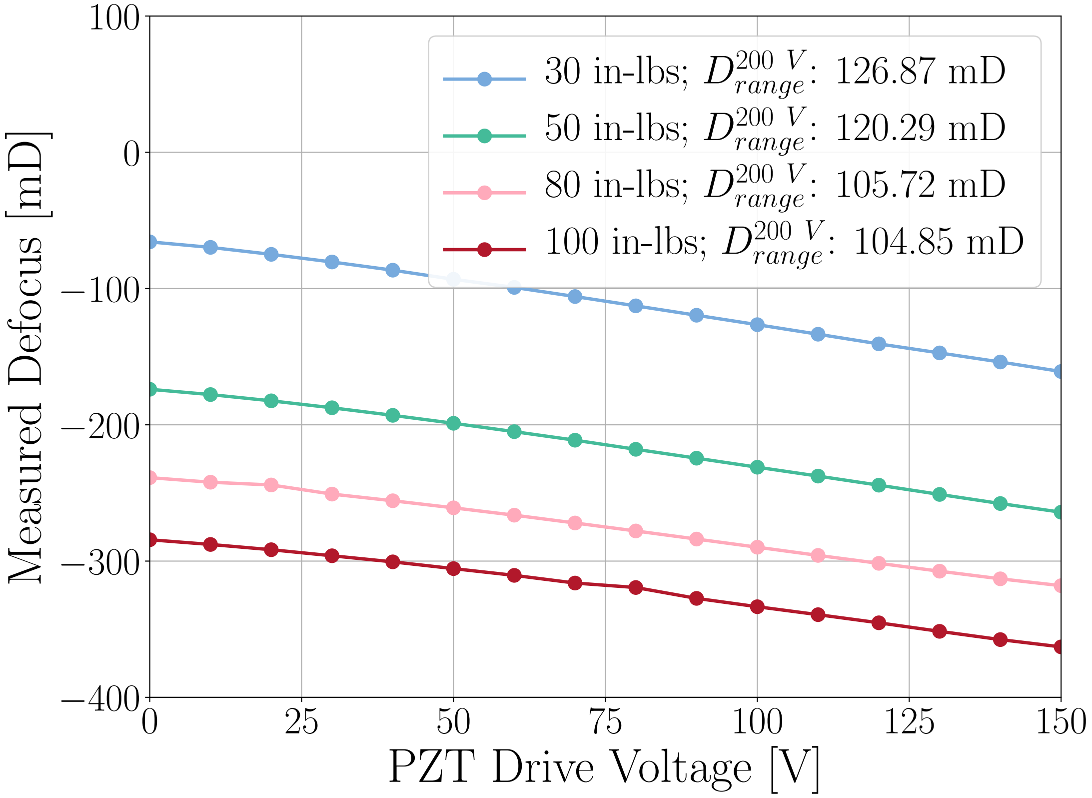

Figure 16: The points represent the measured defocus range (mD) as a function of drive voltages through the PZT, with a static pre-loads of 30, 50, 80 and 100 in-lbs (blue, green, pink and red). The legend summarizes the total defocus range extrapolated over a 200 V drive at the corresponding static pre-loads. We note that the minimal 25 in-lbs preload induces an approximately 60 mD of defocus on the mirror. The static preload by adjusting the torque applied to the pre-loader (no voltage drive) offers a defocus range of over 200 mD (from -65 mD to -285 mD for this prototype). The PZT drive over 200 V offers an additional 120±8 mD of operating range.

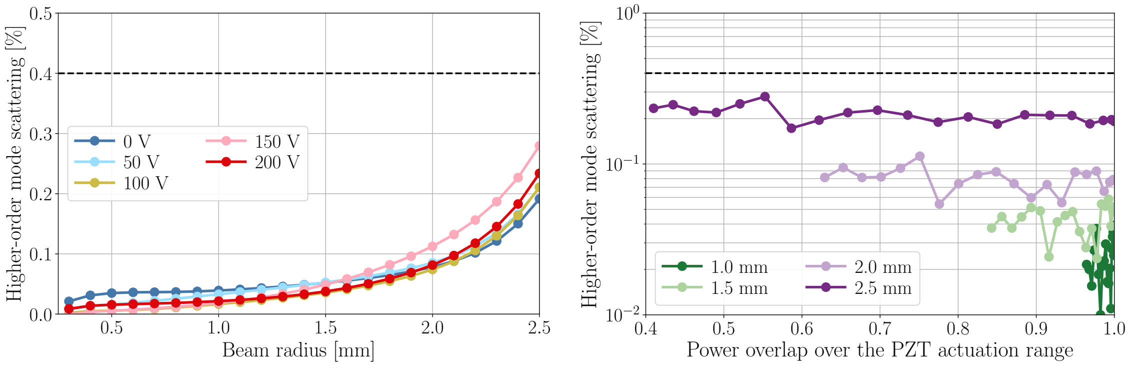

Figure 17: *Left:* The higher-order mode content of piezo-deformable mirrors with 50 in-lbs of preload at 0, 50, 100, 150, and 200 V of drive to the PZT as a function of beam radius. The Zygo interferometer has a pixel resolution of 0.192 mm, which limits the higher-order mode content projection for smaller beam sizes. However, it is expected to be smaller than the higher-order mode content for 0.25 mm beam radius. We find Gaussian beams up to a radius of 2.5 mm experience less than 0.4% of higher-order mode content over the entire range of piezo-deformable mirrors operation. *Right:* The higher-order mode content as a function of power overlap between the incident and the reflected field. As the defocus of the mirror increases with the PZT drive, the power overlap decreases. However, we find the piezo-deformable mirrors ensures higher-order mode content less than 0.4% for Gaussian beams with beam radius up to 2.5 mm over the full actuation range of the PZT.

reflected beam using an ideal Gaussian input beam with a given beam size. The input beam is reflected off a simulated mirror with defocus and tilt as measured by the Zygo (see Fig 16) but with no additional higher order mode content. We calculate the full reflected beam using the measured surface profile and the same ideal Gaussian input beam. The mode-overlap between the nominal and the full reflected beams provides an estimate of the higher-order mode content of the full reflected beam. The left plot of Fig. 17 shows the higher-order mode content as a function of input beam radius over the range of the piezo-deformable mirrors. Alternatively, we can quantify the power-overlap between the input beam and the nominal reflected beam, correcting for pointing errors over the operating range. The right plot of Fig. 17 shows that the piezo-deformable mirror provides low higher-order mode content even when correcting for an overlap mismatch as low as 0.4, demonstrating that the design constraints are met.

The compression fitting scheme discussed in section §3.7.1 is critical to achieving low higher-order mode content. It is crucial to ensure during the process of compression fitting that the mirror has no tilt with respect to the flexure. Any tilt between the mirror and the flexure causes a non-axisymmetric deformation of the mirror after compression fitting. When the mirror is actuated in this configuration, the moment distribution on the mirror circumference generated by the flexure is not axially symmetric, which causes the higher-order mode content to be much higher, typically up to 2-5%.

3.5 Conclusion

We present a novel ultra-high vacuum compatible, flexure-based active mode-matching deformable mirror. The piezo-deformable mirrors presented here have direct implications for improving the sensitivity of aLIGO detectors by reducing the optical losses from mode-mismatch, and by improving the levels (dB) of squeezing. They offer high bandwidth and a large operating range. While under vacuum, the PZT actuator has an operating range of 120±8 mD. In air, adjusting the static preload by using the pre-loader provides an additional 200 mD of adjustment range. The quality of the beam is not degraded and the higher-order mode content is below 0.2% over the full range of actuation. The technology developed here has applications in any optical experiments where mode-matching is critical or active wavefront control is necessary.

3.6 Acknowledgment

LIGO was constructed by the California Institute of Technology and Massachusetts Institute of Technology with funding from the National Science Foundation, and operates under cooperative agreement PHY-1764464. A+ was built under award PHY-1234382. This paper carries LIGO Document Number LIGO P2100315. Parts of this research were conducted by the Australian Research Council Centre of Excellence for Gravitational Wave Discovery (OzGrav), through project number CE170100004.

3.7 Appendix

3.7.1 Compression fitting and assembling the piezo-deformable mirror

In this section, we discuss the procedure to compress fit the mirror inside the aluminum flexure. To induce compression bias at room temperature, the diameter of the mirror is larger than the inner diameter of the flexure. Compression fitting a mirror for adaptive optics was also demonstrated in [51]. The procedure to compression fit the mirror is as follows:

- As the coefficient of thermal expansion of aluminum are higher than fused silica, we can heat the flexure to create clearance to insert the mirror inside. The temperature to perform the compression fit is determined by the following equation
$$\Delta T = T_{\text{fit}} - 300\ K \approx \frac{\delta\phi}{\phi}\frac{1}{\alpha_{\text{flex}}} \tag{3.52}$$
where α_{flex} is the coefficient of thermal expansion of the flexure, ϕ is the diameter of the mirror at 300 K and $\delta\phi$ is the interference between the mirror and the flexure at 300 K, typically 15 μm. The temperature T_{fit} is the approximate temperature to perform the compression fit.

- We use the optical grade surface plate to ensure that the normal from the surface of the mirror is parallel to the normal axis of the flexure plane — ensuring the mirror does not tilt inside the flexure. The mirror, the flexure, and the alignment tool are heated to T_{fit}. To minimize the non-radial deformation of the mirror after compression fit, the barrel of the mirror requires a good surface finish and cylindricity. The prototypes presented here used mirrors with cylindricity $< 5\mu m$ (Thorlabs BB2-E03-5MMT-SP). The piezo-deformable mirrors employed at aLIGO use mirrors with specified cylindricity $< 1\mu m$ (FiveNine Optics).

- At room temperature, place the mirror on the optical grade surface plate, align the flexure face-down such that it just makes contact with the back surface of the mirror along the circumference. Place a weight gently on top of the setup. Next, the temperature is increased in steps 15 K (to $T_{\text{fit}} \sim 550\ K$) until the mirror is all the way inside the flexure. The assembly is then cooled to room temperature, ensuring no disturbance to the setup.

Next, the compression fitted flexure is first loosely attached to the body and the top aligner resting inside the body of the assembly. With the body mirror-side-down, the PZT is engaged with the top aligner and bottom aligner via two nylon rings inserted inside the PZT. A pair of spherical washers and thrust bearing are then placed over the bottom aligner, and the reaction plate is screwed down at the back of the body. The pre-loader is then engaged with the bottom aligner via the spherical washers and thrust bearing. Finally, all the screws in the flexure assembly need to be tightened. All the screws to attach the compression fitted mirror-flexure assembly to the body are torqued to 30 in-lbs. The pre-loader is torqued to at least 25 in-lbs; the maximum allowable torque to the pre-loader, ensuring no damage to the mirror, is 100 in-lbs.

3.7.2 Strain Gauge Readout

The crystalline structure of the piezoelectric material gives rise to hysteresis in the actuation curve as seen in Fig 18. This hysteresis is undesirable for mode-matching applications requiring the ability to revert to a known radius of curvature while the piezo-deformable mirror is otherwise inaccessible inside an ultra-high vacuum environment. The PZT in the piezo-deformable mirror is manufactured with an integrally bonded half-bridge strain gauge readout. The half-bridge is comprised of separate collocated transverse and axial strain gauges, orthogonally mounted with respect to each other on the barrel of the cylindrical PZT. The measurement of strain using

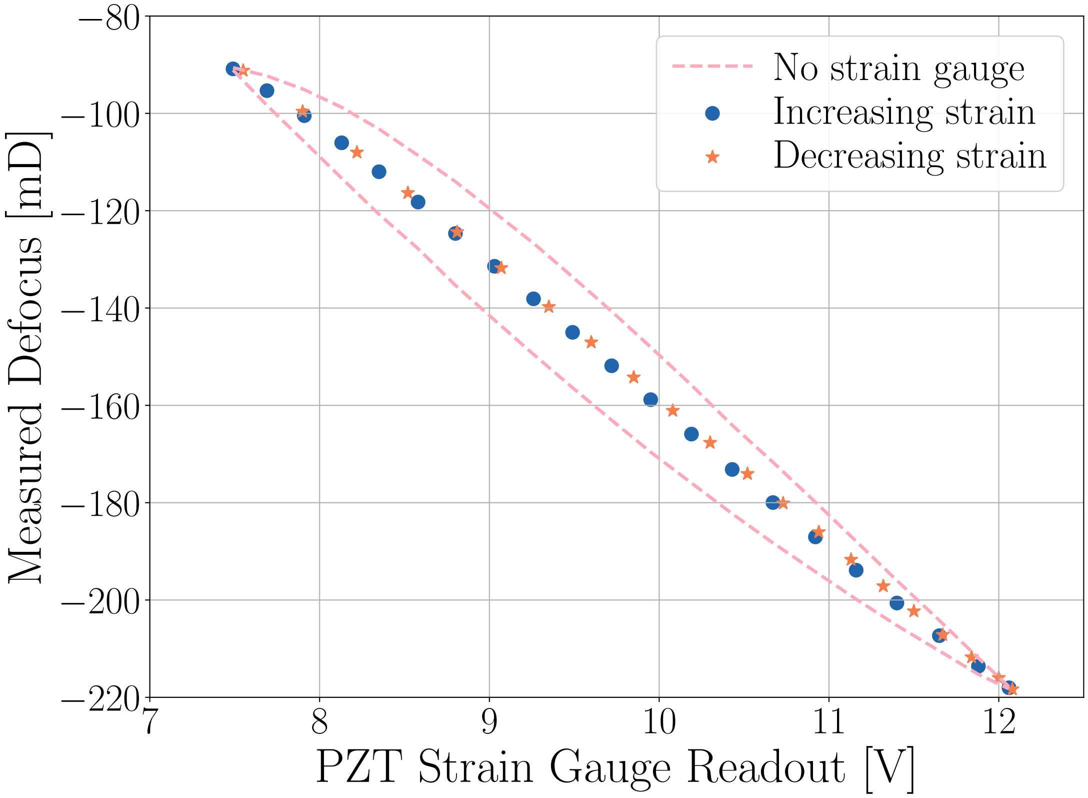

Figure 18: The dashed pink outer boundary to the curve shows the measured defocus resulting from a 200 V peak-to-peak sinusoidal voltage applied to the piezo actuator. The visible hysteretic response creates uncertainty if the drive voltage were used to define the resulting defocus. The blue circles (orange stars) represent the measured defocus at 10V steps of the sinusoidal drive voltage as a function of the strain-gauge readout bonded to the PZT. This illustrates how the strain gauge readout provides a linear and repeatable measurement of the defocus. The linear readout feature in conjunction with the high-bandwidth of the piezo-deformable mirrors enables closed-loop mode-matching and active wavefront applications.

this type of gauge relies on the measurement of small changes in resistance (1 ohm full-scale) associated with the elongation of the conductive elements in the sensor. An axially mounted strain gauge measures the elongation of the PZT as it is driven by an external voltage. As the axial sensor is stretched and compressed, an undesired change in area results from the Poisson-ratio of the piezo-ceramic material much as would be seen by stretching a rubber band. A second transversely mounted strain gauge provides compensation for the unwanted area change. A side benefit to the use of two collocated sensors is inherent temperature compensation to the resulting half bridge circuit. The combined results of these techniques in conjunction with a balanced Wheatstone bridge readout are linear and repeatable defocus measurements as shown in Fig 18.

Chapter 4

High Frame-Rate Phase Camera for High-Resolution Wavefront Sensing in Gravitational-Wave Detectors

We present a novel way of wavefront sensing using a commercially available, continuous wave time-of-flight camera with QVGA-resolution. This CMOS phase camera is capable of sensing externally modulated light sources with frequencies up to 100 MHz. The high-spatial-resolution of the sensor, combined with our integrated control electronics, allows the camera to image power modulation index as low as -62 dBc/second/pixel. The phase camera is applicable to problems where alignment and mode-mismatch sensing is needed and suited for diagnostic and control applications in gravitational-wave detectors. Specifically, we explore the use of the phase camera in sensing the beat signals due to thermal distortions from point-like heat absorbers on the test masses in the Advanced LIGO detectors. The camera is capable of sensing optical path distortions greater than about two nanometers in the Advanced LIGO input mirrors, limited by the phase resolution. In homodyne readout, the performance can reach up to 0.1 nm, limited by the modulation amplitude sensitivity[1].

---

[1] Erik Muñiz*, Varun Srivastava*, Subham Vidyant and Stefan W. Ballmer, Physics Review D 104, 042002, 2021.

4.1 Introduction

The second generation of gravitational-wave detectors Advanced LIGO [26] and Advanced VIRGO [36] have been observing the compact binary mergers for over five years. The first direct detection of gravitational waves from the inspiral and merger of two binary black-holes happened on September 14, 2015, opening up the field of gravitational wave astronomy [8]. Since then there have been two sets of upgrades to improve the sensitivity of the Advanced LIGO and VIRGO detectors [1] and the three observational science runs have confirmed over 50 gravitational wave signals from binary collisions [57, 58].

The Advanced LIGO and VIRGO detectors are dual-recycled Fabry-Perot Michelson interferometers capable of measuring relative peak displacement between the two interferometer arms to less than one attometer [26, 36]. To enable this precise measurement, the core and auxiliary optics are seismically isolated and the feedback loops are set up to actuate on translational and angular degrees of freedom [26]. The error signals to control the optics are derived using Pound-Drever-Hall (PDH) technique [59, 24] from 9 MHz and 45 MHz sidebands modulating the carrier laser beam. These error signals are acquired using radio-frequency (RF) photodiodes - single-segment diodes for length sensing, and four-segment quadrant photodiodes for angular sensing. Similarly, beam waist position and size sensing can be done using bulls eye segment diodes [60], mode converters [25] and aperture-based schemes [61]. Alternatives to this readout scheme using jitter modulation techniques have also been proposed [62].

Since any degradation in the optical wave front will degrade these signals, significant effort has gone into ways to image the RF optical beat pattern of the readout beam for diagnostic purposes. Previously developed sensors for the LIGO and Virgo detectors include scanning-type [63, 64, 65] and optical lock-in [66, 67] phase cameras, all of which require additional optical elements ahead of the photo sensor.

In our work, we redesign the traditional time-of-flight camera to directly record these amplitude-modulated laser beat signals in QVGA resolution (320 × 240 pixels). We achieve this by phase locking the OPT8241 time-of-flight camera to the external reference oscillator that modulates the laser. This approach has the benefit of requiring minimal optical components and beam shaping, making the CMOS phase camera an excellent diagnostic tool for gravitational-wave detectors that can be easily deployed at any optical port of the interferometer. We also demonstrate that this phase camera can be used for generic wavefront sensing.

The sensitivity of interferometric gravitational wave detectors such as Advanced LIGO scales with the amount of power circulating in the arm cavities. Following the O3 upgrade, the Advanced LIGO detectors reached 200 kW of power in the arm cavities [1] for the first time. The high power in the arm cavities exposes point defects in the coatings of the test masses. Under high power these point defects, or point absorbers, burn into the coating of the Advanced LIGO test masses [3], locally heating and deforming the optic. This has proven to be problematic, limiting power buildup in the arm cavities and dark port contrast, both of which limits the sensitivity of the Advanced LIGO detectors. Specifically, the thermo-refractive and thermo-elastic surface deformations due to the point absorbers induce optical path distortions affecting the phasing of the carrier and the modulating sidebands [3]. For the carrier, this detuning results in higher-order spatial modes being resonant in the arm cavity, causing a loss in the detector sensitivity. Additionally, the non-resonant RF sidebands couple into higher-order spatial modes and degrade the alignment and control error signals error.

We aim to use the CMOS phase camera to image the deformations in the laser beat signals that arise from these point defects. In the paper, we briefly describe the principle of operation of time-of-flight cameras in section §4.2. Next, in section §4.3 we describe the hardware and software changes made to reconfigure the time-of-flight camera into a CMOS phase camera. The experimental layout to test the sensitivity of the phase camera and the corresponding noise model to measure amplitude modulated signals is described in section §4.4.1. We model the point absorber to estimate the change in beat signal and correlate it with the sensitivity of the camera in section §4.5. Lastly, we discuss the applicability of the CMOS phase camera in Advanced LIGO and A+ detectors in section §4.6.

4.2 Principle of Operation of Time-of-Flight Cameras

Time-of-flight cameras employ a 2D array of pixels with depth sensing capabilities to independently measure the distance of a particular object in the field of view.

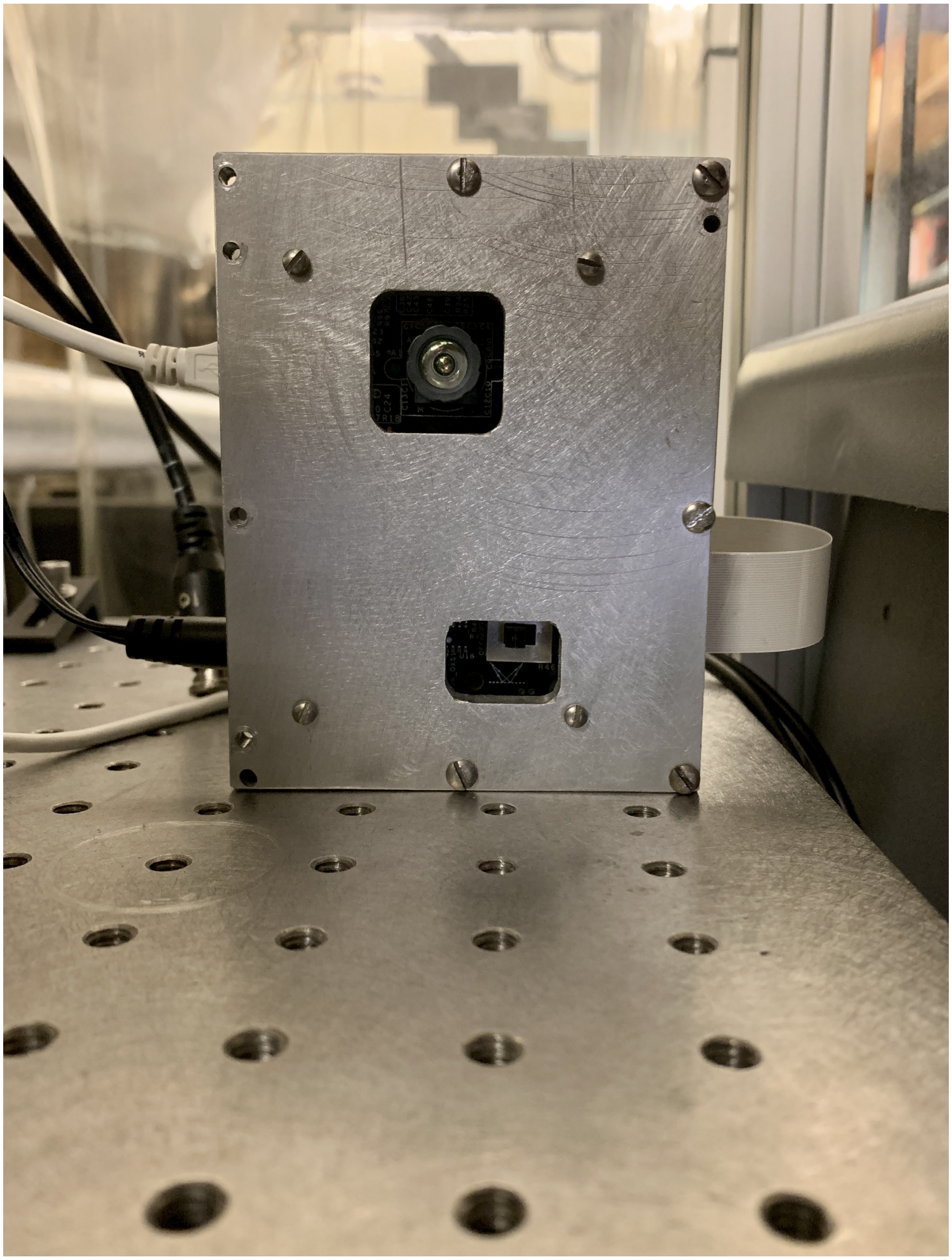

Figure 19: The prototype CMOS phase camera based on the commercially-available OPT8241 time-of-flight sensor. The custom-built enclosure ensures shielding from interference from unwanted RF signals.

Commercially available time-of-flight cameras typically have integrated illumination sources. They rely on either pulse-modulation, directly measuring the pulse travel time, or on continuous-wave amplitude-modulation, measuring a phase delay via demodulation with a local reference. The measured phase delay provides depth information. Since we intend to use the sensor to record the beat map of laser fields we selected the second type sensor for our research.

The amplitude A, phase ϕ and DC value I_0 of the amplitude modulated beam can be found by measuring the gated photo current C at four demodulation phases ($\Phi = 0, \pi/2\ , \pi\ , 3\pi/2$) [68]. We have

$$\mathrm{A} = \frac{\sqrt{\{C(0) - C(\pi)\}^2 + \{C(\pi/2) - C(3\pi/2)\}^2}}{2} \tag{4.53}$$

$$\phi = \measuredangle[(C(0) - C(\pi))\ \ + i(C(\pi/2) - C(3\pi/2))] \tag{4.54}$$

$$I_0 = \frac{C(0) + C(\pi/2) + C(\pi) + C(3\pi/2)}{4} \tag{4.55}$$

4.3 Motivation and Design

For application as a wavefront sensor in gravitational-wave interferometers the time-of-flight camera needs to accept the interferometer RF local oscillator signal as an external reference oscillator source for demodulation. In continuous-wave amplitude-modulated time-of-flight cameras, both the illumination source and pixels are typically driven using the same internal, radio-frequency (RF) oscillator source. Shrestha et al. [69] show that the time-of-flight camera OPT8221 offers flexibility for operation as a standalone demodulation camera with an external signal driving the illumination source and the demodulation within the camera.

The design proposed here uses the OPT8221 camera evaluation board (OPT8241-CDK-EVM), which consists of two primary components: the sensor (OPT8241) and a programmable controller (OPT9221). The OPT9221 is a companion chip to the OPT8241 and is responsible for setting register functions and processing raw data. The sensor is a standard 320 × 240 pixel array (QVGA format) capable of operating at frame rates up to 150 frames per second (fps), although live-streaming with Voxelviewer software [70] is limited to 60 fps. Neighboring pixels are separated by 15 μm and are capable of demodulation up to 100 MHz. In each pixel the charge carriers are sorted into two separate charge storage wells, depending on the state of the local oscillator [71, 72]. The two wells are simultaneously read out and their difference is digitized, removing the DC component from the RF readout. Charge separation becomes less efficient at higher frequencies [73], leading to a reduction in the demodulation amplitude at higher demodulation frequencies.

The camera board can be programmed to provide 12-bit amplitude and phase, as well as 4-bit ambient values in QVGA format. The OPT8241 also features a 850 nm NIR band-pass filter covering, which has a small transmission of about 5% at 1064 nm for normal incidence [74]. We use the sensor at 1064 nm, the laser wavelength used in the LIGO, VIRGO, and KAGRA gravitational wave detectors [26, 36, 75].

For application as an active wavefront sensor the camera board must be reconfigured. First, the internal modulation block of the camera board is disabled via the appropriate configuration of register settings in the OPT9221, allowing it to accept an external reference signal. This reference signal needs to be appropriately stepped in quadrature phase, with $\Phi = 0^{o}, 90^{o}, 180^{o}, 270^{o}$. The frequency of the reference signal can also be dynamically changed between video frames, permitting imaging beat signals from multiple sidebands simultaneously. Thus, the CMOS phase camera is capable of measuring both the spatial and temporal characteristics of the illuminating beam in real-time.

In this section, we present the schematic design for the CMOS phase camera. The various electronic components, along with their functionality, are listed below and illustrated in Fig. 20:

- *Microcontroller*: We use the ARM Cortex-M4-based STM32F407 as a master device. It is programmed to control waveform generation on the Direct Digital Synthesis (DDS) board. The microcontroller transmits a data sequence to initialize each of the individual channels on the DDS board via SPI protocol. The microcontroller also initiates the frame capture sequence by sending an initial trigger pulse to the camera board. Depending on the register settings of the OPT9221 controller, the camera board responds by sending a series of quadrature (quad) exposure pulses, which trigger an interrupt sequence on the microcontroller. This interrupt sequence is used to set the logic levels on the RF switch and/or the synchronization flip-flop to output the appropriately phase-stepped signal corresponding to the quad exposure pulse.

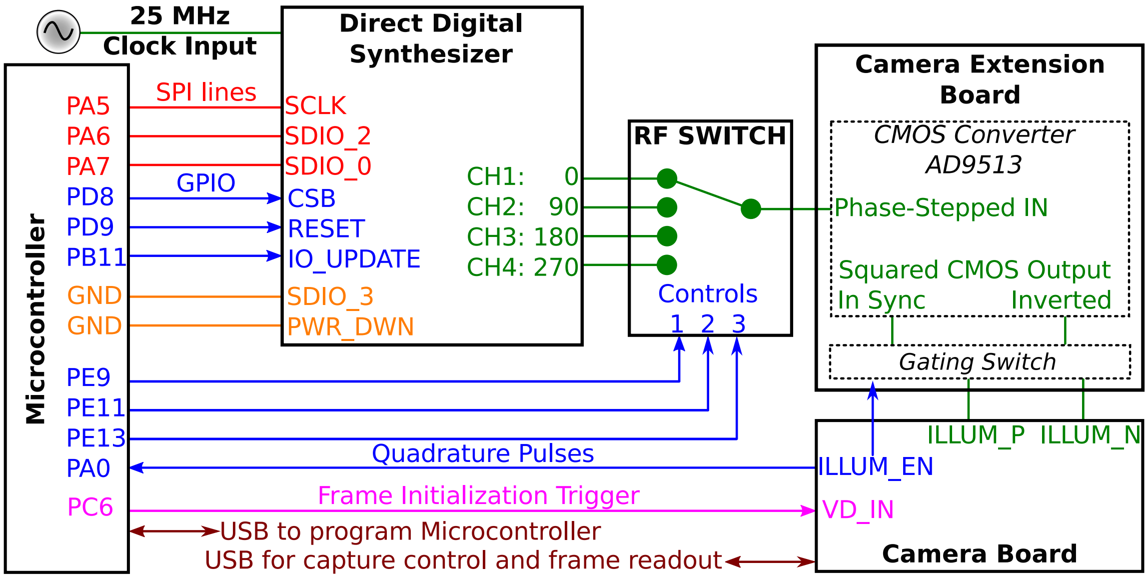

Figure 20: An overview of the phase camera signal chain and design components. The microcontroller acts as the host device controlling waveform generation and image frame capture. The microcontroller initializes the direct digital synthesizer board. Quadrature phase-stepped signals are generated on the four analog output channels of the direct digital synthesizer board. These signals are sent to an RF switch, which passes the appropriate signal via CMOS converter and gating switch to the camera. This gating switch removes the RF signal during the sensor readout to reduce the electronics noise. Every frame is initiated by a frame initialization trigger sent by the microcontroller to the camera board. The camera responds by sending a series of quadrature pulses back to the microcontroller, which are used in an interrupt sequence to set the control signals for the RF switch.

- *Direct Digital Synthesizer (DDS) board*: Waveform generation is handled by the Analog Devices Direct Digital Synthesizer board (AD9959). The AD9959 has four independent synchronized output channels with tunable amplitude, frequency and phase. The external reference local oscillator used to modulate the interferometer input laser serves as the reference clock signal to the DDS board for synchronization. The microcontroller sets frequency, phase and amplitude registers on the DDS board for each channel and activates the settings via a separate I/O-update line. For normal operation the four channels are set to a phase of $\Phi = 0^o,\ 90^o,\ 180^o,\ 270^o$ with respect to the reference clock at the desired demodulation frequency during initialization.

- *RF switch*: A single-pole, four throw RF switch from Mini-Circuits (JSW4-272DR+) is used to switch between the four phased channels from the DDS board, selecting the camera demodulation phase. The RF switch is controlled by the microcontroller. The DDS board and RF switch together can provide an externally referenced and phase-stepped oscillator between 5 MHz to 500 MHz.

- *Synchronization Flip-Flop*: The DDS board register update is only synchronized to the internal reference clock (SYNC_CLK), which is running at a higher frequency than the external reference signal. To avoid random phase jumps on update, a flip-flop is used to trigger the update of the DDS registers synchronized with the rising edge of the external reference signal. There are two schemes to operate the phase camera. First, the four channels of the DDS board are set up during camera initialization, and the flip-flop synchronization to the reference oscillator guarantees the same relative phase on every camera startup. The RF switch is then used to select the channel with the desired demodulation phase. Since this method does not rely on a synchronized register update during operations it is more robust, but also limited to four demodulation phases and a single frequency. In the second approach, we use the flip-flop to actively update the registers and phase-step the output of one of the DDS channels in accordance with the quad pulses from the camera. This scheme, discussed in-depth in section §4.8, allows the camera to image the amplitude-modulated beat at different frequencies in real-time, and permits camera operation with six quads, reducing potential cross-talk from harmonics of the modulation frequencies.

- *CMOS Converter*: To convert the sinusoidal reference signal to a CMOS logic level clock, i.e. 'squaring the clock', we use a high-speed clock distribution integrated circuit (Analog Devices AD9513).
- *Gating Switch*: We use an additional high-speed buffer chip (Texas Instrument's SN74LVC126A) in the signal chain to gate the output demodulation waveform during each quad exposure. Turning the RF signal off during the readout phase between camera exposures significantly reduces the camera electronics noise.

All firmware was developed within the Keil μVision IDE and flashed to the microcontroller via a USB interface. This allows the microcontroller to run as the master device after an initial reset event.

4.4 Performance Characterization

4.4.1 Experimental Setup

To characterize the performance of the CMOS phase camera we used the experimental setup shown in Fig 21. A reference triangular cavity, previously used as pre-mode cleaner cavity (PMC) in the initial LIGO interferometers until 2010, is used to stabilize the frequency of a 1064 nm Nd:YAG laser via Pound-Drever-Hall (PDH) locking. The cavity has a finesse of 165 and features a piezoelectric-actuated mirror at the apex which allows for tuning of the cavity resonance. The carrier field, $E_c = E_0 e^{i\omega_c t}$, is phase-modulated using a resonant electro-optic modulator referenced to a 25-MHz local oscillator. This adds sidebands to the optical carrier field offset at the modulation frequency $\Omega/2\pi$. The peak-to-peak drive voltage of the local oscillator determines the amplitude of the phase modulation index Γ. The field incident on the cavity is given by

$$E_{in} = E_c e^{i\Gamma \cos \Omega t} \approx E_c \left(1 + \frac{i\Gamma}{2} e^{i\Omega t} + \frac{i\Gamma}{2} e^{-i\Omega t}\right) \tag{4.56}$$

To produce a significant amount of amplitude beat signal between carrier and sideband the cavity length was tuned to resonate on a single sideband. Under the simplifying assumption that one sideband passes the cavity 100%, while the other light gets reflected 100%, the reflected field becomes to first order

$$E_{ref} \approx E_c \left(1 + \frac{i\Gamma}{2} e^{-i\Omega t}\right), \tag{4.57}$$

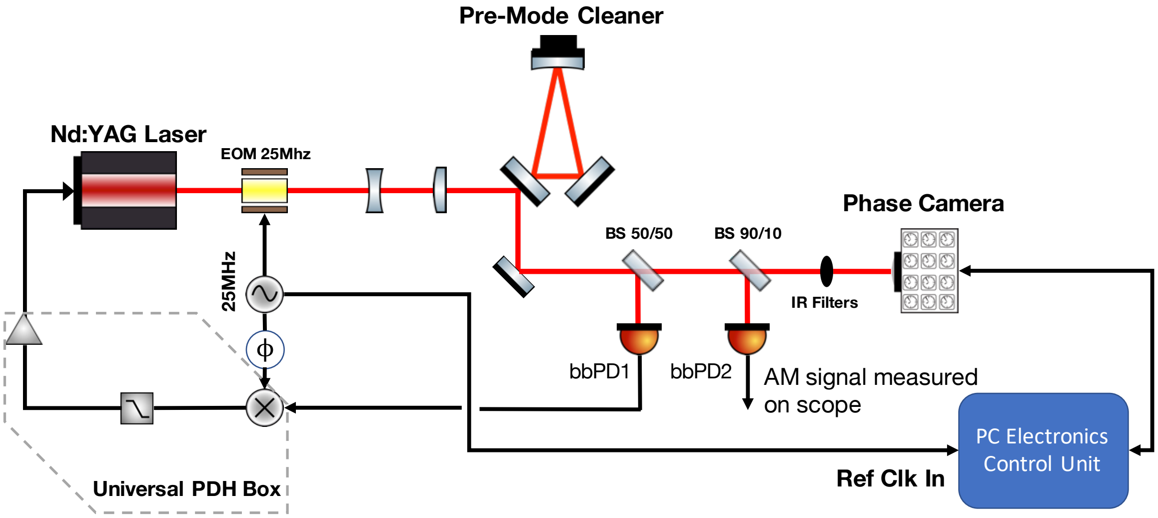

Figure 21: The experimental layout used for testing and quantifying the noise levels of the phase camera. The laser is stabilized by locking to the pre-mode cleaner cavity using the PDH technique. The amplitude-modulated beat signal is generated in the reflection of the cavity when it is locked to one of the 25 MHz sidebands. The bbPD1 is the photodiode sensor used for PDH locking. The bbPD2 is used in calibration and measures the power modulation index of the beam incident on the camera. The total power incident on the camera is attenuated to $\sim$10 μW.

which is then passed through a 50/50 beam splitter where half of the laser light is reflected onto a single-element broadband RF phototdiode (bbPD1) for PDH locking and the other half is directed to the camera. From here, the beam power is split again with 90% of the light going to the camera and 10% incident on a second photodiode (bbPD2) used for calibration — discussed more in section §4.4.2. The power incident on the camera is thus amplitude modulated with power modulation index Γ:

$$\begin{aligned} I_{PC} &= |E_{ref}|^2 \\ &\approx |E_c|^2 \big(1 + \Gamma \sin \Omega t\big) \end{aligned} \tag{4.58}$$

Frequency terms greater than the modulation frequency are filtered by the bandwidth of the camera. In this single-sideband scenario power modulation index Γ is also related to the sideband-to-carrier ratio SCR via

$$\mathrm{SCR}\,[\mathrm{dBc}] = 20 \log_{10} \left(\frac{\Gamma}{2} \right), \tag{4.59}$$

where we use the IEEE's definition [76]. Unlike typical photodetectors, the measured photocurrent is demodulated at Ω in each pixel on the sensor array. The corresponding amplitude and phase maps are then constructed using the measured values of I and Q for each frame. The CMOS phase camera in our experiment was set to capture at a frame rate of 7 Hz with total exposure time of 32 ms, although frame rates of up to 60 Hz are supported.

4.4.2 Calibration

For each frame of the 320 × 240-pixel array, the respective amplitude, phase, and ambient readout channels of the camera are expressed in terms of counts of the analog-to-digital converter or digital numbers (DN). We perform a calibration procedure to determine a calibration factor, κ, which relates the total number of generated photoelectrons in an image to the corresponding DN value. The calibration procedure is as follows:

1. We use the broadband photodiode (bbPD2, see Fig. 21), to determine the modulation index of the beam incident on the camera. We measured its DC transimpedance Z_{dc} to be 1975 Ω and its RF transimpedance Z_{rf} at 25 MHz, the

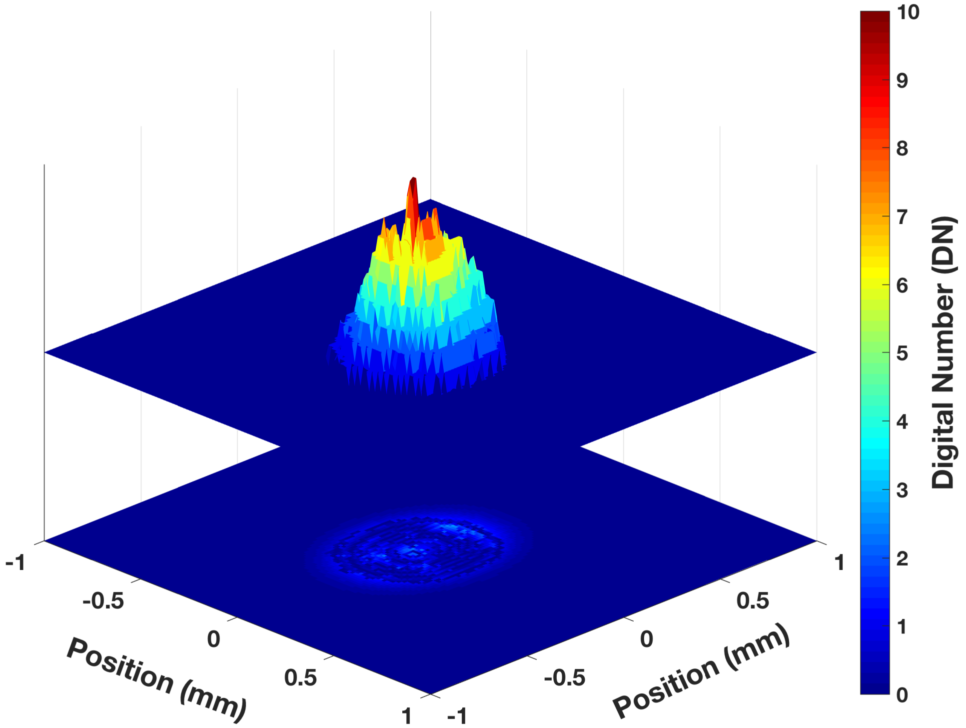

Figure 22: The DC intensity profile, which is used in calibration, is plotted as a function of sensor position. The residual of the Gaussian fit to the DC profile is shown in the plane on the bottom. The dominant 4-bit digitization noise in the DC output is noticeable. In contrast, the RF output is digitized with 12-bit resolution.

frequency of the local oscillator, to be 4750 Ω. Then, the power modulation index (Γ_m) of an arbitrary beam incident on *bbPD2* can be calculated via

$$\Gamma_m = \frac{1}{2} \cdot \frac{V_{pp}^{rf} \cdot Z_{dc}}{Z_{rf} \cdot V_{dc}} \tag{4.60}$$

where the peak-to-peak RF signal (V_{pp}^{rf}) and the mean DC signal (V_{dc}) measured by *bbPD2* are read on an oscilloscope. The factor of 1/2 converts peak-to-peak to amplitude.

2. To quantify the number of photons incident on the camera we measure the incident power (P_{in}) using a calibrated Thorlabs power meter. Since the NIR filter on the camera has a 5% transmission at 1064 nm at normal incidence [74], the total power incident on the camera after the filter (P_{in}^{sensor}) can be calculated. The ambient channel of the camera measures the profile of the incident beam. We fit a Gaussian profile normalized to the P_{in}^{sensor} to get the Gaussian beam parameters and calculate the power density of the beam incident on the sensor, $p_{in}^{sensor}(x, y)$, see Fig. 22. The number of photons per area incident on the sensor during the exposure time T_{exp} can then be estimated by

$$n_p(x, y) = \frac{p_{in}^{sensor}(x, y) \cdot T_{exp}}{h\nu} \tag{4.61}$$

   The exposure time is the sum of each of the quadrature exposure time during which the signal is integrated.

3. The number of photoelectrons generated in each pixel is related to the number of photons via the quantum efficiency η, which for the OPT8241 sensor is approximately 2% for 1064 nm light [73]. Thus we have

$$N_e = \int_{A_{pixel}} n_e(x, y)\ dxdy = \int_{A_{pixel}} \eta \cdot n_p(x, y)\ dxdy \tag{4.62}$$

4. Finally, the calibration factor κ is given by the ratio of the total number of photoelectrons generated to the sum of digital numbers reported in a region of interest (ROI):

$$\kappa_{DC}(e^-/DN) = \frac{\Sigma_{ROI}(N_e)}{\Sigma_{ROI}(DN_{DC})} \tag{4.63}$$

Similarly, the AC calibration is given by

$$\kappa_{AC}(e^-/DN) = \Gamma_m \frac{\Sigma_{ROI}(N_e)}{\Sigma_{ROI}(DN_{AC})}, \tag{4.64}$$

where Γ_m is the modulation index from Eq. 4.60 and we divide by the camera output in the AC readout, DN_{AC}. We estimate a calibration factor of κ_{DC} of $1.9 \cdot 10^5\ e^-/DN$ and κ_{AC} of $1.0 \cdot 10^3\ e^-/DN$.

4.4.3 Noise Sources

The CMOS phase camera offers both the AC and DC readout channels, which are susceptible to noise sources typical to CMOS image sensors. These noise sources can either be temporal or spatial. Temporal noise arises due to the electronic noise from resistive components (i.e. pixel reset noise), dark noise, photon shot noise and other electronics noise related to the image sensor. Spatial noise is primarily due to the pixel-to-pixel imperfections, that is gain and threshold variations in the sensor array.

For the DC readout, the 4-bit digitization of the ambient channel results in large analog-to-digital rounding errors. As a result, the ADC quantization noise is the limiting source of noise for the DC readout. In contrast, the AC readout provides a 12-bit resolution, sufficient for resolving small fluctuations of the measured signal. For the AC readout, the different noise sources of the phase camera are presented below:

1. *Shot Noise* in the camera translates to an effective fluctuation in the measured number of photoelectrons generated in the AC readout channel. The shot noise scales as the square root of the number of electrons generated during the exposure time. The AC shot noise can be estimated as

   $$\sigma_{SN}\ (e^-) \approx \sqrt{2N_e} \tag{4.65}$$

   The factor of $\sqrt{2}$ is due to the demodulation. Shot noise is a fundamental limitation, but our CMOS phase camera is not shot noise limited.

2. *Electronic Noise* includes all noise sources involved in charge conversion and signal processing within the image sensor. Two prominent noise sources in the CMOS-based sensors are the amplifier noise and the pixel reset noise. Both

arise due to the Johnson noise associated with the reset transistor in each pixel. Therefore, the electronic noise (in DN) can be estimated from non-illuminated regions in the frames, using the temporal standard deviation across multiple frames. The effective electronic noise can be reduced by frame- and/or pixel-averaging (i.e. temporal or spatial averaging).

3. *Fixed Pattern Noise* (FPN) describes the spatial noise associated with non-homogeneity between neighboring pixels on the sensor. Fixed pattern noise is dependent on the signal on the sensor and for a given signal can be expressed as [77]

$$\sigma_{FPN} = \alpha\, \tilde{C} + \beta \tag{4.66}$$

where α is the gain and β is a column or row offset in the readout. $\tilde{C}$ represents the true DC signal with additive Gaussian noise, which represents the temporal fluctuations of the signal contributing to the fixed pattern noise due to the gain. Under uniform illumination, one can estimate the pixel fixed pattern noise (in DN) as the spatial standard deviation from the mean. Using the calibration factor calculated in Section §4.4.2, we can express the fixed pattern noise in terms of the number of electrons. As σ_{FPN} varies as a function of the signal intensity, trivial background frame subtraction will not work to improve the SNR. Spatial averaging of frames can reduce the noise at the cost of signal resolution. Technique to subtract fixed pattern noise from phase and amplitude readouts is developed by [77].

Ideally, the limiting noise sources for the CMOS phase camera have a Gaussian distribution [78, 79]. Under this assumption, the variance of each of the quadrature measurements is constant (σ^2). In this case, the total noise in the amplitude (σ_A) can be estimated as the quadrature sum over individual noise sources. The total phase noise (σ_ϕ) is estimated as the ratio of the total noise in amplitude to the mean amplitude of the signal, as phase and amplitude noise should be uncorrelated.

4.4.4 Quantitative Noise Measurement and Sensitivity

Here we quantify the temporal and spatial noise of the CMOS phase camera. The noise performance is characterized using the experimental layout described in Section §4.4.1. To characterize the DC power saturation levels, we vary the intensity of the 1064 nm laser beam incident on the CMOS sensor. We observe pixel saturation at 6μW of incident power with beam radius of 0.25 mm. Additional camera performance parameters are summarized in Tables 1, 2 and 3.

To determine the RF sensing capabilities and noise limitations of the phase camera the DC intensity of the beam incident on the sensor is held constant while the power modulation index is varied by sweeping the cavity, as illustrated in Fig. 21. Using this method, we report performance measurements for power modulation index values from zero to 0.046. The AC calibration factor, calculated in section §4.4.2, is used to convert the measured noise into equivalent number of photoelectrons. The total noise in an individual pixel in a single frame is estimated by adding in quadrature photon shot noise, fixed pattern noise, and electronics noise, all of which are measured with an integration time of 32 ms. The total amplitude and phase noise are measured as the standard deviation of the corresponding image obtained by subtracting two independent illuminated frames and dividing the result by $\sqrt{2}$. The results in Fig. 23 show a close agreement between measured and estimated noise. We find that the shot noise limit is a factor of 8 below the total measured noise and the camera sensitivity is limited by background electronic noise and fixed pattern noise.

The demodulation pixels suppress the DC contribution of the illuminating beam using correlated balance sampling [73, 80]. However, a sufficiently high carrier field intensity will saturate the pixel of the sensor. The dynamic range is the ratio of the saturation point to the noise floor defined as [73]

$$D/R = 20\,\log_{10}(\frac{A_{sat}}{\sigma_{dark}}), \tag{4.67}$$

where A_{sat} is the pixel saturation value, i.e. maximum digital number and σ_{dark} is the dark noise of the pixels. We estimate an operating dynamic range of 75 dB for the phase camera. However, due to the low modulation index of the illuminating beam in our test setup, the camera saturates in DC before reaching the full dynamic range of the amplitude and the phase readouts.

Camera performance for each measurement can also be quantified by calculating the signal-to-noise ratio (SNR). We define the SNR as the ratio of amplitude of the demodulated output A (estimated using spatial averaging) to the measured amplitude noise σ_A.

$$SNR = \frac{A}{\sigma_A} \tag{4.68}$$

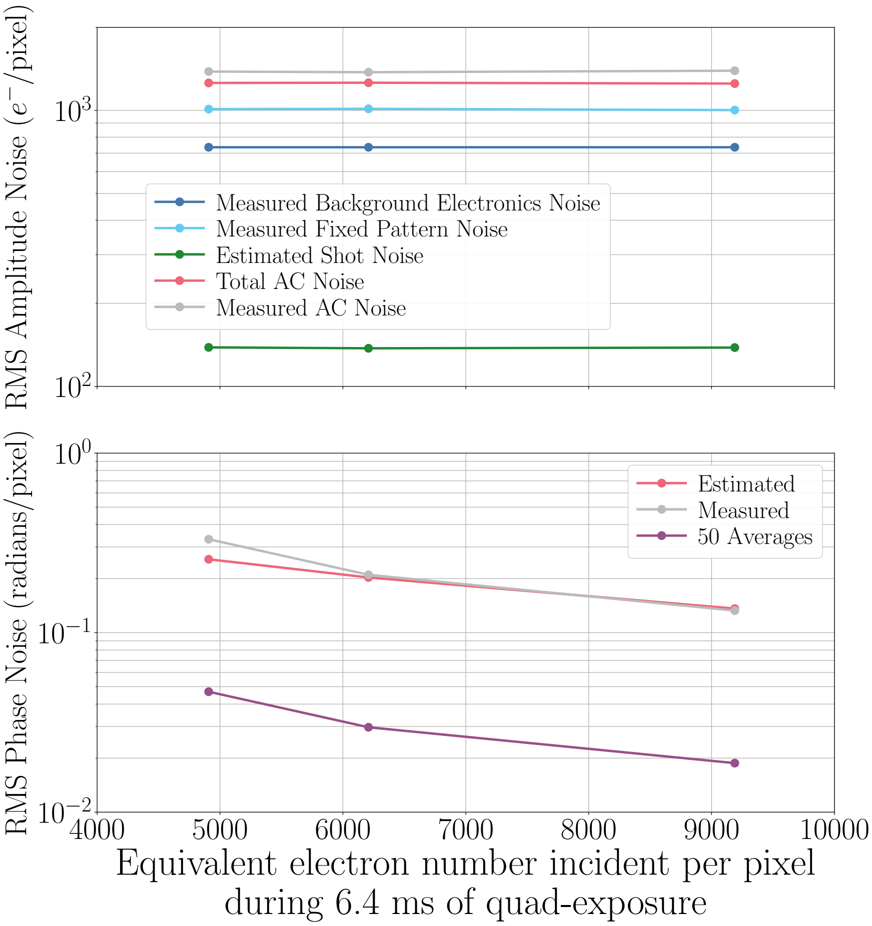

Figure 23: The figure above shows the phase camera noise as the power modulation index of the incident beam is varied at constant beam intensity. The root-mean-square amplitude noise (top) and phase noise (bottom) per pixel of the camera are calculated from a single image captured (no averaging). As the beam profile is the same across these measurements, the sensor area considered is the same. The shot noise and fixed pattern noise remain constant under these illumination conditions. We find that the total measured per pixel noise in phase and amplitude agrees closely with the sum of the budgeted noise sources. The current prototype of the phase camera is predominantly limited by the electronic noise and the shot noise is a factor of 8 below the total noise. The phase noise improves with higher power modulation index and with averaging of frames. The bottom plot also shows the measured per pixel phase noise with 50 frame averages in purple.

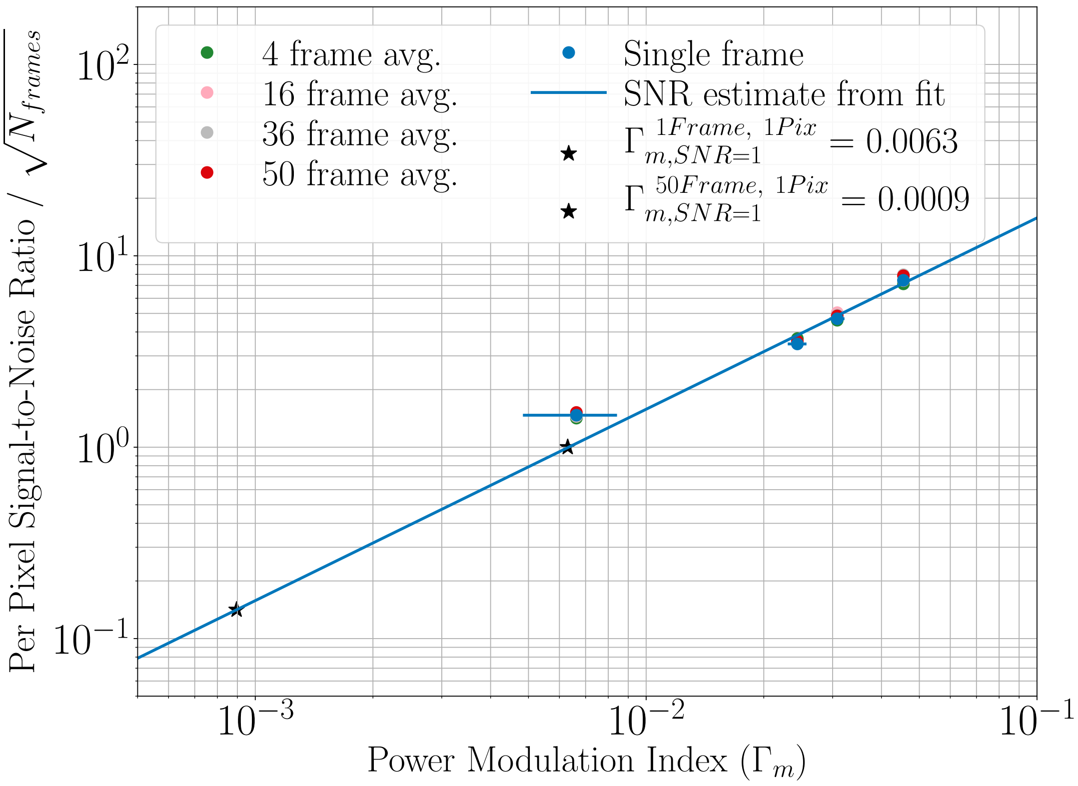

Figure 24: Single-frame-SNR as a function of Γ_m. The y-axis shows the single-frame-SNR, defined as SNR/$\sqrt{N_{frames}}$. The horizontal error bars show the experimental errors in the estimation of the Γ_m using the calibrated *bbPD2* photo detector. We find the SNR improves with the square root of the number of frames and number of pixels, consistent with temporally and spatially independent pixel noise. Pixel averaging can be implemented to improve the SNR at the cost of spatial resolution. The blue line represents a linear fit through the data. Using the fit, we estimate with 50 averages, the CMOS phase camera is capable of sensing RF signals in each pixel with Γ_m as low as 0.0009.

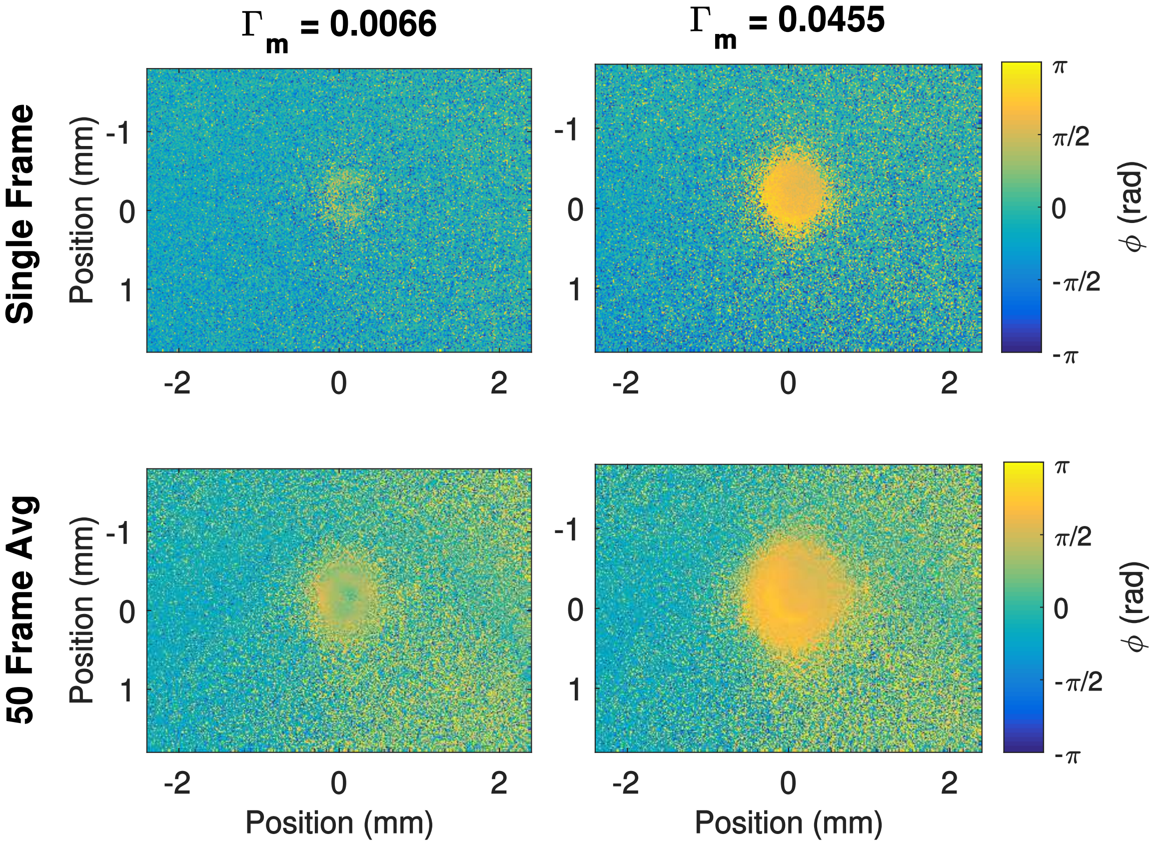

Figure 25: Phase images — single frame (top row) and with 50 averages (bottom row), for incident beams with low (left) and high (right) power modulation index. The phase resolution improves linearly with SNR.

We can define the SNR for individual pixels on a single frame, as well as after spatial and/or temporal averaging, Fig. 24 and 25. The figure shows the SNR as a function of the power modulation index Γ after averaging over a number of frames. The y-axis is scaled by $1/\sqrt{N_{\text{frames}}}$, such that the data points line up if the noise in the frames are independent. We find the SNR scales linearly with the modulation index of the illuminating beam at constant beam intensity. By fitting a linear model to the data, we determine the phase camera can detect signals above a modulation index of 0.0009 using 50 frame averages without any spatial averaging, see Fig. 24 and 25.

Using equation 4.59 we can also find the camera's sensitivity limit ($SNR = 1$) for resolving the sideband-to-carrier ratio SCR in dBc per frame per pixel:

$$\text{SCR}_{\text{LIM}} = 20 \log_{10} \left(\frac{\Gamma^{\text{1fr,1pix}}_{\text{SNR=1}}}{2} \right) = -50\,\text{dBc}_{/\text{fr}/\text{pix}}. \tag{4.69}$$

Since the frame rate for the test data was 7 Hz, and we only used about 50% of the maximum quad integration time per frame (see Tables 1, 2 and 3) we find approximately

$$\text{SCR}_{\text{LIM}} = -62\,\text{dBc}_{/\text{sec}/\text{pix}}. \tag{4.70}$$

4.5 Signal Modeling for Point Absorbers

One of the critical issues limiting the sensitivity of Advanced LIGO is the presence of small (few tens of um diameter) absorptive defects on the test masses, referred to as *point absorbers*. Exposed to the laser field in the interferometer arms, these test mass defects cause local heating and result in local optical path length distortions for the laser field. These optical distortions excite higher-order modes in LIGO's coupled cavities, leading to excess optical loss and limiting the sensitivity of the detectors. Furthermore, the path distortions affect the carrier and sideband phase fronts differently, thus deteriorating the alignment and angular control error signals. A phase camera is capable of mapping these phase front distortions. Error signals can be extracted from the camera output and can be used to control corrective actuators. Unlike conventional quadrant photodiodes, the phase cameras offer a high spatial resolution to resolve the phase front changes due to the point absorbers.

To get an approximate estimate of the phase camera's ability to sense the effect of point absorbers LIGO's input test masses, we present a simplified model without

Capture Settings				
Camera Parameters	Minimum	Typical	Maximum	Comments
Frame Rate (fps)	-	7	60 (150)	Performance characterization was done at 7 fps. We tested the camera up to 60 fps (live-streaming limit). The camera supports up to 150 fps.
Quads	4	4	6	Four quad readout is measured with $\pi/2$ phase-stepped demodulation; Six quad readout is measured with $\pi/3$ phase-stepped demodulation.
Sub-frames	1	1	4	The camera allows the capture of 1-4 sub-frames to construct a single frame. Each sub-frame is constructed with the readout of all the quads above.
Quad Integration time (ms)	1% $\mathrm{DC}_{\mathrm{Exp}}$	6.4 (15%)	30% $\mathrm{DC}_{\mathrm{Exp}}$	Dependent on the frame rate, number of sub-quads and sub-frame and the readout time. The quad integration time cannot exceed 30% of the DC exposure due to the readout and dead time of the CMOS phase camera.
Pixel Resolution (μm)		15		This defines the average size of each pixel on the sensor array.
Sensing Area (mm)		4.8×3.6		The total sensing area of the CMOS sensor.

Table 1: The table summarizes the range of camera capture settings

ILLUMINATION CHARACTERISTICS				
DC Power (nW) [per pixel], estimated with beam size $w_0 = 0.25$ mm	1.5	-	14.6	The minimum input power for the pixels to sense the input beam and the maximum power before the pixels saturate.
DC Power (μW) [sensor; for incident beam of size $w_0 = 0.25$ mm]	0.6	-	6.4	As the spot size of the incident beam increases, both the minimum and maximum DC power can be re-scaled in accordance with per pixel DC power limits above. We caution that this parameter is exposure time dependent.
Demodulation Frequency (MHz)	5	25	100	The performance characterization was done at 25 MHz. The camera supports demodulation frequency up to 100 MHz. The 5 MHz lower limit is due to the RF switch.

Table 2: The table summarizes the absolute rating for the illumination signals.

FRAME CHARACTERIZATION (AT 7 HZ FRAME RATE AND 15% QUAD INTEGRATION TIME)		
Dynamic Range (dB)	75	The dynamic range of the camera as estimated from the dark noise level of the camera.
Γ_m: Single Frame	$6.3^{+2.2}_{-2.2} \cdot 10^{-3}$ - 1	The CMOS phase camera can typically sense as low as 0.0063.
SCR: Single frame	-50^{+3}_{-3} dBc/pixel - 0 dBc/pixel	SCR down to -50 dBc/pixel can be resolved in a single frame.
Γ_m: 50 frames averaged	$0.9^{+0.3}_{-0.3} \cdot 10^{-3}$ - 1	With 50 frames averaged, the camera can sense incident RF beams as low as 0.0009.
SCR: 50 frames averaged	-67^{+3}_{-3} dBc/pixel - 0 dBc/pixel	With 50 frames averaged we can resolve SCR down to -67 dBc/pixel.
Mean AC Noise (e^-)	10^3	

Table 3: The table summarizes the noise levels and sensitivity of the captured frames.

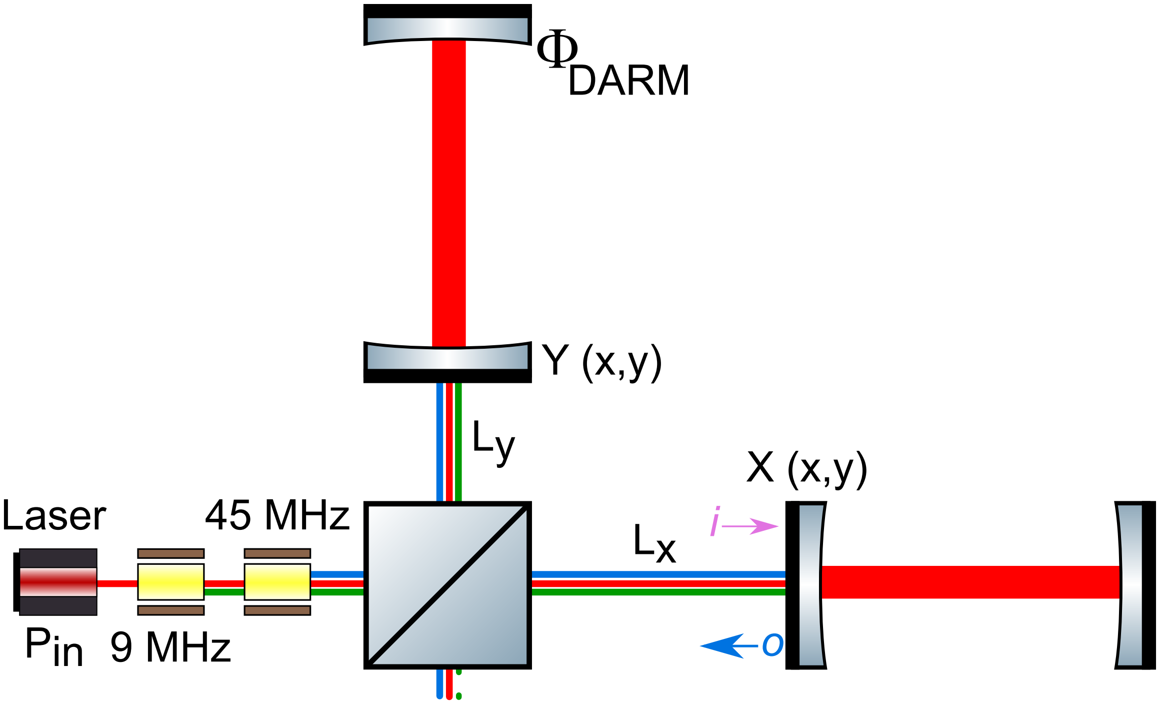

Figure 26: The figure illustrates the simplified Advanced LIGO setup for point absorber modeling. To simplify the simulation we do not include the effects of the power and the signal recycling cavities. Instead, we model the input power to be equal to the power at the beamsplitter during the Advanced LIGO O3 run [1]. The other parameters of the interferometer are summarized in the table 4. The optical path distortions due to the point absorbers is modeled with a Lorentzian profile for each of the input test masses. The carrier and the sideband fields are calculated under plane beam/paraxial approximation and the corresponding beat signals are calculated at the anti-symmetric port of the beamsplitter.

SIMULATION PARAMETERS	
Differential arm offset	10 pm
Arm cavity finesse	446
P_{Homodyne} ref. Beam	50 mW
$P_{\text{in}}^{\text{BS}}$	1500 W
w_0^{BS}	6 cm
L_{Schnupp}	8 cm
Carrier recycling gain	40
45 MHz recycling gain	2
45 MHz phase mod. index	
at input	0.18
at beamsplitter	0.04

Table 4: Simulation Parameters of the interferometer shown in Fig. 26. They approximately correspond to the Advanced LIGO parameters [1].

considering the coupled cavity layout of LIGO, shown in Fig. 26. We initially also ignore Gouy phase shifts because beamsplitter and input test masses are essentially in the same Gouy phase. We will get back to the effect of the output beam Gouy phase shift. While these are oversimplifications, they still allow us the estimate the required sensitivity to pick up the point absorber phase distortions in a phase camera image taken at the interferometer anti-symmetric port. We consider two scenarios, the current Advanced LIGO, which uses DC readout, and the A+ upgrade, which uses homodyne readout without differential arm DC offset. We choose the model parameters in accordance with the existing Advanced LIGO facilities. We assume the carrier and the 9 MHz and 45 MHz sidebands (with modulation index Γ) are incident at the 50/50 beamsplitter. Considering the approximate power-recycling gain of 40 for the carrier and 2 for the 45MHz sidebands we can estimate the power modulation index of the beam incident on the beamsplitter [1, 19]. The beam then propagates from the beamsplitter to the input test mass in each of the arm cavities. We model the response of the point absorbers to first-order, which affects the phase of the sidebands, but leaves the carrier unperturbed. The carrier experiences only a phase shift due to the DARM offset between the two arm cavities:

$$r_x^{car} = +1 \cdot e^{i\Phi_{DARM}/2} \qquad\qquad r_y^{car} = +1 \cdot e^{-i\Phi_{DARM}/2} \tag{4.71}$$

$$r_x^{sb} = -1 \cdot e^{i2k\mathrm{X}(\vec{x},\vec{y})} \qquad\qquad r_y^{sb} = -1 \cdot e^{i2k\mathrm{Y}(\vec{x},\vec{y})} \tag{4.72}$$

where $\mathrm{X}(\vec{x},\vec{y})$ and $\mathrm{Y}(\vec{x},\vec{y})$ are the one-way transmission maps encoding the optical path distortions. Under these simplified assumptions one can calculate the fields of the carrier and sidebands at the anti-symmetric port of the beamsplitter. The beat map between the carrier or the reference beam with the sideband in $\mathcal{I}$ and $\mathcal{Q}$ is given by

$$\mathcal{I}(x,y) = \mathbb{R}e(sb_+^* c + c^* sb_-) \tag{4.73}$$

$$\mathcal{Q}(x,y) = \mathbb{I}m(sb_+^* c + c^* sb_-) \tag{4.74}$$

One can analytically show that in the Gouy phase of the beamsplitter ($\phi = 0$) the beat in $\mathcal{I}(x,y)$ and $\mathcal{Q}(x,y)$ between the carrier and the sidebands at the AS port is first-order independent of the optical path distortions due to the point absorber. We recover the usual DC readout terms:

$$\mathcal{I}(\vec{x},\vec{y}) = 0 \tag{4.75}$$

$$-\mathcal{Q}(\vec{x},\vec{y}) = \Gamma p_{in}(\vec{x},\vec{y}) \sin(\frac{\Phi_{DC}}{2}) \sin(\frac{\omega_s L_s}{c}) \tag{4.76}$$

However, this does not remain true at every Gouy phase in the readout beam. The small point absorber distortion evolves differently with Gouy phase. For simplicity, we can assume that the distortion fields $\mathrm{X}(\vec{x},\vec{y})$ and $\mathrm{X}(\vec{x},\vec{y})$ contains only one higher-order mode of order $N = l + m$. (l and k are for example the Hermite-Gauss mode orders.) Then the $\mathcal{I}$ readout quadrature become

$$\mathcal{I}^{\phi} = k\Gamma p_{in} \sin(\frac{\Phi_{DC}}{2}) \cos(\frac{\omega_s L_s}{c}) \sin(N\phi)(\mathrm{X} - \mathrm{Y}) \tag{4.77}$$

where the spatial shape is given by the beat of the fundamental and the N-th order mode, $\Psi_N(\vec{x},\vec{y}) \cdot \Psi_0(\vec{x},\vec{y})$. Equation 4.77 can be generalized by expanding $\mathrm{X}(\vec{x},\vec{y})$ and $\mathrm{X}(\vec{x},\vec{y})$ in terms of higher order Gaussian modes, which is straight forward, a little complicated, and not necessary if we are only interested in the camera sensitivity limitation.

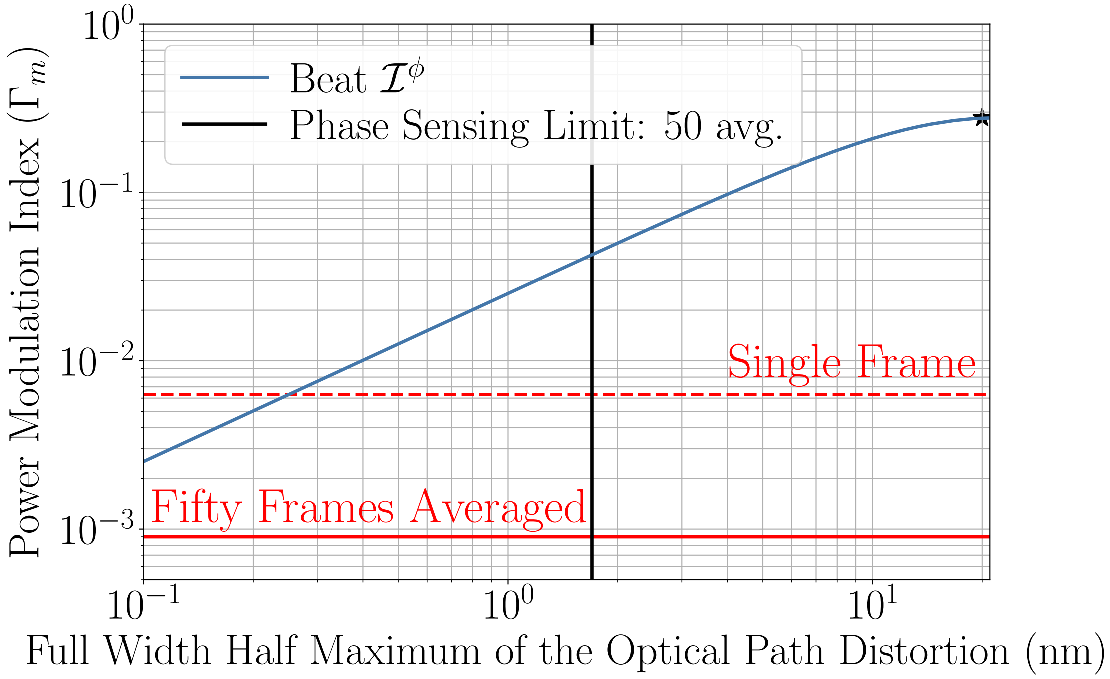

Figure 27: Size of the expected power modulation index in the interferometer anti-symmetric port $\mathcal{I}$-quadrature, as a function of the optical path distortions (OPD) due to a point absorber on an input test mass. The power modulation index scales linearly with the OPD before it plateaus to a constant, which is caused due to the sidebands, 9 MHz and 45 MHz, leaking through the AS port. The red line show the minimum power modulation index that the CMOS phase camera can sense after 50 averaged frames. In homodyne readout, where there is no large orthogonal $\mathcal{Q}$-quadrature signal to compete with, we can sense distortions greater than 0.1 nm using 50 averaged frame. In the current DC readout there is a large $\mathcal{Q}$-quadrature signal due to the differential arm DC offset. The phase resolution of the CMOS phase camera will thus limit sensing capabilities. The dashed black line represents the per pixel phase resolution limit after 50 frame averages (see Fig. 23). Assume the camera is place in the appropriate Gouy phase, we can resolve optical path distortions greater than 2 nm in the DC readout scheme of current Advanced LIGO detectors. Typical optical path distortions due to these point absorbers in Advanced LIGO ranges from few nanometers to a few hundreds of nanometer [1, 3]. The parameters of the simulation are summarized in Table 4.

The presence of a large beat signal in the $\mathcal{Q}$ quadrature from the DC readout scheme means that we also have to worry about the camera phase resolution. The beat map phase rotation is given by

$$\frac{\mathcal{I}^{\phi}}{\mathcal{Q}} = k\cot(\frac{\omega_s L_s}{c})\sin(N\phi)(\mathrm{X}-\mathrm{Y}) \tag{4.78}$$

During the A+ upgrade Advanced LIGO will switch to a homodyne readout scheme, reducing the DC offset to zero, and instead using a separate carrier reference beam as local oscillator. We assume that the reference beam has about the same amplitude as the current carrier due to the DC offset, as this permits using the same sensing and readout electronics. Thus, the expression 4.77 for sensing the effect from the point absorbers remains essentially the same, with one difference: For diagnostic purposes we now have control over the phase α_{Hom} of the reference beam. The $\mathcal{I}$ quadrature thus becomes

$$\mathcal{I}^{\phi} = k\Gamma\sqrt{p_{ref}p_{in}}\cos(\frac{\omega_s L_s}{c})\sin(N\phi-\alpha_{\mathrm{Hom}})(\mathrm{X}-\mathrm{Y}) \tag{4.79}$$

Thus we can pick the beamsplitter Gouy phase $\phi = 0$ a 90 deg rotated reference beam, $\alpha_{\mathrm{Hom}} = \pi/2$, removing the large beat signal in the $\mathcal{Q}$ quadrature and avoiding the phase resolution limitation of the phase camera.

The power modulation index of the beat signal is given by

$$\Gamma_{\mathcal{I}} = \frac{2\mathcal{I}}{DC}; \quad \Gamma_{\mathcal{Q}} = \frac{2\mathcal{Q}}{DC} \tag{4.80}$$

Figure Eq. 27 shows the size of the expected power modulation index signal as a function of the optical path distortion (OPD). The red horizontal dashed line represents the approximate power modulation index sensitivity limit of the phase camera for each pixel. The vertical black dashed lime corresponds to the phase resolution limit of the camera, and is relevant in the presence of a large signal in the orthogonal quadrature due to the interferometer differential arm fringe offset. We expect the phase camera to be sensitive enough to pickup optical path distortions greater than about ~ 2 nm where the readout is limited by phase resolution of the phase camera. Otherwise, the phase camera is capable of sensing OPD due to point absorbers as low as ~ 0.1 nm. Typically, the OPD caused due to point absorbers ranges between tens up to a few hundreds of nanometers [3, 81, 1]. Currently Hartmann wavefront sensors are used to image point absorbers in aLIGO directly. These sensors map the point absorbers onto the surface of the test masses [82], but do not measure their impact on the interferometer. The CMOS phase camera does not directly image the point distortions, but instead measures the change in the interferometer phase front at the AS port caused due to these point defects. Using the model discussed above, we simulate an example case for a typical point absorber [3] with 20 nm of optical path distortion at full width half maximum, see Fig. 28.

4.5.1 Implications for Gravitational Wave Detectors

The simple interferometer model presented above leads us to conclude that the CMOS phase camera developed in our group is capable of diagnosing the effect of point absorbers on the LIGO input test masses when installed at the interferometer anti-symmetric port. The exact Gouy phase of the camera will matter though, as there is no signal in the beamsplitter Gouy phase. Having a separate local oscillator reference beam, either as part of the homodyne readout or as a separate local oscillator for the phase camera, will simplify the image analysis. Lastly, we note that the model presented above does not include the signal recycling cavity and the power recycling cavity of the Advanced LIGO detector. While the power recycling cavity only filters the beam incident on the beamsplitter, the signal recycling cavity will spatially filter the effect of the point absorber, cleaning up the mode. However, with a signal recycling mirror transmission around 32%, the signal recycling cavity has an extremely low finesse, preserving the distortion signal, but also making modeling rather complicated.

4.6 Discussion

We demonstrate a CMOS phase camera that is capable of imaging externally modulated RF beat signals incident on the sensor with high spatial resolution. The noise levels of the camera allow sensing of RF beat signals with a power modulation index as low as 0.0009 with 50 frame averages. The phase camera also has the capability to measure the beat signals at different frequencies and is sensitive to very low incident beam power levels. Lastly, the low latency image acquisition, design compactness, and relatively low cost of the phase camera make it suitable for numerous applications in wavefront diagnostics and sensing.

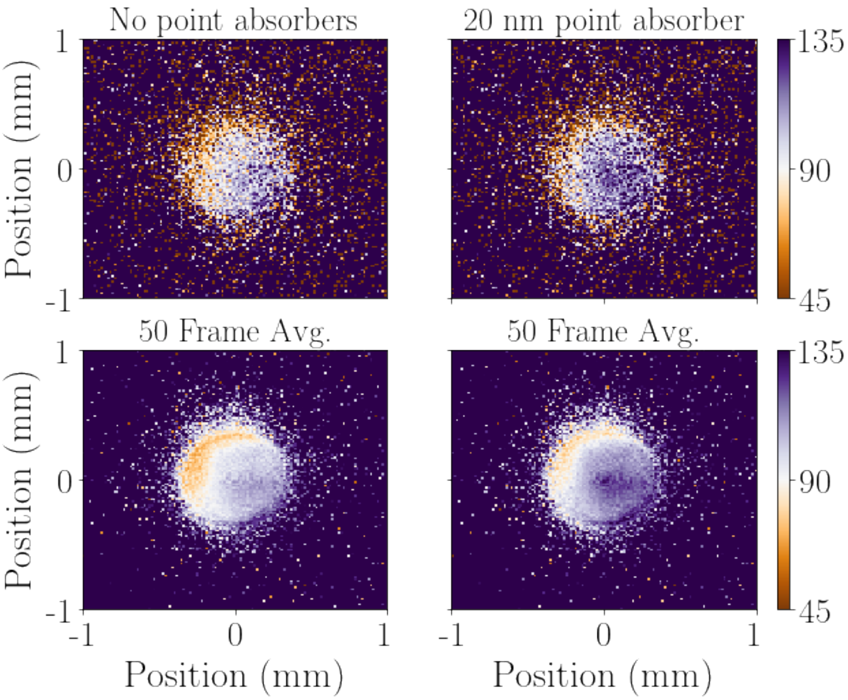

Figure 28: Simulated signal for a point absorber with 20 nm optical path distortion as seen at the anti-symmetric port (no recycling cavity, zero Guoy phase; see text). The 6 cm beam at the beamsplitter in our simulation, Fig 26, is rescaled to match the beam in our test setup (see section §4.4.4), using the test images as reference for the point absorber free data including camera noise. The phase readout is not meaningful outside the illuminated region. The phase maps highlight the phase around $\pi/2 \pm \pi/4$ to illustrate the phase distortions due to the point absorber. Top left: Reference test image for a single frame without any point absorbers. The non-Gaussian features arise from the distorted laser beam in reflection in the experimental setup. Top right: The relative phase distortion due to the point absorber is added to the test image for a single frame. Bottom left and bottom right: Same as top left and top right respectively, but with an average of 50 frames. We measure ∼28 degrees of accumulated phase in the presence of the 20 nm point absorber. This estimate is consistent with the analytical calculation in section §4.5.

The primary application of a phase camera in gravitational-wave detectors is for diagnostic purpose, imaging any unexpected phase front distortions, such as for example those induced by point absorbers on test masses (see section §4.5). However the phase camera can also be useful for controlling alignment and mode-matching in an interferometer. While quadrant-photodiode and bullseye-photodiode-based schemes, with [25] and without [61] optical mode converters, have the advantage of higher signal-to-noise, they offer only four "pixels" across the beam. In particular, the 320×240 pixel resolution of the CMOS phase camera provides the sensing capabilities to operate and control interferometers with higher-order Laguerre-Gauss or Hermite-Gauss modes as the operating resonant mode, a scheme that was proposed to reduce the coupling of thermal noise to the gravitational readout [83, 84]. Additionally, it has been shown that these cameras can be operated synchronously [69], which allows for multiple cameras to simultaneously record the beam in separate Gouy phases.

In summary, we expect that the CMOS phase camera will be an excellent tool for commissioning Advanced LIGO, A+, and future gravitational wave detectors such as Cosmic Explorer [85] or Einstein Telescope [86], and might also have control applications.

4.7 Acknowledgment

This research was funded by the National Science Foundation through the awards NSF PHY-1352511 and NSF PHY-1912536. We also would like thank numerous colleagues in the LIGO, Virgo and KAGRA scientific collaborations for many fruitful discussions.

4.8 Appendix

Imaging of Multiple Modulation Frequencies with the CMOS phase camera

As discussed in section §4.3, a flip-flop (FF) can be integrated with the CMOS phase camera to support four or six quad exposures. The flip-flop also allows the camera to subsequently image beat signals at different modulation frequencies. The electronic setup for this operation is shown in Fig. 29. An RF-switch is used to switch between the modulating frequencies of the local oscillators following the frame capture sequence governed by the microcontroller. The frequency and phase stepped output of the DDS are phase-locked by ensuring the updates are triggered on the rising edge of the local-oscillator by the flip-flop. The functionality of other elements in this scheme is the same as discussed in section §4.3. This setup is particularly useful for application in Advanced LIGO, which allows the CMOS phase camera to image beat signals at 9 MHz and 45 MHz in real time. Using this technique, the CMOS phase camera can image beat signals at different modulation frequencies with a low-latency of 1 Hz.

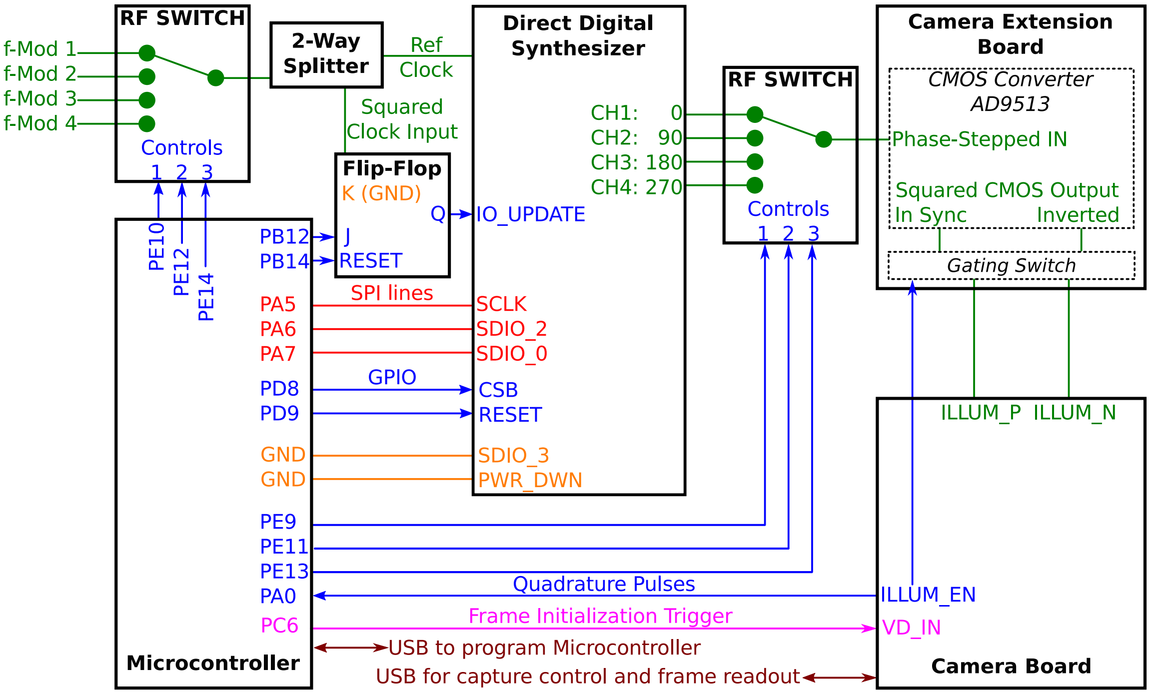

Figure 29: Alternate capture scheme mentioned in section §4.3. It allows simultaneous imaging of RF signals with different modulation frequencies by selecting a separate modulation frequencies for every frame. In this scheme, the microcontroller controls an additional RF switch at the input off the DDS board. A 2-way splitter is used to provide a clock signal input to a flip-flop circuit. The flip-flop ensures a phase-locked output from the DDS by triggering the DDS update on the rising edge of the external local oscillator. The rest of the design block functionality is the same as discussed in Fig. 20. The RF switch at the output of the DDS can be discarded if six sub-quads are desired for image capture. In this scenario, the DDS is configured to phase-step one particular channel in synchronization with the quadrature pulses received by the microcontroller.

Chapter 5

Overview of Cosmic Explorer

In the past five years, the aLIGO and aVirgo detectors have discovered signals from over 65 compact binaries such as coalescing binary black holes (BBH), binary neutron stars (BNS), and possibly even neutron star black hole (NSBH) mergers. These detections have begun to provide deep insight into the astrophysics, population estimates, and dynamics of compact binaries. We now have a new tool for gaining a deeper understanding of the neutron star equation of state, kilonovae dynamics, and r-process nucleosynthesis. The discovery of a large number of BBHs has opened a new window to observational cosmology and allowed us to test general relativity at extreme spacetime curvature, which has never before been explored, and to rule out certain alternative theories of gravity invoked to explain dark energy.

Cosmic Explorer (CE) is a proposed third-generation GW detector to be built in a new, approximately 40 km long L-shaped surface facility in the US. The National Science Foundation is funding an initial study into the science case for CE, its cost, and conceptual design, which should help determine the technology needed to accomplish the discovery potential of CE. Current plans are for CE to be deployed in two stages. The initial detector (CE1) is planned to be built in the 2030s mostly using the existing aLIGO technology such as a 1 μm laser and room-temperature fused silica test masses. The advanced detector (CE2) is planned for the 2040s and will either involve iterating further on 1 μm silica technology or adopting another set of technologies, such as 2 μm lasers and cryogenically cooled silicon test masses as envisioned by LIGO Voyager. In all cases, CE will use heavier test masses, increased circulating arm power, and improved frequency-dependent squeezing to reduce quantum noise.

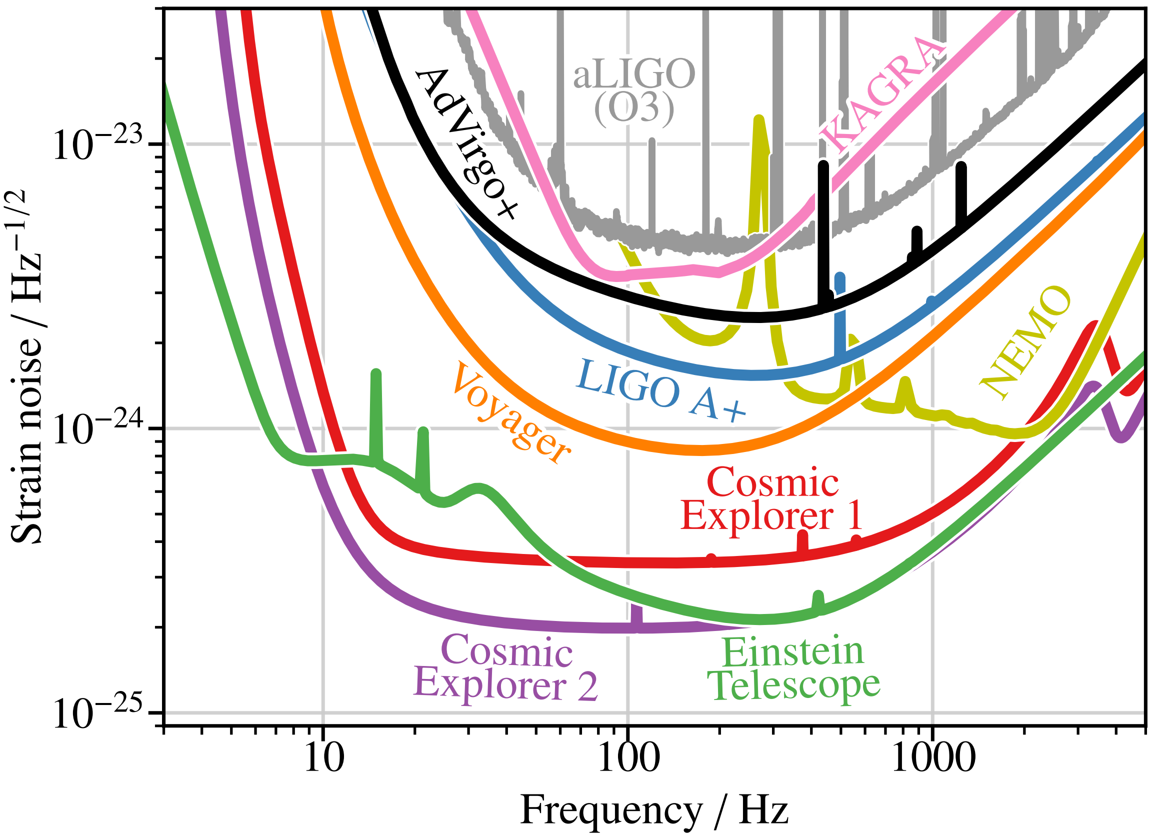

Figure 30: Strain sensitivities of the current and future gravitational-wave detectors. Credit: Evan Hall.

To increase the sensitivity at low frequencies where environmental and thermal noise sources limit the performance, CE plans to take advantage of Newtonian noise suppression techniques, better active seismic isolation, and improved mirror suspensions. The existing noise budget suggests that these design upgrades, along with the longer arm length, will make CE over 10 times more sensitive than the current detectors, see Fig. 30.

According to the current timeline estimates, CE will be observing in concert with Einstein Telescope (ET), and possibly a facility in Australia, to form a global network of third-generation GW detectors. This will have far-reaching consequences for our understanding of the universe. The significantly higher sensitivity of third-generation GW detectors will allow us to detect compact binaries in our local universe with an unprecedented signal-to-noise ratio (from 500 to 5000 or more depending on the source) and localize these events in the sky to within a few tens of square arcminutes. With hundreds of gravitational and electromagnetic observations of compact binaries, we would be able to better understand kilonovae dynamics for different compact binary populations and examine accretion dynamics around BBHs. Additionally, CE and ET observations will help resolve mysteries surrounding the structure of neutron stars, such as the equation of state and the post-merger oscillations of neutron star remnants. A catalog of almost every stellar-mass BBH merger in the universe (Fig. 31) would allow us to test general relativity at extreme curvatures and shed light on the origin of super-massive black holes, specifically if coalescing stellar BBHs served as their seeds. These observations would revolutionize the field of astrophysics, cosmology, and fundamental physics. Learn more at `https://cosmicexplorer.org/`.

5.1 Overview of the Cosmic Explorer Horizon Study Document

The Cosmic Explorer Horizon Study (CEHS) document outlines the key science goals of the Cosmic Explorer detectors and the comparative performance between different detectors and networks of detectors, in their ability to achieve these science goals [47]. CEHS argues the three key science goals of the Cosmic Explorer facility are as follows:

1. *Black holes and neutron stars through cosmic time:* The third-generation gravitational wave detectors like Cosmic Explorer will have sensitivity to detect black

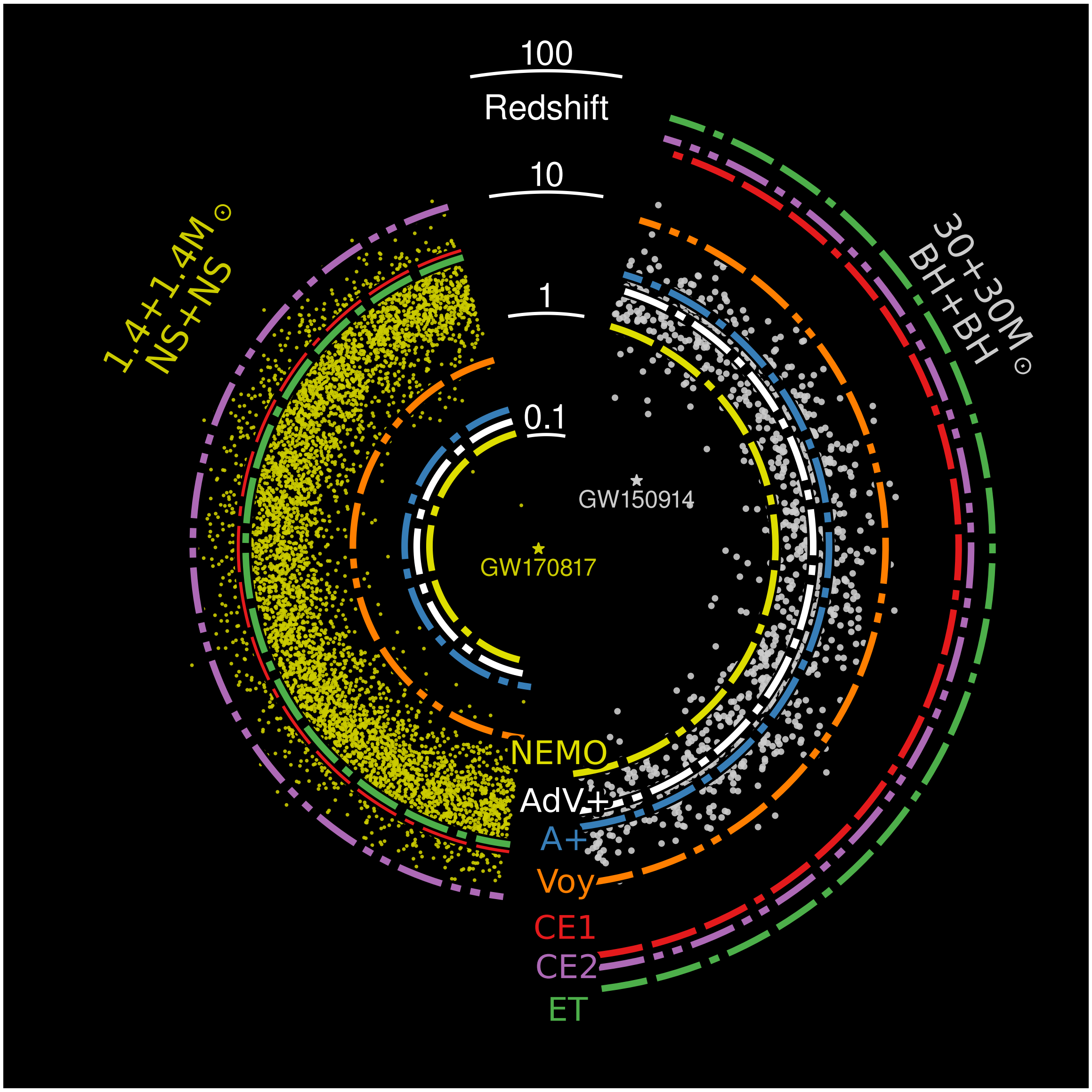

Figure 31: Detectability of compact binaries. The dots represent the distribution of compact binaries in the universe according to existing population models. The dashed contours represent the horizon of the sources that will be detectable by each detector. We will be able to sample the entire known population of compact binaries in our universe with third-generation detectors. Credit: Evan Hall and Salvatore Vitale.

hole binaries formed from the first stars, see Fig. 31.

2. *Dynamics of dense matter:* Neutron stars are the densest objects. As they are under extreme pressure and temperature, they challenge the understanding of fundamental particle physics. This phase space of the nuclear matter is unresolved and not experimentally constrained. Cosmic Explorer facilities will detect $\sim 10^5$ binary neutron stars each year, the loudest of which would facilitate the understanding of extreme matter.

3. *Extreme gravity and fundamental physics:* Due to the unprecedented sensitivity of the Cosmic Explorer detectors, they will offer astounding SNRs, a few detections each year with an SNR greater than 1000. These observed signals will allow tests of general relativity.

Work done for the CEHS towards characterizing the comparative performance of various proposed detectors, and the corresponding network of gravitational wave detectors with Cosmic Explorer, can be found in two technical notes [87, 88]. The next two chapters of the thesis present the work done to design Cosmic Explorer. In chapter 6,the detection prospects of core-collapse supernovae with third-generation gravitational-wave observatories are discussed. Chapter 7 discusses the science-driven tunable design of Cosmic Explorer detectors, which is highlighted within the CEHS document.

Chapter 6

Detection Prospects of Core-Collapse Supernovae with Supernova-Optimized Third-Generation Gravitational-wave Detectors

We discuss how to optimize the third-generation gravitational-wave detector to maximize the range to detect core-collapse supernovae. Based on three-dimensional simulations for core-collapse and the corresponding gravitational-wave waveform emitted, the corresponding detection range for these waveforms is limited to within our galaxy even in the era of third-generation detectors. The corresponding event rate is two per century. We find from the waveforms that to detect core-collapse supernovae with an event rate of one per year, the gravitational-wave detectors need a strain sensitivity of $3{\times}10^{-27}$ $\mathrm{Hz}^{-1/2}$ in a frequency range from 100 Hz to 1500 Hz. We also explore detector configurations technologically beyond the scope of third-generation detectors. We find with these improvements, the event rate for gravitational-wave observations from CCSNe is still low, but is improved to one in twenty years[1].

---

[1] Varun Srivastava, Stefan Ballmer, Duncan A. Brown, Chaitanya Afle, Adam Burrows, David Radice, and David Vartanyan, Physics Review D 100, 043026, 2019.

6.1 Introduction

The Advanced LIGO [89] and VIRGO [90] gravitational-wave detectors observed signals from the coalescence of over ten binary black holes (BBH) and one binary neutron star merger (BNS) [91, 92, 93, 37, 94, 95] by the end of their second science run. Core-collapse supernovae (CCSNe) are a potential astrophysical source of gravitational waves that could be detected by interferometric detectors. The gravitational waves are generated deep in the star, at the collapsing core, and are emitted untouched by the outer envelopes. They contain vital information about the interior of the star and about the core-collapse process, which is not present in the electromagnetic counterpart of the emitted radiation. We can infer various physical parameters such as the nuclear equation of state, rotation rate, pulsation frequencies, etc. from the gravitational wave signal of a CCSNe once it has been detected [96, 97, 98]. However, gravitational waves from CCSNe are yet to be observed [99, 100]. The inferred sensitivity of the aLIGO-VIRGO network to detect CCSNe ranges from a few kiloparsecs (kpc) to a few megaparsecs (Mpc) [101]. The range of a few megaparsecs in [101] corresponds to extreme emission models which assume properties of stars which are unlikely to occur in astrophysical scenarios. The smaller sensitive range of a few kiloparsecs to CCSNe along with low CCSNe rates within galaxies leads to a low gravitational-wave detection probability from CCSNe [102, 103, 104, 105, 106].

The gravitational radiation from CCSNe depends on a complex interplay of general relativity, magneto-hydrodynamics, nuclear, and particle physics. The burst signal, therefore, does not have a simple model, and we have to use numerical simulations to understand its structure. Numerical simulations also help in understanding the frequency content of the gravitational wave signal which is crucial in determining the parameters to tune future detectors towards supernovae.

The three-dimensional (3D) simulations of core-collapse supernovae reveal that their gravitational-wave signatures are broadband with frequencies ranging from a few hertz to a few thousand hertz. The time-changing quadrupole moment of the emitted neutrinos occupies the few Hertz to ten Hertz range, while the higher frequencies are associated with the prompt convection and rotational bounce phase, the proto-neutron-star (PNS) ringing phase, and turbulent motions. [107] and [108] demonstrated that the excitation of the fundamental g- and f-modes of the PNS can be a dominant component and that much of the gravitational wave energy emitted is associated with such PNS oscillations [109, 110]. The frequency ramp with time after the bounce of the latter is a characteristic signature of CCSNe and will reveal the inner dynamics of the residual PNS core and supernova phenomenon once detected. There now exist in the literature numerous 3D CCSNe models that map out the gravitational-wave signatures expected from CCSNe [111, 112, 113, 114, 106, 115]. For this study, we focus on the extensive suite of 3D waveforms found in [106].

In our work, we optimize the design prospects of a third-generation Cosmic-Explorer-like detector to detect gravitational wave signals from CCSNe and discuss the astrophysical consequences. We focus on the prospects for detection of non-rotating or slowly rotating stars since they are likely to be astrophysically more likely [116]. We first review the detection ranges for the second-generation detectors. A significant amount of power is emitted by CCSNe within the gravitational-wave frequency range 500 Hz to 1500 Hz. Therefore, in order to improve the sensitivity of gravitational wave detectors to CCSNe, we need to tune the detector parameters to increase the sensitivity in this bandwidth. With the present models of likely gravitational wave emission from CCSNe [106], we find that the detectable range with a supernovae-optimized Cosmic-Explorer-like third generation detector is still only up to a hundred kiloparsecs. The detector range is therefore limited to CCSNe that occur within our galaxy. The corresponding event rate is approximately two per century [117, 118, 119, 120, 121]. However, the supernovae-optimized detector would improve the signal-to-noise ratio (SNR) for the galactic sources by approximately 25% as compared to the Cosmic-Explorer. For completeness, we also discuss the strain requirements in a detector to achieve CCSNe event rates of the order of one per year. To this end, we address the fundamental sources of noise that limit our sensitivity to achieve this desired strain.

6.2 Gravitational waves from CCSNe

Fig. 32 shows the spectrograms of the waveforms obtained from the simulation for the $19M_\odot$ progenitor. The left column shows the spectrogram of the waveform from the 3D simulation, while the right column shows the spectrogram of the waveform from the 2D simulation. The red vertical dashed line in the right column represents the

Distance	Type-II CCSNe rate (per century)	References
Milky way (D $<$ 30 kpc)	0.6-2.5	[117, 118, 119, 120, 121]
M31 or Andromeda (D $=$ 770 kpc)	0.2-0.83	[122, 121, 123, 119, 121]
M33 (D $=$ 840 kpc)	0.62	[119, 121]
Local Group (D $<$ 3 Mpc)	9	[124, 121]
Edge of Virgo Super-cluster (D $<$ 10 Mpc)	47	[125, 126, 127]
Virgo-cluster (D $<$ 20 Mpc)	210	[126, 128]

Table 5: The cumulative rate of CCSNe in out local universe. To achieve a detection rate of one per year, assuming a 100% duty cycle of the gravitational wave detector, we need a strain sensitivity to have a CCSNe reach of the order of 10 Mpc.

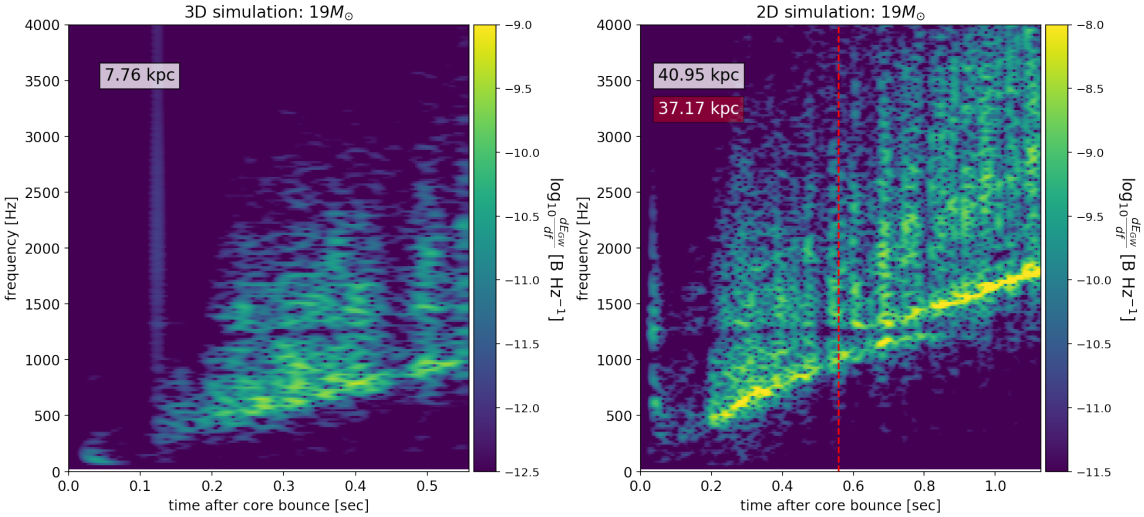

Figure 32: Spectrograms of gravitational-wave waveforms from 3D (left column) and 2D (right column) simulations of $19M_\odot$ progenitor. The number on the top left corner each plot with white background is the distance for which these GW signals have an optimal SNR of 8. For the 2D simulations, we recalculate this distance (shown on red background) by truncating the waveform at the end-time of the corresponding 3D simulation. The red vertical dashed line shows the truncation time.

simulation time of the 3D waveform. For simulations of the same ZAMS mass, both the 2D waveforms and the 3D waveforms show similar behavior in the time-frequency plane. We can see the prompt convection signal for the first ~ 10 milliseconds after the core bounce, followed by the characteristic g/f-mode ring up of the proto-neutron star (PNS) increasing in frequency [129]. For the 2D waveforms, the frequency ranges from $\sim$ 20 Hz to $\sim$ 2000 Hz. The g/f-mode signal of the PNS starts around 200 milliseconds after the core bounce at a frequency of $\sim$ 500 Hz, and 1 sec after the core bounce reaches $\sim$ 1500 Hz. For the waveforms obtained from the 3D simulations, the frequency ranges up to $\sim$ 1000 Hz. This is because the 3D simulations end earlier $(0.4 - 1.0$ sec after core bounce).

We calculate the optimal distance (or the detection distance for optimally-oriented sources) for each of these waveforms, as defined below [130]:

$$d_{opt} = \frac{\sigma}{\rho^*} = \frac{1}{\rho^*}\left[2\int_{f_{\rm low}}^{f_{\rm high}} df \frac{\tilde{h}(f)\tilde{h}^*(f)}{S_h(f)}\right]^{\frac{1}{2}} \tag{6.81}$$

ZAMS Mass	Optimal distance (kpc)			Normalized σ^2 (10Hz-450Hz)		Normalized σ^2 (450Hz-2000Hz)	
	3D	2D	2D truncated	3D	2D	3D	2D
$9M_\odot$	2.43	15.51	15.46	0.342	0.232	0.658	0.767
$11M_\odot$	5.87	31.96	26.68	0.154	0.058	0.845	0.941
$11M_\odot$ (w/o MB)	5.99	28.78	26.04	0.131	0.099	0.869	0.9
$19M_\odot$ (w/o MB)	7.75	40.61	37.18	0.120	0.074	0.880	0.925
$25M_\odot$	13.35	48.26	40.09	0.12	0.069	0.88	0.931
$60M_\odot$	9.63	48.79	36.30	0.211	0.065	0.790	0.935

Table 6: For different ZAMS mass, with and without many-body (MB) approximation the table summarizes the optimal distances for aLIGO and σ^2 for a flat PSD in the frequency bandwidths 10Hz - 450Hz and 450Hz - 2000Hz for waveforms.

where $S_h(f)$ is the power spectral density (PSD) of the detector, $\rho^* = 8$ is the signal-to-noise ratio for an optimal matched filter (optimal SNR) and the limits over the integral are defined by $f_{\rm low}$ and $f_{\rm high}$. We note that for unmodeled searched like CCSNe, matched filter searches is not applicable. Instead, Coherent WaveBurst searches (CWB) or incoherent transient searches (Omicron) are implemented to search for CCSNe in aLIGO-VIRGO strain data [131, 132, 133, 134]. There is mismatch which leads to loss of SNR when one moves from modeled match-filter searches to unmodeled transient wavelet burst searches [135]. The use of optimal SNR in the paper presents an optimistic scenario without any of these losses. We set the lower frequency cutoff, $f_{\rm low} = 10$ Hz and use `aLIGOZeroDetHighPower` [136] as PSD for aLIGO to compute the optimal distances for all the waveforms, which are shown in Table 6. For aLIGO, the average distances for waveforms from 3D simulations are ~ 8 kpc, while the average distances for corresponding 2D numerical simulations are ~ 35.5 kpc. The 3D simulations have shorter times with respect to the 2D simulations, so we truncate the 2D simulations at the same corresponding times to compare the optimal distances. In doing so, the average optimal distance for the waveforms from the 2D simulations is ~ 30 kpc. We find that the 2D waveforms are, on an average, ~ 4 times louder than the 3D waveforms. Therefore, we will only use the waveforms from 3D simulations to tune the third generation detectors for CCSNe and calculate ranges.

Table 6 also shows the optimal signal-to-noise (SNR) σ^2 of the waveforms in two frequency bandwidths : 10Hz - 450Hz and 450Hz - 2000Hz. These σ^2 values have been calculated using a flat PSD (see section §6.5), so that we can infer the distribution of the frequency content of the waveforms without being biased by the noise curves of any detector. We can verify from the spectrograms that almost all of the frequency content is below 2000 Hz. We find that the ratio of σ^2 in the range 10Hz - 450Hz to that in range 450Hz - 2000Hz is ~ 0.2 for 3D simulations while for 2D simulations it is ~ 0.1. This implies that $\sim 80\%$ of the content of the waveforms is in the frequency range 450Hz - 2000Hz. This is crucial since in Secs §6.3 and §6.4, we tune the detector parameters to increase the sensitivity in this frequency range.

In section §6.3, we define a phenomenological CCSNe waveform which is derived from the 3D numerical waveforms. We maximize the range of the phenomenological supernovae waveform (see Fig. 33) with a third-generation Cosmic-Explorer-like detector. We use GWINC to estimate the noise floor for different detector parameters [137]. The maximized range achieved can then be translated into the corresponding event rate of CCSNe, as summarized in table 5 (assuming a 100% detector duty-cycle).

We use the waveforms from [106] to compare the ranges of different waveforms of CCSNe using the Einstein Telescope (ET), the Cosmic Explorer (CE) and the Supernovae-Optimized detector (SN-Opt). In section §6.5, we invert the problem to calculate the strain requirements of a *hypothetical* detector to achieve an event rate of the order of one in two years or in the terms of distances — has a range of the order of 10 Mpc for gravitational-wave signals from CCSNe. Lastly, we consider in section §6.5 detector configurations beyond the third-generation detectors (Hypothetical) and find the ranges for different numerical waveforms of CCSNe.

6.3 Defining a Representative Supernovae Gravitational-Wave Waveform

To maximize the detectable range for CCSNe in a given detector configuration, we need a reference CCSNe waveform that captures the broad features of supernovae waveform. The reference waveform must have the strain amplitude and spectral features similar to any supernovae waveform. We use the waveforms from the 3D simulations of core-collapse [138, 106] to generate a phenomenological model that captures the broad range of features of core-collapse supernovae waveform. We generate the phenomenological waveform to average out the power emission features from different numerical waveforms so that features in any one of the waveforms do not affect the results of the study. Thereby, the phenomenological waveform provides a model-independent approach.

We construct the phenomenological waveform by a sum of sine-Gaussian bursts. A sine-Gaussian can be defined with three parameters, the central frequency f_o, the quality factor or the sharpness of the peak Q and the amplitude scale h_o. The frequency domain representation of a sine-Gaussian can be expressed with these parameters as

$$\tilde{s}(f) = \frac{h_o}{4\sqrt{\pi}} \frac{Q}{f_o} e^{-\frac{(f-f_o)^2 Q^2}{4f^2}} \tag{6.82}$$

The different frequencies are used to model different spectral features of the core-collapse waveform. We choose central frequencies f_o^i for sine-Gaussian using the numerical waveforms from 3D simulations of core-collapse. We choose, by hand, five distinct central frequencies f_o^i which correspond to peak emission in the numerical waveforms. We limit ourselves to five distinct values of frequencies in order to avoid over-fitting the sine-Gaussian phenomenological waveform to the numerical waveforms. We note that the supernovae waveforms have emission at higher frequencies but they are much lower in amplitude. Therefore, for the purposes of optimization, we limit ourselves to an upper limit of 2kHz in the phenomenological waveform.

To build the phenomenological waveform, we divide the frequency domain into four bins ranging from — 10 Hz to 250 Hz, 250 Hz to 500 Hz, 500 Hz to 1 kHz and 1 kHz to 2 kHz. For each of the chosen central frequencies f_o^i, the quality factor Q^i and the amplitude h_o^i are chosen so as to minimize the error in the normalized power in the four different bins of frequencies above. The error in the normalized power in each bin is then added in quadrature for different waveforms and is given by

$$\Delta e = \sqrt{\frac{1}{N-1}\sum_{i}^{N}(\mathrm{Model}_{f_{low}}^{f_{high}} - \mathrm{NR}_{f_{low}}^{f_{high}})^2} \tag{6.83}$$

This approach gives us a simple but robust gravitational waveform, free from the parameter degeneracies but capturing the features of gravitational wave radiation from CCSNe. We will use this to perform optimization and maximize the range for this waveform and thus for CCSNe. The errors in the different frequency bins ranging from 10Hz to 250Hz, 250Hz to 500Hz, 500Hz to 1kHz and 1kHz to 2kHz is 3%, 9%, 2% and 19% respectively. The higher error in the last frequency bin is by the construction of the phenomenological waveform and is added to incorporate the features persistent in the 2D waveforms which show higher emissions in this frequency range discussed in section §6.2. Fig. 33 shows the phenomenological waveform constructed. We incorporate this waveform as a reference supernovae signal within `GWINC` [137]. The ranges, horizon, and reach for the phenomenological waveform can then be calculated by solving for distance D which would rescale the waveform in equation 6.82 as 1/D.

In each of the subsequent sections, we go back to each of the numerical waveforms and recompute the ranges achieved with all the different detector designs considered in our study.

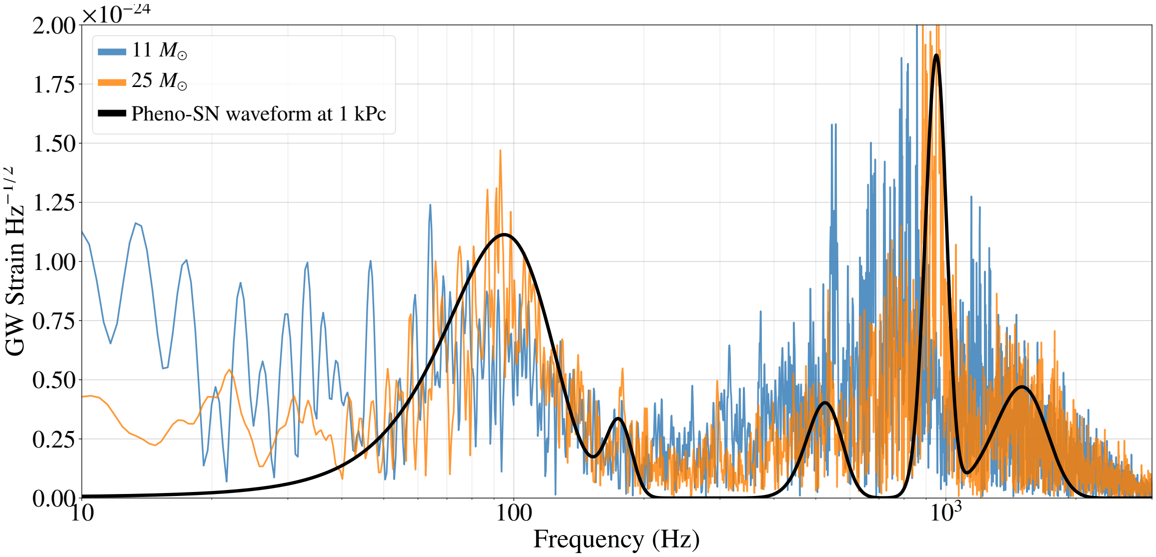

Figure 33: The figure shows the phenomenological waveform used as a representative for gravitational wave emission from CCSNe. The waveform is constructed by using five sine-Gaussian bursts with different central frequencies f_o = 95, 175, 525, 950 and 1500 Hz. The quality factor and the amplitude at each central frequency are then derived by minimizing the normalized power emitted in four different bins of frequency from 10 Hz to 250 Hz, 250 Hz to 500 Hz, 500 Hz to 1000 Hz and 1000 Hz to 2000 Hz. The overall amplitude of the phenomenological waveform is not calculated by the fit and can be rescaled. We are interested in the broad features in frequency in different waveforms which is effectively captured in the phenomenological waveform.

6.4 Optimizing SN detectability for 3G detectors

We use the phenomenological gravitational-wave waveform for CCSNe to explore detector configurations that optimize the Cosmic Explorer detector's sensitivity to CCSNe. To avoid overemphasis on any particular frequency chosen in the phenomenological waveform, we down weight narrow-band configurations during the process of optimization. We also avoid narrow-band designs so that the optimized detector's sensitivity to BNS is greater then 1 Gpc. We will explore the narrow-band configurations with a different approach discussed in section §6.4.3

6.4.1 Broadband Configuration Tuned for Supernovae

Quantum noise is the predominant source of noise which limits the performance of the gravitational-wave detector. Radiation pressure noise limits the detector sensitivity at low frequencies and shot noise limits sensitivity at high frequencies [89, 90, 139]. In our study, we use the design parameters of Cosmic Explorer [140] as the starting point. For the purposes of optimization, we choose the Cosmic Explorer rather than the Einstein Telescope as the former has a better noise performance at frequencies which are relevant to CCSNe. We optimize over the length of the signal recycling cavity (L_{src}) and the transmissivity of the signal recycling mirror (T_{srm}) to maximize the CCSNe detection range. The quantum resonant sidebands can be tuned with these parameters and we exploit this behavior for supernovae tuning similar to the approach used by Buonanno et al. [141] and Martynov et al. [142].

We also study, the effect of the length of the arm cavity (L_{arm}) on supernovae sensitivity. We use Markov Chain Monte Carlo sampling [143] and particle swarm optimization [144] to search the parameter space and maximize the range for the phenomenological waveform for a broadband detector. During the process of maximizing the range, we down-weight the narrow-band configurations with two constraints for sample points. First, the reflectivity of the signal recycling cavity $T_{srm} > 0.01$. Second, the given detector configuration must have a optimal distance for binary neutron stars systems ($m_1 = m_2 = 1.4\ M_\odot$ and $s_{1z} = s_{2z} = 0$) to be greater than 1 Gpc. By doing so, we ensure that the detector's sensitivity is not lost for compact binaries.

The strain sensitivity improves as the square root of the arm length of the detector as long as the gravitational-wave frequency (Ω) is much less than the free spectral range (f_{FSR}) of the Fabry-Perot cavity. The strain sensitivity of the detector does not always improve by scaling the detector as other fundamental sources of noise also change by scaling the length of the detector [145]. As the gravitational wave spectrum of supernovae has some power in a few kilohertz range, we allow the arm length to vary independently similar to the analysis by [146, 142]. Our simulations indicated the optimal length to be close to 40 km, the upper bound value allowed for the length parameter. As a result, we set the length of the arm cavity to 40 km. For a 40 km arm length, the f_{FSR} is 3750 Hz. The sensitivity of the detector is limited by the f_{FSR}, any further increase in the length of the arms will reduce the f_{FSR}, resulting in the loss in sensitivity to CCSNe, where the gravitational wave spectrum persists up to a few kilohertz.

The optimal supernovae zero-detuned detector's noise budget is shown in Fig. 34. We find a longer signal recycling with a length of 180 m compared to 55m for Cosmic Explorer along with a transmissivity of the signal recycling cavity changed to 0.015 improved the detector's sensitivity by improving the quantum noise floor at higher frequencies. The loss in sensitivity around 3 kHz is due to the FSR of the arm cavity. The dip at 4 kHz corresponds to the pole of the signal recycling cavity.

We also consider the effects of detuning the signal recycling cavity. We find detuning the signal recycling cavity with active compensation with the squeezing phase can be used to actively tune the third generation detectors in narrow bins of frequency without losing 15 dB of squeezing. It has been proposed that detuning the ground-based detectors can be useful in testing the general theory of relativity [6] with a joint operation with LISA [147]. We will consider the applicability of these configurations to see if they provide any improvements for CCSNe in section §6.4.2.

The optimization over the length of the signal recycling cavity and the transitivity of the signal recycling mirror to maximize the supernovae range with the phenomenological waveform in Fig. 33 leads to an improvement of approximately 30% in the range of CCSNe as compared to the Cosmic Explorer design. However, extending the range from a 70 kpc to 95 kpc does not add any galaxies in our local universe. The optimized supernovae detector does not increase the detection rate as compared to the Cosmic Explorer. For the sources at a fixed distance, this corresponds to approximately 25% improvement in SNR.

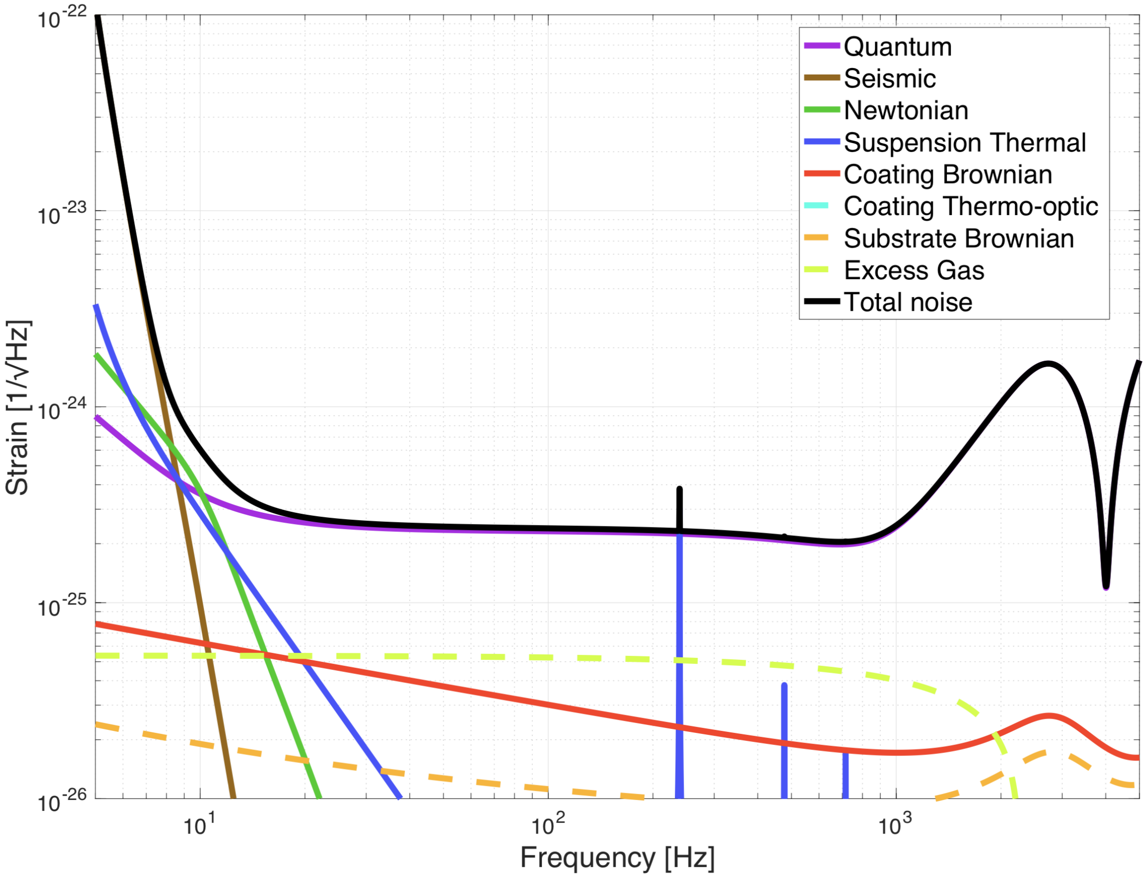

Figure 34: The figure summarizes the noise budget of the supernovae-optimized detector for a gravitational-wave signal with a 45 degrees tilt with respect to the arm cavities [4]. Over the broad range of frequencies of interest, 500 Hz to 1500 Hz, the sensitivity is limited by quantum noise. The dip in sensitivity at 4 kHz corresponds to the pole of the signal recycling cavity.

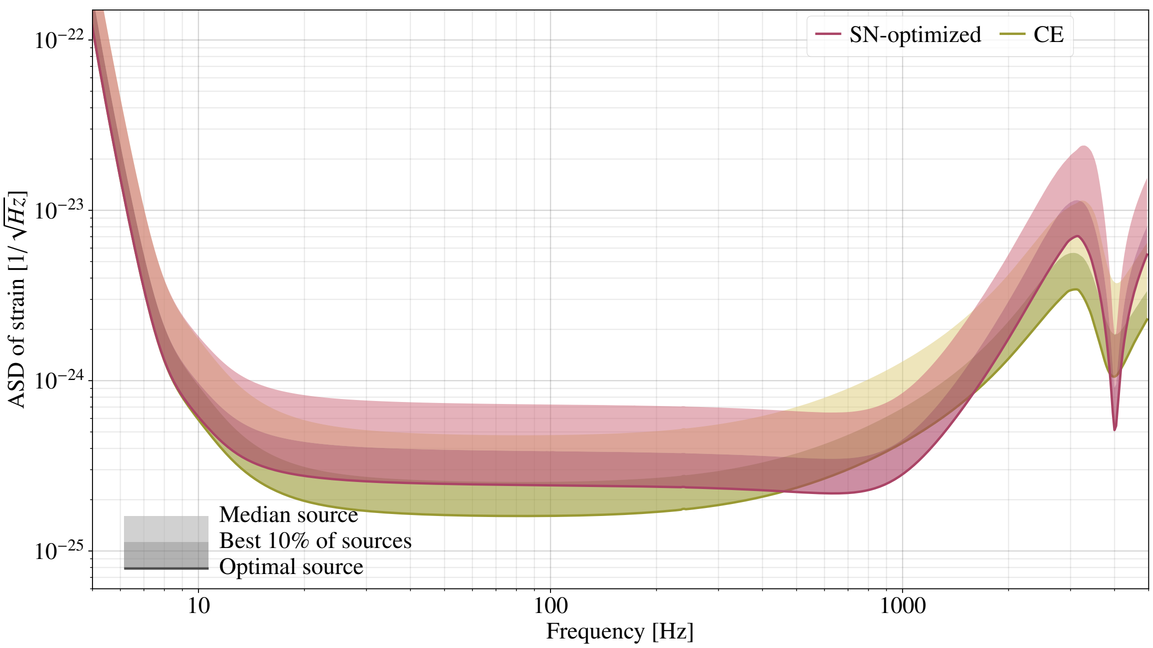

Figure 35: The figure summarizes the sky-averaged and orientation-averaged power spectral density of Cosmic Explorer and supernovae-tuned detector [5]. We see that the Cosmic Explorer has a better noise floor from 10 Hz to 450 Hz. The supernovae-tuned detector has improved sensitivity over the range from 450 Hz to 1600 Hz. The numerical waveforms of CCSNe suggest that a significant amount of power is emitted in this range. The optimization for CCSNe improves the range from 70 kpc to 95 kpc for CCSNe. However, this range improvement does not add any new galaxies. Therefore, the event rate does not change with the improved sensitivity and we are limited to sources within our galaxy.

The Fig. 35 compares the broadband configuration of a zero detuned 40 km detector optimized for CCSNe signals with the design of the Cosmic Explorer, both configurations have a 15dB squeezing. We improve on the sensitivity in the frequency range from 450 Hz to 1550 Hz at the cost of a loss in sensitivity from 10 Hz to 450 Hz. This results in a 15% loss in range for BNS. However, it still provides higher sensitivity for the post-merger signals based on the predicted frequencies of interest for post-merger oscillations [93, 148, 149, 150]. The table 7 summarizes the parameters and their corresponding ranges towards different gravitational-wave sources. One advantage offered by the supernovae optimized configuration is robustness. Without any squeezing, the supernovae optimized detector has a range extending to the LMC, whereas the range of the phenomenological SN waveform with Cosmic Explorer without squeezing is 32 kpc.

Next, we use the noise curves of aLIGO, Cosmic Explorer, Einstein Telescope and Supernovae optimized detector configurations to compute the ranges for the 3D waveforms As stated earlier, the 3D waveforms are representative of astrophysically abundant stars which are not rapidly rotating and the corresponding gravitational wave strain emitted is small. Figure 36 summarizes the ranges of different waveforms based on their ZAMS mass. We see that the sensitivity of the third-generation of gravitational-wave detectors to CCSNe is limited to sources within our galaxy. From the event rates of CCSNe summarized in table 5, we find the corresponding event rate of observation of gravitational waves from CCSNe (assuming a 100 % detector duty-cycle) is approximately one in fifty years.

6.4.2 Detuning a Large Signal Recycling Cavity for Narrow-band Configurations

A significant GW signal from CCSNe lies in the frequency band from 500 Hz to 1500 Hz. The power emitted at different frequencies may vary depending on the astrophysical features of the star - mass, rotation speed, equation of state, etc [151, 152, 138, 106, 153, 154, 111].

In this section, we do not change the detector parameters' such as the transitivity or the length of the signal recycling cavity. This is because these parameters cannot be changed once the detector design is laid out. However, one can detune the signal recycling cavity to maximize sensitivity in a narrow band of frequencies [155, 156].

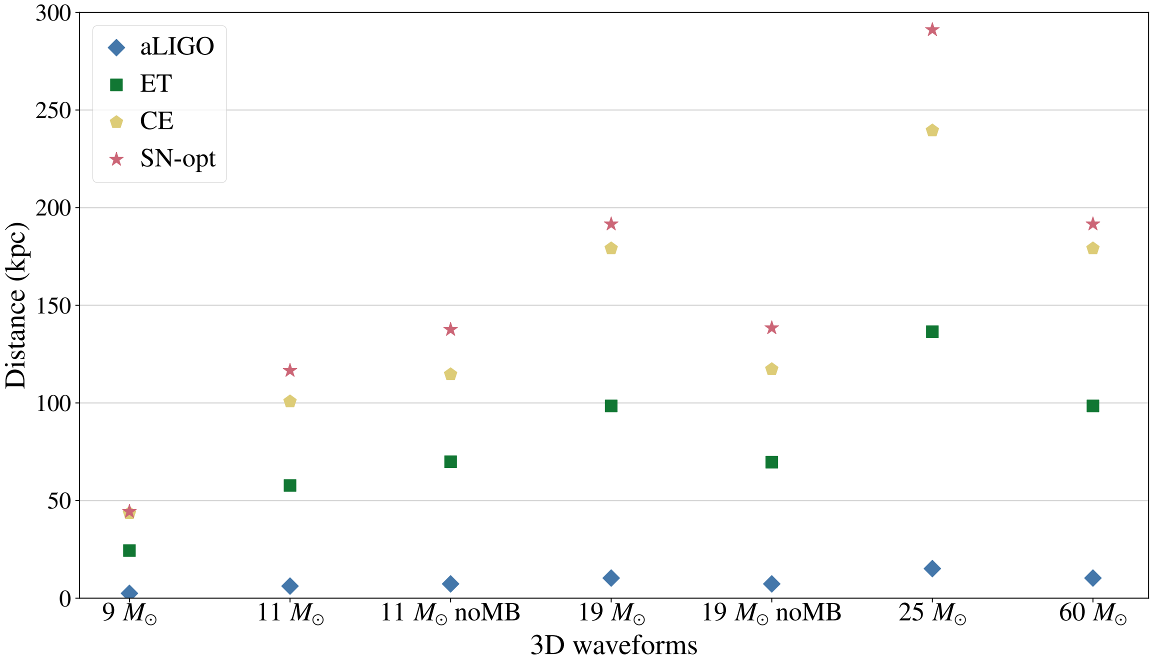

Figure 36: The figure summarizes the distance of the 3D waveforms for different second and third-generation gravitational wave detectors. We see for second-generation advanced LIGO detector that the optimal distances for the 3D numerical waveforms are limited to 10kpc. The optimal distance is so small enough that we are not sensitive to all the galactic supernovae. All the third-generation detectors have optimal distance such that each detector is sensitive enough to detect gravitational waves from galactic CCSNe. However, as evident from the plot above, for a source at a fixed distance, the ET will have the lower SNR as compared to Cosmic Explorer. The supernovae-optimized detector provides approximately a 25% improvement in the SNR as compared to Cosmic Explorer.

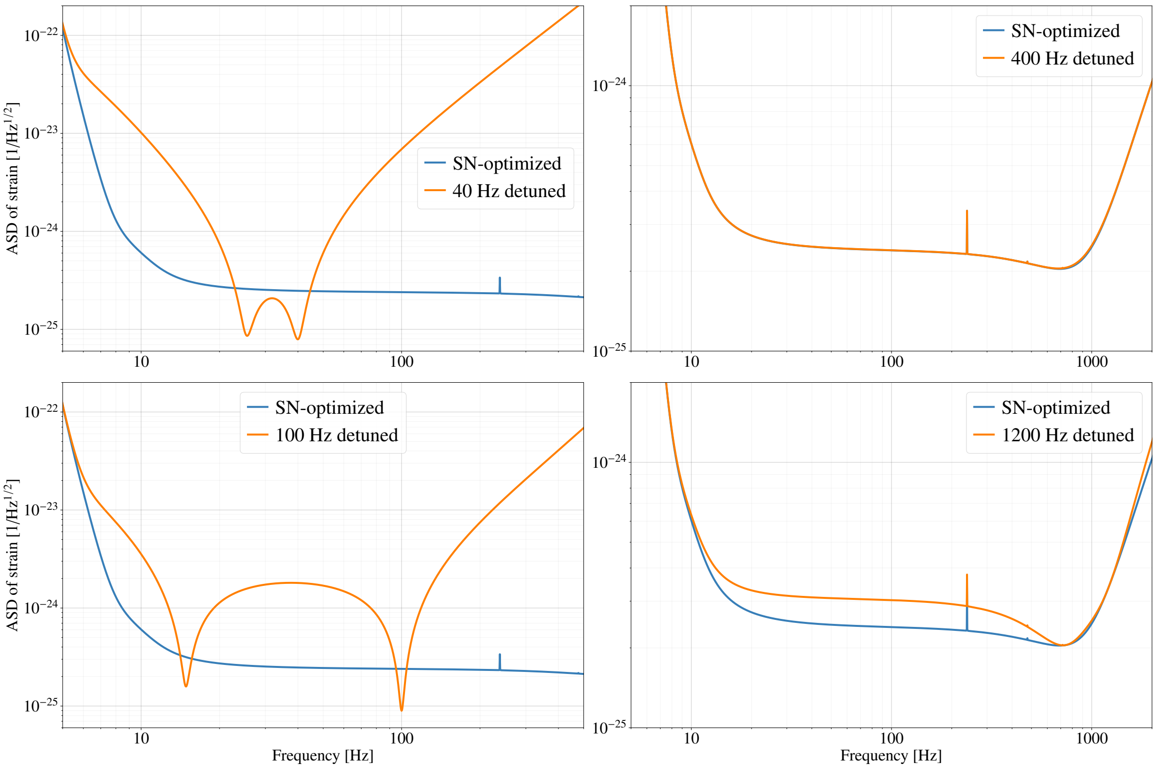

Figure 37: We explore the possibility of detuning the signal recycling cavity to improve the sensitivity towards CCSNe. We find that detuning can be used to improve sensitivity in narrow bins of frequency below 400 Hz. This could, therefore, be used to study the ring-down modes of binary black-holes systems in collaboration with eLISA [6]. However, for improvements to the range of CCSNe, this technique isn't useful.

This response from detuning the signal recycling cavity arises from the two sidebands resonances in quantum noise [141, 139]. We consider the detuning of the signal recycling cavity at different frequencies.

We maintain the frequency dependent squeezing of 15 dB. We achieve 15 dB squeezing in a detuned signal recycling cavity without losing the injected squeezing by actively changing the squeezing angle in accordance with the amount of detuning. Thus, detuning the signal recycling cavity along with actively changing the squeezing angle can be used to switch from a broadband zero-detuned detector to a narrow band detector with greater sensitivity for some frequencies determined by the magnitude of detuning. We perform another tier of optimization in which we actively vary the amount of detuning and the squeezing angle. We limit the amount of detuning in the range from $-\pi/5$ to $\pi/5$ and the squeezing phase is tuned in between $-\pi$ to π. To optimize the detector response at frequencies of 40 Hz, 100 Hz, 400 Hz and 1200 Hz, we inject a sine-Gaussian at each frequency and then maximize the range for this injected signal by varying only the detuning and squeezing angle for the supernovae optimized detector.

We find that detuning the signal can improve the sensitivity of the detector in narrow bins of frequency below 400 Hz. We do not achieve improvements in sensitivity at higher frequencies therefore, we do not improve the range for different models by detuning the detector. There are no improvements in the optimal SNR values for a source at a fixed distance. In summary, detuning the signal recycling cavity is not useful for improving the Cosmic-Explorer-like detector's sensitivity to CCSNe. Instead, detuning the signal recycling cavity at higher frequency degrades the sensitivity of the broadband supernovae-optimized detector. The corresponding results of detuning the signal recycling cavity are summarized in Fig. 37.

6.4.3 Narrow-band Configurations Tuned for Supernovae

The parameters of the broadband supernovae-optimized detector were computed in section §6.4.1 with two constraints. We will in this section relax those constraints and consider narrow-band detector configurations to maximize the range for CCSNe. The phenomenological waveform we developed cannot be used for narrow-band optimization as the fit was performed to match the power of the 3D waveforms over a broad frequency bandwidth. Therefore, we find narrow-band configurations using a different technique.

The length of the signal recycling cavity can be changed to tune the resonant frequency of arising from the coupling of the signal recycling cavity with the arms of the interferometer [157, 141]. The bandwidth of the resonance at a frequency ω_r is given by

$$B = \frac{\mathrm{cT}_{srm}}{4\mathrm{L}_{src}} \tag{6.84}$$

where T_{srm} is the transmissivity of the signal recycling mirror and L_{src} is the length of the signal recycling cavity. We choose the length of the signal recycling cavity at 150m, 300m and 750m are such that the resonant frequency ω_r is at 1000 Hz, 750 Hz and 500 Hz respectively. The equation 6.84 is then inverted for bandwidth ranging from 250 Hz to 1600 Hz and the corresponding values of the transmissivity of the signal recycling mirror are calculated.

We find that a narrow-bandwidth of 250 Hz significantly affects the sensitivity of the detector towards CCSNe. This is expected as we have stated earlier that the frequency spectrum of gravitational wave emission from CCSNe is broadband. The range of improvements achieved by narrow-band detectors at 500 Hz, 750 Hz and 1000 Hz with a bandwidth of 250 Hz are also varying from waveform to waveform and therefore is not model independent 38. When the bandwidth is increased to 1600 Hz the range improves for the 750 Hz narrow-band detector for some of the waveforms as shown in Fig. 38. The L_{src} = 300m and T_{srm} = 0.0064 give this narrow-band detector configuration. The mean improvement in optimal SNR with the 750 Hz narrow-band and 1600 Hz bandwidth detector is approximately 10 % with respect to the supernovae optimized broadband detector. However, we caution that the improvement from narrow banding is not the same across all the 3D numerical waveforms. Moreover, this comes at the cost of significant loss of sensitivity below 400 Hz and above 1100 Hz. The range for BNS drops to 3 Gpc (z=0.9) compared to 3.7 Gpc (z=1.1) for supernovae-optimized Cosmic Explorer and 4.3 Gpc (z=1.4) with respect to the Cosmic Explorer.

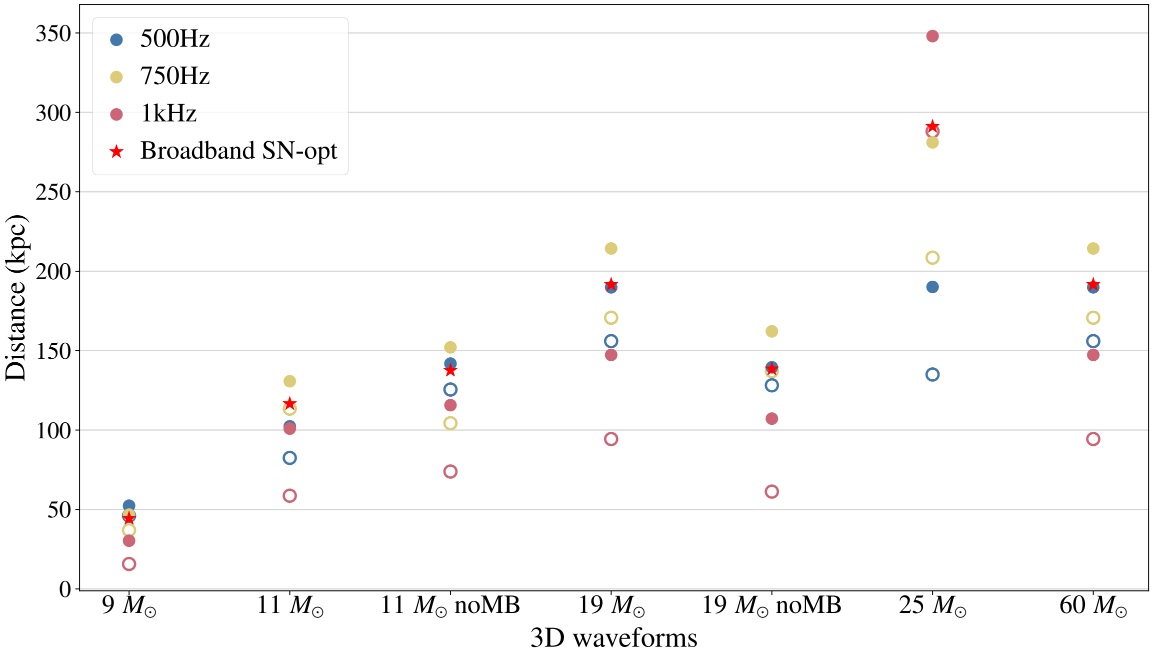

Figure 38: The figure summarizes the optimal distance of the different 3D waveforms for narrow-band detectors at frequencies 500 Hz, 750 Hz and 1000 Hz. The hollow circles denote the narrow-band detectors with a bandwidth of 250 Hz while the filled circles denote the bandwidth of 1600 Hz. The optimal distances from the broadband supernovae-optimized detector are represented as stars. We see tighter narrow-banding with a bandwidth of 250 Hz degrades the performance of the detector. The wider bandwidth of 1600 Hz around the 750 Hz narrow-band detector improves the optimal distances for most of the numerical waveforms.

6.5 Challenges in Building a CCSNe Detector to Achieve Higher Event Rates

In section §6.4.1, we find an optimized third-generation broadband gravitational wave detector for a CCSNe signal has the range only to a few hundred kilo-parsec for the 3D numerical waveforms of CCSNe.

We now address the question of what are the strain requirements for a gravitational-wave detector to be able to detect CCSNe with an event rate of 0.5 per year. From the table 5, we see that this "Hypothetical CCSNe detector" must have a range of $\mathcal{O}(10\ \mathrm{Mpc})$ for CCSNe to achieve an event rate of 0.5 per year. Moreover, for a single detector, we need a signal to noise ratio (SNR) of 8 to define the detection of a signal against the background. Using the two constraints above we can calculate the minimum strain sensitivity required to achieve an event rate of 0.5 per year for the waveforms from 3D numerical simulations. The optimal distance for the numerical waveforms can be calculated by equation 6.81. The limits over the integral are defined by f_{low} and f_{high}. To find the strain requirements for the different waveforms we assume a flat PSD over a broadband range of frequency ranging from f_{low} and f_{high}. We consider two scenarios which are summarized in the figures 39. First, we vary the upper limit of the frequency integrated $-$ f_{High} with the lower limit of integration is held constant at 10 Hz. The second scenario where the upper limit of integration is constant at 2 kHz and we vary the lower frequency limit f_{low}. We find the minimum strain sensitivity required for the gravitational-wave detector to detect the CCSNe with an event rate of 0.5 per year is $3 \times 10^{-27}\ \mathrm{Hz}^{-1/2}$ over a frequency range of 100 Hz to 1500 Hz.

Thus, we need a detector with sensitivity approximately a hundred times better than the Cosmic Explorer design to detect CCSNe with an event rate of 0.5 per year. In the next section §6.5, we will summarize the noise limitations of the third generation detectors and consider design parameters for gravitational-wave detectors beyond the scope of the third-generation to determine the technological hurdles to overcome in order to ever observe gravitational signals from CCSNe more frequently.

It is evident from Fig. 34 that the sensitivity is limited by the quantum noise in the broad range of frequencies. The standard quantum noise limit is dependent primarily on the length of the arm cavities, the test masses and the power of the

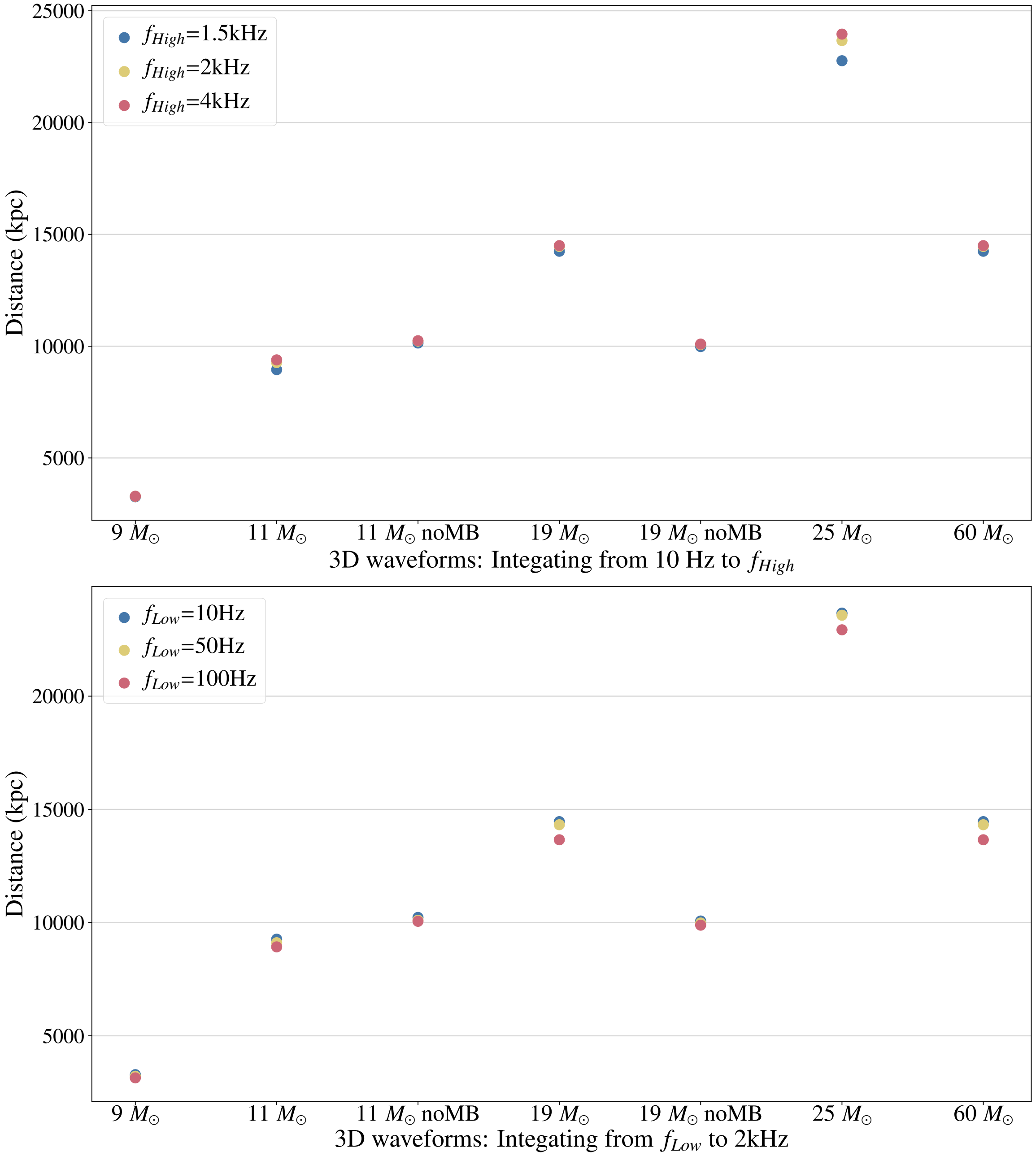

Figure 39: Considering toy detector with a flat PSD of $3{\times}10^{-27}$ $Hz^{-1/2}$ in range 10 Hz to f_{High} (above) and f_{low} to 2 kHz (below), the figure summarizes the range with the corresponding sensitivity and numerical waveform CCSNe corresponding to their ZAMS mass. We see a broadband detector with a strain sensitivity of $3{\times}10^{-27}$ $Hz^{-1/2}$ from 200 Hz to 1.5 kHz is desired to achieve the ranges that would correspond to an observed event rate of one per year for gravitational-waves from CCSNe.

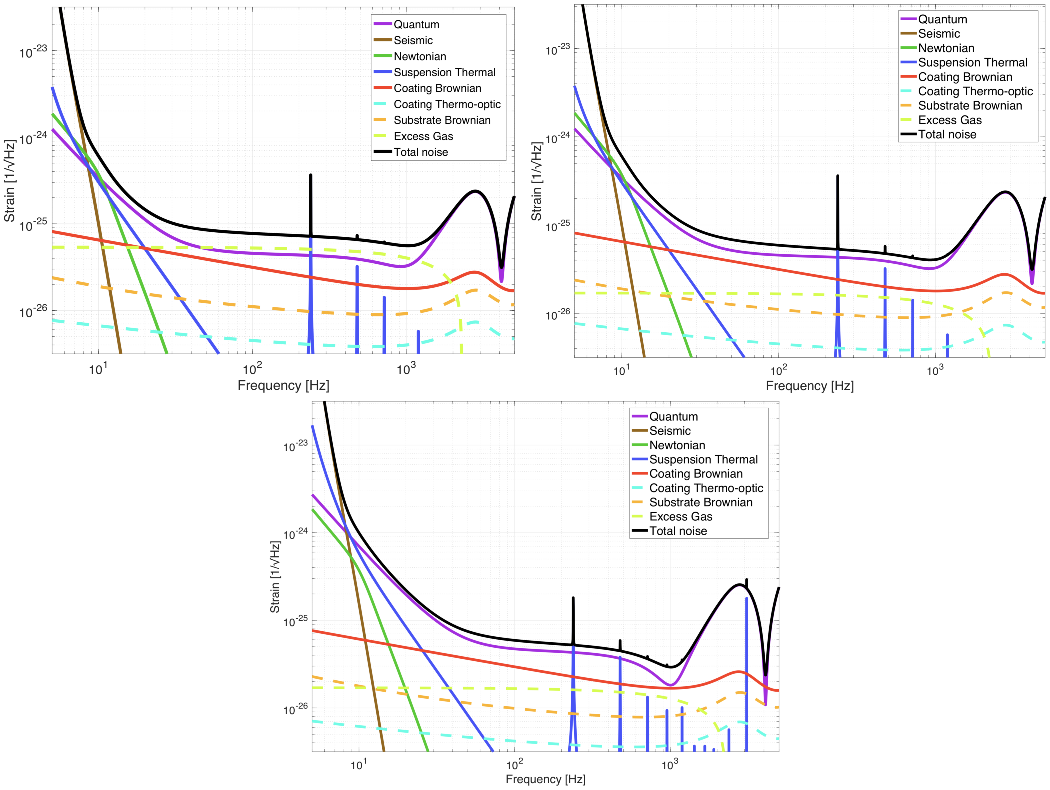

Figure 40: The figure above summarizes the noise budgets for the Hypothetical detector configurations. We see from the figure on the top that the detector's sensitivity is limited by residual gas noise. Therefore, we reduce the residual gas pressure by a factor of ten from CE design. The plot in the middle and bottom plots show optimization results without changing the transmittance of the power recycling cavity and with active changes in the transmittance of the power recycling cavity. Thereby, changing the gain of the power recycling cavity and the finesse of the detector. We will refer to the two detector configurations as Hypothetical-1 and Hypothetical-2 respectively.

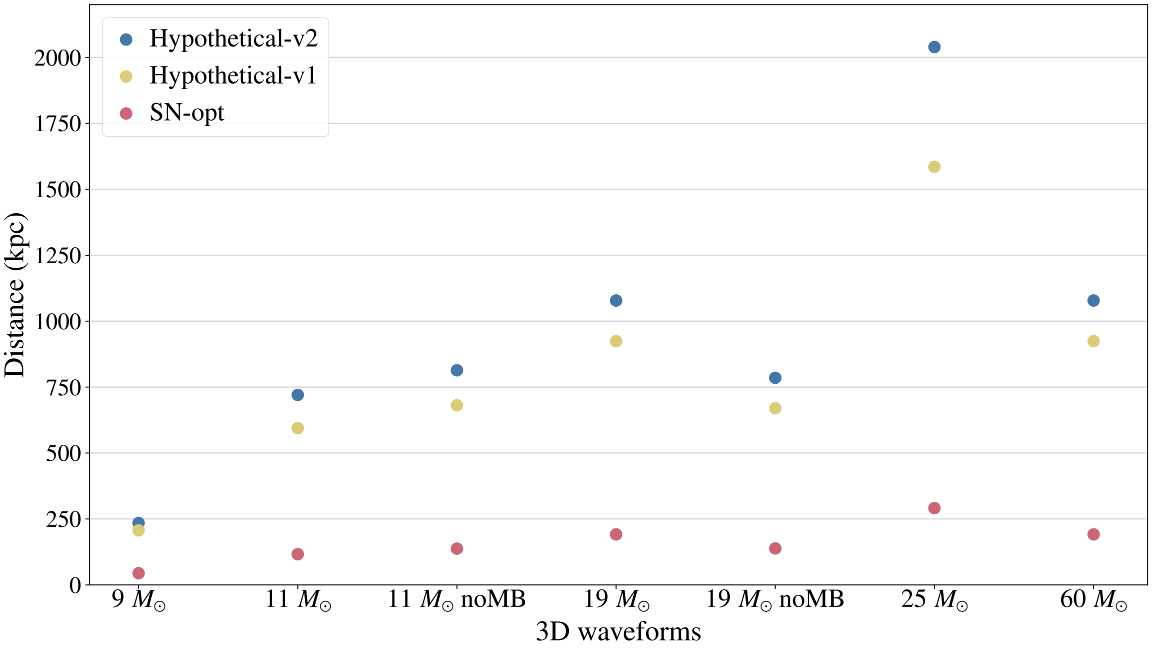

Figure 41: The plot shows with extreme technological upgrades to the third-generation detectors discussed in section §6.5, we optimal distances for the CCSNe is limited to 1Mpc. The event rate for the observation of gravitational waves from CCSNe is still low but improves to one in twenty years.

input laser [158]. The length of the arm cavities cannot be increased any further as the f_{FSR} would significantly affect the performance of the detector at the frequencies of interest. As a result, we set the length of the Hypothetical detectors to 40 kms. Increasing the power of the input laser is the one possibility to reduce quantum noise. We assume an input laser power of 500W. At high frequencies, the quantum noise in the detector manifests itself as shot noise and is limited by photon number arriving at the photo-detector. To see the best we can achieve, we set the photo-detection efficiency of the photo-detector in Hypothetical to 1 (from 0.96 for CE design). For the same reason, we also set the optical and squeezing injection losses in the detector to zero.

The coating thermal noise and the residual gas noise are the next limiting factor in the system. We reduce the substrate absorption by an order of magnitude from CE design. Lastly, as the frequency range of interest is from 100Hz we can sacrifice the sensitivity at lower frequencies. Thus, we can reduce the masses of the mirrors as we are interested in improving the shot noise characteristics of the detector, at the cost of higher radiation pressure noise. In this setup we optimize over the length of the signal recycling cavity L$_{src}$, the transmissivity of the signal recycling mirror T$_{srm}$, the transmissivity of the input test mass T$_{itm}$ and the scale mass parameter to change the masses of the mirror. The optimization over these parameters is aimed at maximizing the range for the representative supernovae waveform, we will reference this optimized detector as *Hypothetical-1*.

The quantum noise limit in a dual-recycled Fabry-Perot interferometer also depends on the gain of the power recycling cavity [141, 139]. We will in another independent optimization also tune the transmissivity of the power recycling mirror T$_{prm}$ along with the above parameters. We define this supernovae-optimized detector as *Hypothetical-2*. The table 7 summarizes the optimal parameters of different detectors. Fig. 40 shows the noise budget of the Supernovae optimized Hypothetical detectors. We see that the residual is the limiting source of the noise. Removing the residual gas noise improves the noise floor of the detector by a factor of two in the wide range of frequencies of interest, see Fig. 40. After removing the residual gas noise, we are limited in sensitivity by quantum noise over the broad range of frequencies.

The strain sensitivity achieved after removing the residual gas noise is $5\times10^{-26}\text{Hz}^{-1/2}$. The improvements in photo-detection efficiency, the input laser power, substrate coatings and minimization of optical losses are not sufficient to achieve a strain sensitivity of the order of 3×10^{-27} Hz$^{-1/2}$ required to detect CCSNe with an event rate of one in two years (see section §6.5).

Lastly, we revisit the numerical waveforms of core-collapse supernovae to see the ranges achieved by the Hypothetical supernovae-optimized detector designs. We find for the 3D waveforms from numerical simulations have a mean distance of 800 kpc, see Fig. 41. Thus, with beyond the third generation detector designs, we would be able to observe core-collapse supernovae from Andromeda. The corresponding event rate is of the order of one in twenty years. The event rate calculation assumes a 100% duty cycle of the detector. The observation rate of gravitational waves from CCSNe is low even for gravitational-wave detectors beyond the scope of the third-generation detectors.

Parameters	aLIGO	Cosmic Explorer-2	SN Optimized	Hypothetical-1	Hypothetical-2
Input Power	125W	220W	220W	500W	500W
SRM transmission	0.325	0.04	0.015	0.0030	0.0122
ITM transmission	0.014	0.014	0.014	0.0036	0.0269
PRM transmission	0.030	0.030	0.030	0.030	0.0011
L_{src}	55m	55m	175m	30m	260m
Finesse	446.25	447.52	447.52	1745.33	233.33
Power Recycling Factor	40.66	65.32	65.32	94.25	1300.09
Arm power	712.43 kW	2025.70 kW	2025.70 kW	26.06 MW	47.61 MW
Thermal load on ITM	0.386 W	1.150 W	1.150 W	13.094 W	24.180 W
Thermal load on BS	0.051 W	0.253 W	0.253 W	0.008 W	0.080 W
BNS range	173.00 Mpc	4.29 Gpc	3.67 Gpc	5.32 Gpc	5.09 Gpc
BNS horizon	394.83 Mpc	11.05 Gpc	9.49 Gpc	12.97 Gpc	12.53 Gpc
BNS reach	246.06 Mpc	8.54 Gpc	6.90 Gpc	11.56 Gpc	10.80 Gpc
BBH range	1.61 Gpc	6.13 Gpc	6.10 Gpc	6.15 Gpc	6.09 Gpc
BBH horizon	3.81 Gpc	11.86 Gpc	11.85 Gpc	11.85 Gpc	11.70 Gpc
BBH reach	2.54 Gpc	11.73 Gpc	11.73 Gpc	11.72 Gpc	11.52 Gpc
Supernovae range	4.34 kpc	71.95 kpc	94.24 kpc	540.53 kpc	716.03 kpc
Supernovae horizon	9.84 kpc	163.08 kpc	213.61 kpc	1225.22 kpc	1623.06 kpc
Supernovae reach	6.10 kpc	101.04 kpc	132.35 kpc	759.15 kpc	1005.65 kpc
Stochastic Omega	2.36e-09	1.82e-13	2.77e-13	1.1e-13	2.58e-13

Table 7: Summary of All Detectors

6.6 Conclusion

We have shown that it is possible to tune a Cosmic Explorer detector to increase the range to CCSNe by approximately 25%. This range improvement does not translate to an increase in detection rate due to the inhomogeneity of the local universe. Therefore, even optimized third-generation gravitational-wave detectors will be limited to CCSNe sources within our galaxy and the Magellanic Clouds. Assuming the detectors have a duty-cycle of 100% the corresponding event rate of CCSNe is one in fifty years. Incorporating the detector downtime and duty-cycle would further decrease the event rate of observed gravitational-wave signals from CCSNe.

However, if such an event were to occur, the broadband supernovae-optimized detector would improve the SNR by of sources by 25%. This improvement would facilitate help understand the properties of the progenitor star in the rare event of CCSNe observation. The supernovae-optimized detector has a slightly reduced sensitivity to the inspiral of neutron stars, but the high-frequency improvements would benefit the study of post-merger signatures and the late-time behavior of the inspiral.

We find that a gravitational-wave detector would require a strain sensitivity of the order of $3{\times}10^{-27}$ Hz$^{-1/2}$, over a frequency range from 100 Hz to 1500 Hz in order to guarantee a high rate of CCSNe detection. At this strain sensitivity, as per the current estimates of the BNS background, the stochastic background from BNS mergers would contribute as the fundamental sources of noise [159]. This along with technological challenges discussed in section §6.5 poses significant hurdles in achieving an event rate of one per year for the observation of gravitational-waves from CCSNe based on the present models and knowledge of gravitational-wave emission from CCSNe. The technological requirements for these upgrades are beyond the requirements for the third-generation detector. With drastic improvements of an input laser power of 500 W and a photo-detection efficiency of 1, an order of magnitude improvement in the residual gas noise and coating noise from the Cosmic Explorer design, and assuming minimal optical losses in *Hypothetical* detectors. We find that after optimizing these detector configurations to maximize for the supernovae range the range extends to Andromeda for some of the CCSNe numerical waveforms. The event rate achieved with such a hypothetical detector is one in twenty years.

6.7 Acknowledgements

We would like to thank Evan Hall and Joshua Smith for their help with `GWINC`. We thank Geoffrey Lovelace and Christopher Wipf for helpful discussions in regards with the astrophysical implications of the results. VS, SB, DAB, and CA thank the National Science Foundation for support through award PHY-1836702. AB, DR, and DV acknowledge support from the U.S. Department of Energy Office of Science and the Office of Advanced Scientific Computing Research via the Scientific Discovery through Advanced Computing (SciDAC4) program and Grant DE-SC0018297 (subaward 00009650), the U.S. NSF under Grants AST-1714267 and PHY-1144374, the DOE/ASCR INCITE program under Contract DE-AC02-06CH11357, a Blue Waters PRAC (under OCI-0725070, OAC-1809073, and ACI-1238993), and the National Energy Research Scientific Computing Center (NERSC) under contract DE-AC03-76SF00098. DAB thanks NSF award PHY-1748958 to the Kavli Institute for Theoretical Physics for support.

Chapter 7

Science-Driven Tunable Design of Cosmic Explorer Detectors

Ground-based gravitational-wave detectors like Cosmic Explorer can be tuned to improve their sensitivity at high or low frequencies by tuning the response of the signal extraction cavity. Enhanced sensitivity above 2 kHz enables measurements of the post-merger gravitational-wave spectrum from binary neutron star mergers, which depends critically on the unknown equation of state of hot, ultra-dense matter. Improved sensitivity below 500 Hz favors precision tests of extreme gravity with black hole ringdown signals and improves the detection prospects while facilitating an improved measurement of source properties for compact binary inspirals at cosmological distances. At intermediate frequencies, a more sensitive detector can better measure the tidal properties of neutron stars. We present and characterize the performance of tuned Cosmic Explorer configurations that are designed to optimize detections across different astrophysical source populations. These tuning options give Cosmic Explorer the flexibility to target a diverse set of science goals with the same detector infrastructure. We find that a 40 km Cosmic Explorer detector outperforms a 20 km in all key science goals other than access to post-merger physics. This suggests that Cosmic Explorer should include at least one 40 km facility. [1]

---

[1] Varun Srivastava, Derek Davis, Kevin Kuns, Philippe Landry, Stefan Ballmer, Matt Evans, Evan Hall, Jocelyn Read, and B.S. Sathyaprakash. Accepted by ApJ; arXiv:2201.10668.

7.1 Introduction

The next-generation of gravitational-wave detectors, Cosmic Explorer [47] and Einstein Telescope [160, 161], are proposed to be operational by the mid-2030s. These detectors are expected to be 10 times more sensitive than current advanced LIGO [162] and VIRGO [163] observatories. This allows the next-generation of gravitational-wave facilities to observe compact binaries coalescences throughout the universe. The observation of gravitational-waves from diverse astrophysical sources opens avenues for novel scientific discovery and astrophysical understanding, which has been articulated the GWIC 3G Science Book [164], the Einstein Telescope Science Case [165], and the Cosmic Explorer Horizon Study [47]. In particular, the Cosmic Explorer Horizon Study identifies three key science goals — mapping the cosmic history of merging black holes and neutron stars, exploring the nature of extreme matter through neutron star mergers, and testing fundamental physics and gravity in the strong-field regime. These science goals rely on observation of gravitational-waves from different astrophysical sources or astrophysical processes. The prospects of their observation depend on the sensitivity of Cosmic Explorer facilities in the relevant frequency band.

Signals at the low end of the frequency spectrum, below 500 Hz, include black hole ringdowns, continuous gravitational waves from rotating neutron stars, and compact binary inspirals at cosmological distances. Because general relativity makes a precise prediction for the quasinormal modes of the remnant black hole ringdown formed after compact binary mergers, it allows for a critical test of Einstein's theory [166, 167, 168, 169]. Continuous gravitational waves from isolated or accreting binary neutron stars carry information about crustal, thermal or magnetic deformations or internal mode excitations [170, 171, 172]. Observations of a large population of compact binaries at high redshift with precise source information is useful to constrain cosmological parameters, and trace the evolution of the compact binary populations, understand their formation channels and their progenitors across cosmic time [173, 174].

At intermediate frequencies from 500 to 1500 Hz, tidal effects from neutron star mergers imprint on the gravitational waveform [175, 176, 177]. They reveal the internal structure of neutron stars, which tells us about the properties of zero-temperature supranuclear matter, namely its equation of state. More precise gravitational-wave measurements of neutron-star tidal deformability can advance our understanding of dense matter, especially in conjunction with electromagnetic observations of neutron stars [178, 179, 180].

The post-merger gravitational waves from the oscillating remnants of binary neutron star coalescences lie at the high-frequency end of the spectrum, above 2 kHz. The post-merger oscillations depend sensitively on the structure and evolution of the hot, hypermassive neutron star remnant, which attains the highest matter densities in the Universe. Given that these signals are likely not detectable with Advanced LIGO and Virgo — even with so-called A+ technology or the proposed Voyager technology [181]. However, Einstein Telescope, Cosmic Explorer and NEMO [160, 161, 47, 182] will shed light on unexplored regions of the phase diagram of quantum chromodynamics by delivering reliable post-merger observations.

The large scale of the proposed third-generation gravitational-wave observatories endows them with broadband sensitivity from a few Hz to several kHz. This will not only enable them to capture the vast astrophysical population of known compact binary sources, but also opens the exciting possibility of unraveling new gravitational-wave sources, such as supernovae, isolated pulsars, or exotic compact objects. Here we introduce a design for Cosmic Explorer that allows for tuning its sensitivity between observing runs to maximize its scientific output. We present Cosmic Explorer tunings that optimize sensitivity to low-, intermediate- and high-frequency sources. The tuned configurations provide enhanced sensitivity in a frequency band that is optimized for detecting the corresponding astrophysical sources. This is particularly beneficial for future gravitational-wave detectors where increasing the circulating power will be challenging and may be technologically infeasible.

We discuss the tunable design of Cosmic Explorer in section §7.2. section §7.2.1 provides a summary of the different gravitational-wave detector networks considered, and a summary of the tuned Cosmic Explorer configurations. The configurations with an improved sensitivity at high frequencies are discussed in section §7.3. The section first summarizes the current understanding of the nature of post-merger signals in section §7.3.1, and is followed by the post-merger tuning in section §7.3.2. Tuning focused to improve the measurement of the tidal deformability of binary neutron stars, and the corresponding improvement is summarized in section section §7.3.3. The low frequency tuning is discussed in section §7.4, and the relative improvement in the detection prospects of sources at high redshift is summarized in section §7.4.1 and section §7.4.3. The impact on the observation of the ringdown of black hole remnants and the continuous wave sources is discussed in section §7.4.4 and section §7.4.2, respectively. Limitations to these high and low frequency tuned configurations is discussed in section §7.5. section §7.6 summarizes the key results of our paper.

7.2 Tunable Design of Cosmic Explorer

The reference design and the technological advances required to achieve Cosmic Explorer's unprecedented sensitivity are discussed in the Cosmic Explorer Horizon Study [47] and in [183]. Unlike second-generation gravitational wave detectors [162, 163, 184], Cosmic Explorer's design makes it feasible to optimize its sensitivity for a specific science goal with only minor modifications to the detector between observing runs.

Cosmic Explorer is designed as a dual-recycled Fabry-Pérot Michelson interferometer, which relies on the differential arm motion for the gravitational-wave readout, as shown in Fig. 42. Each arm of the Michelson interferometer consists of two highly reflective mirrors, which serve as test masses and form a Fabry-Pérot cavity to increase the power stored in the arms. While this enhances the detector's sensitivity to low-frequency signals that vary slowly compared to the storage time of light in the arm cavities, it attenuates signals above this frequency, which defines the bandwidth of the detector. A power recycling mirror placed at the symmetric port forms a power recycling cavity which further increases the power stored in the arms, but has no effect on the shape of the interferometer's response to differential arm motion.

The addition of a signal extraction mirror (SEM) to the antisymmetric port forms a signal extraction cavity (SEC)[2] which shapes the interferometer's response without decreasing the circulating power in the arms [185]. This extraction cavity creates an optical resonance located at[3] [186, 44]

$$f_{\mathrm{s}} = \frac{c}{4\pi}\sqrt{\frac{T_{\mathrm{i}}}{L_{\mathrm{a}} L_{\mathrm{s}}}} = \frac{c}{2}\frac{1}{\sqrt{2\pi\mathcal{F} L_{\mathrm{a}} L_{\mathrm{s}}}} \tag{7.85}$$

---

[2] This is also sometimes referred to as a signal recycling cavity (SRC).

[3] These equations are valid for third generation detectors and NEMO but require corrections for LIGO due to its more transmissive SEM [44].

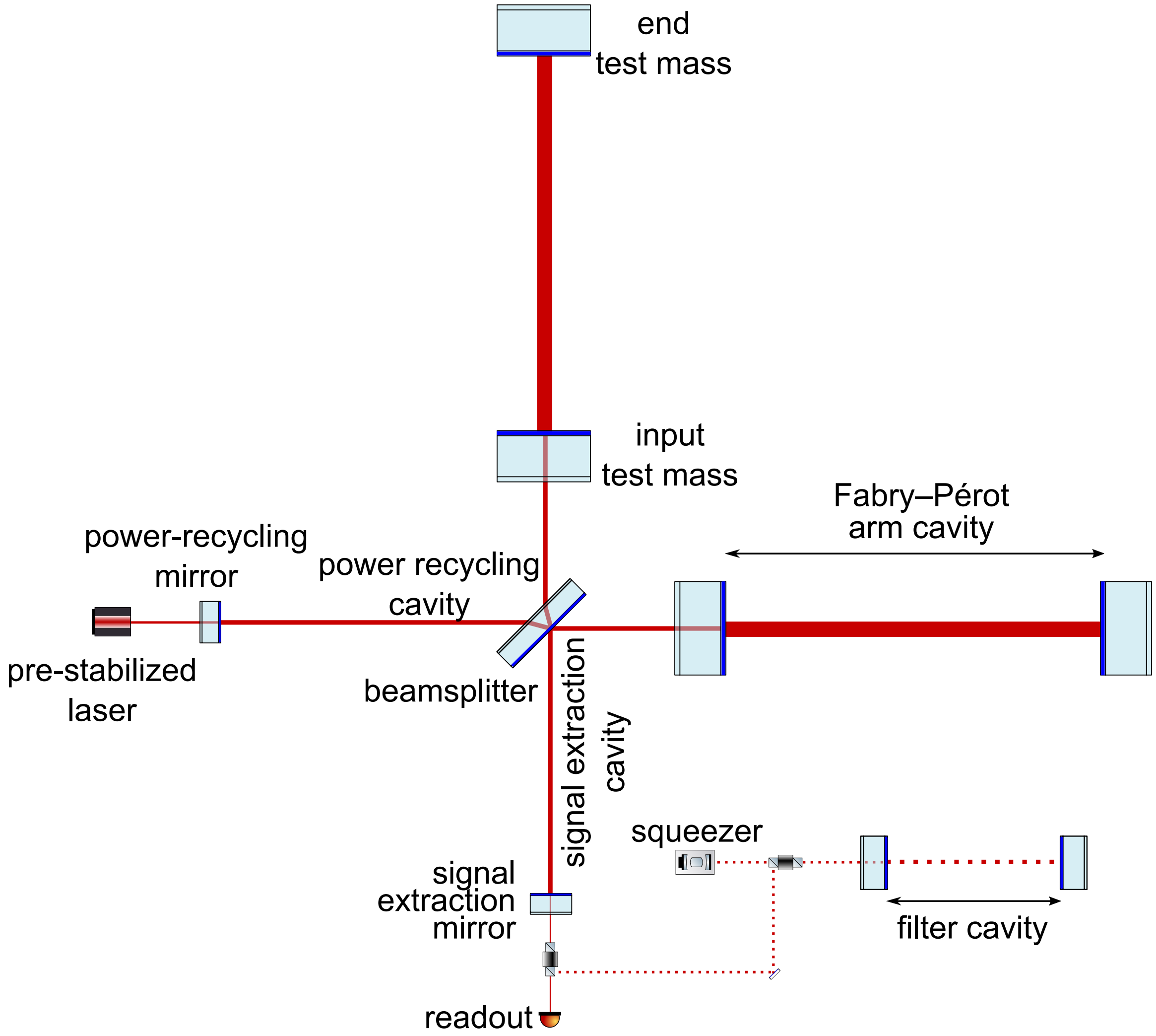

Figure 42: Simplified optical layout of the Cosmic Explorer interferometer.

with bandwidth

$$\gamma_{\mathrm{s}} = \frac{cT_{\mathrm{s}}}{8\pi L_{\mathrm{s}}}, \tag{7.86}$$

where L_{a} is the length of the arms, L_{s} is the length of the SEC, T_{s} is the transmissivity of the SEM, T_{i} is the transmissivity of the input test masses (ITMs), and $\mathcal{F} = 2\pi/T_{\mathrm{i}}$ is the finesse of the arm cavities. In the simplest case where the light is resonant in the SEC, the resulting coupled cavity forms a compound mirror with an effective reflectivity less than that of the ITMs, thus increasing the bandwidth of the interferometer without decreasing the power stored in the arm cavities.

The bandwidth of the second resonance is too broad to have an effect in current gravitational wave detectors (it is about 80 kHz for LIGO), but it can improve the sensitivity centered around f_{s} if it is narrowed by creating a "resonant dip" in the detector's noise spectral density [186, 182]. Once the parameters of the arms are fixed, the length of the SEC is chosen to target a frequency band of interest according to Eq. 7.85, and then the transmissivity of the SEM is chosen to determine the width of this resonance according to Eq. 7.86. This is the principle behind the NEMO detector's tuning for studying postmerger neutron star physics with a "long SRC" [182], but it is important to note that it is the bandwidth of the resonance — not the length of the SEC — that matters. The bandwidth can be narrowed by increasing the reflectivity of the SEM or by increasing the length of the SEC. Cosmic Explorer's long arms require both a relatively short SEC to target postmerger gravitational waves combined with a more highly reflective SEM to narrow the bandwidth. Lowering the transmissivity of the SEM broadens the bandwidth of this resonance, removing the resonant dip in the noise, and improves the low and midband frequencies.

To be able to modify the tuning between observing runs to target different science goals, the required changes to the detector must be minimal in practice. For this reason, we assume that the arm cavities and the length of the SEC are constant, and that only the SEM can be switched between observing runs — a relatively straightforward change. Note that this means the location of the resonant dip in the sensitivity f_{s} is fixed by the infrastructure; only its width γ_{s} can be tuned.

Since the sensitivity is degraded near the free spectral range $f_{\mathrm{fsr}} = c/2L_{\mathrm{a}}$ [187], increasing the arm length beyond 40 km, for which $f_{\mathrm{fsr}} \approx 3.7$ kHz, is not constructive. This motivates our consideration of a 20 km detector with a correspondingly higher $f_{\mathrm{fsr}} \approx 7.5$ kHz, which has better high-frequency sensitivity at the expense of worse broadband sensitivity.

7.2.1 Network of Gravitational-wave Detectors and Cosmic Explorer Configurations

We consider the Cosmic Explorer observatory in a background of different plausible gravitational-wave detector networks. However, to underscore the importance of the Cosmic Explorer detectors we also consider networks in its absence. These networks are summarized below:

- *Second generation or 2G* network that assumes aLIGO Hanford, Livingston and India are observing at A+ sensitivity. Advanced VIRGO and KAGRA at their design sensitivity.
- *Voyager* network that assumes aLIGO Hanford, Livingston and India are observing at Voyager sensitivity. Advanced VIRGO and KAGRA at their design sensitivity.
- *Tuned Voyager India* network that assumes aLIGO Hanford and Livingston are observing at Voyager sensitivity. LIGO India is observing in a post-merger optimized configuration. Advanced VIRGO and KAGRA at their design sensitivity.
- *Voyager+ET* network that assumes aLIGO Hanford, Livingston and India are observing at Voyager sensitivity. Advanced VIRGO and KAGRA at their design sensitivity. ET is operating at it's design sensitivity.

As stated earlier, each Cosmic Explorer detector can operate in three different configurations that are tuned for either low frequencies (LF, section §7.4), compact binary signals (CB, the nominal broadband tuning), or high frequency signals — either post-merger (PM, section §7.3.2) or tidal (section §7.3.3). We explore design options for Cosmic Explorer facilities with arm-lengths of 10, 20, 30, and 40 km. For simplicity, we will focus on the design with a baseline arm length of 20 km and 40 km. The various tuned Cosmic Explorer sensitivities are labeled as follows

- *20:CB or 40:CB* represents a 20 km or a 40 km Cosmic Explorer detector, respectively, observing for compact binary. This configuration serves as a baseline configuration to compare improvements from tuning.

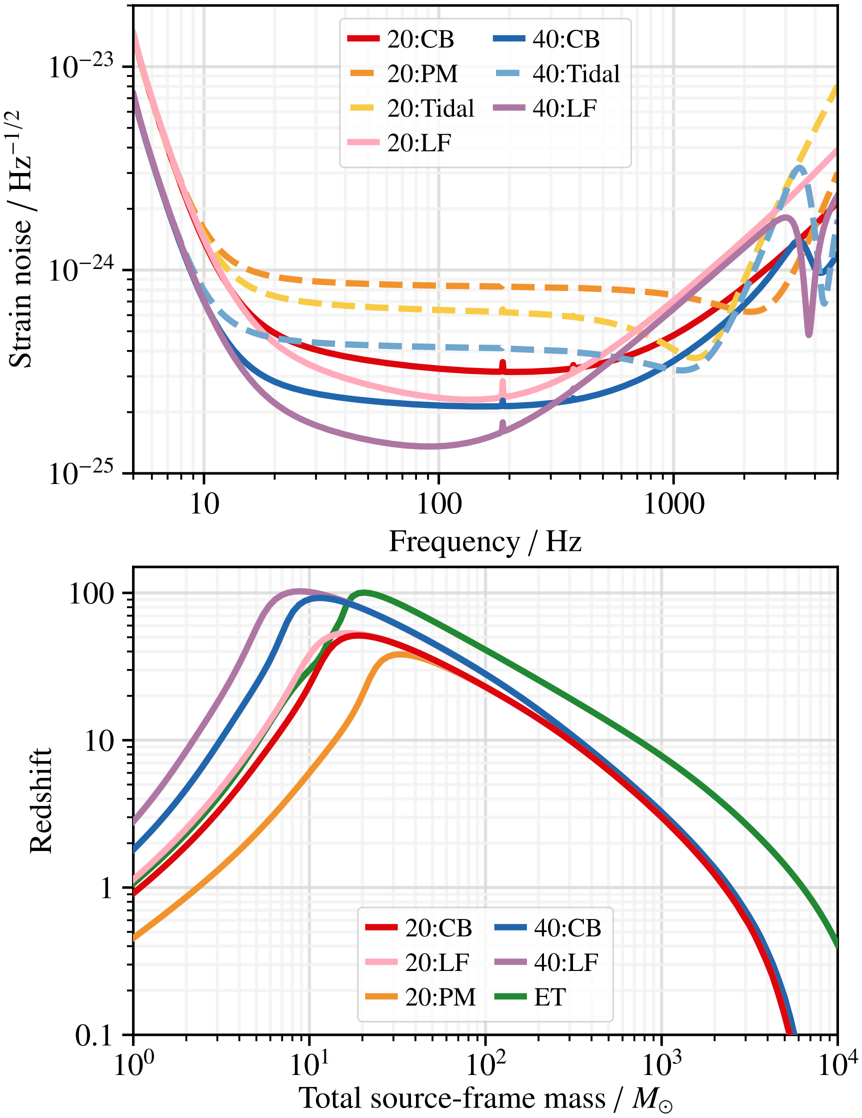

Figure 43: The top plot summarizes the strain sensitivity of the tuned configurations of interest of the 20 km and 40 km Cosmic Explorer (CE) detectors. The compact binary (CB) configuration is the design sensitivity of respective (40 km or 20 km) observatory. Each detector can be tuned to observe with a high-frequency optimized sensitivity — postmerger optimized (PM) or binary neutron-star tidal (Tidal), and a low-frequency optimized sensitivity (LF). The bottom plot shows the horizon redshift as a function of total mass (equal component mass binary) for the corresponding detector configuration along with Einstein Telescope (ET).

Parameters	CE:40	CE:20
L_a	40 km	20 km
Arm Power	1.5 MW	1.5 MW
$\mathcal{F}$	450	450
SEC losses	500 ppm	500 ppm
Compact binary, Post-merger and Low-Frequency		
L_s	20 m	34 m
T_s (CB)	0.02	0.04
T_s (PM)	-	4.5×10^{-3}
T_s (LF)	0.125	0.15
Compact binary', Tidal and Low-Frequency'		
L_s	60 m	190 m
T_s (CB')	0.02	0.04
T_s (Tidal)	4.5×10^{-3}	8×10^{-3}
T_s (LF')	0.125	0.15

Table 8: Cosmic Explorer parameters for the configurations discussed here. It is possible to switch between the compact binary, low-frequency, and one of the two high-frequency tunings (either post-merger or tidal) by changing the signal extraction mirror. However, it is not possible to switch between the two high-frequency configurations as the signal extraction cavity length needs to be changed as well. NOTE — CB' and LF' are the compact binary and low-frequency configurations with the alternate Cosmic Explorer infrastructure used for the tidal tuning. These configurations have similar sensitivities to CB and LF, but are not considered explicitly in this paper.

- *20:PM* represents a 20 km Cosmic Explorer detector which is optimized for post-merger oscillations. The 40 km post-merger is not considered as it has marginal improvement in post-merger sensitivity due to the reduced sensitivity at the $f_{\mathrm{fsr}} \approx 3.7\,\mathrm{kHz}$.
- *20:Tidal or 40:Tidal* represents a 20 km or a 40 km Cosmic Explorer detector, respectively, observing with an improved sensitivity for measuring the tidal effects in binary neutron-star mergers.
- *20:LF or 40:LF* represents a 20 km or a 40 km Cosmic Explorer detector, respectively, observing in low-frequency optimized configuration.

The corresponding spectra for the 20 km and 40 km detectors along with the tunable configurations is summarized in Fig. 43 while the parameters are summarized in Table 8.

We consider these Cosmic Explorer observatories in a background *2G* network, *Einstein Telescope* (ET) network, and *Cosmic Explorer South* (CES) observatory. Cosmic Explorer South is assumed to be a 20 km post-merger optimized detector.

7.3 High Frequency Configurations

7.3.1 Post-merger signal

The remnant of a binary neutron star merger is hot, dense and rapidly rotating. Depending on mass, spin, magnetic field strength, the unknown equation of state of dense matter at finite temperature, and the processes of neutrino emission, the remnant may collapse immediately to a black hole or remain as a (meta-)stable neutron star supported by uniform or differential rotation (see [188] for a recent review). In the latter case, merger-induced oscillations of the remnant produce post-merger gravitational waves. These gravitational waves have a complex frequency-domain morphology. A characteristic peak frequency is attributable to the fundamental quadrupole oscillation mode [189, 190, 191], and secondary frequency-domain peaks are due to transient non-axisymmetric deformations and the interaction between quadrupole and quasi-radial modes [192]. The amplitude and duration of the post-merger emission are particularly sensitive to processes involving magnetic field amplification and neutrino production [193].

Observations of post-merger signals from a population of binary neutron star mergers can probe finite-temperature matter across the density scale realized in hypermassive remnants. Joint pre- and post-merger gravitational wave observations are especially valuable as a potential tracer of hadron-quark phase transitions at supranuclear densities [194, 195]. Post-merger spectra averaged over the whole-sky and source population of the binary neutron star mergers are overplotted in Fig. 44 for two choices of equation of state.

The sensitivity of gravitational-wave detectors to the post-merger signal has been studied in the context of Advanced LIGO and Virgo [196, 197]. Only the loudest binary neutron-star mergers are expected to yield detectable post-merger gravitational radiation for second-generation gravitational-wave detectors. The prospects for third-generation gravitational-wave detectors are more optimistic. In this study, we use post-merger waveforms from the CoRe database of numerical simulations of binary neutron star mergers [198]. The simulations span 164 distinct binaries, with total masses ranging from 2.4 to 3.5 $M_\odot$, and 17 different equations of state. In the time-series waveform of the inspiral, merger, ringdown, and post-merger of binary neutron stars, the post-merger oscillations of the remnant are defined after the amplitude of the ringdown has damped down to zero (or a numerical minimum). The post-merger SNR is then defined for the post-merger-only part of the waveform h_{pm} according to

$$\mathrm{SNR}_{\mathrm{pm}}^2 = 4\,\mathfrak{Re}\int_{f_{\mathrm{min}}}^{f_{\mathrm{max}}} \frac{\tilde{h}_{\mathrm{pm}}(f)\tilde{h}^*_{\mathrm{pm}}(f)}{S(f)}\,df \tag{7.87}$$

where we integrate the post-merger part of the waveform from $f_{\mathrm{min}} = 1\,\mathrm{kHz}$ to $f_{\mathrm{max}} = 4\,\mathrm{kHz}$ to calculate the post-merger SNR, $\tilde{h}_{pm}$ represents the Fourier transform of h_{pm}, * denotes the complex conjugate, and $S(f)$ is the detector noise spectrum [199].

7.3.2 Post-merger Tuning

We consider two stages of post-merger optimized tuning. First, tuning of the proposed CE design with respect to current equation of state constraints [40, 200, 178, 201, 179, 180, 202, 203, 204, 205, 206, 207]. Second, a more aggressive tuning based on potential future improvements in our knowledge of the post-merger frequencies as the constraints on the equation of state improve, which we simulate by fixing the equation of state.

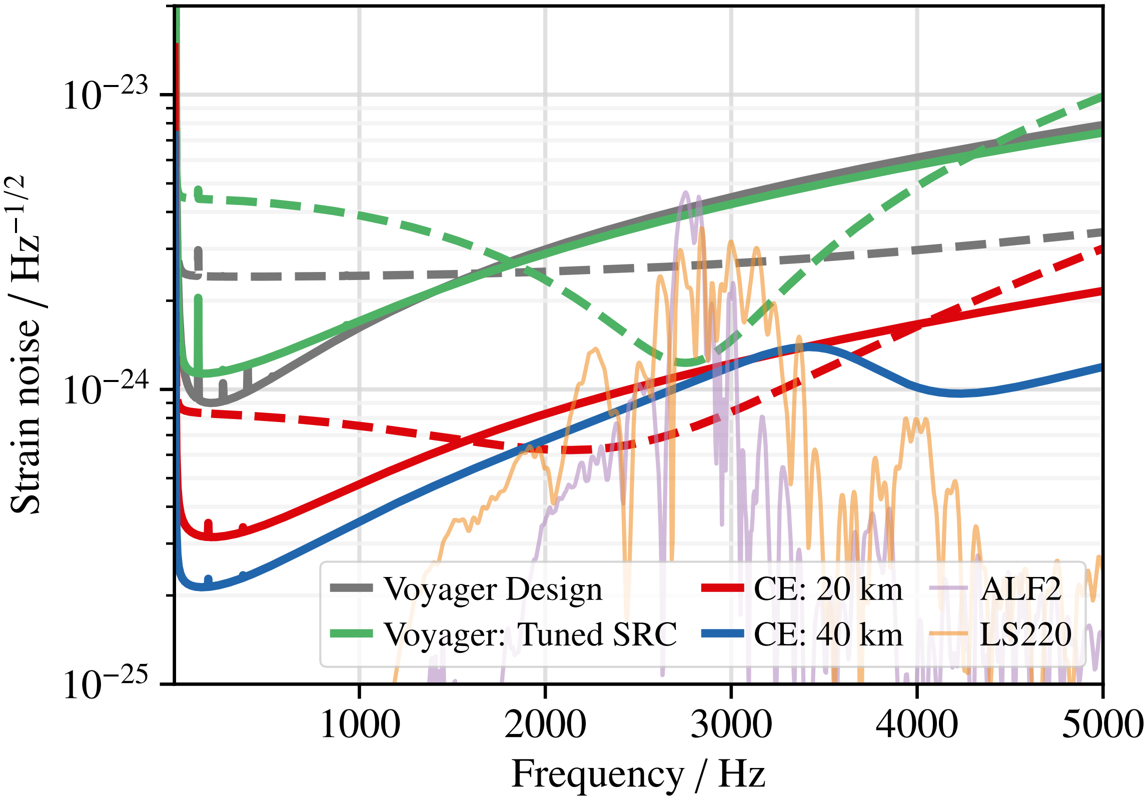

Figure 44: The solid lines shows the strain sensitivity of the corresponding detector in compact binary and the dashed line shows the post-merger tuned configuration. The purple and the orange traces show the sky-averaged source-averaged spectrum of the post-merger signal for the equation of states ALF2 and the LS220, respectively. These traces highlight the post-merger signal of the population of neutron stars extends over a wide range of frequencies, which are equation of state dependent. Proposed narrow-band configurations with a bandwidth of few tens hertz like detuned signal recycling cavity are therefore of limited applications for the observation of the post-merger signal, specially when the chances of observation of post-merger signals with a high SNR (>8) is low.

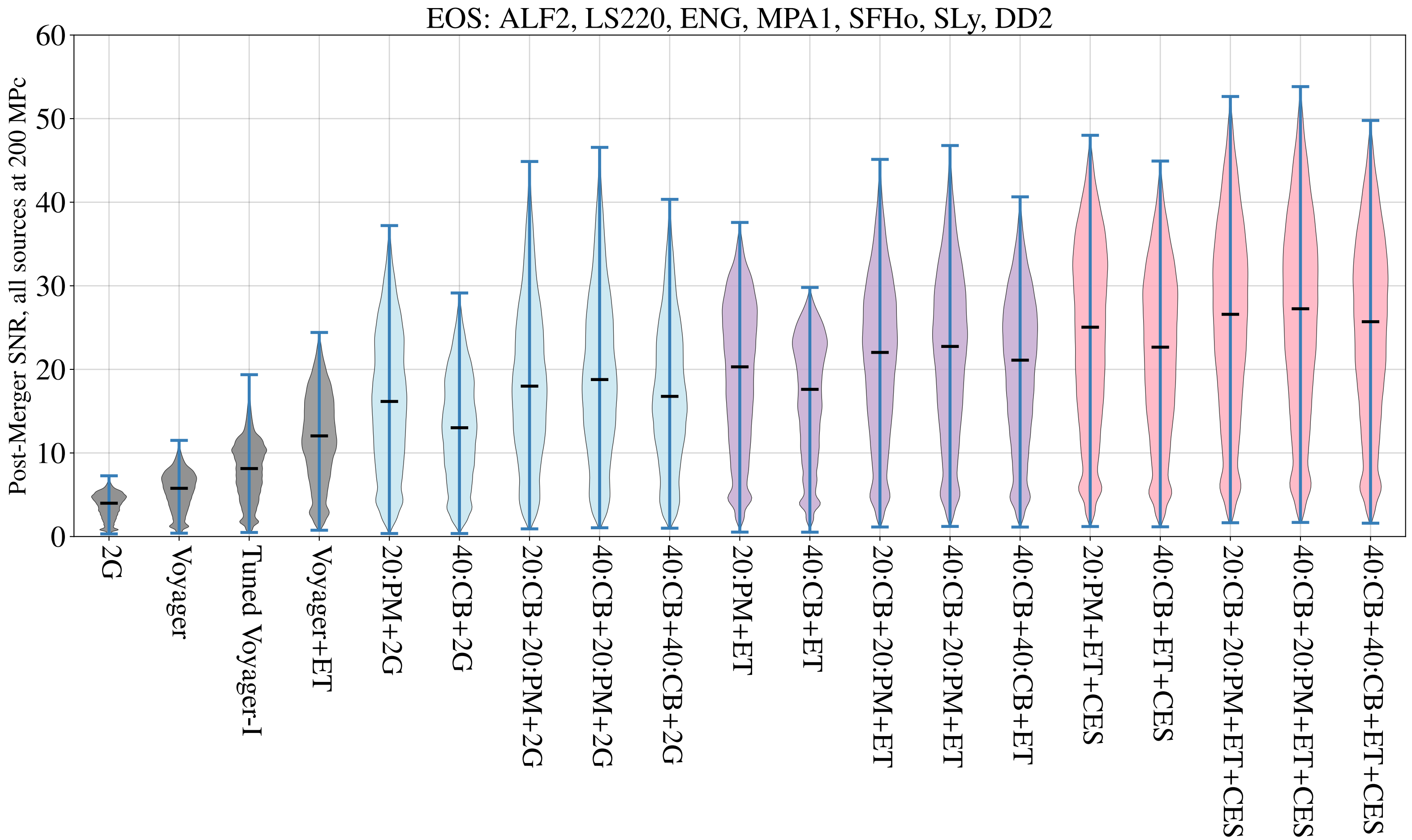

Figure 45: Sky-averaged, source-averaged, EoS-averaged (see section §7.3.1) SNR of the post-merger signal for 160 k binary neutron star sources at 200 Mpc. The performance of networks in the absence of Cosmic Explorer detectors are shown in gray, Cosmic Explorer in a background of 2G networks are shown in blue, networks with Cosmic Explorer and Einstein Telescope are shown in purple, and networks with Cosmic Explorer, Einstein Telescope, and an additional Cosmic Explorer South observatory are shown in pink. section §7.2.1 defines all the networks compared above.

We also explore post-merger tuning possibilities for gravitational-wave detectors for the proposed Voyager upgrade to the current 4 km LIGO facilities. For aLIGO Hanford and Livingston we only consider changing the transmissivity of the signal extraction mirror. However, as the aLIGO India facility is still under construction, we allow the length of the signal extraction cavity to change as well. We refer to this post-merger optimized configuration as *Tuned Voyager India*. Note this does not affect the optimal broadband sensitivity of the LIGO India facility but allows the possibility for it to operate in a high-frequency tuned configuration.

The length of the signal extraction cavity (SEC) and transmissivity of the signal extraction mirror (SEM) are optimized for the 20 and 40 km Cosmic Explorer detectors by maximizing the SNR of a constant post-merger strain of $1 \times 10^{-25}\,/\,\mathrm{Hz}^{1/2}$ from 2 kHz to 4 kHz. The Cosmic Explorer facility is built with this optimal SEC length for post-merger signals and the SEM transmissivities are then changed to switch between the compact binary and low-frequency tunings.

As the observation of the post-merger oscillation signal will be limited to nearby sources, it is critical to ensure the post-merger tuned configuration is optimal for a population of sources. Given the low astrophysical rate, the narrow-band configurations increase the risk of missing the post-merger signal completely, owing to the uncertainty in the equation of state and the source parameters. To quantify the prospects of observation of post-merger oscillations in the above networks, we marginalize over the plausible equation of states in the CoRe database with a broad range of component masses of binary neutron stars [40, 200, 178, 201, 179, 180, 202, 203, 204, 205, 206, 207]. For all of the plausible equation of states, the post-merger signal is injected across the sky at a fixed distances of 100 Mpc, 200 Mpc, 500 Mpc and 1 Gpc. The frequency shift of the post-merger signal due to the cosmological redshift is considered. The post-merger signal is then projected on the different detectors considered in the study; see section §7.2.1. The post-merger SNR of the network is calculated by the quadrature sum of the SNRs in each detector. Fig. 45 summarizes the post-merger SNR for approximately 160 k injections at 200 Mpc averaged over the different equations of state. We find that the 20 km post-merger optimized Cosmic Explorer offers the loudest post-merger SNRs across all plausible neutron star equations of state. It is important to note that the non-observation of post-merger signals with third-generation gravitational-wave detectors will hint at softer equations of state, which do not support post-merger oscillations of the hypermassive remnant.

To constrain the hot equation of state and observe phase transitions in the post-merger remnant requires multiple observations of binary neutron star mergers across the mass spectrum. Using the median of the sky-averaged, equation of state-averaged, post-merger SNRs, and an observed merger rate of 320 $\mathrm{Gpc}^{-3}\mathrm{yr}^{-1}$ [37, 38], we find that a 40 km Cosmic Explorer in a background of 2G networks will detect 40 events per year with a post-merger SNR greater than 8. Two 40 km Cosmic Explorer detectors can observe 80 such events. A single 20 km post-merger optimized detector can observe 80 such sources each year while a network of a 40 km and a 20 km Cosmic Explorer can observe 120 post-merger signals each year. Each of these signals can then be coherently combined to constrain the neutron star equation of state, and facilitate the understanding of hot, dense matter [208, 209]

One may wish to revisit the post-merger tuning *if*, over the next decade, constraints on the neutron star equation of state improve *prior* to the construction of Cosmic Explorer. However, significant improvement from the proposed post-merger tuning will be limited for two reasons. First, any improvements coming from narrowing the bandwidth of the high frequency dip are equation of state dependent. As an example of this scenario, we choose two equations of state from the CoRe database that sample the population of binary neutron stars — ALF2 and LS220. We inject each of these numerical waveforms/sources assuming an isotropic distribution across the sky and uniform in volume from 30 Mpc to 600 Mpc. The corresponding strains are then averaged, which allows one to access the frequencies of interest for the population of sources for the particular equation of state; see Fig. 44. For ALF2, the bandwidth of the 20 km post-merger optimized CE can be further tuned to provide an improvement but further improvements in post-merger SNR from bandwidth tuning are limited for LS220. This is because the post-merger signal of LS220 spans a wide frequency band. Any narrow-band configuration will therefore be non-optimal. Second, even if it were beneficial to narrow the bandwidth, it would be technically extremely challenging to do so due to loss in the signal extraction cavity; see section §7.5 for a detailed discussion.

7.3.3 BNS Tidal Effects

Instead of the post-merger tuning, the Cosmic Explorer detectors can be tuned to improve the measurement of neutron-star tidal parameters, which are dependent on the cold equation of state. The non-zero tidal deformability of the neutron stars in a compact binary coalescence changes the gravitational-wave phase accumulated over hundreds of cycles during the inspiral. The measurability of tidal effects is facilitated by improved sensitivity at higher frequencies, close to the contact frequency of the merger. We find Cosmic Explorer configurations tuned to target the late inspiral up to the contact frequency for a population of binary neutron stars using a similar analysis as that used to find the post-merger tunings discussed in section §7.3.2 using a phenomenological waveform with strain proportional to frequency between 500 Hz and 1500 Hz.

We quantify the benefits of specific configurations using the integrated measurability of tidal effects in the gravitational-wave signal. The measurability per unit frequency of tidal effects is proportional to $f/S(f)$, where $S(f)$ is the power spectral density of the detector [210]. We approximate the relative measurability of tidal effects in binary neutron mergers for different configurations of Cosmic Explorer by this integral. We integrate from 10 Hz up to the contact frequency, C_f, of the binary neutron star system. Hence, we define the tidal measurability, M_Λ, as

$$M_\Lambda = \int_{10\,\mathrm{Hz}}^{C_f} \frac{f}{S(f)}\,df \tag{7.88}$$

The contact frequency is used as the upper bound of integration to separate this measurement from post-merger measurements.

As the measurability function is independent of the equation of state, the ratio of the tidal measurability for two detector configurations is only a function of the detector noise spectrum and this contact frequency, which determines the bounds of integration in Eq. 7.88. We use this relationship to compare the tidal measurability of a variety of systems with different Cosmic Explorer configurations.

The contact frequency of a binary system with two equal mass neutron stars of mass m and radius $R(m)$ is given by [201]

$$C_f(m) = (1530\,\mathrm{Hz})\left(\frac{m}{1.4\,M_\odot}\right)^{1/2}\left(\frac{R(m)}{12.62\,\mathrm{km}}\right)^{-2/3}. \tag{7.89}$$

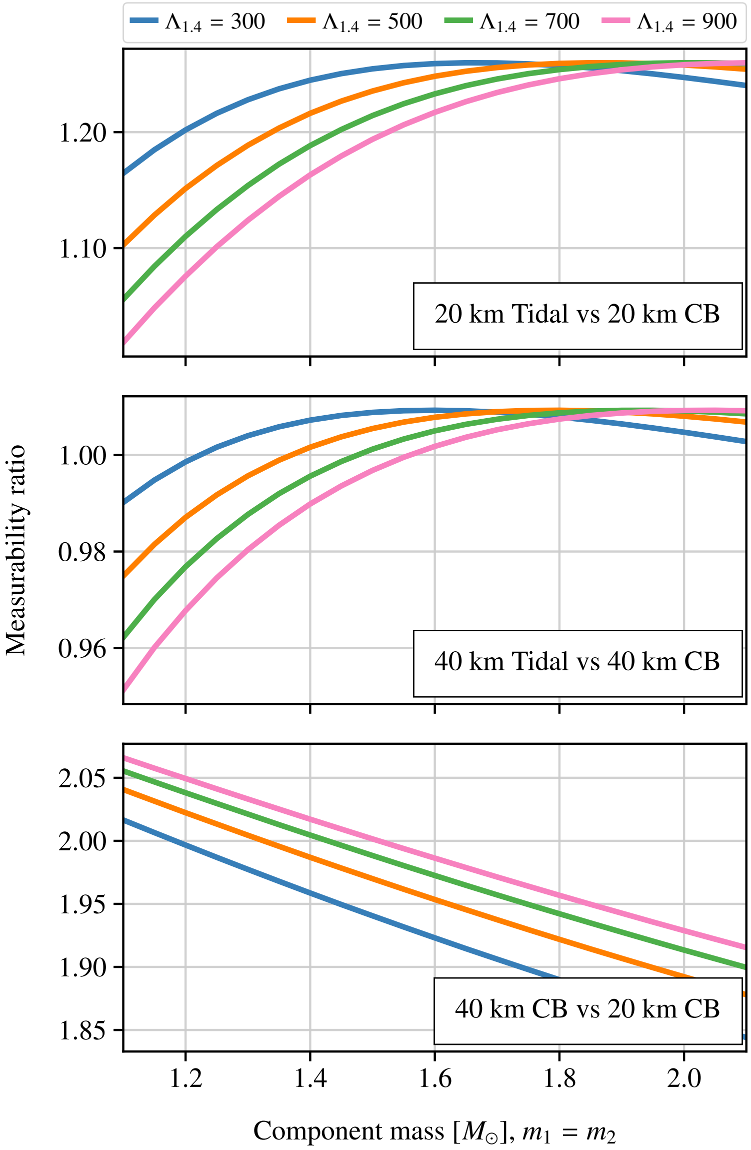

Figure 46: Ratio of measurable tidal information for a Cosmic Explorer detector tuned to tidal measurements versus a broadband configuration. In both the 20 km and 40 km case, a detector can be tuned to improve the measurability of the tidal deformability. Comparing a 20 km and 40 km facility, the 40 km case would significantly increase the overall tidal measurability, although the additional benefits for a 40 km tidal configuration are reduced. In fact, a 40 km broadband configuration would measure tidal effects better than a 20 km tidal detector for all equations of state and masses considered.

To approximate the contact frequency over a wide range of masses, we assume that all neutron stars have a constant radius, determined by the radius of a 1.4 solar mass neutron star with tidal deformability $\Lambda_{1.4}$. This common radius $R_{1.4}$ is [201]

$$R(m) \approx R_{1.4} = (12.62\,\mathrm{km}) \left(\frac{\Lambda_{1.4}}{500}\right)^{1/6} . \tag{7.90}$$

To verify that this calculation of M_Λ holds for state-of-the-art waveforms, we have compared this analytic approximation to the measurability per unit frequency of IMRPhenomDNRTidal waveforms [211, 176]. This is done computationally by calculating the gradient of the match versus frequency for two waveforms with similar tidal deformability values. We confirm that the analytic result holds up until the contact frequency for the range of masses and tidal deformability values explored in this work.

Fig. 46 shows the results of this comparison for both 40 km and 20 km tidal configurations of Cosmic Explorer. Over a range of masses and values for $\Lambda_{1.4}$, a tidal configuration for a 20 km Cosmic Explorer increases the tidal sensitivity by up to 25 %, while a tidal configuration for a 40 km Cosmic Explorer only increases the tidal measurability by up to 10 %. The mass for which the tidal measurability ratio is maximized at a fixed value of $\Lambda_{1.4}$ is determined by the frequency range where the detector sensitivity is maximized by the tidal configuration. The optimal configuration is such that the maximal sensitivity peak is set to just below the expected contact frequency. In practice, the exact tidal configuration can be set to the optimal configuration based on tidal information already known from second generation observations and the mass range of interest. Comparing between different facilities, a 40 km broadband detector increases the tidal measurability by up to 105 % compared to a 20 km broadband detector.

7.4 Low Frequency Configuration

In this section, we motivate low frequency tuned configurations focused on improving the detection probability of the binary-black hole population at high redshifts, such as from the remnants of POP-III stars [212, 213, 214, 215, 216] and seed black-hole binaries [217, 218, 219]. These populations are at high redshift and are comprised of heavier binaries [166, 167, 168], which limits their predominant gravitational-wave signals to below 50 Hz [220]. Low frequency improvements facilitate improved tests of General Relativity. A key test of General Relativity is to precisely measure the amplitude and frequency (as a function of mass and spin) of the quasinormal modes of black hole remnants [221, 169, 222]. The loudest sources observed with third-generation gravitational-wave detectors will provide the most stringent tests of General Relativity. Thus, we will focus on sources which are close and we can safely assume that this binary population is comprised of stellar mass black-holes. The low frequency tuning is complimentary to the high frequency tuning and can be realized by switching the reflectivity of the signal extraction mirror.

At a fixed distance, heavier mass binaries have higher gravitational-wave amplitudes, and the remnant has lower quasinormal frequencies. The low frequency tuned configurations are tuned by maximizing the SNR using a phenomenological frequency-domain waveform of the fundamental ringdown of stellar mass black holes. We use astrophysically weighted populations to construct the phenomenological waveform [223]. We will quantify the performance of the low frequency tuned configuration in the next sections.

7.4.1 SNR Improvements from low-frequency tuning

To quantify the performance of low frequency tuned configurations, we compute the optimal SNR of equal mass binaries, with total mass ranging from $1\,M_\odot$ to $10^4\,M_\odot$. This population is considered at different distances (or redshift) to quantify the effects of the cosmological redshift of the gravitational-wave spectrum in the detector frame. The Fig. 47 summarizes the comparisons between the broadband and the low-frequency tuned configuration. We find that for a large number of the binaries, a 40 km low frequency tuned configuration provides up to 30 % improvement from the broadband detector. A 20 km low frequency tuned detector provides up to 15 % improvement relative to the broadband configuration. These improvements are achieved even for sources at high redshifts. In particular, for heavier compact binaries at a redshift of 10 or higher, like POP-III star population, this improvement in SNR will improve the detection prospects.

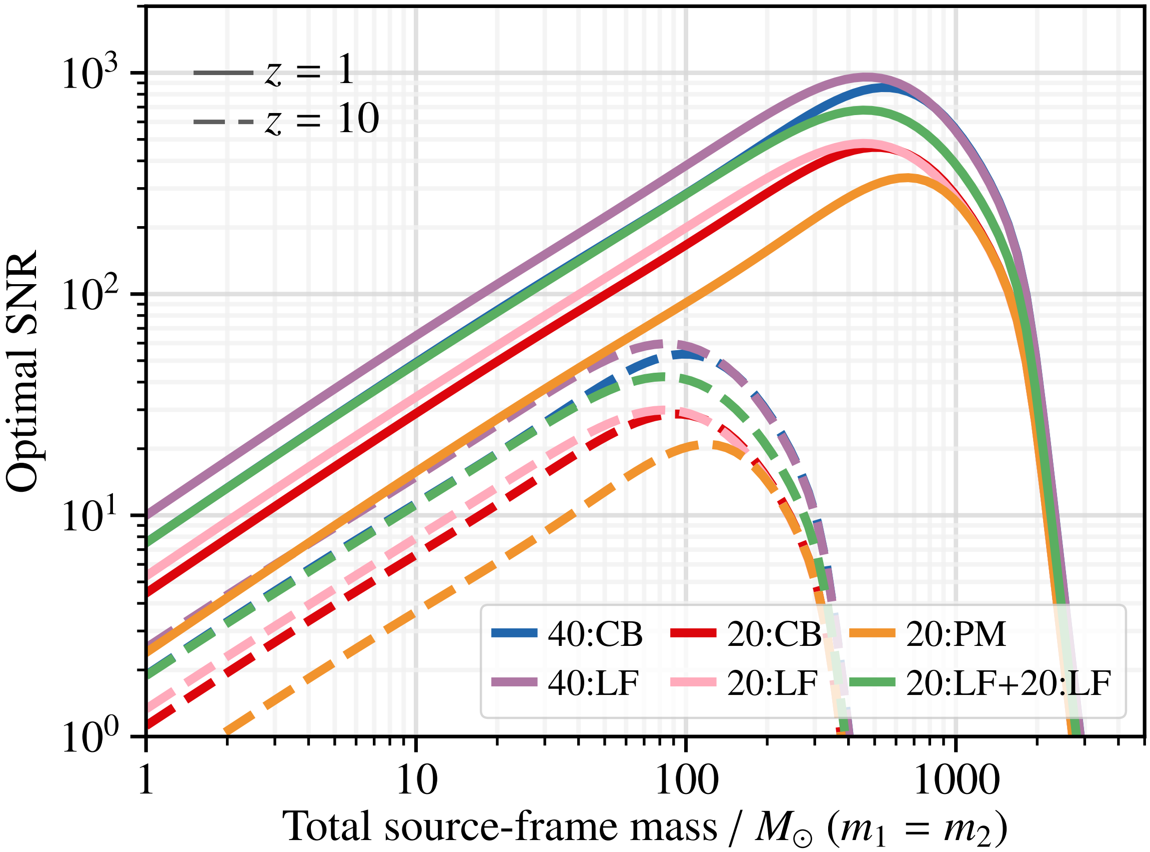

Figure 47: The optimal SNRs as a function of the total mass of the binary with two equal mass components. A 20 km low frequency tuned detector provides up to 15 % improvement in SNR relative to the broadband configuration while a low frequency tuned 40 km detector provides a 30 % improvement.

7.4.2 Continuous Waves

Neutron stars with rotational frequencies in the audio band could be a source of continuous gravitational waves for Cosmic Explorer, lasting for millions of years. Neutron stars that are perfectly spherically symmetric or are spinning about their symmetry axis emit no radiation since their quadrupole would not vary with time. However, non-axisymmetric neutron stars emit gravitational waves at twice their spin frequency $f_{\rm GW} = 2 f_{\rm spin}$. Their amplitude depends on the ellipticity $\epsilon \equiv (I_{xx} - I_{yy})/I_{zz}$, where I_{kk}, $k = x, y, z$, are the principal moments-of-inertia with respect to the rotation axis. For a neutron star at a distance D the amplitude is

$$h \sim \frac{4\pi^2 G}{c^4 D}\, \epsilon\, I_{zz}\, f_{\rm GW}^2 \tag{7.91}$$

Typical neutron star moments are $I_{zz} \sim 3 \times 10^{38}\,\mathrm{kg\,m^2}$. The Crab pulsar (B0531+21) with a spin frequency of 30 Hz (gravitational-wave frequency of 60 Hz), located at a distance of 2 kpc, will have an amplitude of $h \simeq 5.7 \times 10^{-29}$ if its ellipticity is $\epsilon \sim 10^{-8}$. The only way to find such signals is to matched filter the data over a year accumulating billions of wave cycles in the Fourier transform of the data demodulated to account for Earth's rotation and revolution and pulsar's spin down. Indeed, the signal-to-noise ratio grows as the square-root of the integration period or the number of wave cycles. The characteristic strain amplitude h_c of a signal integrated over a time T is $h_c = h\sqrt{T}$, which for Crab would be $h_c \sim 3 \times 10^{-25}\,/\,\mathrm{Hz}^{1/2}(\epsilon/10^{-8})$ for an integration period of $T = 1\,\mathrm{yr}$. A millisecond pulsar with a spin frequency of 300 Hz but the same ellipticity will be 100 times louder.

Signals with characteristic amplitude larger than the amplitude noise spectral density would be detectable with loudness proportional to their height above the noise amplitude. A 40 km Cosmic Explorer tuned to lower frequencies (Fig. 43, 40 km:LF), will have the best sensitivity to neutron stars of spin frequencies 20 − 200 Hz. For example, the Crab pulsar would be detectable if its ellipticity was $\epsilon > 3 \times 10^{-8}$ after a year's integration. In general, neutron stars of spin frequencies in the range 10 − 200 Hz (GW frequencies of 20 − 400 Hz) would be accessible to Cosmic Explorer tuned to low frequencies if their ellipticities are larger than about 10 parts per billion or more precisely if

$$\epsilon \geq 10^{-8} \left(\frac{f_{\rm GW}}{200\,\mathrm{Hz}}\right)^{-2} \left(\frac{D}{10\,\mathrm{kpc}}\right) \left(\frac{T}{1\,\mathrm{yr}}\right)^{-1/2}. \tag{7.92}$$

The ellipticity is roughly equal to the fractional difference in the size of a neutron star along two principal directions orthogonal to the spin axis. Thus, Cosmic Explorer will be able to constrain fractional difference in the equatorial radii of a millisecond pulsar as small as 100 µm.

7.4.3 BNS signals from high redshifts

While the tidally tuned configurations discussed in section §7.3.3 are beneficial for measurements of tidal properties in the local universe, such configurations will not simultaneously be optimal for significantly redshifted signals. For signals at extremely high redshifts ($z > 2.0$), an interferometer tuned to low frequencies will provide a better measurement of tidal parameters. To compare the low frequency tuned configuration to a broadband configuration, we use the tidal measurability metric that was introduced in section §7.3.3. The ratio between the tidal measurability of a broadband detector and a detector tuned to low frequencies can be seen in Fig. 48. For both the 40 km and 20 km case, a detector tuned to low frequencies will be able to better measure the tidal information from high redshift events. The redshifting of detector-frame contact frequency for these distant events explains the increase in measurability ratio with respect to redshift. Furthermore, a 40 km detector has higher tidal measurability than a 20 km detector from signals at any redshift.

Although the measurement of a universal nuclear equation of state will be driven by events in the local universe [224], measurements of the equation of state at high redshifts will provide additional cosmological information. Tidal information from high-redshift events is a potential way to accurately measure the Hubble constant using only gravitational-wave observations [225]. Probes of high redshift events will also allow any potential time-evolution of the nuclear equation of state to be measured. Any variation in the measured equation of state could indicate physics beyond the Standard Model [226, 227].

7.4.4 Exploring the Nature of Extreme Gravity

The population of binary black-holes observed by the aLIGO and VIRGO detectors has facilitated key tests of the theory of General Relativity [166, 167, 168]. These

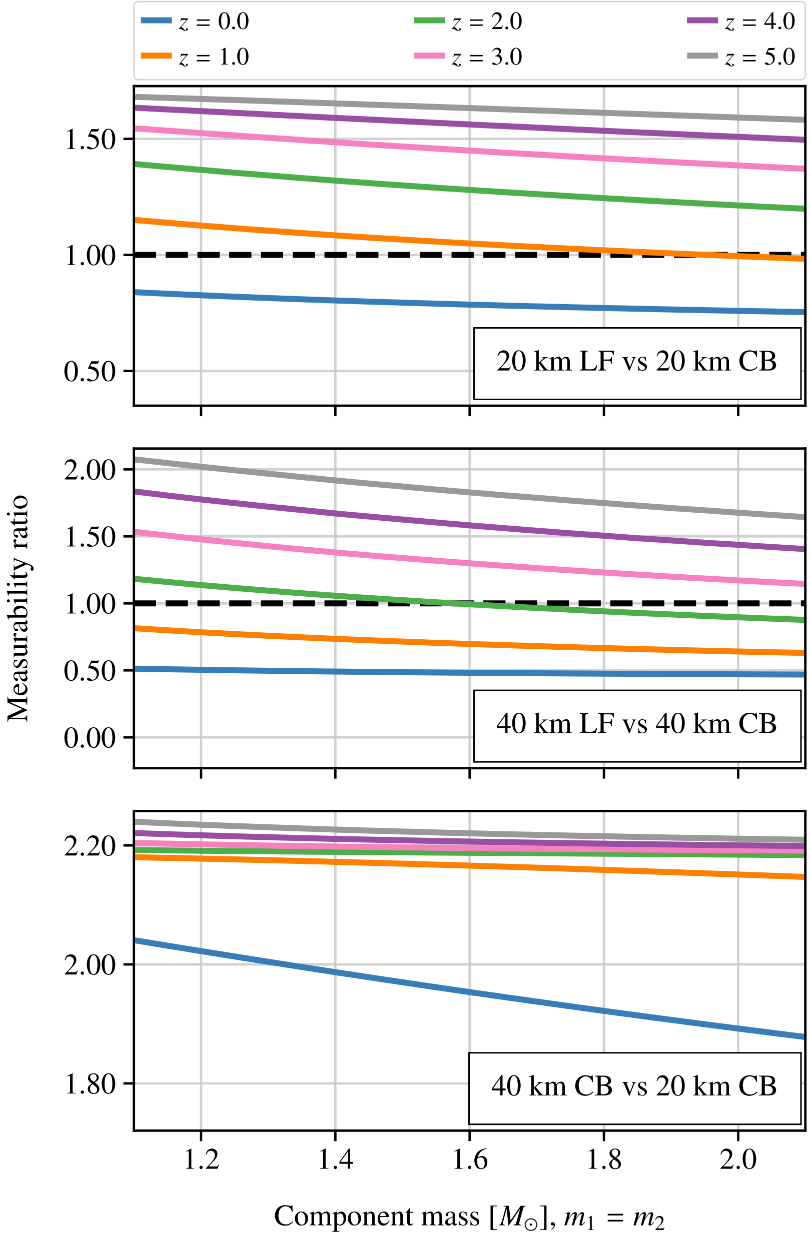

Figure 48: Ratio of measurable tidal information for a Cosmic Explorer detector tuned to low frequencies versus a broadband configuration for different redshifts. Also shown is this ratio for a 40 km facility in a broadband configuration versus a 20 km facility also in a broadband configuration. In all cases, $\Lambda_{1.4}$ is assumed to be 500. For redshifts greater than $1-2$, the amount of tidal information available is greater with a low frequency configuration than with a broadband configuration and a 40 km facility is better than a 20 km facility.

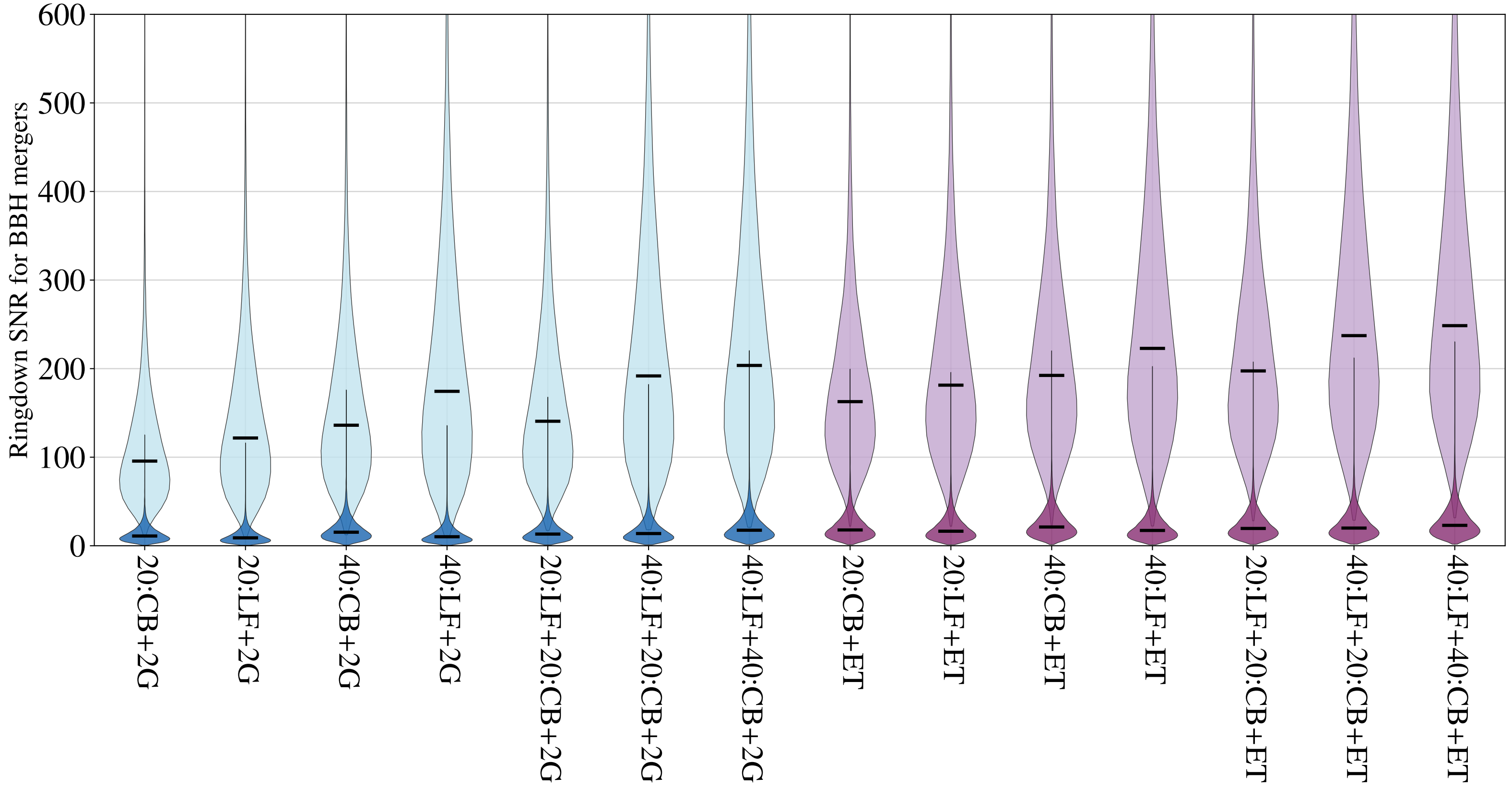

Figure 49: Sky-averaged and source-averaged distribution of the ringdown SNR of the 100 loudest events observed with Cosmic Explorer observatories each year (section §7.4.4) using the observed merger rate of 23.8 $\mathrm{Gpc}^{-3}\,\mathrm{yr}^{-1}$ for binary black holes, and 50 k injections each of low-mass binaries (darker shade) and heavier stellar-mass binaries (lighter shade). The low-frequency optimized configuration improves the observational prospects of the ringdown modes of the remnant black holes. A network of Einstein Telescope and Cosmic Explorer observatories will offer the most stringent tests of General Relativity. section §7.2.1 defines all the networks compared above.

tests of General Relativity include measurement of the consistency of the inspiral-merger-ringdown signal, the spin-induced moments, and polarization of the observed gravitational wave signal. The measurement of the respective amplitude and frequencies of these quasinormal modes is referred to as black-hole spectroscopy. Any deviation of the observed spectral features from the predictions of General Relativity will challenge the theory. We use the SNR of the inspiral-merger-ringdown (discussed in section §7.4.1), and the ringdown SNR of the remnant black-hole to quantify the performance of Cosmic Explorer configuration to explore the nature of extreme gravity.

The loudest signals during Cosmic Explorer are expected to provide the best tests to General Relativity. We consider a population of 50 k sources each of lighter and heavier stellar mass binaries. The lighter-mass binaries are injected uniformly in component mass between 5 $M_\odot$ and 10 $M_\odot$, and the heavier-mass binaries are injected uniformly in mass between 10 $M_\odot$ and 70 $M_\odot$. Both of these source populations are injected uniformly in volume between 100 Mpc and 950 Mpc. Using the observed binary black-hole merger rate of 23.8 $\mathrm{Gpc}^{-3}\mathrm{yr}^{-1}$ [37, 38], this corresponds to the 100 loudest sources detectable each year with Cosmic Explorer. The sky-averaged source-parameter-averaged distribution of the ringdown SNR of the lighter and heavier populations is shown in Fig. 49. In a background network of 2G detectors, we find the median ringdown SNR of the 100 loudest binary black-hole sources with a 20 km Cosmic Explorer is 120 and is 175 with a 40 km. The performance of two 40 km Cosmic Explorer detectors and a network of a 40 km and a 20 km Cosmic Explorer is similar. The ringdown SNR for the 100 loudest events improves significantly with Einstein Telescope in the network, Fig. 49.

7.5 Technological drivers and limitations

In this section we summarize how the noise sources and design choices limit the sensitivity of the various detectors and configurations in order to motivate the research and development (R&D) necessary to maximize the scientific output. It is important to note that most noises are reduced as the arm length is increased and only the quantum noise is affected by the choice of tuning.

For all of the post-merger and tidal configurations, the detectors are limited by quantum noise above ∼20 Hz. Reducing quantum noise relies on increasing the power stored in the arm cavities, increasing the injected squeezing, and reducing all sources of loss — such as optical, mode-mismatch, scattering, etc. Fig. 50 shows the contributions of the various noises to the total quantum noise for the 20 km post-merger configuration, as well as the total noise in black. Reducing loss along the input to and output from the main interferometer, including increasing the quantum efficiency of the photodiodes, is essential in achieving the quantum noise targets in the mid-band frequencies. However, at higher frequencies the losses in the signal extraction cavity (SEC) dominate and limit the sensitivity near the resonant dip for these configurations. SEC loss limits the bandwidth of the compact binary tunings and is not as significant for the low frequency tunings.

Reducing loss in the SEC is thus one of the most critical areas of research needed to realize the high frequency sensitivity goals of Cosmic Explorer. Since SEC loss is independent of both the tuning and the arm length [47, 228], it both reduces the sensitivity near the resonant dip *and* limits the frequency to which that dip can be pushed as is illustrated in Fig. 50. The current noise estimates assume a loss of 500 ppm which includes both optical and mode-mismatch losses discussed below. The corresponding loss in the aLIGO detectors is estimated to be roughly 10 times larger.

The requirements on matching the optical modes between the various optical cavities of the interferometer are likely to be exceedingly strict, and mismatch between these modes is, in some cases, an extra source of SEC loss [44]. Continued development of adaptive mode matching techniques [229, 230, 231, 232, 233, 66, 234] is thus one crucial area of R&D necessary to maximize the high frequency sensitivity.

The quantum noise limiting Cosmic Explorer is inversely proportional to the square root of the arm power, and it is thus important to store high power in the arm cavities. The Cosmic Explorer design calls for 1.5 MW arm power, twice as much as the Advanced LIGO design. The arm power in the current detectors has been limited by the presence of particulates in the mirror coatings which absorb the laser power in localized points and thermally distort the mirrors [3, 56, 235]. Removing, or otherwise compensating the effects of this contamination, is an active area of research. Even if the coatings no longer have this contamination, the power absorbed in the test mass substrates and coatings creates both a thermoelastic deformation of the mirror and a thermally induced lens. All of these effects produce wavefront distortions that require

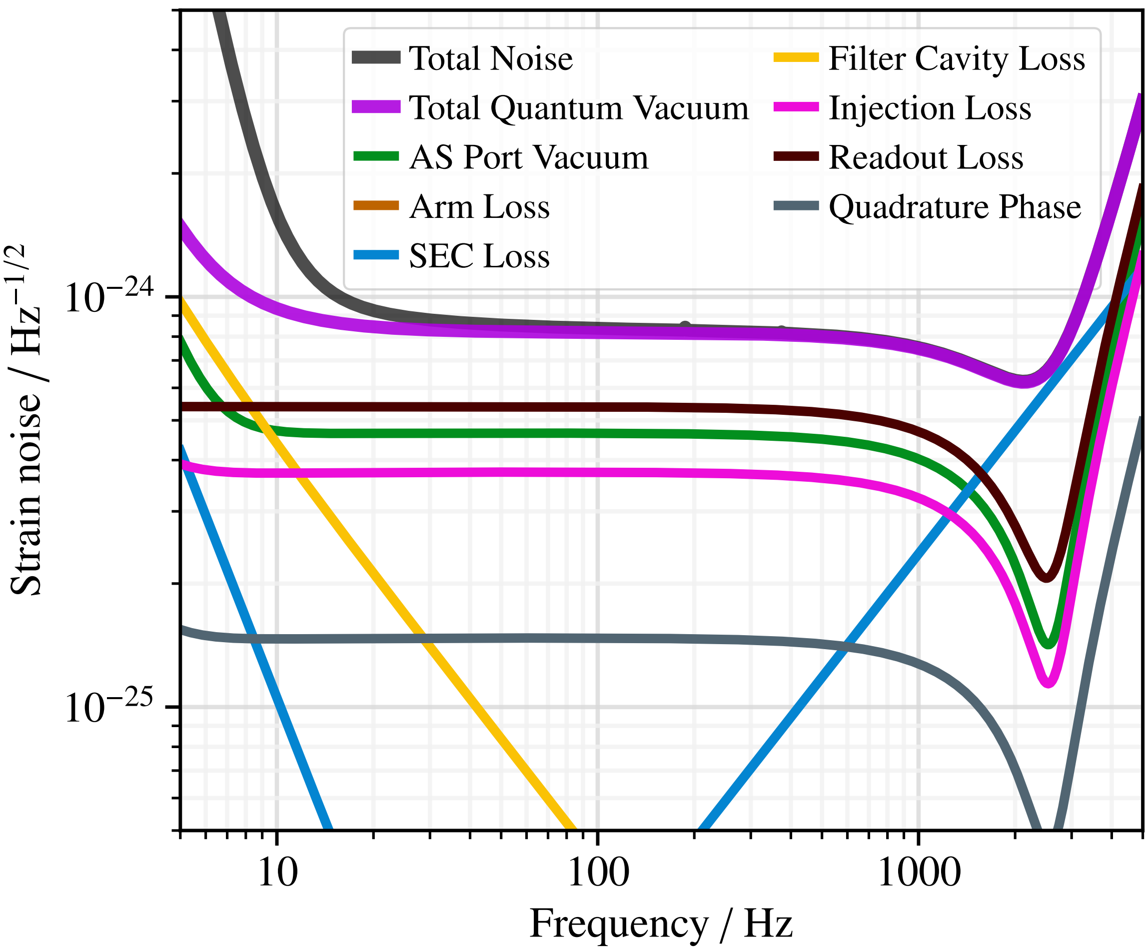

Figure 50: Quantum noise contributions for the 20 km post merger tuned configuration. The total quantum noise (purple) is the sum of the fundamental quantum noise (green) and noises coming from various loss mechanisms and technical noises (other solid colored curves). The black curve is the total noise of the 20 km instrument with an signal extraction loss (SEC) of 500 ppm. The SEC limits the sensitivity and location of the high frequency resonant dip. A much lower SEC loss of 10 ppm is required to suppress its noise contribution below the readout losses in the 20 km postmerger optimized detector. This underscores the need for research into mitigating SEC losses.

high-resolution wavefront sensing [236, 237, 238, 239] and need to be corrected with the adaptive optics discussed above.

Quantum noise is particularly affected by the design of the arm and signal extraction cavities. As shown in Eq. 7.85,7.86, for a fixed arm length, the arm cavity finesse $\mathcal{F}$, the SEC length L_s, and the signal extraction mirror transmissivity T_s determine both the location and width of the resonant dip for the post-merger and tidally tuned configurations. Several considerations are important in choosing the finesse. First, SEC loss scales as $\sqrt{\mathcal{F}}$, and so choosing a small finesse directly lowers the high frequency noise. However, indirect effects limit how small $\mathcal{F}$ can be reduced. The power stored in the arm cavities is enhanced by a factor of $\mathcal{F}$. Therefore, for a fixed arm power, increasing $\mathcal{F}$ reduces the power traversing the input test mass and beamsplitter substrates, thus decreasing the power absorbed in these substrates and reducing the associated thermal effects. Furthermore, the coupling of noise from auxiliary degrees of freedom into the gravitational wave signal is suppressed by increasing $\mathcal{F}$. Pending further study, the preliminary Cosmic Explorer design uses the same value of $\mathcal{F} = 450$ as does LIGO. Note from Eq. 7.85 that increasing $\mathcal{F}$ also directly lowers the location of the resonant dip.

With the cavity finesse set, the SEC length determines the location of the resonant dip according to Eq. 7.85. The difficulty of matching the optical modes between the SEC and arm cavities, a source of SEC loss as discussed above, is increased as L_s is decreased. The optimal length is $L_\mathrm{s} = 34\,\mathrm{m}$ for the 20 km post-merger tuning, which is quite short — $L_\mathrm{s} = 55\,\mathrm{m}$ for LIGO and the mode matching problem is more difficult for Cosmic Explorer due to its larger beams required by its longer arms [240]. If the length of the SEC needs to be increased, the location of the resonant dip will be decreased with a corresponding reduction in post-merger sensitivity.

The non-quantum noises are not directly affected by the choice of tuning; however, most scale inversely with some power of the arm length [241, 47]. Indeed, one of the major technical advantages of the Cosmic Explorer design is that much of the increased sensitivity over the second generation detectors, in the mid to high frequencies, comes from increasing the arm length and does not rely significantly on reducing the displacement noises. The 40 km detector is clearly advantageous here and provides a larger margin of error than that of the 20 km detector in the event that some noises do not meet their projected sensitivities.

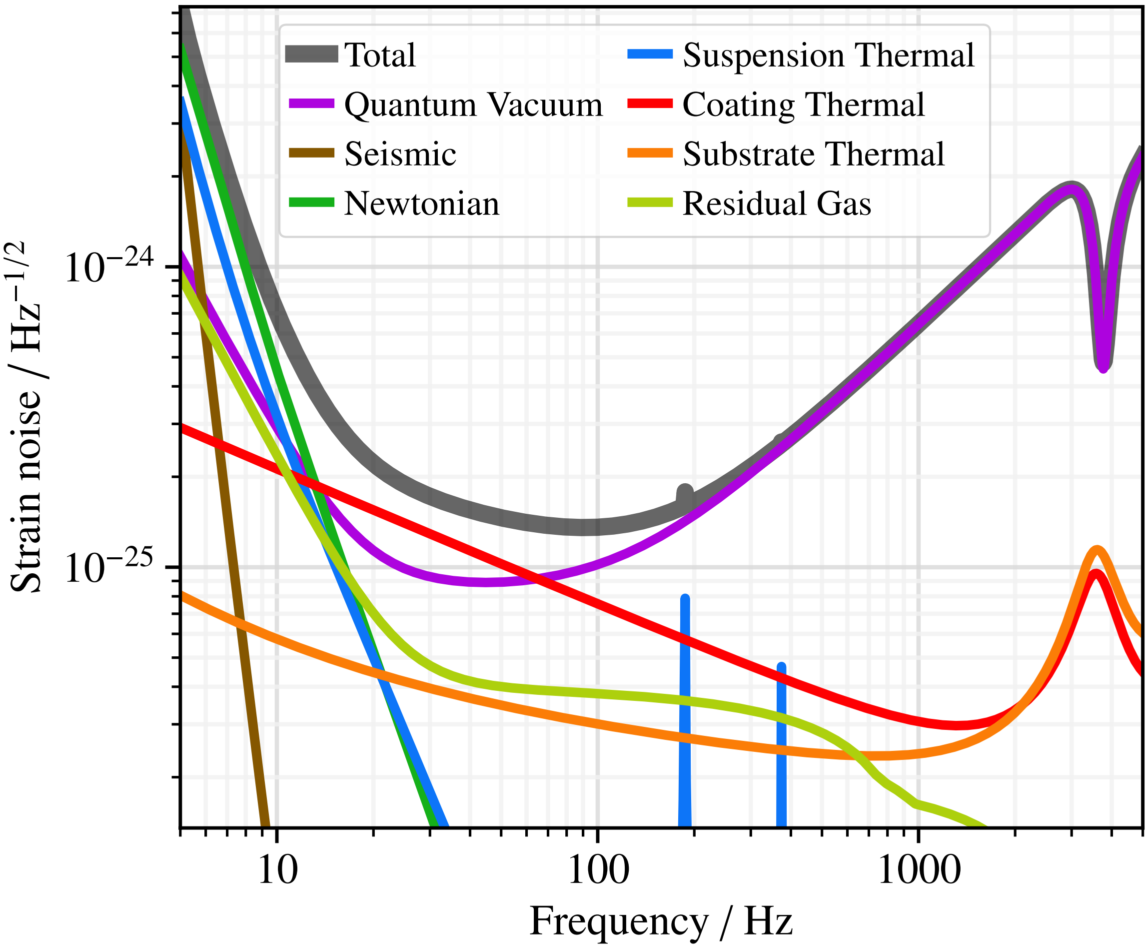

Figure 51: The noise budget of the low frequency tuned 40 km detector. We note that the low frequency sensitivity is limited by the thermal losses in the coatings of the test masses. With improved coatings with lower loss, the thermal noise can be mitigated or cryogenic technology proposed in the Voyager detector can be implemented to improve both the broadband and the low frequency tuned sensitivity of the 40 km detector.

The most significant of these noises above ∼20 Hz is thermal noise in the test mass coatings. This noise is significant for the compact binary tuning up to ∼50 Hz for the 40 km detector and up to ∼200 Hz for the 20 km detector. It is especially important for the low frequency tuned configurations in which quantum noise is reduced below this thermal noise, as is shown in Fig. 51. Reducing coating thermal noise is thus an important area of research for realizing the low frequency sensitivity. The Cosmic Explorer design assumes that the same optical coatings will be used as those used in the A+ upgrade to Advanced LIGO [242] which targets a factor of two decrease in coating thermal noise. Promising candidates have been identified [243], though these coatings have not yet been realized. Crystalline AlGaAs coatings are a particularly promising option on the Cosmic Explorer time scale [244, 245] which would allow Cosmic Explorer to surpass the low frequency sensitivity shown in Fig. 51, though much research is needed to make them a reality.

The many low-frequency noises particularly important for the science discussed in section §7.4 — most significantly Newtonian gravity gradients, seismic, and thermal noise from the test mass suspensions — and the technological advances necessary to meet the Cosmic Explorer targets are discussed in detail in [183].

An alternative technology using cryogenic silicon test masses and a 2 µm laser [181] has been identified as a potential upgrade to the baseline Cosmic Explorer technology of room-temperature fused silica test masses and a 1 µm laser and could also be used should thermal effects in the baseline technology prove intractable [47]. There are several new considerations with this technology [183]. First, the light traversing the substrates of the test masses experiences a phase noise due to the temperature dependence of the index of refraction which is a potentially significant low frequency noise source for the silicon technology, especially for the 20 km detector, due to silicon's larger thermorefractive coefficient and thermal conductivity. This thermorefractive noise is suppressed by a factor of $\sqrt{\mathcal{F}}$, however, which presents a trade off between low frequency sensitivity favoring large $\mathcal{F}$, and high frequency sensitivity favoring small $\mathcal{F}$ to minimize SEC loss. Second, the need to radiatively cool the cryogenic test masses imposes a strict heat budget [181] which adds an additional constraint on how low $\mathcal{F}$ can be made to limit the power absorbed in the optics. This makes developing low absorption and high quality silicon substrates and optical coatings for 2 µm light particularly important. Finally, manufacturing high quantum efficiency photodiodes for 2 µm light is a critical area of R&D necessary to minimize readout loss (c.f. Fig. 50) for this technology.

7.6 Discussions

Tests of General Relativity, such as polarization measurements and precise tests of high-spin black-holes, require multiple detectors [166, 167, 168]. Moreover, three or more third-generation gravitational-wave detectors are required to localize the source in the sky and to measure the source distance precise enough to confirm the sources at high redshifts [47, 251]. This suggests that two Cosmic Explorer facilities along with Einstein Telescope are necessary to achieve the key science goals of third-generation gravitational-wave detectors described here.

We assert that having at least one 40 km Cosmic Explorer detector is integral in achieving the key science goal of Cosmic Explorer as it outperforms a 20 km in all science goals other than the access to post-merger physics. Research into mitigating SEC losses is key to the success of the 20 km Cosmic Explorer detector to achieve the science goals that depend on achieving improved high-frequency sensitivity. [251] and the [47] assert that a network of third-generation detectors is indispensable. In particular, the precise determination of the source redshift and sky localization necessitates a network of three third-generation detectors — two Cosmic Explorer and Einstein Telescope. The key findings and benefits from tuning are summarized in the Table 9. Lastly, we note that we consider a handful of metrics to quantify the performance of different tuned configurations. We urge the broader gravitational wave astronomical community to perform in-depth analysis other than the SNR metric used in the study.

High-frequency tuning	• A 20 km post-merger optimized detector improves the chances of observing the post-merger signal, critical to the understanding of hot dense matter, see section §7.3.2. • The high frequency tuned CE (see section §7.3.2 and section §7.3.3) improves the ringdown signal-to-noise for lighter black-holes and for the discovery potential of exotic objects [246, 247, 248, 249, 250]. • A tidal optimized detector improves the measurement of tidal parameters of neutron stars at low redshifts, enabling an improved measurement of the cold equation of state using the loudest signals detected by Cosmic Explorer, see section §7.3.3.
Low frequency tuning	• Improves the detection prospects of heavier population of POP-III stars at high redshift, see section §7.4.1. • Improves the observational prospects of continuous waves sources below 300 Hz, see section §7.4.2. • Improves the measurement of tidal parameters of neutron stars at high redshifts, enabling an improved measurement as a function of the age of the neutron stars, see section §7.4.3. • Improves the ringdown signal-to-noise for heavier black-holes, see section §7.4.4.

Table 9: A summary of the key results in this work. A single 20 km Cosmic Explorer does not provide the ability to detect sources out to a redshift of 100, Fig. 43. A 40 km detector provides unparalleled signal-to-noise ratio, Fig. 47.

Acknowledgments

The authors would like to thank Reed Essick and Daniel Brown for a careful review of the manuscript. VS and SB thank the National Science Foundation for support through award PHY-1836702 and PHY-1912536. DD is supported by the National Science Foundation as part of the LIGO Laboratory, which operates under cooperative agreement PHY-1764464. KK and ME thank the National Science Foundation for support through award PHY-1836814. PL is supported by the Natural Sciences and Engineering Research Council of Canada (NSERC). EDH is supported by the MathWorks, Inc. JR thanks the National Science Foundation for support through awards PHY-1806962 and PHY-2110441. BSS thanks the National Science Foundation for support through awards PHY-2012083, PHY-1836779 and AST-2006384.

Bibliography

[1] Aaron Buikema, Craig Cahillane, GL Mansell, CD Blair, R Abbott, C Adams, RX Adhikari, A Ananyeva, S Appert, K Arai, et al. Sensitivity and performance of the advanced ligo detectors in the third observing run. *Physical Review D*, 102(6):062003, 2020.

[2] Terra Hardwick and Craig Ingram. aLIGO Optical Sensors Graphic (PSL 1064 nm beam). Technical Report LIGO-G1601619, LIGO, 2016.

[3] Aidan F. Brooks et al. Point absorbers in Advanced LIGO. *Appl. Opt.*, 60(13):4047, May 2021.

[4] Roland Schilling. Angular and frequency response of lisa. *Classical and Quantum Gravity*, 14(6):1513, 1997.

[5] Reed Essick, Salvatore Vitale, and Matthew Evans. Frequency-dependent responses in third generation gravitational-wave detectors. *Physical Review D*, 96(8):084004, 2017.

[6] Rhondale Tso, Davide Gerosa, and Yanbei Chen. Optimizing LIGO with LISA forewarnings to improve black-hole spectroscopy. *arXiv preprint arXiv:1807.00075*, 2018.

[7] Daniel M. Popper. Red Shift in the Spectrum of 40 Eridani B. *Astrophysical J.*, 120:316, September 1954.

[8] B. P. Abbott et al. Observation of gravitational waves from a binary black hole merger. *Physical review letters*, 116(6):61102, 2016.

[9] C. T. Bolton. Identification of Cygnus X-1 with HDE 226868. *Nature*, 235(5336):271–273, February 1972.

[10] B. Louise Webster and Paul Murdin. Cygnus X-1-a Spectroscopic Binary with a Heavy Companion ? *Nature*, 235(5332):37–38, January 1972.

[11] Peter R Saulson. *Fundamentals of interferometric gravitational wave detectors.* World Scientific, 1994.

[12] S M Aston, M A Barton, A S Bell, N Beveridge, B Bland, A J Brummitt, G Cagnoli, C A Cantley, L Carbone, A V Cumming, L Cunningham, R M Cutler, R J S Greenhalgh, G D Hammond, K Haughian, T M Hayler, A Heptonstall, J Heefner, D Hoyland, J Hough, R Jones, J S Kissel, R Kumar, N A Lockerbie, D Lodhia, I W Martin, P G Murray, J O'Dell, M V Plissi, S Reid, J Romie, N A Robertson, S Rowan, B Shapiro, C C Speake, K A Strain, K V Tokmakov, C Torrie, A A van Veggel, A Vecchio, and I Wilmut. Update on quadruple suspension design for advanced LIGO. *Classical and Quantum Gravity*, 29(23):235004, oct 2012.

[13] F Matichard, B Lantz, R Mittleman, K Mason, J Kissel, B Abbott, S Biscans, J McIver, R Abbott, S Abbott, E Allwine, S Barnum, J Birch, C Celerier, D Clark, D Coyne, D DeBra, R DeRosa, M Evans, S Foley, P Fritschel, J A Giaime, C Gray, G Grabeel, J Hanson, C Hardham, M Hillard, W Hua, C Kucharczyk, M Landry, A Le Roux, V Lhuillier, D Macleod, M Macinnis, R Mitchell, B O'Reilly, D Ottaway, H Paris, A Pele, M Puma, H Radkins, C Ramet, M Robinson, L Ruet, P Sarin, D Shoemaker, A Stein, J Thomas, M Vargas, K Venkateswara, J Warner, and S Wen. Seismic isolation of advanced LIGO: Review of strategy, instrumentation and performance. *Classical and Quantum Gravity*, 32(18):185003, aug 2015.

[14] Jennifer C. Driggers, Jan Harms, and Rana X. Adhikari. Subtraction of newtonian noise using optimized sensor arrays. *Phys. Rev. D*, 86:102001, Nov 2012.

[15] Jan Harms and Stefan Hild. Passive newtonian noise suppression for gravitational-wave observatories based on shaping of the local topography. *Classical and Quantum Gravity*, 31(18):185011, aug 2014.

[16] Peter R. Saulson. Thermal noise in mechanical experiments. *Phys. Rev. D*, 42:2437–2445, Oct 1990.

[17] John A. Sidles and Daniel Sigg. Optical torques in suspended Fabry Perot interferometers. *Physics Letters A*, 354(3):167–172, May 2006.

[18] Hang Yu. *Astrophysical signatures of neutron stars in compact binaries and experimental improvements on gravitational-wave detectors*. PhD thesis, Massachusetts Institute of Technology, 2019.

[19] Craig Cahillane. *Controlling and Calibrating Interferometric Gravitational Wave Detectors*. PhD thesis, California Institute of Technology, 2021.

[20] Nergis Mavalvala. *Alignment issues in laser interferometric gravitational-wave detectors*. PhD thesis, Massachusetts Institute of Technology, 1997.

[21] Dana Z. Anderson. Alignment of resonant optical cavities. *Appl. Opt.*, 23(17):2944–2949, Sep 1984.

[22] Euan Morrison, Brian J. Meers, David I. Robertson, and Henry Ward. Automatic alignment of optical interferometers. *Appl. Opt.*, 33(22):5041–5049, Aug 1994.

[23] Euan Morrison, Brian J. Meers, David I. Robertson, and Henry Ward. Experimental demonstration of an automatic alignment system for optical interferometers. *Appl. Opt.*, 33(22):5037–5040, Aug 1994.

[24] Peter Fritschel, Nergis Mavalvala, David Shoemaker, Daniel Sigg, Michael Zucker, and Gabriela González. Alignment of an interferometric gravitational wave detector. *Appl. Opt.*, 37(28):6734–6747, Oct 1998.

[25] Fabian Magaña-Sandoval, Thomas Vo, Daniel Vander-Hyde, JR Sanders, and Stefan W Ballmer. Sensing optical cavity mismatch with a mode-converter and quadrant photodiode. *Physical Review D*, 100(10):102001, 2019.

[26] J. Aasi et al. Advanced LIGO. *Classical and quantum gravity*, 32(7):74001, 2015.

[27] Koji Arai, Sam Barnum, Peter Fritschel, Jeff Lewis, and Sam Waldman. Output Mode Cleaner Design. Technical Report LIGO-T1000276, LIGO, 2010.

[28] Bram Slagmolen, Adam Mullavey, Rana Adhikari, and David McClelland. Tip-tilt mirror specifications and design. Technical Report LIGO-T0900096, LIGO, 2009.

[29] Bram Slagmolen, Adam Mullavey, John Miller, and David McClelland. aLIGO ISC Beam Steering - Tip-Tilt Mirror Design. Technical Report LIGO-T1000042, LIGO, 2010.

[30] Jay Heefner, Michael Meyer, Calum Torrie, Norna Robertson, Derek Bridges, Mark Barton, Janeen Romie, Jeffrey Kissel, Sam Barnum, and Jeffrey Lewis. OMC Suspension Final Design Document. Technical Report LIGO-T0900060, LIGO, 2009.

[31] N. Smith-Lefebvre, S. Ballmer, M. Evans, S. Waldman, K. Kawabe, V. Frolov, and N. Mavalvala. Optimal alignment sensing of a readout mode cleaner cavity. *Opt. Lett.*, 36(22):4365–4367, Nov 2011.

[32] Haocun YU. *Quantum Correlations in Advanced LIGO.* PhD thesis, Massachusetts Institute of Technology, 2020.

[33] Jay Heefner and Mohana Mageswaran. aLIGO HAM-A Coil Driver. Technical Report LIGO-D1100117, LIGO, 2011.

[34] Rich Abbott and Jeffrey Kissel. SUS HAM-A Coil Driver Design Study. Technical Report LIGO-T1200264, LIGO, 2012.

[35] Jeff Kissel. LIGO DAC Noise Models. Technical Report LIGO-E1800243, LIGO, 2018.

[36] F. Acernese et al. Advanced Virgo: a second-generation interferometric gravitational wave detector. *Classical and Quantum Gravity*, 32(2):24001, 2014.

[37] B P Abbott et al. GWTC-1: A Gravitational-Wave Transient Catalog of Compact Binary Mergers Observed by LIGO and Virgo during the First and Second Observing Runs. *Phys. Rev. X*, 9(3):31040, sep 2019.

[38] R. Abbott et al. GWTC-2: Compact Binary Coalescences Observed by LIGO and Virgo During the First Half of the Third Observing Run, 2020.

[39] R Abbott, TD Abbott, F Acernese, K Ackley, C Adams, N Adhikari, RX Adhikari, VB Adya, C Affeldt, D Agarwal, et al. Gwtc-3: Compact binary coalescences observed by ligo and virgo during the second part of the third observing run. *arXiv preprint arXiv:2111.03606*, 2021.

[40] B. P. Abbott et al. GW170817: Observation of Gravitational Waves from a Binary Neutron Star Inspiral. *Phys. Rev. Lett.*, 119(16):161101, oct 2017.

[41] B. P. Abbott et al. GW190425: Observation of a compact binary coalescence with total mass $\sim 3.4\ \mathrm{M}_{\odot}$. *The Astrophysical Journal*, 892(1):L3, March 2020.

[42] R. Abbott et al. Observation of gravitational waves from two neutron star–black hole coalescences. *The Astrophysical Journal Letters*, 915(1):L5, jun 2021.

[43] M. Tse et al. Quantum-enhanced advanced ligo detectors in the era of gravitational-wave astronomy. *Phys. Rev. Lett.*, 123:231107, Dec 2019.

[44] L. McCuller, S. E. Dwyer, A. C. Green, Haocun Yu, K. Kuns, L. Barsotti, C. D. Blair, D. D. Brown, A. Effler, M. Evans, A. Fernandez-Galiana, P. Fritschel, V. V. Frolov, N. Kijbunchoo, G. L. Mansell, F. Matichard, N. Mavalvala, D. E. McClelland, T. McRae, A. Mullavey, D. Sigg, B. J. J. Slagmolen, M. Tse, T. Vo, R. L. Ward, C. Whittle, R. Abbott, C. Adams, R. X. Adhikari, A. Ananyeva, S. Appert, K. Arai, J. S. Areeda, Y. Asali, S. M. Aston, C. Austin, A. M. Baer, M. Ball, S. W. Ballmer, S. Banagiri, D. Barker, J. Bartlett, B. K. Berger, J. Betzwieser, D. Bhattacharjee, G. Billingsley, S. Biscans, R. M. Blair, N. Bode, P. Booker, R. Bork, A. Bramley, A. F. Brooks, A. Buikema, C. Cahillane, K. C. Cannon, X. Chen, A. A. Ciobanu, F. Clara, C. M. Compton, S. J. Cooper, K. R. Corley, S. T. Countryman, P. B. Covas, D. C. Coyne, L. E. H. Datrier, D. Davis, C. Di Fronzo, K. L. Dooley, J. C. Driggers, T. Etzel, T. M. Evans, J. Feicht, P. Fulda, M. Fyffe, J. A. Giaime, K. D. Giardina, P. Godwin, E. Goetz, S. Gras, C. Gray, R. Gray, E. K. Gustafson, R. Gustafson, J. Hanks, J. Hanson, T. Hardwick, R. K. Hasskew, M. C. Heintze, A. F. Helmling-Cornell, N. A. Holland, J. D. Jones, S. Kandhasamy, S. Karki, M. Kasprzack, K. Kawabe, P. J. King, J. S. Kissel, Rahul Kumar, M. Landry, B. B. Lane, B. Lantz, M. Laxen, Y. K. Lecoeuche, J. Leviton, J. Liu, M. Lormand, A. P. Lundgren, R. Macas,

M. MacInnis, D. M. Macleod, S. Márka, Z. Márka, D. V. Martynov, K. Mason, T. J. Massinger, R. McCarthy, S. McCormick, J. McIver, G. Mendell, K. Merfeld, E. L. Merilh, F. Meylahn, T. Mistry, R. Mittleman, G. Moreno, C. M. Mow-Lowry, S. Mozzon, T. J. N. Nelson, P. Nguyen, L. K. Nuttall, J. Oberling, Richard J. Oram, C. Osthelder, D. J. Ottaway, H. Overmier, J. R. Palamos, W. Parker, E. Payne, A. Pele, R. Penhorwood, C. J. Perez, M. Pirello, H. Radkins, K. E. Ramirez, J. W. Richardson, K. Riles, N. A. Robertson, J. G. Rollins, C. L. Romel, J. H. Romie, M. P. Ross, K. Ryan, T. Sadecki, E. J. Sanchez, L. E. Sanchez, T. R. Saravanan, R. L. Savage, D. Schaetzl, R. Schnabel, R. M. S. Schofield, E. Schwartz, D. Sellers, T. Shaffer, J. R. Smith, S. Soni, B. Sorazu, A. P. Spencer, K. A. Strain, L. Sun, M. J. Szczepańczyk, M. Thomas, P. Thomas, K. A. Thorne, K. Toland, C. I. Torrie, G. Traylor, A. L. Urban, G. Vajente, G. Valdes, D. C. Vander-Hyde, P. J. Veitch, K. Venkateswara, G. Venugopalan, A. D. Viets, C. Vorvick, M. Wade, J. Warner, B. Weaver, R. Weiss, B. Willke, C. C. Wipf, L. Xiao, H. Yamamoto, Hang Yu, L. Zhang, M. E. Zucker, and J. Zweizig. Ligo's quantum response to squeezed states. *Phys. Rev. D*, 104:062006, Sep 2021.

[45] John Miller, Lisa Barsotti, Salvatore Vitale, Peter Fritschel, Matthew Evans, and Daniel Sigg. Prospects for doubling the range of Advanced LIGO. *Phys. Rev. D*, 91:062005, Mar 2015.

[46] L Barsotti, L Mcculler, M Evans, and P Fritschel. The A+ design curve. Technical Report LIGO-T1800042, LIGO, 2018.

[47] Matthew Evans et al. A horizon study for cosmic explorer: Science, observatories, and community. *arXiv preprint arXiv:2109.09882*, 2021.

[48] François Roddier. *The design of an adaptive optics system*, chapter 3-7, pages 23–168. Cambridge University Press, 1999.

[49] Andrei Tokovinin, Sandrine Thomas, and Gleb Vdovin. Using 50-mm electrostatic membrane deformable mirror in astronomical adaptive optics. In *Advancements in Adaptive Optics*, volume 5490, pages 580–585. International Society for Optics and Photonics, 2004.

[50] Peter Rausch, Sven Verpoort, and Ulrich Wittrock. Unimorph deformable mirror for space telescopes: environmental testing. *Optics express*, 24(2):1528–1542, 2016.

[51] Huy Tuong Cao, Sebastian W. S. Ng, Minkyun Noh, Aidan Brooks, Fabrice Matichard, and Peter J. Veitch. Enhancing the dynamic range of deformable mirrors with compression bias. *Opt. Express*, 28(26):38480–38490, Dec 2020.

[52] L Mcculler and L Barsotti. Design Requirement Document of the A+ filter cavity and relay optics for frequency dependent squeezing. Technical Report LIGO-T1800447, LIGO, 2018.

[53] KA Strain and BN Shapiro. Damping and local control of mirror suspensions for laser interferometric gravitational wave detectors. *Review of Scientific Instruments*, 83(4):044501, 2012.

[54] M. Noh et al. Active optical mode matching for the quantum squeezing cavities and upcoming ligo upgrades. In *Proceedings of the 2020 ASPE Spring Topical Meeting on Design and Control of Precision Mechatronic Systems*, pages 110–112, United States, May 2020. American Society for Precision Engineering.

[55] GariLynn Billingsley, Hikoaki Yamamoto, and Liyuan Zhang. Characterization of the advanced ligo core optics. Technical Report P1700029, California Institute of Technology, 2017.

[56] Wenxuan Jia. Title of wen's paper, 2021. In preparation.

[57] BP Abbott, Richard Abbott, TD Abbott, S Abraham, F Acernese, K Ackley, C Adams, RX Adhikari, VB Adya, C Affeldt, et al. Gwtc-1: a gravitational-wave transient catalog of compact binary mergers observed by ligo and virgo during the first and second observing runs. *Physical Review X*, 9(3):031040, 2019.

[58] R Abbott, TD Abbott, S Abraham, F Acernese, K Ackley, A Adams, C Adams, RX Adhikari, VB Adya, C Affeldt, et al. Gwtc-2: Compact binary coalescences observed by ligo and virgo during the first half of the third observing run. *arXiv preprint arXiv:2010.14527*, 2020.

[59] Eric D Black. An introduction to pound–drever–hall laser frequency stabilization. *American journal of physics*, 69(1):79–87, 2001.

[60] Guido Mueller, Qi-ze Shu, Rana Adhikari, DB Tanner, David Reitze, Daniel Sigg, Nergis Mavalvala, and Jordan Camp. Determination and optimization of mode matching into optical cavities by heterodyne detection. *Optics letters*, 25(4):266–268, 2000.

[61] John Miller and Matthew Evans. Length control of an optical resonator using second-order transverse modes. *Optics letters*, 39(8):2495–2498, 2014.

[62] P. Fulda, D. Voss, C. Mueller, L. F. Ortega, G. Ciani, G. Mueller, and D. B. Tanner. Alignment sensing for optical cavities using radio-frequency jitter modulation. *Appl. Opt.*, 56(13):3879–3888, May 2017.

[63] Keisuke Goda, David Ottaway, Blair Connelly, Rana Adhikari, Nergis Mavalvala, and Andri Gretarsson. Frequency-resolving spatiotemporal wave-front sensor. *Opt. Lett.*, 29(13):1452–1454, Jul 2004.

[64] L Van der Schaaf, K Agatsuma, Martin Van Beuzekom, M Gebyehu, and J Van Den Brand. Advanced virgo phase cameras. In *Journal of Physics: Conference Series*, volume 718, page 072008. IOP Publishing, 2016.

[65] Kazuhiro Agatsuma, Laura van der Schaaf, Martin Van Beuzekom, David Rabeling, and Jo van Den Brand. High-performance phase camera as a frequency selective laser wavefront sensor for gravitational wave detectors. *Optics express*, 27(13):18533–18548, 2019.

[66] Huy Tuong Cao, Daniel D. Brown, Peter J. Veitch, and David J. Ottaway. Optical lock-in camera for gravitational wave detectors. *Opt. Express*, 28(10):14405–14413, May 2020.

[67] Daniel D Brown, Huy Tuong Cao, Alexei Ciobanu, Peter Veitch, and David Ottaway. Differential wavefront sensing and control using radio-frequency optical demodulation. *arXiv preprint arXiv:2103.01034*, 2021.

[68] *Demodulation pixels in CCD and CMOS technologies for time-of-flight ranging*, volume 3965, 2000.

[69] S. Shrestha, F. Heide, W. Heidrich, and G. Wetzstein. Computational imaging with multi-camera time-of-flight systems. *ACM Trans. Graph. (SIGGRAPH)*, 2016.

[70] Texas Instruments. *Voxel Viewer: Quick Start Guide*, 9 2015. Rev. A.

[71] Texas Instruments. *Introduction to the Time-of-Flight (ToF) System Design*, 5 2014. Rev. D.

[72] Rudolf Schwarte, Zhanping Xu, Horst-Guenther Heinol, Joachim Olk, Ruediger Klein, Bernd Buxbaum, Helmut Fischer, and Juergen Schulte. New electro-optical mixing and correlating sensor: facilities and applications of the photonic mixer device (pmd). In *Sensors, Sensor Systems, and Sensor Data Processing*, volume 3100, pages 245–253. International Society for Optics and Photonics, 1997.

[73] Robert Lange. *3D time-of-flight distance measurement with custom solid-state image sensors in CMOS/CCD-technology*. PhD thesis, Universität Siegen, 2000.

[74] Texas Instruments. *OPT8241 3D Time-of-Flight Sensor*, 6 2015. Rev. B.

[75] Yoichi Aso, Yuta Michimura, Kentaro Somiya, Masaki Ando, Osamu Miyakawa, Takanori Sekiguchi, Daisuke Tatsumi, Hiroaki Yamamoto, Kagra Collaboration, et al. Interferometer design of the kagra gravitational wave detector. *Physical Review D*, 88(4):043007, 2013.

[76] IEEE. Ieee standard definitions of physical quantities for fundamental frequency and time metrology-random instabilities. *IEEE Std 1139-1999*, pages 1–40, 1999.

[77] Mihail Georgiev, Robert Bregović, and Atanas Gotchev. Fixed-pattern noise modeling and removal in time-of-flight sensing. *IEEE Transactions on Instrumentation and Measurement*, 65(4):808–820, 2015.

[78] Vlad Toronov, Enrico D'Amico, Dennis Hueber, Enrico Gratton, Beniamino Barbieri, and Andrew Webb. Optimization of the signal-to-noise ratio of frequency-domain instrumentation for near-infrared spectro-imaging of the human brain. *Optics Express*, 11(21):2717–2729, 2003.

[79] Holger Rapp, Mario Frank, Fred A Hamprecht, and B Jahne. A theoretical and experimental investigation of the systematic errors and statistical uncertainties of time-of-flight-cameras. *International Journal of Intelligent Systems Technologies and Applications*, 5(3-4):402–413, 2008.

[80] Miguel H. Conde. *Compressive Sensing for the Photonic Mixer Device*. Springer Vieweg, 2017.

[81] Thomas V Vo. *Adaptive Mode Matching in Advanced LIGO and Beyond*. PhD thesis, Syracuse University, 2019.

[82] Aidan F. Brooks, Thu-Lan Kelly, Peter J. Veitch, and Jesper Munch. Ultra-sensitive wavefront measurement using a hartmann sensor. *Opt. Express*, 15(16):10370–10375, Aug 2007.

[83] M. Granata, C. Buy, R. Ward, and M. Barsuglia. Higher-order laguerre-gauss mode generation and interferometry for gravitational wave detectors. *Phys. Rev. Lett.*, 105:231102, Nov 2010.

[84] Ludovico Carbone, Paul Fulda, Charlotte Bond, Frank Brueckner, Daniel Brown, Mengyao Wang, Deepali Lodhia, Rebecca Palmer, and Andreas Freise. The generation of higher-order laguerre-gauss optical beams for high-precision interferometry. *JoVE (Journal of Visualized Experiments)*, (78):e50564, 2013.

[85] Evan D Hall, Kevin Kuns, Joshua R Smith, Yuntao Bai, Christopher Wipf, Sebastien Biscans, Rana X Adhikari, Koji Arai, Stefan Ballmer, Lisa Barsotti, et al. Gravitational-wave physics with cosmic explorer: limits to low-frequency sensitivity. *arXiv preprint arXiv:2012.03608*, 2020.

[86] M Punturo, M Abernathy, F Acernese, B Allen, Nils Andersson, K Arun, F Barone, B Barr, M Barsuglia, M Beker, et al. The einstein telescope: a third-generation gravitational wave observatory. *Classical and Quantum Gravity*, 27(19):194002, 2010.

[87] Varun Srivastava, Kevin Kuns, Evan Hall, Stefan Ballmer, and Salvatore Vitale. Cehs: Metric for black holes and neutron stars throughout cosmic time, and

testing general relativity. Technical Report CE-T2100009, Cosmic Explorer, 2021.

[88] Varun Srivastava, Philippe Landry, Stefan Ballmer, and Jocelyn Read. Understanding dynamics of dense matter through observation of astrophysical populations. Technical Report CE-T2100010, Cosmic Explorer, 2021.

[89] Junaid Aasi, BP Abbott, Richard Abbott, Thomas Abbott, MR Abernathy, Kendall Ackley, Carl Adams, Thomas Adams, Paolo Addesso, RX Adhikari, et al. Advanced ligo. *Classical and quantum gravity*, 32(7):074001, 2015.

[90] F Acernese, M Agathos, K Agatsuma, D Aisa, N Allemandou, A Allocca, J Amarni, P Astone, G Balestri, G Ballardin, et al. Advanced virgo: a second-generation interferometric gravitational wave detector. *Classical and Quantum Gravity*, 32(2):024001, 2014.

[91] Benjamin P Abbott, Richard Abbott, TD Abbott, MR Abernathy, Fausto Acernese, Kendall Ackley, Carl Adams, Thomas Adams, Paolo Addesso, RX Adhikari, et al. Observation of gravitational waves from a binary black hole merger. *Physical review letters*, 116(6):061102, 2016.

[92] Benjamin P Abbott, R Abbott, TD Abbott, MR Abernathy, F Acernese, K Ackley, C Adams, T Adams, P Addesso, RX Adhikari, et al. Gw151226: Observation of gravitational waves from a 22-solar-mass binary black hole coalescence. *Physical review letters*, 116(24):241103, 2016.

[93] Benjamin P Abbott, Rich Abbott, TD Abbott, Fausto Acernese, Kendall Ackley, Carl Adams, Thomas Adams, Paolo Addesso, RX Adhikari, VB Adya, et al. Gw170817: observation of gravitational waves from a binary neutron star inspiral. *Physical Review Letters*, 119(16):161101, 2017.

[94] Tejaswi Venumadhav, Barak Zackay, Javier Roulet, Liang Dai, and Matias Zaldarriaga. New binary black hole mergers in the second observing run of advanced ligo and advanced virgo. *arXiv preprint arXiv:1904.07214*, 2019.

[95] Alexander H Nitz, Collin Capano, Alex B Nielsen, Steven Reyes, Rebecca White, Duncan A Brown, and Badri Krishnan. 1-ogc: The first open

gravitational-wave catalog of binary mergers from analysis of public advanced ligo data. *The Astrophysical Journal*, 872(2):195, 2019.

[96] Alejandro Torres-Forné, Pablo Cerdá-Durán, Martin Obergaulinger, Bernhard Muller, and José A Font. Universal relations for gravitational-wave asteroseismology of proto-neutron stars. *arXiv preprint arXiv:1902.10048*, 2019.

[97] Sherwood Richers, Christian D Ott, Ernazar Abdikamalov, Evan O'Connor, and Chris Sullivan. Equation of state effects on gravitational waves from rotating core collapse. *Physical Review D*, 95(6):063019, 2017.

[98] Ernazar Abdikamalov, Sarah Gossan, Alexandra M DeMaio, and Christian D Ott. Measuring the angular momentum distribution in core-collapse supernova progenitors with gravitational waves. *Physical Review D*, 90(4):044001, 2014.

[99] Benjamin P Abbott, Richard Abbott, TD Abbott, MR Abernathy, F Acernese, K Ackley, C Adams, T Adams, P Addesso, RX Adhikari, et al. First targeted search for gravitational-wave bursts from core-collapse supernovae in data of first-generation laser interferometer detectors. *Physical Review D*, 94(10):102001, 2016.

[100] BP Abbott, R Abbott, TD Abbott, S Abraham, F Acernese, K Ackley, C Adams, RX Adhikari, VB Adya, C Affeldt, et al. All-sky search for short gravitational-wave bursts in the second advanced ligo and advanced virgo run. *arXiv preprint arXiv:1905.03457*, 2019.

[101] S E Gossan, P Sutton, A Stuver, M Zanolin, K Gill, and C D Ott. Observing gravitational waves from core-collapse supernovae in the advanced detector era. *Phys. Rev. D*, 93(4):42002, feb 2016.

[102] Weidong Li, Jesse Leaman, Ryan Chornock, Alexei V Filippenko, Dovi Poznanski, Mohan Ganeshalingam, Xiaofeng Wang, Maryam Modjaz, Saurabh Jha, Ryan J Foley, and Others. Nearby supernova rates from the Lick Observatory Supernova Search–II. The observed luminosity functions and fractions of supernovae in a complete sample. *Monthly Notices of the Royal Astronomical Society*, 412(3):1441–1472, 2011.

[103] Weidong Li, Ryan Chornock, Jesse Leaman, Alexei V Filippenko, Dovi Poznanski, Xiaofeng Wang, Mohan Ganeshalingam, and Filippo Mannucci. Nearby supernova rates from the Lick Observatory Supernova Search–III. The rate–size relation, and the rates as a function of galaxy Hubble type and colour. *Monthly Notices of the Royal Astronomical Society*, 412(3):1473–1507, 2011.

[104] ML Graham, DJ Sand, CJ Bildfell, CJ Pritchet, D Zaritsky, H Hoekstra, DW Just, S Herbert-Fort, S Sivanandam, and RJ Foley. The type ii supernova rate in z 0.1 galaxy clusters from the multi-epoch nearby cluster survey. *The Astrophysical Journal*, 753(1):68, 2012.

[105] Lin Xiao and JJ Eldridge. Core-collapse supernova rate synthesis within 11 mpc. *Monthly Notices of the Royal Astronomical Society*, 452(3):2597–2605, 2015.

[106] D. Radice, V. Morozova, A. Burrows, D. Vartanyan, and H. Nagakura. Characterizing the Gravitational Wave Signal from Core-collapse Supernovae. *Astrophysical J.*, 876:L9, May 2019.

[107] J. W. Murphy, C. D. Ott, and A. Burrows. A Model for Gravitational Wave Emission from Neutrino-Driven Core-Collapse Supernovae. *Astrophysical J.*, 707:1173–1190, December 2009.

[108] V. Morozova, D. Radice, A. Burrows, and D. Vartanyan. The Gravitational Wave Signal from Core-collapse Supernovae. *Astrophysical J.*, 861:10, July 2018.

[109] Bernhard Müller, Hans-Thomas Janka, and Andreas Marek. A NEW MULTIDIMENSIONAL GENERAL RELATIVISTIC NEUTRINO HYDRODYNAMICS CODE OF CORE-COLLAPSE SUPERNOVAE. III. GRAVITATIONAL WAVE SIGNALS FROM SUPERNOVA EXPLOSION MODELS. *The Astrophysical Journal*, 766(1):43, mar 2013.

[110] Pablo Cerdá-Durán, Nicolas DeBrye, Miguel A. Aloy, José A. Font, and Martin Obergaulinger. GRAVITATIONAL WAVE SIGNATURES IN BLACK HOLE FORMING CORE COLLAPSE. *The Astrophysical Journal*, 779(2):L18, dec 2013.

[111] T. Kuroda, T. Takiwaki, and K. Kotake. Gravitational wave signatures from low-mode spiral instabilities in rapidly rotating supernova cores. *Phys. Rev. D*, 89(4):044011, February 2014.

[112] H. Andresen, B. Müller, E. Müller, and H.-T. Janka. Gravitational wave signals from 3D neutrino hydrodynamics simulations of core-collapse supernovae. *Mon. Not. Roy. Astr. Soc.*, 468:2032–2051, June 2017.

[113] K. N. Yakunin, A. Mezzacappa, P. Marronetti, E. J. Lentz, S. W. Bruenn, W. R. Hix, O. E. B. Messer, E. Endeve, J. M. Blondin, and J. A. Harris. The Gravitational Wave Signal of a Core Collapse Supernova Explosion of a 15M$_\odot$ Star. *ArXiv e-prints*, January 2017.

[114] Takami Kuroda, Kei Kotake, Kazuhiro Hayama, and Tomoya Takiwaki. Correlated Signatures of Gravitational-Wave and Neutrino Emission in Three-Dimensional General-Relativistic Core-Collapse Supernova Simulations. *Astrophys. J.*, 851(1):62, 2017.

[115] Jade Powell and Bernhard Müller. Gravitational wave emission from 3d explosion models of core-collapse supernovae with low and normal explosion energies. *arXiv preprint arXiv:1812.05738*, 2018.

[116] John M Scalo. The stellar initial mass function. *Fundamentals of cosmic physics*, 11:1–278, 1986.

[117] Scott M Adams, CS Kochanek, John F Beacom, Mark R Vagins, and KZ Stanek. Observing the next galactic supernova. *The Astrophysical Journal*, 778(2):164, 2013.

[118] E Cappellaro, M Turatto, D Yu Tsvetkov, OS Bartunov, C Pollas, R Evans, and M Hamuy. The rate of supernovae from the combined sample of five searches. *Astron. Astrophys*, 322:431–441, 1997.

[119] FX Timmes and SE Woosley. Gamma-ray line signals from 26al and 60fe in the galaxies of the local group. *The Astrophysical Journal Letters*, 481(2):L81, 1997.

[120] Michael J Pierce, Douglas L Welch, Robert D McClure, Sidney van den Bergh, Renè Racine, and Peter B Stetson. The hubble constant and virgo cluster distance from observations of cepheid variables. *Nature*, 371(6496):385, 1994.

[121] GA Tammann, W Loeffler, and A Schroeder. The galactic supernova rate. *The Astrophysical Journal Supplement Series*, 92:487–493, 1994.

[122] Massimo Capaccioli, Massimo Della Valle, Mauro D'Onofrio, and Leonida Rosino. Properties of the nova population in m31. *The Astronomical Journal*, 97:1622–1633, 1989.

[123] Wendy L Freedman and Barry F Madore. An empirical test for the metallicity sensitivity of the cepheid period-luminosity relation. *The Astrophysical Journal*, 365:186–194, 1990.

[124] S Mattila and WPS Meikle. Supernovae in the nuclear regions of starburst galaxies. *Monthly Notices of the Royal Astronomical Society*, 324(2):325–342, 2001.

[125] M. T. Botticella, S. J. Smartt, R. C. Kennicutt, E. Cappellaro, M. Sereno, and J. C. Lee. A comparison between star formation rate diagnostics and rate of core collapse supernovae within 11 Mpc. *Astron. and Astrophys.*, 537:A132, Jan 2012.

[126] S Mattila, Tomas Dahlén, Andreas Efstathiou, Erkki Kankare, Jens Melinder, Almudena Alonso-Herrero, MÁ Pérez-Torres, S Ryder, P Väisänen, and Göran Östlin. Core-collapse supernovae missed by optical surveys. *The Astrophysical Journal*, 756(2):111, 2012.

[127] Matthew D Kistler, Hasan Yüksel, Shin'ichiro Ando, John F Beacom, and Yoichiro Suzuki. Core-collapse astrophysics with a five-megaton neutrino detector. *Physical Review D*, 83(12):123008, 2011.

[128] Sidney van den Bergh and Gustav A Tammann. Galactic and extragalactic supernova rates. *Annual Review of Astronomy and Astrophysics*, 29(1):363–407, 1991.

[129] Viktoriya Morozova, David Radice, Adam Burrows, and David Vartanyan. The Gravitational Wave Signal from Core-collapse Supernovae. *The Astrophysical Journal*, 861(1):10, jun 2018.

[130] Lee Samuel Finn and David F Chernoff. Observing binary inspiral in gravitational radiation: One interferometer. *Physical Review D*, 47(6):2198, 1993.

[131] Benjamin P Abbott, R Abbott, TD Abbott, MR Abernathy, F Acernese, K Ackley, C Adams, T Adams, P Addesso, RX Adhikari, et al. All-sky search for short gravitational-wave bursts in the first advanced ligo run. *Physical Review D*, 95(4):042003, 2017.

[132] S Klimenko, G Vedovato, M Drago, F Salemi, V Tiwari, GA Prodi, C Lazzaro, K Ackley, S Tiwari, CF Da Silva, et al. Method for detection and reconstruction of gravitational wave transients with networks of advanced detectors. *Physical Review D*, 93(4):042004, 2016.

[133] Ryan Lynch, Salvatore Vitale, Reed Essick, Erik Katsavounidis, and Florent Robinet. Information-theoretic approach to the gravitational-wave burst detection problem. *Physical Review D*, 95(10):104046, 2017.

[134] Warren G Anderson, Patrick R Brady, Jolien DE Creighton, and Eanna E Flanagan. Excess power statistic for detection of burst sources of gravitational radiation. *Physical Review D*, 63(4):042003, 2001.

[135] Benjamin P Abbott, R Abbott, TD Abbott, MR Abernathy, F Acernese, K Ackley, C Adams, T Adams, P Addesso, RX Adhikari, et al. Observing gravitational-wave transient gw150914 with minimal assumptions. *Physical Review D*, 93(12):122004, 2016.

[136] LIGO Scientific Collaboration. LIGO Algorithm Library - LALSuite. free software (GPL), 2018.

[137] The LIGO Scientific Collaboration. Gravitational Wave Interferometer Noise Calculator.

[138] Adam Burrows, David Radice, and David Vartanyan. Three-dimensional supernova explosion simulations of 9-, 10-, 11-, 12-, and 13-M$_{odot}$ stars. *Monthly Notices of the Royal Astronomical Society*, 485(3):3153–3168, 2019.

[139] Alessandra Buonanno, Yanbei Chen, and Nergis Mavalvala. Quantum noise in laser-interferometer gravitational-wave detectors with a heterodyne readout scheme. *Physical Review D*, 67(12):122005, 2003.

[140] Benjamin P Abbott, R Abbott, T D Abbott, M R Abernathy, K Ackley, C Adams, P Addesso, R X Adhikari, V B Adya, C Affeldt, and Others. Exploring the sensitivity of next generation gravitational wave detectors. *Classical and Quantum Gravity*, 34(4):44001, 2017.

[141] Alessandra Buonanno and Yanbei Chen. Improving the sensitivity to gravitational-wave sources by modifying the input-output optics of advanced interferometers. *Physical Review D*, 69(10):102004, 2004.

[142] Denis Martynov, Haixing Miao, Huan Yang, Francisco Hernandez Vivanco, Eric Thrane, Rory Smith, Paul Lasky, William E East, Rana Adhikari, Andreas Bauswein, and Others. Exploring the sensitivity of gravitational wave detectors to neutron star physics. *arXiv preprint arXiv:1901.03885*, 2019.

[143] W. K. Hastings. Monte carlo sampling methods using markov chains and their applications. *Biometrika*, 57(1):97–109, 1970.

[144] James Kennedy and Russell Eberhart. Particle swarm optimization. *Proceedings of ICNN'95 - International Conference on Neural Networks*, pages 1942–1948, 1995.

[145] Sheila Dwyer, Daniel Sigg, Stefan W Ballmer, Lisa Barsotti, Nergis Mavalvala, and Matthew Evans. Gravitational wave detector with cosmological reach. *Physical Review D*, 91(8):082001, 2015.

[146] Haixing Miao, Huan Yang, and Denis Martynov. Towards the design of gravitational-wave detectors for probing neutron-star physics. *Phys. Rev. D*, 98(4):44044, aug 2018.

[147] Karsten Danzmann, LISA Study Team, and Others. LISA: Laser interferometer space antenna for gravitational wave measurements. *Classical and Quantum Gravity*, 13(11A):A247, 1996.

[148] Andreas Bauswein, Niels-Uwe F Bastian, David B Blaschke, Katerina Chatziioannou, James A Clark, Tobias Fischer, and Micaela Oertel. Identifying a first-order phase transition in neutron-star mergers through gravitational waves. *Physical review letters*, 122(6):061102, 2019.

[149] Sukanta Bose, Kabir Chakravarti, Luciano Rezzolla, BS Sathyaprakash, and Kentaro Takami. Neutron-star radius from a population of binary neutron star mergers. *Physical review letters*, 120(3):031102, 2018.

[150] Kentaro Takami, Luciano Rezzolla, and Luca Baiotti. Constraining the equation of state of neutron stars from binary mergers. *Physical Review Letters*, 113(9):091104, 2014.

[151] Harald Dimmelmeier, Christian D. Ott, Andreas Marek, and H.-Thomas Janka. Gravitational wave burst signal from core collapse of rotating stars. *Phys. Rev. D*, 78:064056, Sep 2008.

[152] A Burrows, L Dessart, E Livne, C.˜D. Ott, and J Murphy. Simulations of Magnetically Driven Supernova and Hypernova Explosions in the Context of Rapid Rotation. *Astrophysical J.*, 664:416–434, jul 2007.

[153] A Heger, S E Woosley, and H C Spruit. Presupernova Evolution of Differentially Rotating Massive Stars Including Magnetic Fields. *The Astrophysical Journal*, 626(1):350–363, jun 2005.

[154] A. Marek, H. T. Janka, and E. Müller. Equation-of-state dependent features in shock-oscillation modulated neutrino and gravitational-wave signals from supernovae. *Astron. and Astrophys.*, 496(2):475–494, Mar 2009.

[155] Stefan Hild, Hartmut Grote, Martin Hewitson, Harald Lück, JR Smith, KA Strain, Benno Willke, and Karsten Danzmann. Demonstration and comparison of tuned and detuned signal recycling in a large-scale gravitational wave detector. *Classical and Quantum Gravity*, 24(6):1513, 2007.

[156] Robert Lawrence Ward. *Length sensing and control of a prototype advanced interferometric gravitational wave detector*. PhD thesis, California Institute of Technology, 2010.

[157] Brian J Meers. Recycling in laser-interferometric gravitational-wave detectors. *Physical Review D*, 38(8):2317, 1988.

[158] Vladimir B Braginsky and F Ya Khalili. Quantum nondemolition measurements: the route from toys to tools. *Reviews of Modern Physics*, 68(1):1, 1996.

[159] Benjamin P Abbott, R Abbott, TD Abbott, F Acernese, K Ackley, C Adams, T Adams, P Addesso, RX Adhikari, VB Adya, et al. Gw170817: Implications for the stochastic gravitational-wave background from compact binary coalescences. *Physical review letters*, 120(9):091101, 2018.

[160] M Abernathy, F Acernese, P Ajith, B Allen, P Amaro-Seoane, N Andersson, S Aoudia, P Astone, B Krishnan, L Barack, et al. Einstein Gravitational Wave Telescope Conceptual Design Study. Technical Report ET–0106C–10, Einstein Telescope, 2011.

[161] ET Steering Committee. ET design report update 2020. Technical Report ET-0007A-20, Einstein Telescope, nov 2020.

[162] J. Aasi et al. Advanced LIGO. *Class. Quant. Grav.*, 32:074001, 2015.

[163] F. Acernese et al. Advanced Virgo: a second-generation interferometric gravitational wave detector. *Class. Quant. Grav.*, 32(2):024001, 2015.

[164] Vicky Kalogera, BS Sathyaprakash, Matthew Bailes, Marie-Anne Bizouard, Alessandra Buonanno, Adam Burrows, Monica Colpi, Matt Evans, Stephen Fairhurst, Stefan Hild, et al. The next generation global gravitational wave observatory: The science book. *arXiv preprint arXiv:2111.06990*, 2021.

[165] Michele Maggiore, Chris Van Den Broeck, Nicola Bartolo, Enis Belgacem, Daniele Bertacca, Marie Anne Bizouard, Marica Branchesi, Sebastien Clesse, Stefano Foffa, Juan García-Bellido, and et al. Science case for the Einstein telescope. *JCAP*, 2020(3):050, March 2020.

[166] B. P. Abbott et al. Tests of general relativity with gw150914. *Phys. Rev. Lett.*, 116:221101, May 2016.

[167] B. P. Abbott et al. Tests of general relativity with the binary black hole signals from the ligo-virgo catalog gwtc-1. *Phys. Rev. D*, 100:104036, Nov 2019.

[168] R. Abbott et al. Tests of general relativity with binary black holes from the second ligo-virgo gravitational-wave transient catalog. *Phys. Rev. D*, 103:122002, Jun 2021.

[169] Emanuele Berti, Kent Yagi, Huan Yang, and Nicolás Yunes. Extreme gravity tests with gravitational waves from compact binary coalescences:(ii) ringdown. *General Relativity and Gravitation*, 50(5):1–37, 2018.

[170] Chris Van Den Broeck. The gravitational wave spectrum of non-axisymmetric, freely precessing neutron stars. *Classical and Quantum Gravity*, 22(9):1825–1839, apr 2005.

[171] Maximiliano Isi, Matthew Pitkin, and Alan J. Weinstein. Probing dynamical gravity with the polarization of continuous gravitational waves. *Phys. Rev. D*, 96:042001, Aug 2017.

[172] Magdalena Sieniawska and Michał Bejger. Continuous gravitational waves from neutron stars: Current status and prospects. *Universe*, 5(11), 2019.

[173] B. P. Abbott et al. Binary black hole population properties inferred from the first and second observing runs of advanced LIGO and advanced virgo. *The Astrophysical Journal*, 882(2):L24, sep 2019.

[174] R. Abbott et al. Population properties of compact objects from the second LIGO–virgo gravitational-wave transient catalog. *The Astrophysical Journal Letters*, 913(1):L7, may 2021.

[175] Tanja Hinderer, Andrea Taracchini, Francois Foucart, Alessandra Buonanno, Jan Steinhoff, Matthew Duez, Lawrence E. Kidder, Harald P. Pfeiffer, Mark A. Scheel, Bela Szilagyi, Kenta Hotokezaka, Koutarou Kyutoku, Masaru Shibata,

and Cory W. Carpenter. Effects of neutron-star dynamic tides on gravitational waveforms within the effective-one-body approach. *Phys. Rev. Lett.*, 116:181101, May 2016.

[176] Tim Dietrich, Sebastiano Bernuzzi, and Wolfgang Tichy. Closed-form tidal approximants for binary neutron star gravitational waveforms constructed from high-resolution numerical relativity simulations. *Phys. Rev. D*, 96(12):121501, 2017.

[177] Tim Dietrich, Sebastian Khan, Reetika Dudi, Shasvath J. Kapadia, Prayush Kumar, Alessandro Nagar, Frank Ohme, Francesco Pannarale, Anuradha Samajdar, Sebastiano Bernuzzi, Gregorio Carullo, Walter Del Pozzo, Maria Haney, Charalampos Markakis, Michael Pürrer, Gunnar Riemenschneider, Yoshinta Eka Setyawati, Ka Wa Tsang, and Chris Van Den Broeck. Matter imprints in waveform models for neutron star binaries: Tidal and self-spin effects. *Phys. Rev. D*, 99:024029, Jan 2019.

[178] B. P. Abbott et al. Multi-messenger observations of a binary neutron star merger. *The Astrophysical Journal*, 848(2):L12, oct 2017.

[179] David Radice, Albino Perego, Francesco Zappa, and Sebastiano Bernuzzi. GW170817: Joint constraint on the neutron star equation of state from multi-messenger observations. *The Astrophysical Journal*, 852(2):L29, jan 2018.

[180] David Radice and Liang Dai. Multimessenger parameter estimation of gw170817. *The European Physical Journal A*, 55(4):1–7, 2019.

[181] R. X. Adhikari et al. A cryogenic silicon interferometer for gravitational-wave detection. *Class. Quant. Grav.*, 37(16):165003, 2020.

[182] K. Ackley et al. Neutron star extreme matter observatory: A kilohertz-band gravitational-wave detector in the global network. *Publications of the Astronomical Society of Australia*, 37:e047, November 2020.

[183] Evan D. Hall et al. Gravitational-wave physics with Cosmic Explorer: Limits to low-frequency sensitivity. *Phys. Rev. D*, 103(12):122004, 2021.

[184] T. Akutsu et al. KAGRA: 2.5 Generation Interferometric Gravitational Wave Detector. *Nature Astron.*, 3(1):35–40, 2019.

[185] J. Mizuno, K. A. Strain, P. G. Nelson, J. M. Chen, R. Schilling, A. Rüdiger, W. Winkler, and K. Danzmann. Resonant sideband extraction: a new configuration for interferometric gravitational wave detectors. *Physics Letters A*, 175(5):273–276, April 1993.

[186] Denis Martynov et al. Exploring the sensitivity of gravitational wave detectors to neutron star physics. *Phys. Rev. D*, 99(10):102004, 2019.

[187] Reed Essick, Salvatore Vitale, and Matthew Evans. Frequency-dependent responses in third generation gravitational-wave detectors. *Phys. Rev. D*, 96(8):084004, 2017.

[188] Tim Dietrich, Tanja Hinderer, and Anuradha Samajdar. Interpreting binary neutron star mergers: describing the binary neutron star dynamics, modelling gravitational waveforms, and analyzing detections. *GReGr*, 53(3):27, March 2021.

[189] Andreas Bauswein, Nikolaos Stergioulas, and Hans-Thomas Janka. Exploring properties of high-density matter through remnants of neutron-star mergers. *European Physical Journal A*, 52:56, March 2016.

[190] A. Bauswein and H. T. Janka. Measuring Neutron-Star Properties via Gravitational Waves from Neutron-Star Mergers. *Phys. Rev. Lett.*, 108(1):011101, January 2012.

[191] A Bauswein, H-T Janka, K Hebeler, and A Schwenk. Equation-of-state dependence of the gravitational-wave signal from the ring-down phase of neutron-star mergers. *Physical Review D*, 86(6):63001, 2012.

[192] A. Bauswein and N. Stergioulas. Unified picture of the post-merger dynamics and gravitational wave emission in neutron star mergers. *Phys. Rev. D*, 91(12):124056, June 2015.

[193] Nikhil Sarin and Paul D. Lasky. The evolution of binary neutron star post-merger remnants: a review. *GReGr*, 53(6):59, June 2021.

[194] Andreas Bauswein, Niels-Uwe F. Bastian, David B. Blaschke, Katerina Chatziioannou, James A. Clark, Tobias Fischer, and Micaela Oertel. Identifying a First-Order Phase Transition in Neutron-Star Mergers through Gravitational Waves. *PhRvL*, 122(6):061102, February 2019.

[195] Elias R. Most, L. Jens Papenfort, Veronica Dexheimer, Matthias Hanauske, Stefan Schramm, Horst Stöcker, and Luciano Rezzolla. Signatures of Quark-Hadron Phase Transitions in General-Relativistic Neutron-Star Mergers. *PhRvL*, 122(6):061101, February 2019.

[196] J. A. Clark, A. Bauswein, N. Stergioulas, and D. Shoemaker. Observing gravitational waves from the post-merger phase of binary neutron star coalescence. *Classical and Quantum Gravity*, 33(8):085003, April 2016.

[197] Andoni Torres-Rivas, Katerina Chatziioannou, Andreas Bauswein, and James Alexander Clark. Observing the post-merger signal of GW170817-like events with improved gravitational-wave detectors. *Phys. Rev. D*, 99(4):044014, February 2019.

[198] Tim Dietrich, David Radice, Sebastiano Bernuzzi, Francesco Zappa, Albino Perego, Bernd Brügmann, Swami Vivekanandji Chaurasia, Reetika Dudi, Wolfgang Tichy, and Maximiliano Ujevic. CoRe database of binary neutron star merger waveforms. *CQGra*, 35(24):24LT01, December 2018.

[199] Jocelyn S. Read, Luca Baiotti, Jolien D. E. Creighton, John L. Friedman, Bruno Giacomazzo, Koutarou Kyutoku, Charalampos Markakis, Luciano Rezzolla, Masaru Shibata, and Keisuke Taniguchi. Matter effects on binary neutron star waveforms. *PhRvD*, 88(4):044042, August 2013.

[200] B. P. Abbott et al. Gw170817: Measurements of neutron star radii and equation of state. *Phys. Rev. Lett.*, 121:161101, Oct 2018.

[201] Soumi De, Daniel Finstad, James M. Lattimer, Duncan A. Brown, Edo Berger, and Christopher M. Biwer. Tidal Deformabilities and Radii of Neutron Stars from the Observation of GW170817. *Phys. Rev. Lett.*, 121(9):091102, 2018. [Erratum: Phys.Rev.Lett. 121, 259902 (2018)].

[202] Zack Carson, Katerina Chatziioannou, Carl-Johan Haster, Kent Yagi, and Nicolás Yunes. Equation-of-state insensitive relations after GW170817. *Phys. Rev. D*, 99(8):083016, April 2019.

[203] Collin D Capano, Ingo Tews, Stephanie M Brown, Ben Margalit, Soumi De, Sumit Kumar, Duncan A Brown, Badri Krishnan, and Sanjay Reddy. Stringent constraints on neutron-star radii from multimessenger observations and nuclear theory. *Nature Astronomy*, 4:625–632, 2020.

[204] M. C. Miller, F. K. Lamb, A. J. Dittmann, S. Bogdanov, Z. Arzoumanian, K. C. Gendreau, S. Guillot, A. K. Harding, W. C. G. Ho, J. M. Lattimer, and et al. PSR J0030+0451 Mass and Radius from NICER Data and Implications for the Properties of Neutron Star Matter. *ApJL*, 887(1):L24, December 2019.

[205] T. E. Riley, A. L. Watts, S. Bogdanov, P. S. Ray, R. M. Ludlam, S. Guillot, Z. Arzoumanian, C. L. Baker, A. V. Bilous, D. Chakrabarty, and et al. A NICER View of PSR J0030+0451: Millisecond Pulsar Parameter Estimation. *ApJL*, 887(1):L21, December 2019.

[206] M. C. Miller, F. K. Lamb, A. J. Dittmann, S. Bogdanov, Z. Arzoumanian, K. C. Gendreau, S. Guillot, W. C. G. Ho, J. M. Lattimer, M. Loewenstein, and et al. The Radius of PSR J0740+6620 from NICER and XMM-Newton Data. *arXiv*, page arXiv:2105.06979, May 2021.

[207] Thomas E. Riley, Anna L. Watts, Paul S. Ray, Slavko Bogdanov, Sebastien Guillot, Sharon M. Morsink, Anna V. Bilous, Zaven Arzoumanian, Devarshi Choudhury, Julia S. Deneva, and et al. A NICER View of the Massive Pulsar PSR J0740+6620 Informed by Radio Timing and XMM-Newton Spectroscopy. *arXiv*, page arXiv:2105.06980, May 2021.

[208] Sukanta Bose, Kabir Chakravarti, Luciano Rezzolla, B. S. Sathyaprakash, and Kentaro Takami. Neutron-star radius from a population of binary neutron star mergers. *Phys. Rev. Lett.*, 120:031102, Jan 2018.

[209] Ka Wa Tsang, Tim Dietrich, and Chris Van Den Broeck. Modeling the post-merger gravitational wave signal and extracting binary properties from future binary neutron star detections. *Phys. Rev. D*, 100:044047, Aug 2019.

[210] Thibault Damour, Alessandro Nagar, and Loic Villain. Measurability of the tidal polarizability of neutron stars in late-inspiral gravitational-wave signals. *Phys. Rev. D*, 85:123007, 2012.

[211] Tim Dietrich et al. Matter imprints in waveform models for neutron star binaries: Tidal and self-spin effects. *Phys. Rev. D*, 99(2):024029, 2019.

[212] S. E. Woosley and Thomas A. Weaver. The Evolution and Explosion of Massive Stars. II. Explosive Hydrodynamics and Nucleosynthesis. *Astrophysical Journal Supplement Series*, 101:181, November 1995.

[213] Jeremiah P. Ostriker and Nickolay Y. Gnedin. Reheating of the universe and population III. *The Astrophysical Journal*, 472(2):L63–L67, dec 1996.

[214] Volker Bromm, Paolo S. Coppi, and Richard B. Larson. The formation of the first stars. i. the primordial star-forming cloud. *The Astrophysical Journal*, 564(1):23–51, jan 2002.

[215] A. Heger and S. E. Woosley. The nucleosynthetic signature of population III. *The Astrophysical Journal*, 567(1):532–543, mar 2002.

[216] D. Schaerer. On the properties of massive Population III stars and metal-free stellar populations. *Astron. and Astrophys.*, 382:28–42, January 2002.

[217] Laura Ferrarese and David Merritt. A fundamental relation between supermassive black holes and their host galaxies. *The Astrophysical Journal*, 539(1):L9–L12, aug 2000.

[218] John Kormendy and Luis C. Ho. Coevolution (or not) of supermassive black holes and host galaxies. *Annual Review of Astronomy and Astrophysics*, 51(1):511–653, 2013.

[219] Jenny E. Greene, Jay Strader, and Luis C. Ho. Intermediate-mass black holes. *Annual Review of Astronomy and Astrophysics*, 58(1):257–312, 2020.

[220] Ken K. Y. Ng, Salvatore Vitale, Will M. Farr, and Carl L. Rodriguez. Probing multiple populations of compact binaries with third-generation gravitational-wave detectors. *The Astrophysical Journal Letters*, 913(1):L5, may 2021.

[221] Emanuele Berti, Kent Yagi, and Nicolás Yunes. Extreme gravity tests with gravitational waves from compact binary coalescences:(i) inspiral–merger. *General Relativity and Gravitation*, 50(4):1–45, 2018.

[222] Vitor Cardoso, Masashi Kimura, Andrea Maselli, Emanuele Berti, Caio F. B. Macedo, and Ryan McManus. Parametrized black hole quasinormal ringdown: Decoupled equations for nonrotating black holes. *Phys. Rev. D*, 99:104077, May 2019.

[223] Varun Srivastava, Stefan Ballmer, Duncan A. Brown, Chaitanya Afle, Adam Burrows, David Radice, and David Vartanyan. Detection prospects of core-collapse supernovae with supernova-optimized third-generation gravitational-wave detectors. *Phys. Rev. D*, 100:043026, Aug 2019.

[224] Francisco Hernandez Vivanco, Rory Smith, Eric Thrane, Paul D. Lasky, Colm Talbot, and Vivien Raymond. Measuring the neutron star equation of state with gravitational waves: The first forty binary neutron star merger observations. *Phys. Rev. D*, 100(10):103009, 2019.

[225] C. Messenger and J. Read. Measuring a cosmological distance-redshift relationship using only gravitational wave observations of binary neutron star coalescences. *Phys. Rev. Lett.*, 108:091101, 2012.

[226] S. Smerechynskyi, M. Tsizh, and B. Novosyadlyj. Impact of dynamical dark energy on the neutron star equilibrium. *JCAP*, 02:045, 2021.

[227] Tolga Güver, Arif Emre Erkoca, Mary Hall Reno, and Ina Sarcevic. On the capture of dark matter by neutron stars. *JCAP*, 05:013, 2014.

[228] Haixing Miao, Nicolas D. Smith, and Matthew Evans. Quantum Limit for Laser Interferometric Gravitational-Wave Detectors from Optical Dissipation. *Physical Review X*, 9(1):011053, January 2019.

[229] R. A. Day, G. Vajente, M. Kasprzack, and J. Marque. Reduction of higher order mode generation in large scale gravitational wave interferometers by central heating residual aberration correction. *Phys. Rev. D*, 87:082003, Apr 2013.

[230] H Wittel, H Lück, C Affeldt, K L Dooley, H Grote, J R Leong, M Prijatelj, E Schreiber, J Slutsky, K Strain, M Was, B Willke, and K Danzmann. Thermal correction of astigmatism in the gravitational wave observatory GEO 600. *Classical and Quantum Gravity*, 31(6):065008, feb 2014.

[231] Aidan F. Brooks, Benjamin Abbott, Muzammil A. Arain, Giacomo Ciani, Ayodele Cole, Greg Grabeel, Eric Gustafson, Chris Guido, Matthew Heintze, Alastair Heptonstall, Mindy Jacobson, Won Kim, Eleanor King, Alexander Lynch, Stephen O'Connor, David Ottaway, Ken Mailand, Guido Mueller, Jesper Munch, Virginio Sannibale, Zhenhua Shao, Michael Smith, Peter Veitch, Thomas Vo, Cheryl Vorvick, and Phil Willems. Overview of advanced ligo adaptive optics. *Appl. Opt.*, 55(29):8256–8265, Oct 2016.

[232] Sebastian Steinlechner, Niels-Ole Rohweder, Mikhail Korobko, Daniel Töyrä, Andreas Freise, and Roman Schnabel. Mitigating mode-matching loss in nonclassical laser interferometry. *Phys. Rev. Lett.*, 121:263602, Dec 2018.

[233] H. Wittel, C. Affeldt, A. Bisht, S. Doravari, H. Grote, J. Lough, H. Lück, E. Schreiber, K. A. Strain, and K. Danzmann. Matrix heater in the gravitational wave observatory geo 600. *Opt. Express*, 26(18):22687–22697, Sep 2018.

[234] Varun Srivastava, Georgia Mansell, Camille Makarem, Minkyun Noh, Richard Abbott, Stefan Ballmer, GariLynn Billingsley, Aidan Brooks, Huy Tuong Cao, Peter Fritschel, Don Griffith, Wenxuan Jia, Marie Kasprzack, Myron MacInnis, Sebastian Ng, Luis Sanchez, Calum Torrie, Peter Veitch, and Fabrice Matichard. Piezo-deformable Mirrors for Active Mode Matching in Advanced LIGO. *arXiv e-prints*, page arXiv:2110.00674, October 2021.

[235] Aaron Buikema et al. Sensitivity and performance of the Advanced LIGO detectors in the third observing run. *Phys. Rev. D*, 102(6):062003, 2020.

[236] Kazuhiro Agatsuma, Laura van der Schaaf, Martin van Beuzekom, David Rabeling, and Jo van den Brand. High-performance phase camera as a frequency selective laser wavefront sensor for gravitational wave detectors. *Opt. Express*, 27(13):18533–18548, Jun 2019.

[237] Huy Tuong Cao, Daniel D. Brown, Peter J. Veitch, and David J. Ottaway. Optical lock-in camera for gravitational wave detectors. *Opt. Express*, 28(10):14405–14413, May 2020.

[238] Erik Muñiz, Varun Srivastava, Subham Vidyant, and Stefan W. Ballmer. High frame-rate phase camera for high-resolution wavefront sensing in gravitational-wave detectors. *Phys. Rev. D*, 104:042002, Aug 2021.

[239] Daniel Brown, Huy Tuong Cao, Alexei Ciobanu, Peter Veitch, and David Ottaway. Differential wavefront sensing and control using radio-frequency optical demodulation. *Opt. Express*, 29(11):15995–16006, May 2021.

[240] Samuel Rowlinson, Artemiy Dmitriev, Aaron W. Jones, Teng Zhang, and Andreas Freise. Feasibility study of beam-expanding telescopes in the interferometer arms for the einstein telescope. *Phys. Rev. D*, 103:023004, Jan 2021.

[241] B. P. Abbott et al. Exploring the sensitivity of next generation gravitational wave detectors. *Classical and Quantum Gravity*, 34(4):044001, February 2017.

[242] John Miller, Lisa Barsotti, Salvatore Vitale, Peter Fritschel, Matthew Evans, and Daniel Sigg. Prospects for doubling the range of Advanced LIGO. *Phys. Rev. D*, 91:062005, 2015.

[243] Gabriele Vajente, Le Yang, Aaron Davenport, Mariana Fazio, Alena Ananyeva, Liyuan Zhang, Garilynn Billingsley, Kiran Prasai, Ashot Markosyan, Riccardo Bassiri, Martin M. Fejer, Martin Chicoine, François Schiettekatte, and Carmen S. Menoni. Low Mechanical Loss TiO_2 :GeO_2 Coatings for Reduced Thermal Noise in Gravitational Wave Interferometers. *Phys. Rev. Lett.*, 127(7):071101, August 2021.

[244] Steven D. Penn, Maya M. Kinley-Hanlon, Ian A. O. MacMillan, Paula Heu, David Follman, Christoph Deutsch, Garrett D. Cole, and Gregory M. Harry. Mechanical ringdown studies of large-area substrate-transferred gaas/algaas crystalline coatings. *J. Opt. Soc. Am. B*, 36(4):C15–C21, Apr 2019.

[245] P. Koch, G. D. Cole, C. Deutsch, D. Follman, P. Heu, M. Kinley-Hanlon, R. Kirchhoff, S. Leavey, J. Lehmann, P. Oppermann, A. K. Rai, Z. Tornasi,

J. Wöhler, D. S. Wu, T. Zederbauer, and H. Lück. Thickness uniformity measurements and damage threshold tests of large-area GaAs/AlGaAs crystalline coatings for precision interferometry. *Optics Express*, 27(25):36731, December 2019.

[246] Pawel O. Mazur and Emil Mottola. Gravitational vacuum condensate stars. *Proceedings of the National Academy of Sciences*, 101(26):9545–9550, 2004.

[247] Cecilia B M H Chirenti and Luciano Rezzolla. How to tell a gravastar from a black hole. *Classical and Quantum Gravity*, 24(16):4191–4206, jul 2007.

[248] Cecilia Chirenti and Luciano Rezzolla. Did gw150914 produce a rotating gravastar? *Phys. Rev. D*, 94:084016, Oct 2016.

[249] Vitor Cardoso, Edgardo Franzin, and Paolo Pani. Is the gravitational-wave ringdown a probe of the event horizon? *Phys. Rev. Lett.*, 116:171101, Apr 2016.

[250] Randy S. Conklin. Gravitational wave perturbations on a kerr background and applications for echoes. *Phys. Rev. D*, 101:044045, Feb 2020.

[251] Ssohrab Borhanian and B Sathyaprakash. Listening to the universe with next generation ground-based gravitational-wave detectors. *In preparation*, 2021.

Varun Srivastava

Publication List

2665 Kingsgate Way, Apt A208
Richland, WA
USA 99354
☎ *+1 (315) 515 7389*
✉ *vasrivas@syr.edu*

Selected Publications

1. **Piezo-deformable Mirrors for Active Mode Matching in Advanced LIGO**, Varun Srivastava, Georgia Mansell, Camille Makarem, Minkyun Noh, Richard Abbott, Stefan Ballmer, GariLynn Billingsley, Aidan Brooks, Huy Tuong Cao, Peter Fritschel, Don Griffith, Wenxuan Jia, Marie Kasprzack, Myron MacInnis, Sebastian Ng, Luis Sanchez, Calum Torrie, Peter Veitch, Fabrice Matichard, arxiv:2110.00674.
2. **A Horizon Study for Cosmic Explorer: Science, Observatories, and Community**, Matthew Evans, Rana X Adhikari, Chaitanya Afle, Stefan W. Ballmer, Sylvia Biscoveanu, Ssohrab Borhanian, Duncan A. Brown, Yanbei Chen, Robert Eisenstein, Alexandra Gruson, Anuradha Gupta, Evan D. Hall, Rachael Huxford, Brittany Kamai, Rahul Kashyap, Jeff S. Kissel, Kevin Kuns, Philippe Landry, Amber Lenon, Geoffrey Lovelace, Lee McCuller, Ken K. Y. Ng, Alexander H. Nitz, Jocelyn Read, B. S. Sathyaprakash, David H. Shoemaker, Bram J. J. Slagmolen, Joshua R. Smith, Varun Srivastava, Ling Sun, Salvatore Vitale, Rainer Weiss, arxiv:2109.09882.
3. **High Frame-Rate Phase Camera for High-Resolution Wavefront Sensing in Gravitational-Wave Detectors**, Erik Muñiz*, Varun Srivastava*, Subham Vidyant and Stefan W. Ballmer, Physics Review D 104, 042002, 2021.
4. **Detection Prospects of Core-Collapse Supernovae with Supernova-Optimized Third-Generation Gravitational-Wave Detectors**, Varun Srivastava, Stefan Ballmer, Duncan A. Brown, Chaitanya Afle, Adam Burrows, David Radice, and David Vartanyan, Physics Review D 100, 043026, 2019.
5. **Toward Low-Latency Coincident Precessing and Coherent Aligned-Spin Gravitational-Wave Searches of Compact Binary Coalescences with Particle Swarm Optimization**, Varun Srivastava, K Rajesh Nayak and Sukanta Bose, arxiv:1811.02401.
6. **Geographic and Annual Influences on Optical Follow-up of Gravitational Wave Events**, Varun Srivastava, Varun Bhalerao, Aravind P. Ravi, Archisman Ghosh, and Sukanta Bose, The Astrophysical Journal, 838, 1, 46, 2017.

Publications In Preparation

1. **Science-Driven Tunable design of Cosmic Explorer Detectors**
Varun Srivastava, Derek Davis, Kevin Kuns, Philippe Landry, Stefan Ballmer, Matt Evans, Evan Hall, Jocelyn Read, and B.S. Sathyaprakash.
2. **Differentiating Between the Neutron-Star Equation of State from Post-Merger Signal**
Sunil Choudhary, Varun Srivastava, Sukanta Bose et. al.

Selected LIGO/CE Technical Documents

1. **Understanding Dynamics of Dense Matter through Observation of Astrophysical Populations**,
   Varun Srivastava, Philippe Landry, Stefan Ballmer and Jocelyn Read, CE–T2100010
2. **Cosmic Explorer Horizon Study: Metric for Black Holes and Neutron Stars Throughout Cosmic Time, and Testing General Relativity.**
   Varun Srivastava, Kevin Kuns, Evan Hall, Stefan Ballmer and Salvatore Vitale, CE–T2100009
3. **Cryogenic Budget for CE2: Silicon**
   Varun Srivastava, Stefan Ballmer, Kevin Kuns and Christopher Wipf, CE–G2100004
4. **Sensitivity Curves for the Cosmic Explorer Trade Study**
   Varun Srivastava, Kevin Kuns, Evan Hall, Stefan Ballmer and Matt Evans, CE-T2000007
5. **Results of SAMS Piezo Deformable Mirror Flexure with Zygo Interferometer**
   Varun Srivastava, Georgia Mansell, Fabrice Matichard et al. LIGO-T2000381

Drafts of the publications in preparation can be requested. The technical documents with restricted access to LVK members can be shared with confidentiality.

2665 Kingsgate Way, Apt A208
Richland, WA
USA 99354
☎ *+1 (315) 515 7389*
✉ *vasrivas@syr.edu*

Varun Srivastava

Education

2017-Present **PhD, Physics**, *Syracuse University*, Syracuse, NY, USA.

2012–2017 **Joint BS-MS with distinction, Physics**, *Indian Institute of Science Education and Research (IISER)*, Pune, India.

Skills

Programming Languages: C++, Python, and Matlab.
Optics: Lasers, Laser amplifiers, PDH locking, mode-matching, modulators, wavefront sensing, sensors.
Optics Simulation and Control: Finesse, GracedB, and Simulink. Control loop and feedback design.
Imaging and Sensors: Time-of-flight sensors, Zygo image processing.
Data Analysis: (`LIGO`) PyCBC, LSCSofts and LALSuite. (`CERN`) ROOT. Bayesian inference, optimization.
Electronics: Programming micro-controllers (μVision, CubeMX), LabView(some), and Eagle.
3D Designs: Autodesk Inventor, Tinkercad and 3D printing.
Condensed Matter: Floating-zone, X-ray diffraction, and scanning electron microscopy.

Research Experience

Aug. 2017 – Present **Research Assistant**, *Syracuse University, Syracuse NY, Supervisor: Prof. Stefan Ballmer*.

- Develop a high frame-rate phase camera for high-resolution wavefront sensing in visible-near infrared using a time-of-flight sensor.
- Design and test a novel low noise, high-bandwidth, ultra-high vacuum compatible, flexure-based piezo-deformable actuator for active wavefront control and mode-matching.
- Optimize the design of Cosmic Explorer detectors to offer science-driven tunable configurations.
- Explore the detection prospects of gravitational waves from core-collapse supernovae with third-generation supernova-optimized third-generation gravitational-wave detectors.
- Heat budget for silicon mirrors to choose the design parameters of an alternate design of cryogenic Cosmic Explorer, and characterize metrics for science goals of Cosmic Explorer.
- Measure absolute distances with sub-micrometer precision in real time for precision measurement of the gravitational constant.
- Set up angular sensing and control schemes for LIGO Hanford observatory.
- Investigate output-beam jitter coupling at the aLIGO observatories.
- Upgrading the high-power pre-stabilized laser at LIGO Hanford.

May 2016 – Aug. 2017 **Research Intern**, *IUCAA Pune, Supervisors: Prof. Rajesh Nayak and Prof. Sukanta Bose*.
Development of the particle swarm optimization (PSO) algorithm to search for gravitational waves at reduced computational cost and improved parameter estimation during the detection stage.

Aug. 2015 – May 2016 **Project Student**, *IUCAA Pune, Supervisors: Dr. Varun Bhalerao and Prof. Sukanta Bose*.
Study geographic and annual influences on optical follow-up of gravitational wave events to facilitate the locational choice for a global array of telescopes for electromagnetic follow-up.

May – Aug. 2015 **Summer Intern**, *AEI Hannover, Supervisor: Prof. Harald Lück*.
Design a vacuum compatible electro-optic modulator for the reference cavity to stabilize the laser, and design control loops for the auto-alignment of the laser beam.

Jan. – Apr. 2015 **Project Student**, *IISER Pune, Supervisor: Prof. Surjeet Singh*.
Experimental condensed matter; synthesis of spin-ladder crystals using floating-zone method. Use X-ray diffraction and scanning electron microscope to investigate crystal structure.

May 2014 – Apr. 2015 **Research Intern**, *IISER Pune, Supervisors: Prof. Sourabh Dube and Prof. Seema Sharma*.
Constrain the lower-mass limit on the existence of the doubly-charged Higgs particle using the observed cross-section by the ATLAS collaboration.

Scholarships and Achievements

1. **LSC Fellow, LIGO Lab, Hanford**: 2020-2022.
2. **Syracuse University Fellow**: 2019 – 2020.
3. **Syracuse University Fellow**: 2017 – 2018.
4. **AEI Hannover, DAAD-WISE Scholar**: 2015.
5. **DST-INSPIRE Fellow**: 2012 – 2017.
6. **Madhava Mathematics Olympiad Merit**: 2013.

Selected Publications and LIGO/CE Technical Documents

Selected Publications in experimental optics, electronics and big-data analysis.

1. **Piezo-deformable Mirrors for Active Mode Matching in Advanced LIGO**, Varun Srivastava, Georgia Mansell, Camille Makarem et al. arxiv:2110.00674.
2. **A Horizon Study for Cosmic Explorer: Science, Observatories, and Community**, Matthew Evans et al. arxiv:2109.09882.
3. **High Frame-Rate Phase Camera for High-Resolution Wavefront Sensing in Gravitational-Wave Detectors**, Erik Muñiz*, Varun Srivastava*, Subham Vidyant and Stefan W. Ballmer, Physics Review D 104, 042002, 2021.
4. **Detection Prospects of Core-Collapse Supernovae with Supernova-Optimized Third-Generation Gravitational-Wave Detectors**, Varun Srivastava, Stefan Ballmer, Duncan A. Brown et al. Physics Review D 100, 043026, 2019.
5. **Toward Low-Latency Coincident Precessing and Coherent Aligned-Spin Gravitational-Wave Searches of Compact Binary Coalescences with Particle Swarm Optimization**, Varun Srivastava, K Rajesh Nayak and Sukanta Bose, arxiv:1811.02401.
6. **Geographic and Annual Influences on Optical Follow-up of Gravitational Wave Events**, Varun Srivastava, Varun Bhalerao, Aravind P. Ravi, Archisman Ghosh, and Sukanta Bose, The Astrophysical Journal, 838, 1, 46, 2017.
7. *In preparation* **Science-Driven Tunable Design of Cosmic Explorer Detectors**, Varun Srivastava, Derek Davis, Kevin Kuns et al.
8. *In preparation* **Differentiating Between the Neutron Star Equation of State from the Post-Merger Signal**, Sunil Choudhary, Varun Srivastava, Sukanta Bose et al.

SELECTED FIRST AUTHOR TECHNICAL DOCUMENTS

Cryogenic heat budget for Cosmic Explorer silicon detector, CE–G2100004.
Metric for black holes and neutron stars throughout cosmic time, and testing general relativity, CE-T2100009.
Understanding dynamics of dense matter through observation of astrophysical populations, CE-T2100010.